(NASA-CR-151559) DETECTION OF LONG WAVELENGTH INFRARED AT MODERATE TEMPERATURES Final Report (Honeywell, Inc.) 191 p HC A09/MF A01 CSCL 20F

N78-13876

G3/74 Unclas 53659

DETECTION OF LONG WAVELENGTH INFRARED AT MODERATE TEMPERATURES

FINAL TECHNICAL REPORT

APRIL 1977

NASA CONTRACT NAS9-14180, MODIFICATION 5S

Prepared for

NATIONAL AERONAUTICS AND SPACE ADMINISTRATION
LYNDON B. JOHNSON SPACE CENTER
HOUSTON, TEXAS 77058

Prepared by:

T.J. Tredwell
Project Engineer

Approved by:

M.B. Reine
Program Manager

HONEYWELL
Defense Electronics Division
Electro-Optics Center
2 Forbes Road
Lexington, Massachusetts 02173

PREFACE

This is the final technical report for NASA Contract NAS9-14180, Modification 5S, entitled "Detection of Long Wavelength Infrared at Moderate Temperatures". This report covers work performed during the period from November 1, 1975 through March 15, 1977.

This work was performed for NASA Lyndon B. Johnson Space Center, Houston, Texas by the Honeywell Electro-Optics Center (EOC) in Lexington, Massachusetts in cooperation with the Honeywell Corporate Research Center (CRC) in Bloomington, Minnesota.

The Contract Monitor for this program was Mr. James E. Kessel of NASA Lyndon B. Johnson Space Center. Mr. Richard R. Pichard of NASA Lyndon B. Johnson Space Center initiated this program and was Contract Monitor during its initial months.

The Project Engineer for this program was Dr. Timothy J. Tredwell and the Program Manager was Dr. Marion B. Reine.

Due to the wide diversity of areas investigated, the program required contributions from a number of people. Section 2 ("Signal and Noise in Quantum Detectors") and Section 3 ("Materials for Quantum Detectors") were prepared by Dr. G. D. Long of Honeywell Corporate Research Center with assistance from Dr. Paul Peterson and Mr. S. Schuldt also of Honeywell Corporate Research Center. Section 4 ("Present Performance and Ultimate Limits of Photodiodes") and Section 5 ("Present performance and Ultimate Limits of Photoconductors") were prepared by Dr. T. J. Tredwell with assistance from Mr. S. J. Tobin. Section 6 ("Pyroelectric Detectors") was prepared by Dr. P. C. Leung with assistance from Dr. A. M. Chiang, and Dr. N. R. Butler. Section 7 ("Conclusion and Recommendations") was prepared by Drs. T. J. Tredwell and G. D. Long.

TABLE OF CONTENTS

TABLE OF CONTENTS (Contd)

SECTION 1

INTRODUCTION

Detection of infrared radiation in the 8 to 12 micrometer spectral band has found widespread application during the past two decades for a variety of space, military and industrial applications. The atmospheric transmission window at 8 to 12 micrometers, combined with the occurrence at approximately 10 micrometers of the peak in the spectral power distribution for emission from a 300 K blackbody radiator, have made this band important for collection of thermal information about the earth from a satellite.

For satellite-based applications, the operating temperature of the detector is of critical importance. For multi-spectral sensors, the visible channels may be operated at 300 K and the channels in the 1.55-2.35 micrometer spectral region may be operated at 193 K - 250 K. However, detectors for the 8 - 14 μm channel require cooling to 60 - 90 K. On the one hand, as the operating temperature is increased the detector sensitivity decreases rapidly. On the other hand, severe size, power and weight constraints for space operation dictate as high an operating temperature as possible. Thus, development of infrared detectors which are capable of operating at elevated temperatures with adequate sensitivity has substantial payoff in terms of sensor weight and cost.

1.1 PROGRAM OBJECTIVES

The objective of this study was to define the most promising technical approaches for the advanced development of 8-12 micrometer detectors operating at elevated temperatures. The investigation consisted of three tasks. The first task was to determine the theoretical limits to performance of 8-12 micrometer detectors. The two classes of detectors considered were quantum detectors (photoconductive and photovoltaic) and thermal detectors (pyroelectrics, bolometers etc). An analytic model of signal and noise in both quantum detectors and pyroelectric detectors was developed and candidate materials for both detector types identified and examined. The second task was to determine the present status of both quantum and thermal detectors and isolate the parameters limiting operating temperature and detectivity. The final task was to identify the areas of research and development likely to lead to detector performance near the theoretical limit.

1.2 PROGRAM SUMMARY

The two classes of detectors considered for detection of 8-12 micrometer radiation were quantum detectors and thermal detectors. Quantum detectors include photovoltaic detectors (such as p-n junctions, heterojunctions, Schottky barrier photodiodes and charge storage (CID) devices and photoconductive detectors, both intrinsic and extrinsic. Thermal detectors include bolometers and pyroelectric detectors. Of the thermal detectors, the pyroelectric appeared to offer the best

prospects for most NASA applications and was the only thermal detector studied in detail.

The first task was to determine the theoretical limits for elevated temperature operation of 8-14 μm quantum detectors. Due to the inherent disadvantage of extrinsic quantum detectors in operating temperature as compared to intrinsic quantum detectors, only intrinsic detectors were considered in detail.

The theory of intrinsic quantum detectors is considered in detail in Section 2. The signal mechanism is creation of electron-hole pairs by incoming radiation; the noise mechanism at high temperatures is thermal generation of electron-hole pairs. It was found that there is a theoretical limit to detectivity for quantum detectors which depends only on the bandgap of the semiconductor for E_g, the operating temperature T, and the index of refraction of the semiconductor n:

$$D^*_\lambda = \frac{0.32\,\lambda}{E_g\, n} \sqrt{\frac{h}{8\pi\, kT}} \exp\,(E_g/2kT) \qquad (1.1)$$

where λ is the wavelength, k is Boltzmann's constant and h is Planck's constant.

In order for a quantum detector to achieve that limit a number of conditions must be met. The most fundamental of these is a condition on the minority carrier lifetime. The maximum D^*_λ can be achieved if the minority carrier lifetime is limited only by radiative recombination.

In addition, it was found that for a photodiode or photoconductor to achieve the theoretical limit to detectivity, the semiconductor volume must be reduced to that necessary to collect signal. For a photodiode this can be achieved by an electrically-reflecting backside contact, a device design originally developed for silicon solar cells.

The second task was to identify candidate detector materials and determine material parameters. It was determined in Task 1 that all semiconductor materials of equal band-gaps could achieve approximately the same detectivity if they could achieve minority-carrier lifetimes limited only by radiative recombination. Thus, the primary objective of the study of materials for quantum detectors was to determine if any presently used material or any new material could achieve lifetimes limited only by radiation recombination.

The other recombination mechanisms which can limit lifetime are Auger recombination and Shockley-Read recombination. Shockley-Read recombination depends on the defects in the semiconductor and as such is not an inherent limitation. Auger recombination is a fundamental limitation and depends strongly on semiconductor band structures. On this program the general dependence of Auger lifetime on band structure was examined and calculations of Auger lifetime were made for both p-type (Hg,Cd)Te and degenerate n-type (Hg,Cd)Te.

Actual 8-14 μm detector materials fall well below the theoretical limit. The present performance of 8-14 μm photovoltaic and photoconductive detectors was examined. The objective of Task 3 was to assess present performance at elevated temperatures, model the available data to isolate the parameters limiting performance and finally to assess what improvement is possible. The results of this study are reported in Section 4 for photovoltaic detectors and Section 5 for photoconductive detectors.

In addition to quantum detectors, thermal detectors were also examined on this program. The thermal detector judged most likely to fulfill future NASA requirements was the pyroelectric; this type of detector was examined in detail. Pyroelectrics offer a fundamental advantage over quantum detectors in that they operate at room temperature. The disadvantages include low sensitivity, poor frequency response, low [illegible] requirements and difficulty in achieving high sensitivity in small area elements.

Of these disadvantages the low detectivity at moderate frequencies appears to be the most important. The theoretical limit to detectivity for a pyroelectric is 1.8×10^{10} cm $Hz^{\frac{1}{2}}/W$. The best present detectors approach within a factor of 3 of the theoretical limit at low frequencies (10 Hz) and large element size (0.6 mm diameter). The parameters limiting present pyroelectrics were examined and the development needed to achieve theoretical limited detectivity at moderate frequencies and small element sizes were assessed. The results of this study are given in Section 6.

Finally, based on the results of this study a number of conclusions emerged. These are summarized in Section 7 along with recommendations for further development.

SECTION 2

QUANTUM DETECTORS: SIGNAL & NOISE MECHANISMS

2.1 INTRODUCTION

Infrared quantum detectors must be cooled to achieve very high detectivity at long wavelengths. The longer the wavelength of maximum detector response, the lower must be the detector operating temperature. It is desirable in practice to be able to operate a detector with minimum cooling, i.e., at the highest possible temperature.

We address here in Section 2 the question of how the signal and noise mechanisms limit maximum possible operating temperature of an infrared quantum detector. In doing this we determine the spectral detectivity D^*_λ vs temperature T. We analyze this question from a very fundamental point of view by deriving the theoretically achievable detector performance, assuming that the detector performance is not limited by crystal defects in the active material of the detector or by the technology of detector fabrication (surface treatment, electrical contacts, etc). Thus we assume essentially perfect detector material and device technology in this fundamental analysis.

Many empirical studies have already been made of detectivity vs temperature in photovoltaic and photoconductive detectors, but the samples studied may not have had optimum properties. We want to establish the basic theoretical potentialities of the photovoltaic and intrinsic photoconductive modes with respect to operating temperature, because they are the detection modes used in photon detectors. We do not consider extrinsic photon detectors, because it is well known that they always require lower operating temperatures than the intrinsic detectors. Nor do we consider thermal detectors here (e.g., pyroelectrics).

We want to determine the temperature dependence of the maximum possible detectivity of a photon detector. The (spectral) detectivity D^*_λ is given in general by:

$$D^*_\lambda = R_\lambda(I_s)A^{1/2}(\Delta f)^{1/2}/I_n; \qquad (2.1)$$

see Table 2.1 for definition of symbols. The total noise current I_n is the summation in quadrature of the several different noise mechanisms limiting D^*_λ. In the following analysis we will assume that only the fundamental internal noise mechanisms in the detector are important; i.e., we will neglect such extraneous mechanisms as 1/f noise and noise in the signal-processing electronics, and will also neglect noise due to carriers generated by background radiation. This assumption is consistent with our objective of deriving the best theoretically achievable performance. However, this assumption must not be forgotten, because in practice these extraneous noise mechanisms may often not be negligible.

Table 2.1

DEFINITIONS OF SYMBOLS

A	Detector area absorbing photon flux
c	Speed of light
D	Carrier diffusion coefficient
D^*_λ	Spectral detectivity
e (subscript)	Electron
E	Energy of carrier
E_g	Energy gap
Δf	Frequency bandwidth
g, g_{th}	Generation rate of carriers, thermal generation rate
G	Photoconductive gain
h	Planck's constant
h (subscript)	Hole
I_b	Photocurrent due to background radiation
I_n	Noise current
I_s	Signal current
k	Electron or hole wavenumber
k_B	Boltzmann's constant
ℓ	Photoconductive detector length
L	Carrier diffusion length
n_i	Intrinsic carrier concentration
p (subscript)	Quantity in p-type region
q	Electronic charge
R	Detector resistance
R_r	Radiative recombination rate
R_λ	Spectral responsivity
t	Photoconductive detector thickness in direction of photon flux, or thickness of active layer in photovoltaic detector
T	Absolute temperature
V	Applied voltage
W	Space-charge layer width

Table 2.1

DEFINITIONS OF SYMBOLS (continued)

α	Optical absorption coefficient
η	Quantum efficiency
λ	Photon wavelength
μ	Carrier mobility
τ	Carrier lifetime
ϕ_b	Photon flux density from background

In the following subsections we will first analyze the photovoltaic mode to determine how its maximum possible detectivity depends upon temperature. Then we will compare the more complicated intrinsic photoconductive mode with the photovoltaic. Finally, we will draw conclusions from the results of these analyses, including their implications with respect to detector materials.

2.2 PHOTOVOLTAIC DETECTORS

2.2.1 General Theory

We will treat only pn junction photovoltaic detectors. Photovoltaic detectors are sometimes made alternatively as Schottky barriers, but even then the active region of the detector is often a pn junction within the material formed by surface-layer type inversion. Shot noise is the fundamental mechanism in photovoltaic (pv) detectors. The shot noise current is:(2.1,2.2)

$$I_n^2(pv) = 2q\left\{\frac{I_{sat}}{\beta}\left[\exp\left(qV/\beta k_B T\right) + 1\right]\right\}\Delta f \tag{2.2}$$

in a detector with a diode current-voltage characteristic of the form:

$$I = I_{sat}\left[\exp\left(qV/\beta k_B T\right) - 1\right], \tag{2.3}$$

where I_{sat} is the reverse-biased diode saturation current. We have $\beta = 1$ in an ideal pn junction in which there is only minority-carrier diffusion current. If electron-hole generation and recombination in the space-charge region of the pn junction also provided current, then we would have $1 < \beta < 2$. The current responsivity is:

$$R_\lambda\left(I_s\right) = q\eta\lambda/hc, \tag{2.4}$$

since $G = 1$ in a pv detector. Substituting equations 2.2 and 2.4 into equation 2.1, we get:

$$D^*_\lambda(pv) = \frac{\eta\lambda}{\sqrt{2}hc\sqrt{\frac{I_{sat}}{\beta qA}\left[\exp\left(qV/\beta kT\right) + 1\right]}}. \tag{2.5}$$

In practice a pv detector is invariably operated either unbiased ($V = 0$) or with a reverse (negative) bias voltage, so that the terms in square brackets in equation 2.5 lie between 2 and 1, causing a $\sqrt{2}$ variation in D^*_λ. The problem of maximizing D^*_λ mainly involves minimizing I_{sat}, as well as maximizing the quantum efficiency η.

Photovoltaic detectors are often characterized alternatively in terms of their "$R_o A$ products," where R_o is the dynamic junction resistance at zero bias voltage ($V = 0$) and A is the junction area. Since:

$$R_o = \left(\frac{dI}{dV}\right)_o^{-1}, \tag{2.6}$$

we get from equation 2.3:

$$R_o^{-1} = \frac{qI_{sat}}{\beta k_B T} \tag{2.7}$$

for $V = 0$, and then from equation 2.5 we get (at $v = 0$):

$$D^*_\lambda(pv) = \frac{\eta\lambda q}{hc}\sqrt{\frac{R_o A}{4k_B T}} \tag{2.8}$$

as the relationship between D^*_λ and $R_o A$. It is sometimes convenient to use $R_o A$, because this quantity is so easily measured on a pn junction.

2.2.2 Simple pn Junction

A general model of a pn junction pv detector is shown in Figure 2.1, following Melngailis and Harman.[2.1] The junction saturation current is composed in general of two components: current due to diffusion of minority carriers in the p- and n-type regions and current due to generation of electron-hole pairs within the junction space-charge layer of width W. We can reduce I_{sat} by doping both sides of the junction quite heavily to make W narrow and the minority-carrier concentrations low. The space-charge layer width W can often be made narrow enough that the generation current is negligible compared to the diffusion current, and this is the desired "best case." Furthermore, the D^*_λ or $R_o A$ product must ultimately be limited by diffusion current as the detector operating temperature is raised, because the diffusion current increases the most rapidly with temperature; see Figure 4.1. There will be no loss of generality in our conclusions by assuming for simplicity that the p-type region in Figure 2.1 is much less heavily doped than the n-type region and of such a design that hole diffusion current in the n-type region can be neglected; however, we will discuss this assumption further later in 2.2.3.

Then we have the familiar expression:[2.3]

$$I_{sat} = \frac{qAD_e p}{L_e} = \frac{qAL_e p}{\tau_e} \tag{2.9}$$

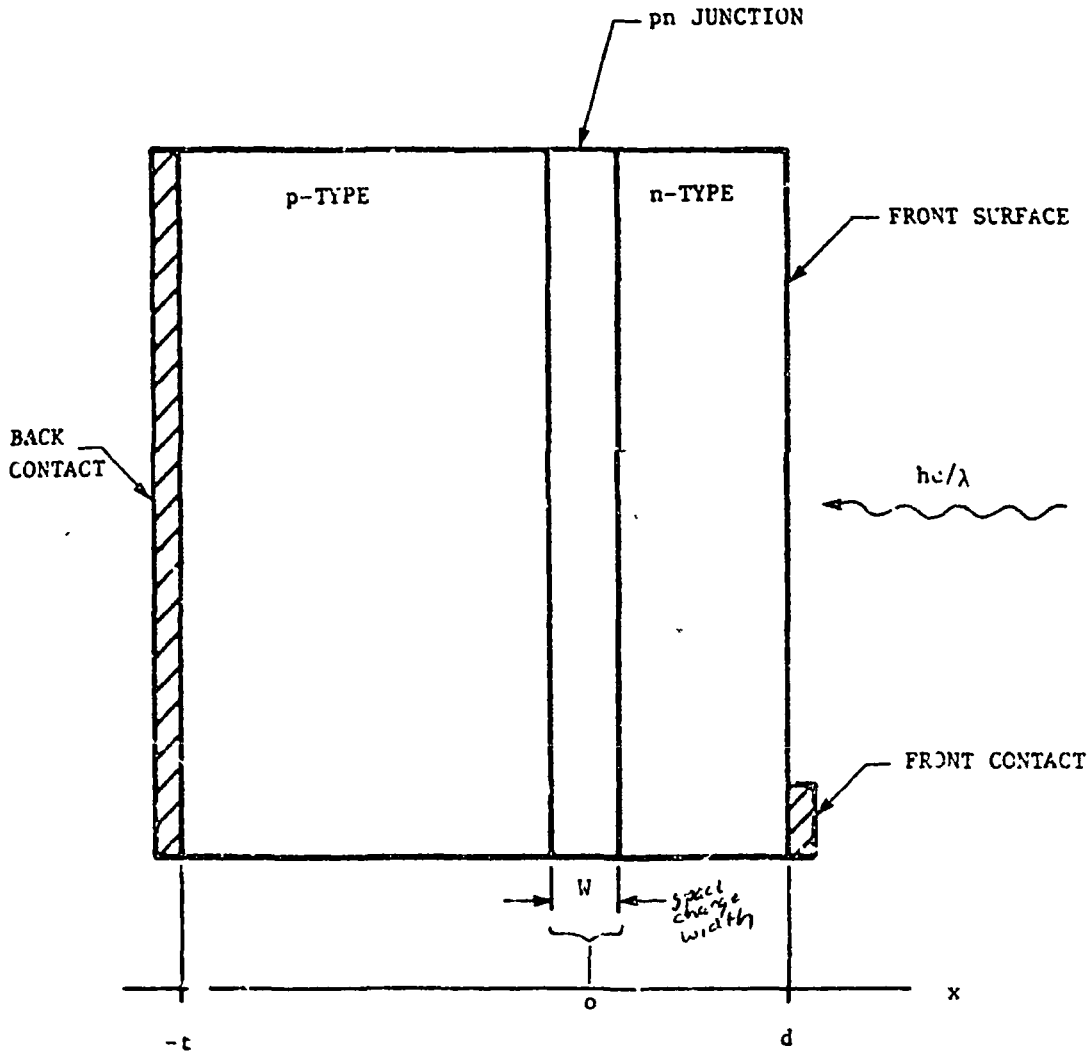

Figure 2.1 GENERAL CONFIGURATION OF p-n PHOTODIODE

for the case in which the electron diffusion length L_e << t, where t is the width of the p-type region, we have used $L_e^2 = D_e \tau_e$ in deriving the second form of equation 2.9. Equation 2.9 also follows directly from the analysis of Melngailis and Harman,[2.1] their equation 37, since coth $(t/L_e) \approx 1$ when L_e << t. From the "generation-recombination theorem" of Burgess,[2.4] we know that the thermal generation rate of minority carriers satisfies:

$$g_{th} = n_p At/\tau_e, \tag{2.10}$$

where At is the total volume of semiconductor, within which carriers are thermally generated. Substituting equation 2.10 into the second form of equation 2.9, we get:

$$\frac{I_{sat}}{q} = g_{th} \frac{L_e}{t}. \tag{2.11}$$

and substituting equation 2.11 into equation 2.5, we get:

$$D^*_\lambda(pv) = \frac{\eta\lambda}{2hc} \sqrt{\frac{At}{g_{th} L_e}}, \tag{2.5a}$$

where we have assumed that $\beta = 1$ and also that $\exp(qV/k_\beta T) = 1$ which means $V = 0$.

Another potentially useful case is when $t << L_e$ and the back contact is a "reflector" of minority carriers.[2.5] Such an "electrically reflecting" contact corresponds to the boundary condition $dn_p/dx = 0$ on the minority-carrier concentration gradient at that contact. See Section 2.3 for a discussion of this kind of contact. This boundary condition can be realized in principle by an abrupt p^+-p barrier, i.e., by making the back contact in Figure 2.1 be a more heavily doped (p^+) p-type region. If the p^+-p space charge layer is thin enough that generation current from it can be neglected, and if diffusion current in the p^+ region is also negligible, then the above boundary condition will apply exactly. It can be shown that for this case of a reflecting contact one obtains in the general result of Melngailis and Harman,[2.1] their equation 37, $\tanh(t/L_e)$ instead of $\coth(t/L_e)$. Then when $t << L_e$, the saturation current is given simply by:

$$\frac{I_{sat}}{q} = g_{th} \tag{2.12}$$

as the analog of equation 2.11, since $\tanh(b/L_e) \approx b/L_e$. Substituting equation 2.12 into equation 2.5, we have:

$$D^*_\lambda(pv) = \frac{\eta\lambda}{2hc}\sqrt{\frac{A}{g_{th}}}, \qquad (2.5b)$$

again assuming $\beta = 1$ and $\exp(qV/k_BT) = 1$.

We must now determine which case, equation 2.11 or equation 2.12, can give potentially the lower I_{sat} and therefore the better photovoltaic detector at a given temperature. Consider L_e and t. The p-type region in Figure 2.1 need be only thick enough to absorb most of the infrared signal radiation so that the quantum efficiency can be high. An absorption thickness of $2.5\alpha^{-1}$ will absorb over 90% of the unreflected radiation. For any known semiconductor one finds $\alpha = 10^3$ to 10^4 cm^{-1} near the λ_{co} wavelength, so that we must have L_e or $t > 2.5 \times 10^{-4}$ to 2.5×10^{-3} cm to absorb the radiation usefully. There is nothing to prevent making it small enough to satisfy this condition, provided we can achieve the $dn_p/dx = 0$ boundary condition, because t is simply a geometrical parameter. However, L_e is determined by material parameters in the p-type region. How small can L_e be? Using the Einstein relation ($qD = \mu k_BT$), we have:

$$L_e = \sqrt{D_e\tau_e} = \sqrt{\mu_e\tau_e k_BT/q}. \qquad (2.13)$$

The values of μ_e and τ_e can cover wide ranges in various semiconductors and as functions of temperature. However, here we are considering quite pure material (and consequently relatively long carrier lifetimes) and semiconductors with relatively narrow energy gaps (and consequently rather high carrier mobilities). From experience we can estimate that often we will have values of $\mu_e \gtrsim 10^3$ $cm^2/V\text{-}s$ and $\tau_e \gtrsim 10^{-6}$ s, at T = 77K for example, equation 2.13 would give $L_e \gtrsim 3 \times 10^{-3}$ cm. Thus, we can expect that usually L_e will be larger than t need be to absorb nearly all the radiation, and that, therefore, the case of equation 2.5b will yield the lower value of I_{sat}. In other words usually we will have $L_e/t > 1$, so that equation 2.5b will give a higher D^*_λ than equation 2.5a.

We must next consider the temperature dependence of D^*_λ. We require I_{sat} small to achieve high D^*_λ. The dominant temperature dependence of I_{sat} is through g_{th}, which increases with temperatures, see equations 2.11 and 2.12. The L_e in equation 2.11 may also depend upon temperature, but only weakly so. Thus the maximum operating temperature of a pv detector will be that at which g_{th} is so high that I_{sat} can no longer permit the required D^*_λ. Clearly, for a given value of g_{th}, that maximum temperature will be higher for whichever length, L_e or t, is lower. We have already argued that t can usually be smaller than L_e in the case of equation 2.11, so that the case of equation 2.12 will usually permit the highest possible detector operating temperature. Thus, a conclusion of this subsection on photovoltaic detectors is that to maximize the detector operating temperature, one must usually make the photovoltaic detector with an "electrically reflecting" contact. This conclusion assumes, of course, that the "reflecting" boundary condition can be achieved.

2.2.3 Heterojunction

A "heterojunction" is a pn junction between semiconductors having different energy gaps. We will discuss briefly how such a junction can be useful in optimizing the performance of a photovoltaic infrared detector.

For comparable doping levels and carrier diffusion lengths, the side of the heterojunction with the wider energy gap will contribute less dark current than the narrow gap side, and far less if the difference in gaps is considerable. The pv detector can be designed so that the photodetection occurs by carriers photoexcited in the narrow gap region, and with the wide-gap region on the front side facing the radiation to be detected. The wide-gap region then has several useful features:

- It acts as a window to transmit the radiation to be detected to the pn-junction and narrow gap side.
- This window "cuts off" or becomes opaque at a wavelength corresponding to its gap, so that it can exclude undesirable background radiation of shorter wavelengths.
- The wide-gap layer isolates the photoexcited carriers from the bare front surface of the detector, where their recombination rate could be very high.

Thus the principal utility of a heterojunction is not in the pn junction itself, but rather in the advantageous features of the wide-gap side. The theory developed earlier for a simple pn junction still applies here, since in that analysis we had assumed diffusion current from only one side of the pn junction anyway.

Heterojunctions are often used in high-performance solar cells for essentially the same reasons as those cited above. And they have sometimes been incorporated into the design of pv infrared detectors, especially those made of lead salt compounds and alloys.

2.3 "ELECTRICALLY REFLECTING" CONTACTS

The primary goal in developing an infrared detector is to achieve background noise limited (BLIP) performance. To do this we must make the "dark" noise of the detector negligible compared to the background noise. In a photovoltaic detector the dark noise is shot noise and is proportional to the dark leakage current of the device; thus, we must minimize the leakage current. Let us consider how to do so.

The model in Figure 2.1 is general enough to account for the properties of any pn junction photovoltaic infrared detector. Carriers are photoexcited by the radiation hc/λ, and most of those within a diffusion length of the junction are separated by the junction field to give a photovoltage. We can simplify the understanding of this detector model without losing any essential physics by assuming the n-type region to be thin and more heavily doped than the p-type region, so that the junction current is controlled by photoexcitation and diffusion of carriers in the p-type region. Actually, this is often the way such detectors are designed in practice. Also, we assume that generation-recombination current from the junction space-charge layer of width W is negligible; this is the "best" possible case, because the junction current is then due only to minority-carrier diffusion and is, therefore, minimum.

So we have a pn junction detector in which the dark leakage current is due to diffusion of minority-carrier electrons from the p-type region within a diffusion length L_e of the junction. In most semiconductor materials with reasonably high carrier mobilities and not terribly short carrier lifetimes, the diffusion length is > 10 μm.

The infrared absorption coefficient near the intrinsic absorption edge is typically > 10^3 cm^{-1}, so that the absorption length, that thickness within which most of the radiation is absorbed, is < 10^{-3} cm (=10 μm). Thus the p-type region in Figure 2.1 need not be thicker than roughly 10 micrometers to absorb most of the radiation. Why not make it thicker anyway? Well, we must still minimize the dark leakage current, and the thinner the layer of p-type material from which electrons can be extracted for the leakage current, the lower that current will be. So we want the p-type region to be as thin as possible while still thick enough to absorb most of the radiation. Of course, if it is then thinner than a diffusion length, which it usually will be, the back contact is within "range" of the junction as a possible source of carriers to be extracted by the junction.

Thus the problem of minimizing the dark leakage current reduces to that of making the back contact a "non-source" of minority carriers. This non-source property is not obtained with an ordinary neutral metallic ohmic contact, because such a contact acts as a high recombination - or generation-rate surface and is therefore an excellent source of minority carriers; in fact such a contact less than a diffusion length from the junction gives a larger leakage current than if the p-type region were very thick.

What we need is a "p^+ contact"; i.e., the back contact must be made such that it is a heavily-doped semiconductor layer having fewer minority carriers than the p-type region. This type of contact is illustrated in comparison with a conventional pv detector design in Figure 2.2 The same kind of result could be achieved instead by grading the doping in the p-type region away from the contact (moving to the left of the junction in Figure 2.1). By either method we reduce the number of minority carriers available to contribute to the dark leakage current of the device.

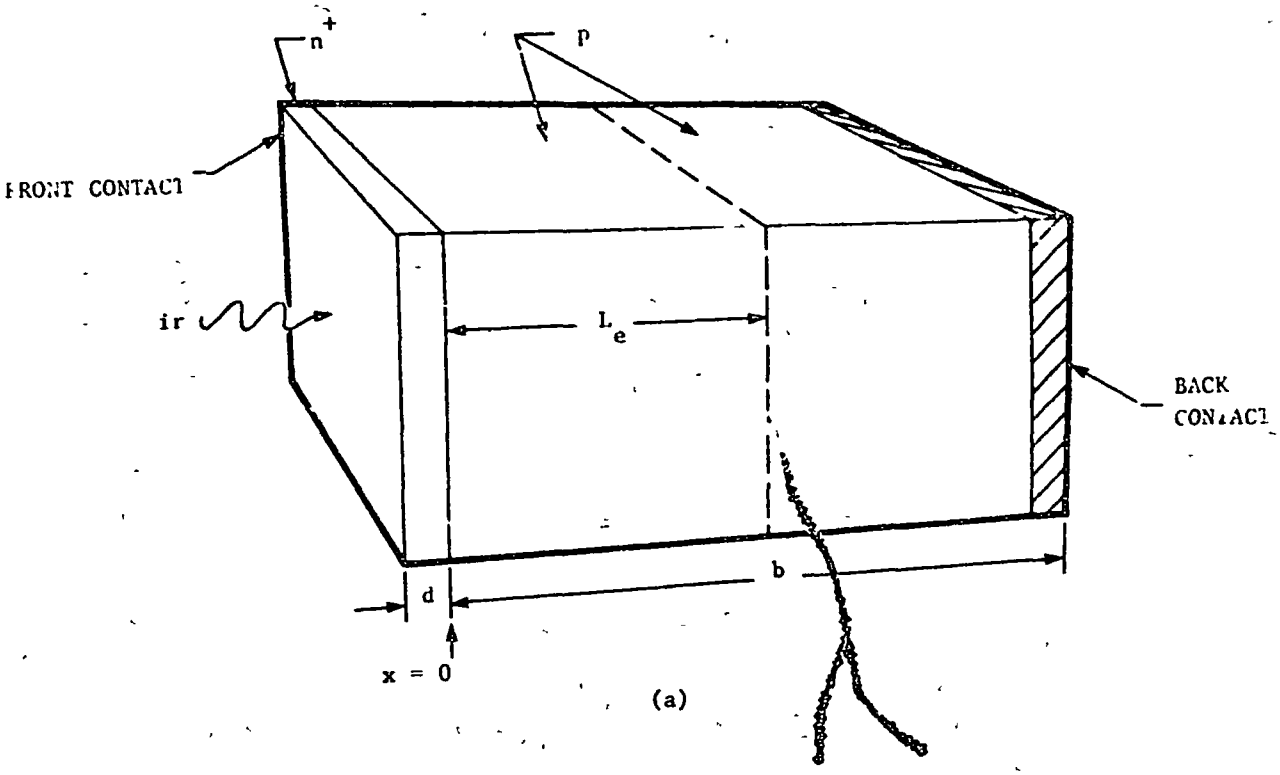

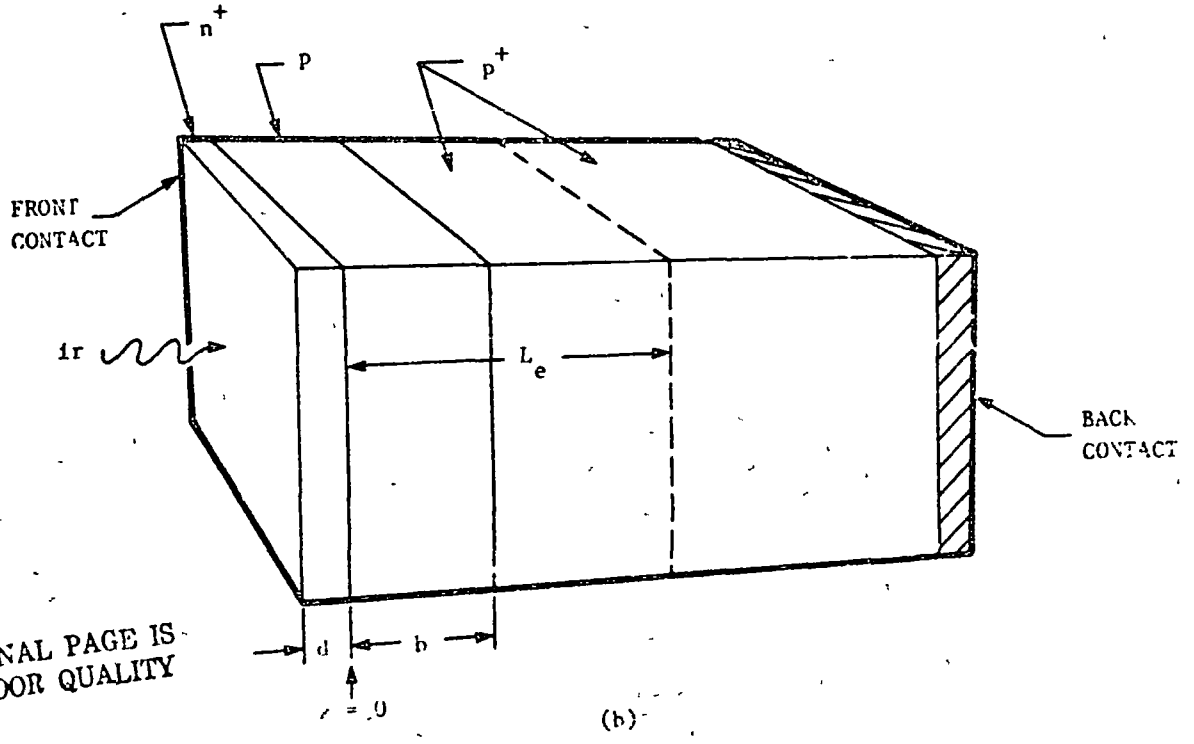

ORIGINAL PAGE IS OF POOR QUALITY

Figure 2.2 (a) CONVENTIONAL DESIGN, (b) REFLECTING INTERFACE (p^+-p)

To be strictly accurate, we must realize that the diffusion current is proportional to the gradient of the minority-carrier concentration. Thus, if the carrier lifetime should increase strongly with carrier concentration, the benefit of the p^+ contact or graded doping could be reduced or even cancelled. It is cancelled in fact for pure Auger recombination, see reference 4.5 of Section 4.

A p^+-p (or n^+-n) contact can be thought of as an electrical reflector of minority carriers. This is because there is a potential barrier to the flow of minority carriers at such a contact, as can be seen by drawing an energy band diagram. Minority carriers hitting the barrier are "reflected." In contrast, a purely metallic contact, at which the quasi-Fermi levels in the semiconductor come together, acts as a sink for minority carriers.

The importance of the nature of the back contact to photovoltaic detector optimization does not seem to be adequately recognized. One might argue that people usually make the back contact with a metal containing a dopant of the same type as the semiconductor just to be sure to get a low-resistance contact, so that they are using the correct approach anyway even if not realizing it. However, the full advantage can be achieved only if the heavily-doped region is less than a minority-carrier diffusion length from the pn junction. Clearly understanding the role of the back contact in detector optimization should help toward obtaining the best possible contact.

The following excerpt from a recent review article on silicon solar cells by Wolf[2.6] has arguments similar to the above:

> "Regions of high recombination rates, such as surfaces and particularly ohmic contacts, can act as minority carrier sinks in competition with the barrier field if they are located within a few diffusion lengths from the barrier. This effect takes place in thin cells with long diffusion lengths, where the ohmic contact covers the back surface of the cell. Incorporation of a positive impurity density gradient toward such a high recombination region creates an internal electric field which reflects the minority carriers away from the sink, thus neutralizing its effect. If such a field is incorporated in front of the back surface contact, one talks of a "BSF cell" (back surface field cell)."

This excerpt is an example of how the importance of the back contact is well recognized by people developing solar cells of high conversion efficiency.

Further work needs to be done on this topic to determine how to minimize the dark leakage current of a pn junction photovoltaic detector by using all possible methods ("electrically reflecting" back contact, graded doping in p-type region of the Figure 2.1 example, etc).

2.4 PHOTOCONDUCTIVE DETECTORS

The theory of an intrinsic photoconductive detector is considerably more complicated than that of a photovoltaic detector. We cannot cover all aspects of the photoconductor theory in this report, and some of it is in fact still incomplete. However, we will carry the theory far enough to establish the intercomparison of photoconductive and photovoltaic detectors for the objectives of this project. We will first summarize the theory in general, and then consider some of its detailed aspects.

2.4.1 General Theory

A schematic model of this detector mode is shown in Figure 2.3. Generation-recombination (gr) noise and Johnson noise are the fundamental mechanisms in photoconductive (pc) detectors. The total noise current can be written as:

$$I_n^2(pc) = 4q\left[qg_{th}G^2 + \frac{k_BT}{qR}\right]\Delta f. \qquad (2.14)$$

The first term in the brackets in equation 2.14 represents gr noise due to thermal equilibrium carriers in the semiconductor; this term can be derived from the more common expression for gr noise. The second term represents the Johnson noise, where the photoconductor resistance R can vary with the background photon flux density. The photoconductive gain G in equation 2.14 generally depends upon the bias voltage applied to the photoconductor. At high bias voltages minority-carrier sweepout effects occur and the gr noise terms must be multiplied by a numerical factor a, where $1/2 \leq a \leq 1$. The current responsivity of the pc detector is:

$$R_\lambda(I_s) = q\eta\lambda G/hc, \qquad (2.15)$$

since one can have $G \neq 1$ in a photoconductor. Substituting equations 2.14 and 2.15 into equation 2.1, we get:

$$D^*_\lambda(pc) = \frac{\eta\lambda}{2hc\sqrt{\frac{g_{th}}{A} + \frac{k_BT}{q^2G^2RA}}}. \qquad (2.16)$$

The problem of maximizing D^*_λ in this detector mode is more complicated than for pv detectors, because two terms must be minimized in the denominator of equation 2.16.

The second term under the radical in equation 2.16 essentially dictates the choice of photoconductor material. To be suitable at all, a photoconductor material must offer high photoconductive gain G and/or high resistance R. The gain is given in general by:

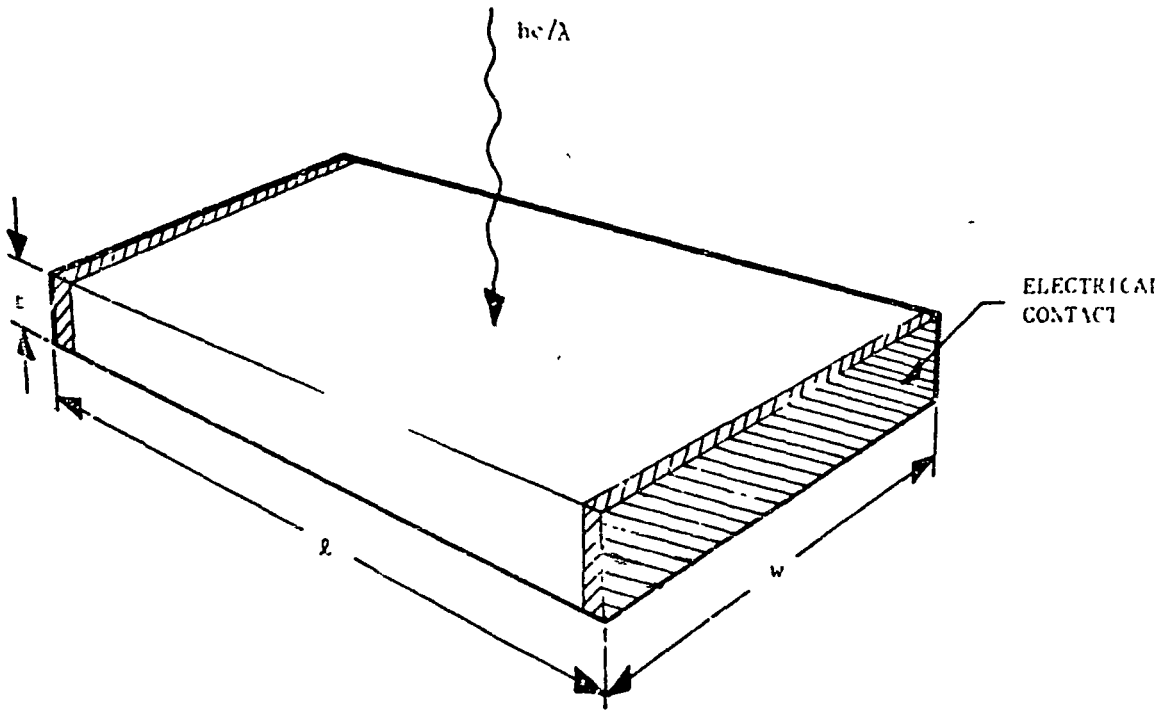

Figure 2.3 SCHEMATIC MODEL OF A PHOTOCONDUCTIVE DETECTOR

$$G = \tau/t_d = b_\mu \mu \tau \varepsilon, \qquad (2.17)$$

where μ and τ are the minority-carrier mobility and lifetime, b_μ is the mobility ratio, and t_d is the drift time of a minority carrier in the electric field ε biasing the photoconductor. The gain can be enhanced by increasing ε, but minority-carrier sweepout will eventually cause a saturation of G. Another method of gain enhancement is to operate under conditions in which minority-carrier trapping effectively reduces the minority-carrier mobility and thereby increases the effective mobility ratio b_μ, even without trapping, so that G can be very high. However, as the operating temperature rises, G may drop from one or more of the following causes. The lifetime τ decreases exponentially with increasing temperature when only intrinsic recombination mechanisms are active (radiative, Auger). Also, the detector resistance, R, drops exponentially with temperature when the semiconductor becomes intrinsic, making it more difficult to apply a high ε without excessive Joule heating. Of course, this drop of R also acts directly to increase the $k_B T/q^2 G^2 RA$ term in equation 2.16. The conclusion of this paragraph is that this term must be evaluated carefully as a function of temperature for any photoconductive detector to determine whether or not it will limit the maximum operating temperature. If we assume that this term can be made negligible, then the other term in equation 2.16 will limit the maximum operating temperature, in which case equation 2.16 reduces to:

$$D^*_\lambda(pc) = \frac{\eta\lambda}{2hc}\sqrt{\frac{A}{g_{th}}}. \qquad (2.16a)$$

This equation is identical to equation 2.5b for the best-case pv detector

2.4.2 Detailed Theory

We have outlined the theory of an intrinsic photoconductive detector in general terms above. Here we will consider many of the detailed aspects of the theory, to identify the conditions required to satisfy equation 2.16a. Special attention will be given to the effects of background radiation, which must be taken into account as an inseparable part of the problem for an intrinsic photoconductor.

If ϕ photons/cm^2-s of $\lambda < \lambda_{co}$ are incident on a photoconductor, $\eta\phi$ are absorbed and converted into photoexcited electrons, where η is the quantum efficiency. These photoexcited electrons reduce the resistance of the photoconductor. If the photoconductor current is held essentially constant by means of a high series load resistor, the reduced resistance is measured as a decrease in the IR drop across the photoconductor. The spectral (voltage) responsivity is defined in this case as the incremental rate of change in voltage (dV) with respect to the incident signal radiation power (dW):

$$R_\lambda = |dV/dW| = (1/\ell w)(\lambda/hc)|dV/d\phi|, \tag{2.18}$$

where

$$dW = (\ell W)(hc/\lambda)d\phi$$

is the power in watts corresponding to the flux density $d\phi$ falling on the detector surface area ℓw. If the external circuit is a voltage source instead of a current source, the response is measured as a change in current and the spectral (current) responsivity may be defined:

$$R_\lambda = |dI/dW| = (1/\ell w)(\lambda/hc)|dI/d\phi|. \tag{2.19}$$

The absolute marks have been added to equations 2.18 and 2.19 to show that the magnitude of the change is relevant but not the sign.

In proceeding with the derivation of R_λ, it will be observed that the resistance change, and hence the electrical signal, may depend on any optical bias such as background radiation. The observed signal corresponds to the change in resistance between optical bias only and optical bias plus signal radiation. If the optical bias is large, the resistance change may differ, because of nonlinear material properties, from that for low or zero optical bias. The nonlinearities begin to show up when the density of excess electrons maintained by the bias radiation is comparable to the thermal densities n_o and p_o. This condition is likely to hold in (Hg,Cd)Te when the background is a 300K blackbody.

It is assumed that the photoconductor material is perfect to the extent that all thermal and optical transitions are between the valence and conduction bands; i.e., trapping and Shockley-Read recombination processes are negligible. Then for the excess (photoexcited) carriers, $\Delta n = \Delta p$. For the moment, the effects of ambipolar drift in the applied electric field will be ignored, and Δn, Δp will be assumed constant throughout the material.

From Ohm's law for a constant current and a resistance change $d\Omega$,

$$dV = (V/\Omega_B)d\Omega, \tag{2.20}$$

or for a constant voltage,

$$dI = -(I/\Omega_B)d\Omega, \tag{2.21}$$

where the B subscript denotes the steady state value at the optical bias level. Equations 2.18 and 2.19 then become:

$$R_\lambda(\text{voltage}) = (1/\ell w)(\lambda/hc)(V/\Omega_B)\ |d\Omega/d\phi| \tag{2.22}$$

$$R_\lambda(\text{current}) = (1/\ell w)(\lambda/hc)(I/\Omega_B)\ |d\Omega/d\phi|. \tag{2.23}$$

If n_B and p_B are the electron and hole densities at the optical bias level, μ_h is the hole mobility and b is the mobility ratio, the resistance Ω_B is expressed:

$$\Omega_B = \ell/\left[wtq(bn_B + p_B)\mu_h\right], \tag{2.24}$$

so that the derivative, according to the condition dn = dp, is:

$$|d\Omega/d\phi| = \Omega_B \cdot (dn/d\phi) \cdot (b + 1)/(bn_B + p_B). \tag{2.25}$$

In order to evaluate $dn/d\phi$, we note from statistical balance at the two different steady states, neglecting drift, that:

$$R(n_B) = \eta\phi_B/t, \tag{2.26}$$

$$R(n_B + dn) = \eta\phi_B/t + \eta d\phi/t, \tag{2.27}$$

where R is the net thermal recombination rate at the bias plus signal radiation level, and $\eta\phi_B/t$, $\eta d\phi/t$ are respectively the bias radiation and signal radiation photoexcitation rates. If $R(n_B + dn)$ is expressed as a first order expansion about $R(n_B)$ and equation 2.26 subtracted from the result, it follows that:

$$\left[\frac{d}{dn} R(n_B)\right] dn = \eta d\phi/t. \tag{2.28}$$

The inverse, $\left[\frac{d}{dn} R(n_B)\right]^{-1}$, is the well-known lifetime of added carriers, or incremental lifetime, $\hat{\tau}(n_B)$. It is the lifetime of the extra carriers generated by the signal $d\phi$ when n_B is the steady state electron density maintained by the background ϕ_B. According to this definition, equation 2.28 becomes:

$$dn/d\phi = \eta\hat{\tau}(n_B)/t. \tag{2.29}$$

On substitution back through equation 2.25, the responsivity expression 2.22 becomes:

$$R_\lambda(\text{voltage}) = (1/\ell wt) \cdot (\lambda/hc) \cdot \eta V\hat{\tau}\,(n_B)(b + 1)/(bn_B + p_B), \tag{2.30}$$

and R_λ(current) is the same but with I substituted for V.

It is significant that the responsivity derived here contains the incremental lifetime instead of the ordinary lifetime:

$$\tau = (n_B - n_o)/R(n_B),$$

which is often erroneously applied. At low optical bias levels ($n_B \sim n_o$) the difference is not noticed since τ and $\hat{\tau}$ are numerically the same. As n_B increases, both τ and $\hat{\tau}$ decrease but not at the same rate. If $n_B - n_o >> n_o + p_o$, the lifetimes differ by a factor of two or more.

The effective $\hat{\tau}$ is further reduced by minority-carrier sweepout due to the applied electric field. This also affects the concentration densities n_B and p_B calculated from steady state balance. The details of these calculations are given in Appendix A.

Under the conditions assumed above of intrinsic generation-recombination processes ($\Delta n = \Delta p$) and negligible sweepout effects, the low frequency ($\hat{\tau}\omega << 1$) gr noise voltage[2.4] is given by:

$$V_{gr} = \frac{2V}{(\ell wt)^{1/2}} \frac{(b+1)}{bn_B + p_B} \cdot \langle (n-n_B)^2 \rangle^{1/2} \cdot \left[\hat{\tau}(n_B)\right]^{1/2} \cdot (\Delta f)^{1/2}, \quad (2.31)$$

where n_B again is the average steady state electron density at optical bias, Δf is the frequency bandwidth of the measurement, and $\langle (n-n_B)^2 \rangle$ is the variance of the statistical fluctuations of n about n_B. According to the gr theorem[2.4] the latter is given by:

$$\langle (n-n_B)^2 \rangle = g(n_B) \cdot \hat{\tau}(n_B) = r(n_B) \cdot \hat{\tau}(n_B), \quad (2.32)$$

where g and r are respectively the electron-hole generation and recombination rates, which are equal in the steady state. Hence,

$$V_{g-r} = \frac{2V}{(\ell wt)^{1/2}} \frac{(b+1)}{bn_B - p_B} \cdot \left[g(n_B)\right]^{1/2} \cdot \hat{\tau}(n_B) \cdot (\Delta f)^{1/2}. \quad (2.33)$$

Equation 2.31 has sometimes appeared in the literature with the quantity $n_B p_B/(n_B + p_B)$ substituted for the variance. This is not generally valid according to equation 2.32 except in case either that the optical bias is small or that Auger processes are unimportant compared to radiative processes. The variance is not equal to $n_B p_B/(n_B + p_B)$ if $n_B - n_o \lesssim n_o + p_o$ and Auger effects are important.

As in the case for R_λ, corrections to the gr noise are necessary to account for sweepout effects. These are included in Appendix.

The other fundamental type of noise in photoconductors is the Johnson noise:

$$V_J = \left[4kT\Omega\Delta f\right]^{1/2}, \quad (2.34)$$

where k = Boltzmann's constant, T = Kelvin temperature, Ω = resistance, and Δf is the frequency bandwidth.

A measure of the ability of an infrared detector to produce an electrical signal above the noise level is its detectivity. In terms of voltages the spectral detectivity D^*_λ is defined by:

$$D^*_\lambda = R_\lambda(V_s)(Aw)^{1/2}(\Delta f)^{1/2}/V_n, \tag{2.35}$$

where $R_\lambda(V_s)$ is the spectral voltage responsivity and V_n the total noise:

$$V_n = \left[V_{gr}^2 + V_J^2\right]^{1/2}. \tag{2.36}$$

A rather compact formula for the photoconductor D^*_λ is obtained by combining equations 2.35, 2.36, 2.30, and 2.33:

$$D^*_\lambda \quad (\eta\lambda/2hc)\left[tg(n_B)\right]^{-1/2} K/(1 + K^2)^{1/2}, \tag{2.37}$$

where

$$K = v_{gr}/v_J \tag{2.38}$$

and $g(n_B)$ is the total electron-hole generation rate:

$$g(n_B) = Bn_i^2 + G_{ee}\left(\frac{n_B}{n_o}\right) + G_{hh}\left(\frac{p_B}{p_o}\right) + \frac{\eta\Phi B}{t}. \tag{2.39}$$

From equation 2.37 it is apparent that D^*_λ is maximized by making the thickness and $g(n_B)$ small while making K large. The B, G_{ee}, and G_{hh} factors in $g(n_B)$ are strongly increasing functions of temperature. This is the principal incentive for operating the photoconductor at low temperatures. If, on the other hand, the temperature is so low that $g(n_B)$ is dominated by the last (background) term, there is little point in reducing it further.

It is also desirable to have $K \gg 1$ so that $K/(1 + K^2)^{1/2}$ approaches its maximum of 1. By substitution for v_{gr} and v_J from equations 2.31 and 2.34 it is found that:

$$K = \frac{qV}{kT}\,\frac{\mu_R V\tau}{\ell^2}\,\frac{\langle(n-n_B)^2\rangle}{bn_B + p_B}^{1/2}. \tag{2.40}$$

The factor $\langle(n-n_B)^2\rangle/(bn_B + p_B)$ is roughly equal to $n_B p_B \left[(n_B + p_B)(bn_B + p_B)\right]^{-1}$ which does not depend strongly upon the temperature. Then the temperature dependence of K is dominated by $(\tau/T)^{1/2}$, which clearly increases with decreasing temperature. Hence, maximizing τ is the second reason for operating the detector at low temperatures.

If $g(n_B) \approx \frac{\eta\phi_B}{t}$ (i.e., external photoexcitation greatly exceeds thermal pair generation) and $K \gg 1$, the background-limited performance (BLIP) is approached:

$$(D^*_\lambda)_{BLIP} = (\eta\lambda/2hc)/(n_B)^{1/2}. \qquad (2.41)$$

2.5 CONCLUSIONS

Thus both detector modes have the same theoretical maximum, represented by either equation 2.5b or 2.16a. To achieve high $D^*_\lambda(max)$ in either mode one must have a low thermal generation rate g_{th} as well as high quantum efficiency η. Material properties can affect $D^*_\lambda(max)$ only through g_{th} and η, assuming that λ is fixed by the desired detector wavelength response.

The potential maximum operating temperature for both detector modes, pv and pc, is the same, provided that the detectors are made of the same material so that g_{th} is identical. However, one must usually make the photovoltaic detector with an "electrically reflecting" back contact if the pv detector is to reach this maximum, this conclusion does not seem to have been recognized in previous work on pv detectors. On the other hand, the intrinsic photoconductive detector must remain "good enough", in terms of high G^2RA product as the temperature goes up, that the neglect of the $k_BT/q\ G\ R_A$ term assumed in equation 2.16a is valid.

Let us now recall the factors of 2 mentioned earlier. If the pv detector were reverse biased with a large enough negative voltage, then the achievable D^*_λ would be $\sqrt{2}$ higher than that of equation 2.5b. This factor of $\sqrt{2}$ has often been thought of as a fundamental advantage of a pv detector over a pc; however, the situation is not so straightforward. If an intrinsic pc detector were operated in the minority-carrier sweepout condition, its mean square noise current would be multiplied by a coefficient a, where $1/2 \leq a \leq 1$, and its D^*_λ could be enhanced also by up to $\sqrt{2}$, but this sweepout effect is not yet understood fully.

2.6 REFERENCES

2.1 J. Melngailis and T.C. Harman, Semiconductors and Semimetals 5, Ed. by R.K. Willardson and A.C. Beer (Academic Press, New York 1970) pp 111-174.

2.2 G.R. Pruett and R.L. Petritz, Proc. IRE 47, 1524 (1959).

2.3 W. Shockley, Bell System Tech. J. 28, 435 (1949).

2.4 K.M. van Vliet, Proc. IRE 46, 1004 (1958); K.M. van Vliet, Appl. Optics 6, 1145 (1967).

2.5 D. Long, "Photovoltaic and Photoconductive Infrared Detectors," chapter to be published in volume of Topics in Applied Physics, ed. by R.J. Keyes.

2.6 M. Wolf, J. Vac. Sci. Technol. 12, 984 (1975), specifically p 989.

SECTION 3

SEMICONDUCTOR MATERIALS

3.1 INTRODUCTION

In Section 2 we showed theoretically that the maximum possible D^*_λ of an infrared quantum detector at any temperature is given by:

$$D^*_\lambda(\max) = \frac{\eta\lambda}{2hc}\sqrt{\frac{A}{g_{th}}}. \tag{3.1}$$

Equation 3.1 applies to the "best-case" material and design of either a photovoltaic detector or an intrinsic photoconductive detector. One can hope to increase D^*_λ by a factor of up to $\sqrt{2}$ in these detectors by using large bias voltages, but we will ignore that detail here.

Given that one can achieve the nearly perfect semiconductor crystal material required by equation 3.1, the question is what intrinsic (defect-independent) properties are required of that material to maximize the D^*_λ of equation 3.1. There are three material-dependent parameters in equation 3.1: λ, η, and g_{th}.

The maximum or "cutoff" wavelength λ_{co} which is near the peak D^*_λ is fixed by the energy gap of the semiconductor. Alloy semiconductors such as $Hg_{1-x}Cd_xTe$ and $Pb_{1-x}Sn_xTe$ are especially desirable, since their energy gaps can be adjusted continuously over wide ranges, giving designable values of λ_{co}. However, an elemental or compound semiconductor can be just as useful if its gap corresponds closely to the necessary λ_{co}.

Any optimized detector will have an anti-reflection coating, so that the quantum efficiency is well approximated by: (3.1)

$$\eta \approx 1 - \exp(-\alpha t). \tag{3.2}$$

In an intrinsic detector material with negligible crystal imperfections, the thermal generation rate will be equivalent to the sum of the band-to-band radiative and Auger recombination rates; i.e.,

$$g_{th} = At(R_r + R_A). \tag{3.3}$$

Substitution of equations 3.2 and 3.3 into equation 3.1 gives.

$$D^*_\lambda(\max) = \frac{\lambda}{2hc}\,\frac{1-\exp(-\alpha t)}{\sqrt{\alpha t}}\sqrt{\frac{\alpha}{R_r + R_A}}. \tag{3.4}$$

The thickness t of the photodetective region of the detector will, of course, be chosen to maximize the value of $[1-\exp(-\alpha t)]/\sqrt{\alpha t}$ for the value of α of the material used; this maximum occurs when $\alpha t = 1.256$ and is:

$$D^*_\lambda(\max) = 0.32 \frac{\lambda}{hc}\sqrt{\frac{\alpha}{R_r + R_A}} . \qquad (3.5)$$

We have now reduced the problem to consideration of the two recombination rates and the optical absorption coefficient. One wants to minimize R_r and R_A and maximize α to maximize D^*_λ.

3.2 AUGER RECOMBINATION

3.2.1 Introduction

Auger recombination involves the collision of two electrons (or holes) within the conduction (or valence) band whereby one gains energy to be excited to a higher band state, while the other makes a transition to the other band.[3.1] This recombination mechanism is very much band-structure dependent. There is not yet a complete theory of Auger recombination for all types of band structure, but the theory has been worked out for some materials which are used in infrared quantum detectors.

Petersen extended the theory for non-degenerate n-type $Hg_{1-x}Cd_xTe$ several years ago,[3.7] and then Kinch et al,[3.3] confirmed the theory by matching it with their carrier-lifetime data for n-type $Hg_{0.8}Cd_{0.2}Te$; Auger recombination is a relatively strong mechanism in n-type $Hg_{1-x}Cd_xTe$. In this project Petersen has extended the theory to p-type $Hg_{1-x}Cd_xTe$ and verified that Auger recombination is very weak in that type of material; see 3.2.2 below. The difference in the strength of Auger recombination in n-type and p-type $Hg_{1-x}Cd_xTe$ is due to the very different shapes of the valence and conduction bands; see Figure 3.1. All zinc-blende crystal structure semiconductors with energy gaps narrow enough for infrared detection have band structures like that in Figure 3.1. These include the III-V compounds such as InSb and InAs, as well as those II-VI's having the zinc blende structure such as $Hg_{1-x}Cd_xTe$. The form of the band structure is fixed by the crystal symmetry.

In very recent work Petersen has extended the theory of Auger recombination to statistically-degenerate n-type $Hg_{1-x}Cd_xTe$.[3.4] The essential result is that the Auger mechanism is weakened considerably compared to that in non-degenerate $Hg_{1-x}Cd_xTe$ of the same alloy composition x (and therefore the same energy gap). This conclusion is important to the design of the optimum pn junction $Hg_{1-x}Cd_xTe$ detector, which will include an n^+p pn-junction with the photodetection occurring in the less heavily doped p-type region; this point will be discussed further later. Suffice it to say here that if the n^+ region is statistically degenerate, its Auger recombination will be much weaker than otherwise expected from the high carrier concentration, so that diffusion current from the n^+ region can be small and the corresponding shot noise negligible.

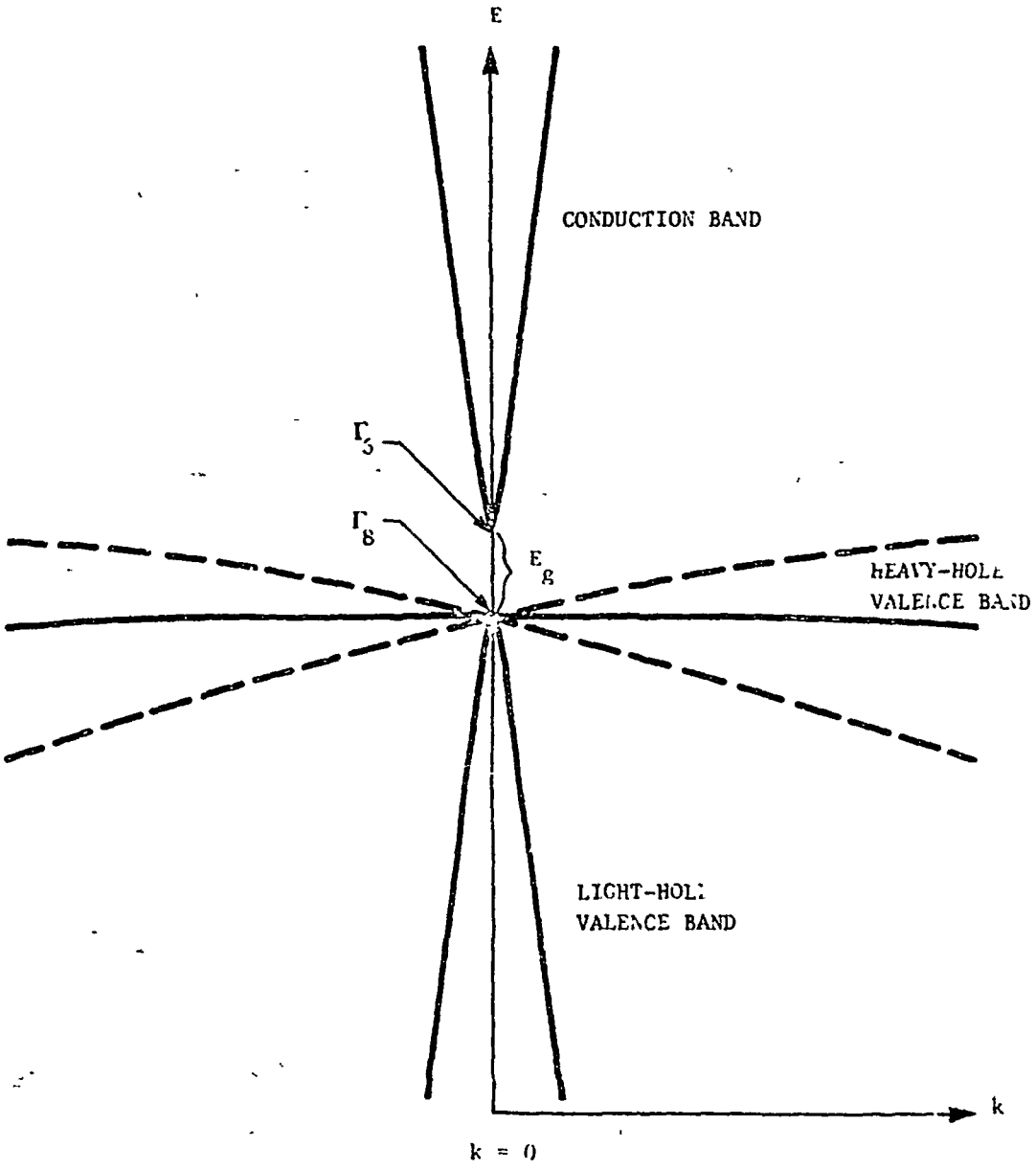

Figure 3-1 ENERGY BAND STRUCTURE OF ZINC BLENDE CRYSTAL STRUCTURE SEMICONDUCTORS.

77-1-6

Very recently Emtage[3.5] has developed the theory of Auger recombination for $Pb_{1-x}Sn_xTe$ and shown that it is a relatively strong mechanism in these alloys. The mechanism is practically the same in n-type and p-type $Pb_{1-x}Sn_xTe$, because the valence and conduction band structures are essentially identical, being of the "many-valley" type. Before Emtage's work it had been thought that Auger recombination was weak in $Pb_{1-x}Sn_xTe$; see for example the review by Melngailis and Harman.[3.6] Emtage realized, however, that intervalley transitions must be included in the theory, and they lead to a strong total Auger recombination. Emtage's theory is confirmed implicitly by the experimental observation that the R_oA products found in pn junction detectors made of $Pb_{1-x}Sn_xTe$ have never exceeded an apparent ceiling which is consistent with the Auger lifetime derived by Emtage. The $Pb_{1-x}Sn_xTe$ alloys are IV-VI compound semiconductors having the NaCl crystal structure. Other IV-VI compounds which are PbTe-rich which can be used as infrared quantum detector materials, such as $Pb_{1-x}Sn_xTe$ and $Pb_{1-x}Ge_xTe$, can be expected to have similar Auger recombination, since their band structures are similar to th of $Pb_{1-x}Sn_xTe$. In this project we have carried out a critical review of Emtage's theory and confirmed its theoretical validity.

3.2.2 Auger Recombination in p-Type $Hg_{1-x}Cd_xTe$

Auger recombination, the reciprocal process to impact ionization, is a band-to-band three-body interaction in which the energy loss of the recombining electron-hole is used to excite a third particle (electron or hole) high in its band. Hence, the Auger mechanism is very sensitive to the band structure of the semiconductor. For a simple two-band semiconductor model in which the E vs k relationship for both bands is parabolic, there are two cases of interest: $\mu = m_c/m_v << 1$ and $\mu = 1$; m_c and m_v are the electron and hole effective mass, respectively. For parabolic bands the effective mass is constant. In this section, we will review the dependence of the Auger lifetime τ_A on μ, with special emphasis on the two limiting cases described above.

The continuity equation for electrons is:

$$\frac{\partial n}{\partial t} = G_{ext} + (G_n - R_n) + \frac{1}{e}\nabla \cdot \vec{J}_n \qquad (3.6)$$

where n and $\vec{J}_n$ are the electron concentration and current, respectively; $G_n - R_n$ is the net generation rate due to thermal processes, and G_{ext} is the generation rate due to external sources.

For this discussion we define the Auger lifetime, τ_A, by:

$$G_A - R_A = -\left(\frac{n-n_o}{\tau_A}\right) , \qquad (3.7)$$

where G_A and R_A are the Auger generation and recombination rates, respectively, per unit volume. The subscript zero, e.g., n_o, implies equilibrium conditions. There are many definitions of lifetime; however, the lifetime defined by equation 3.2 is that which determines the reverse bias saturation current in a diffusion limited p-n junction.[3.7] This lifetime is also appropriate for the discussion of photoconductivity in the low excitation limit.[3.8]

The two Auger recombination processes possible for a simple two-band model are shown in Figure 3.2.

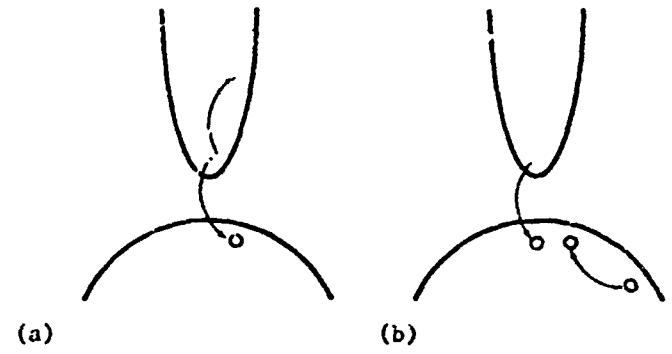

Figure 3.2 (a) AUGER RECOMBINATION BY AN ELECTRON-ELECTRON (ee) COLLISION, (b) AUGER RECOMBINATION BY A HOLE-HOLE (hh) COLLISION. THE ARROWS DENOTE ELECTRON TRANSITIONS.

The Auger rates for non-degenerate statistics can be written:[3.9]

$$G_A - R_A = \left\{(G_{ee})\left(\frac{n}{n_o}\right) - (G_{ee})\left(\frac{n^2 p}{n_o^2 p_o}\right)\right\} + \left\{(G_{hh})\left(\frac{p}{p_o}\right) - (G_{hh})\left(\frac{p^2 n}{p_o^2 n}\right)\right\}$$

$$= -\frac{(np-n_i^2)(G_{ee} n p_o + G_{hh} p n_o)}{n_i^4} = -\left(\frac{n-n_o}{\tau_A}\right), \qquad (3.8)$$

where n_i is the intrinsic electron concentration. If $n-n_o = p-p_o = \Delta n$, the expression for the electron Auger lifetime becomes:

$$\tau_A = \frac{n_i^4}{(n_o+p_o+\Delta n)(C_{ee}np_o+C_{hh}pn_o)} \quad . \tag{3.9}$$

The equilibrium generation rates for electron-electron and hole-hole processes, G_{ee} and G_{hh}, for parabolic bands are given in mks units by: (3.9,3.10)

$$G_{ee} = \left[\frac{(8)(2\pi)^{5/2}e^4 m_o}{(4\pi)^2 \cdot h^3}\right] \cdot \left[\frac{\left(\frac{m_c}{m_o}\right)|F_1F_2|^2}{(\kappa_\infty^2)(1+\mu)^{1/2}(1+2\mu)}\right] x$$

$$x\ (n_o)\left(\frac{kT}{E_g}\right)^{3/2} \exp\left[-\left(\frac{1+2\mu}{1+\mu}\right)\frac{E_g}{kT}\right] cm^{-3}s^{-1} \tag{3.10}$$

$$G_{hh} = \left[\frac{(8)(2\pi)^{5/2}e^4 m_o}{(4\pi)^2 h^3}\right] \left[\frac{\left(\frac{m_v}{m_o}\right)|F_1F_2|^2}{(\kappa_\infty^2)(1+\frac{1}{\mu})^{1/2}(1+\frac{2}{\mu})}\right] x$$

$$x\ (p_o)\left(\frac{kT}{E_g}\right)^{3/2} \exp\left[-\left(\frac{2+\mu}{1+\mu}\right)\frac{E_g}{kT}\right] cm^{-3}s^{-1}, \tag{3.11}$$

where κ_∞ is the high frequency dielectric constant, E_g is the semiconductor energy bandgap, and $|F_1F_2|^2$ is the square of the product of the overlap integrals. (3.10)

Note that when $\mu << 1$, $G_{ee} \sim e^{-\frac{E_g}{kT}}$ and $G_{hh} \sim e^{-\frac{2E_g}{kT}}$ so that for this case the electron-electron process is dominant. When $\mu \gg 1$ both G_{ee} and G_{hh} vary as $e^{-\frac{3}{2}\left(\frac{E_g}{kT}\right)}$. For nondegenerate statistics it is convenient to write τ_A in the form:

$$\tau_A = \frac{(2n_i^2)(n_o/2G_{ee})}{(n_o+p_o+\Delta n)\left[(n_o+\Delta n) + (\beta)(p_o+\Delta n)\right]} \quad , \tag{3.12}$$

where

$$\beta = \frac{n_o G_{hh}}{p_o G_{ee}} = \frac{(\mu^{1/2})(1+2\mu)}{(2+\mu)} \exp\left[-\left(\frac{1-\mu}{1+\mu}\right)\left(\frac{E_G}{kT}\right)\right]. \tag{3.12a}$$

Note that $\beta(\mu << 1) << 1$ and $\beta(\mu=1) = 1$. The intrinsic electron Auger lifetime for these two limiting cases of band structure becomes:

$$\tau_{A_i} \ (\mu << 1) = \frac{n_i}{2G_{ee}} \tag{3.13a}$$

$$\tau_{A_i} \ (\mu=1) = \frac{n_i}{4G_{ee}} \ . \tag{3.13b}$$

It is frequently stated that the Auger lifetime varies as the inverse square of the carrier concentration (i.e., for n-type material $\tau_A \propto 1/n_o^2$). That this is so is evident from equation 3.12 for the situations $\Delta n << n_o$, $\beta = 1$ and $\Delta n << n_o$, $\beta p_o >> n_o$. In these regimes:

$$\tau_A(n_o>\beta p_o) = 2\left(\frac{n_i^2}{n_o^2}\right)\left(\frac{n_o}{2G_{ee}}\right) = 2\left(\frac{n_i^2}{n_o^2}\right)\tau_{A_i} \propto \frac{\exp\left[\frac{\mu}{1+\mu}\ \frac{E_g}{kT}\right]}{n_o^2} \ . \tag{3.14a}$$

for n-type material, and:

$$\tau_A\left(p_o > \frac{n_i}{\sqrt{\beta}}\right) = 2\left(\frac{n_i^2}{\beta p_o^2}\right)\left(\frac{n_o}{2G_{ee}}\right) = \frac{2}{\beta}\left(\frac{n_i^2}{p_o^2}\right)\left(\tau_{A_i}\right) \propto \frac{\exp\left[\frac{\mu}{1+\mu}\ \frac{E_g}{kT}\right]}{\beta p_o^2} \tag{3.14b}$$

for p-type material. Note that $(n_o/2G_{ee}) = \tau_{A_i}$ is independent of the carrier concentration.

In Figure 3.1, for the case where the excess carrier concentration is small compared with the intrinsic carrier concentration, we show the dependence of the Auger lifetime on the carrier concentration for several values of μ. Note

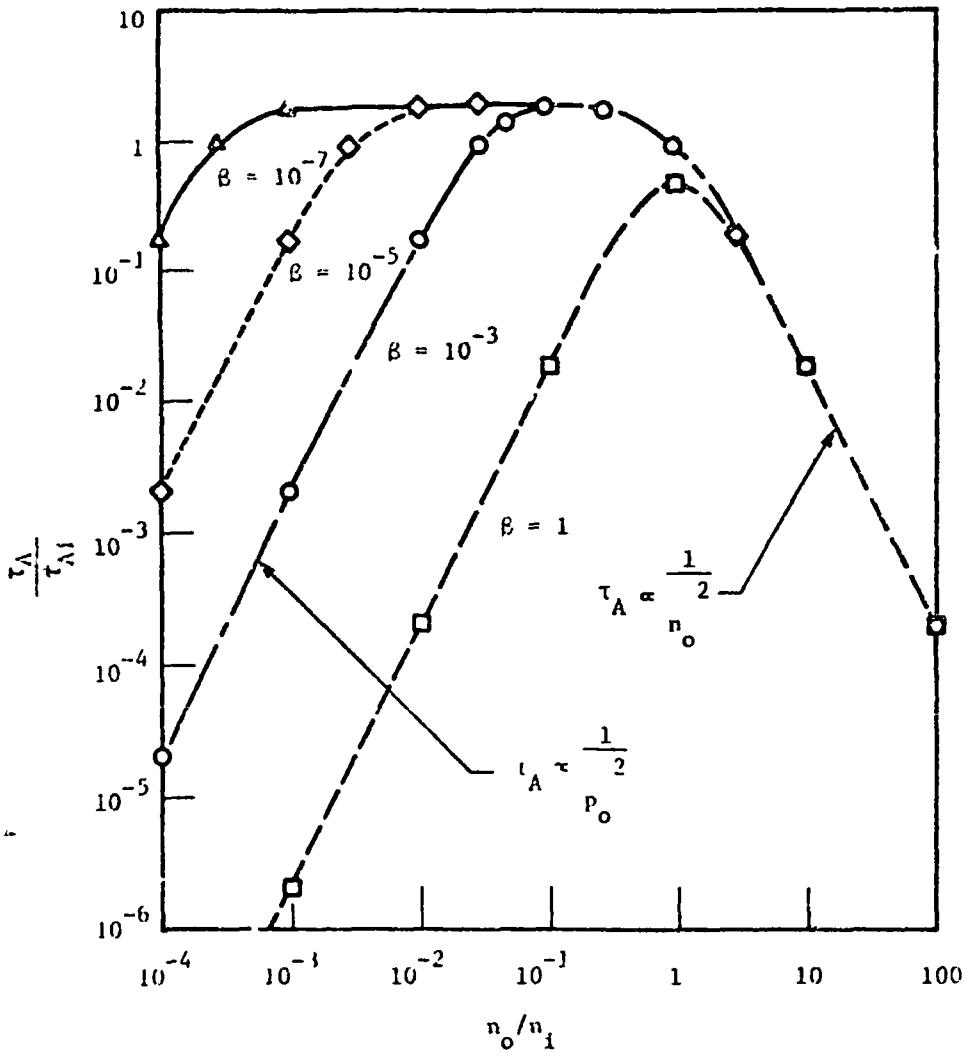

Figure 3.3 RATIO OF THE AUGER LIFETIME TO THE INTRINSIC LIFETIME AS A FUNCTION OF CARRIER CONCENTRATION.

77-1-6

that for the approximations discussed above, for n-type material, and for $\beta \leq 1$, the lifetime varies as n_o^{-2} over most of the range of carrier concentrations. For p-type material, however, the Auger lifetime is relatively insensitive to the carrier concentration in the region where $\beta \leq n_o/p_o$. In this regime:

$$\tau_A \left(p_o < \frac{n_i}{\sqrt{\beta}}\right) \rightarrow 2\,\tau_{A_i}. \tag{3.15}$$

Figure 3.3 clearly demonstrates that for a semiconductor in which $\beta << 1$, there is a large asymmetry in the Auger lifetime with respect to the type of the majority carrier concentration. Note that for the case $\beta >> 1$ a similar asymmetry would exist with n-type material having a significantly longer lifetime than p-type material. However, for the two semiconductors of interest in this discussion, i.e., (Hg,Cd)Te and (Pb,Sn)Te, $\beta << 1$ and $\beta = 1$, respectively, so we will limit ourselves to the situation where $\beta \leq 1$.

Let us now discuss the implications of the above discussion for $Hg_{1-x}Cd_xTe$. From equation 3.12 we see that $\beta = \beta(E_g, \mu, T)$.[3.11] For E_g we use the expression of Schmit and Stelzer:

$$E_g = -0.25 + 1.59x + (5.233 \times 10^{-4})(1-2.08x)(T) + 0.327x^3. \tag{3.16}$$

For the electron effective mass we use:[3.12]

$$m_c^* = \frac{3\hbar^2 E_g}{4P^2 m_o} = 0.0706\,E_g, \tag{3.17}$$

where m_o is the free electron mass, P is the matrix element from $\vec{k} \cdot \vec{p}$ theory, and, E_g is the energy gap in electron volts. For the hole effective mass we use the value 0.55.[3.13] Incorporating the above into equation 3.12 we calculate β as a function of x for several values of temperature. The results are shown in Figure 3.4. Note that as the x-value increases and temperature decreases the value of β decreases. According to equation 3.14b small values of β yield a large value for the Auger lifetime in p-type material. In the doping regime where equation 3.14b is valid ($p_o > n_i/\sqrt{\beta}$) the Auger lifetime is a factor of β^{-1} larger in p-type material than in n-type material with the same doping concentration.

The Auger lifetime for $Hg_{1-x}Cd_xTe$ can be determined if n_o, p_o, n_i, β, τ_{A_i} and An are known. In Figure 3.5 we plot $\tau_{A_i} = n_i/2G_{ee}$ as a function of x for several temperatures. In this computation we have assumed a constant value of 0.25[3.13] for the overlap integrals, and have used $\epsilon_\infty = 9.5 + (3.5)\left(\frac{0.6-x}{0.43}\right)$[3.14] for the high frequency dielectric constant. For the sake of convenience we include

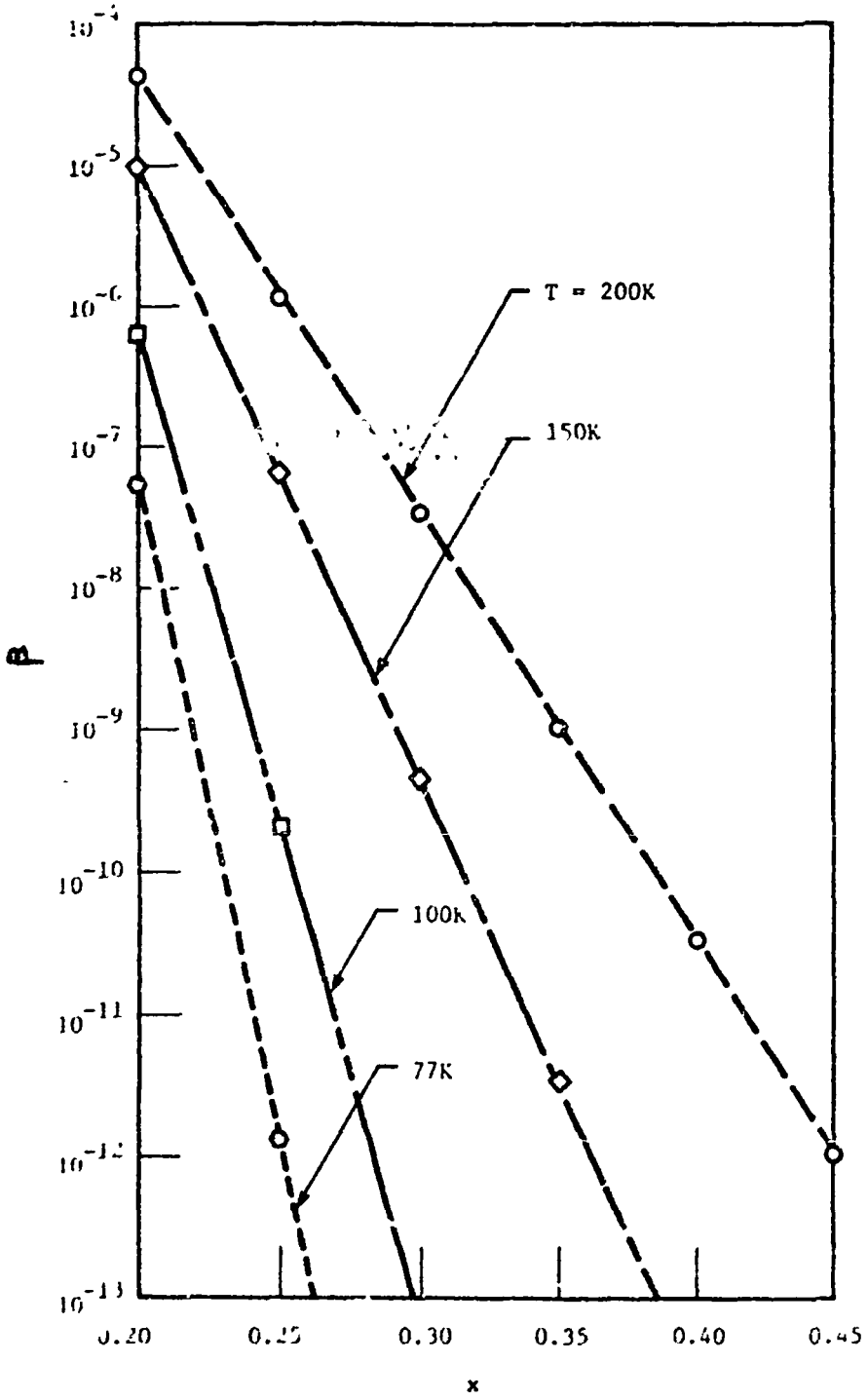

Figure 3.4 β (DEFINED IN TEXT) AS A FUNCTION OF x VALUE.

77-1-6

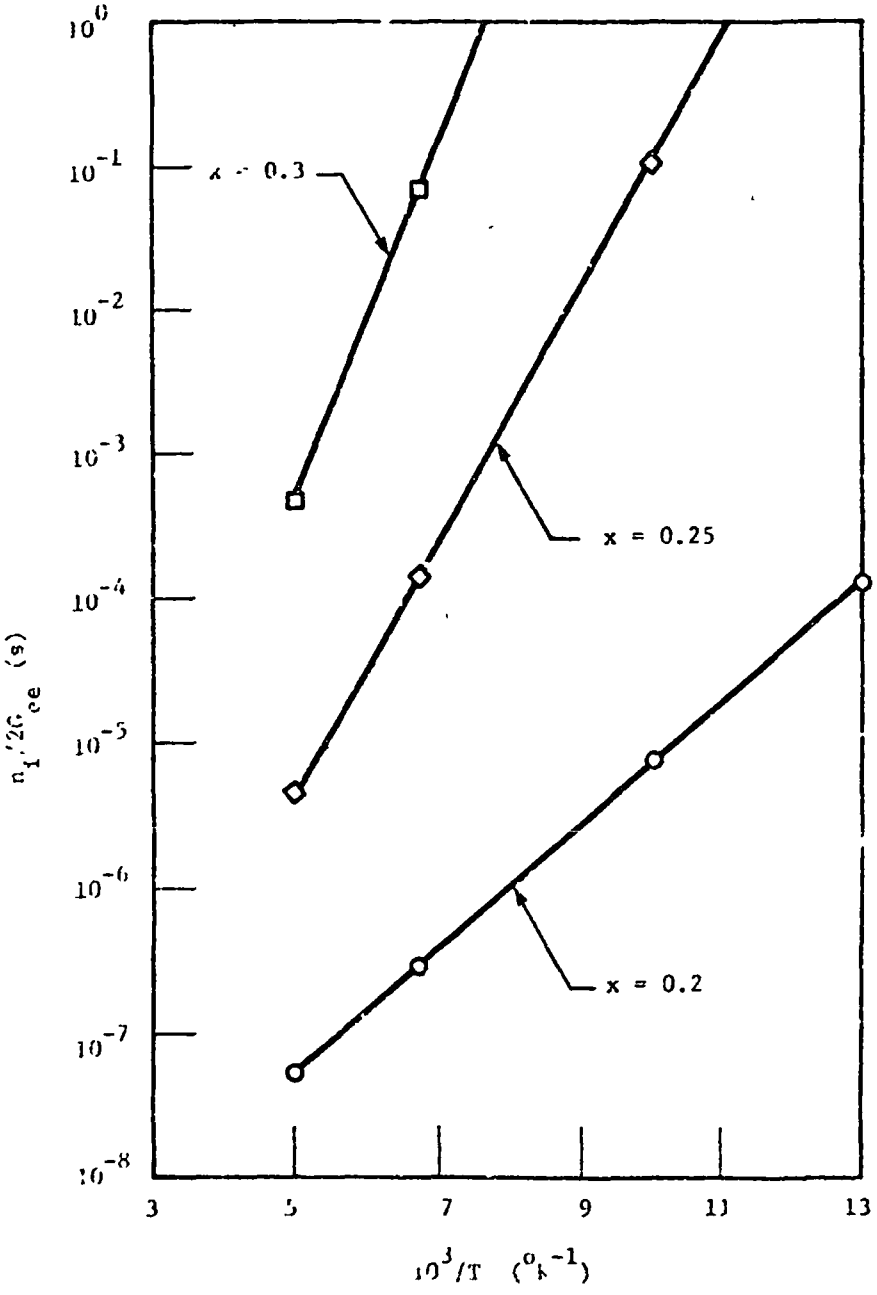

Figure 3.5 INTRINSIC MINORITY LIFETIME ($n_i/2G_{ee}$) AS A FUNCTION OF RECIPROCAL TEMPERATURE.

a graph of Schmit's (see Figure 3.6) calculation of the intrinsic carrier concentration for $Hg_{1-x}Cd_xTe$. The data presented in Figures 3.3, 3.4, 3.5, and 3.6 permit a graphical determination of the Auger lifetimes for most cases of interest. Note that for $x \geq 0.2$ and $T \leq 200$, $\beta \leq 10^{-4}$. Thus, in (Hg,Cd)Te the Auger lifetime in this range of x-values and temperatures, the lifetime in p-type material will be significantly longer than in equally-doped n-type material.

In (Pb,Sn)Te, as discussed above, the effective mass ratio is unity, and the band structure pertinent to charge transfer has four valence and four conduction bands at the center of the <111> zone faces. Emtage has shown[3.5] that when intervalley scattering via the Auger mechanism is taken into consideration the Auger lifetime is significantly shorter than that which is calculated from a single valley model. Emtage's result gives:

$$\tau_A = \frac{(4\pi)^2}{(2\pi)^{5/2}} \frac{N^2}{N'} \frac{\epsilon_o^2 \kappa_\infty^2}{n^2 e^4} \frac{(E_g)^{7/2}}{(kT)^{1/2}} \frac{(m_\ell)^{1/2}(m_t)^{3/2}}{\hbar^3} \exp\left(\frac{rE_g}{kT}\right), \qquad (3.18)$$

where N=4 is the number of valleys, $N'=3$ is the number of valleys into which scattering can occur from a single valley, ϵ_o is the permittivity of free space $\kappa_\infty = 36$ is the high frequency dielectric constant, n is the carrier concentration, E_g the energy bandgap, $m_\ell = 0.14$ the longitudinal effective mass, $m_t = 0.014$ the transverse effective mass, and $r = m_t/m_\ell$. Equation 3.18 is valid only for $E_g << \kappa T$ and $r << 1$. Note that r in this expression plays a role similar to μ in equation 3.14 in that both factors act to reduce the lifetime. Note that Emtage's theory which includes the effects of intervalley scattering gives a much shorter lifetime than does the theory which neglects this type of scattering. Hence, according to this result the Auger mechanism is much stronger in (Pb,Sn)Te than was previously believed.

In Figure 3.7, using equation 3.18 we show the dependence of the Auger lifetime on carrier concentration for (Pb,Sn)Te for an energy gap of 0.1 eV and for temperatures of 77K and 200K. The theory is marginally good at 200K. For sake of comparison in the same figure, using the theory outlined above, we plot the Auger lifetime for (Hg,Cd)Te for a constant 0.1 eV energy gap at the same temperatures.

It is of interest to compare the Auger lifetime with the radiative lifetime, since it is either one or the other of these two mechanisms which provides the limiting lifetime. The radiative lifetime is given by:[3.6]

$$\tau_R = \frac{n_i^2}{R_r(n_o + p_o + \delta_n)} \qquad (3.19)$$

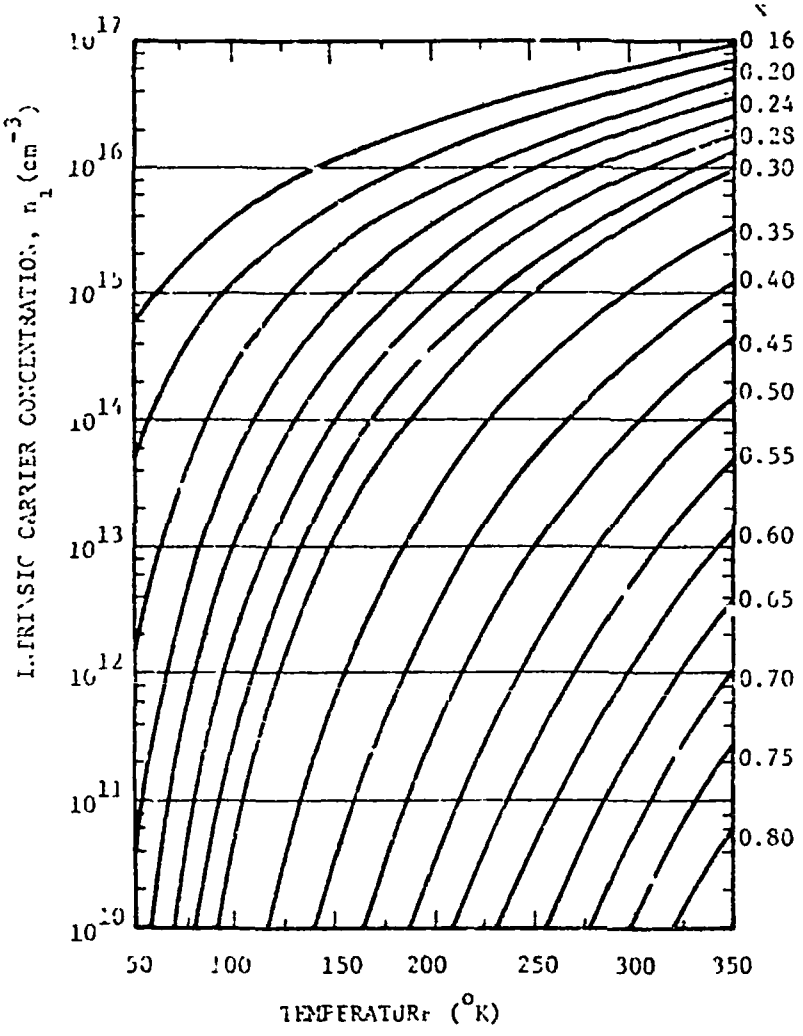

Figure 3.6 CALCULATED TEMPERATURE DEPENDENCE OF THE INTRINSIC CARRIER CONCENTRATION OF $Hg_{1-x}Cd_xTe$ FOR $0.16 \leq x \leq 0.80$.

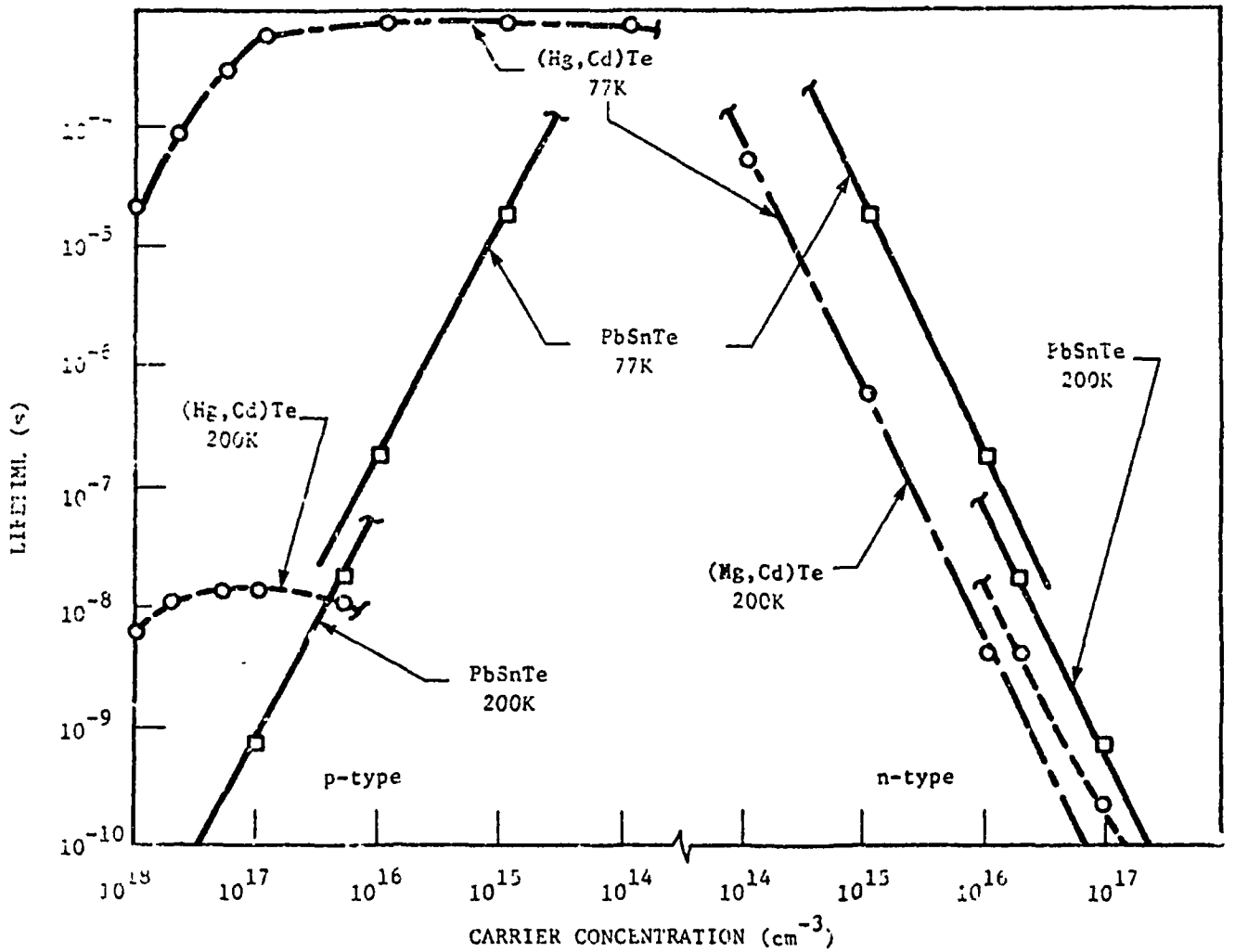

Figure 3.7 AUGER LIFETIME FOR PbSnTe AND (Hg,Cd)Te AS A FUNCTION OF CARRIER CONCENTRATION. THE ENERGY GAP IS CONSTANT (0.1 eV) FOR BOTH MATERIALS.

where n_i is the intrinsic carrier concentration, n_o is the majority carrier concentration, p_o is the minority carrier concentration and R_r is the radiative recombination rate. The radiative lifetime is symmetric with respect to carrier type. The radiative recombination rate depends strongly on the absorption coefficient. We follow the work of Kinch et al[3.3] and the work of Melngailis and Harman[3.6] to calculate the radiative lifetime in (Hg,Cd)Te and (Pb,Sn)Te, respectively. The results of these computations for a constant 0.1 eV energy bandgap at 77K and 200K are shown in Figure 3.8. These calculations are valid only for nondegenerate statistics.

For (Hg,Cd)Te and (Pb,Sn)Te, we make the following observations concerning the Auger and radiative lifetimes in nondegenerate material:

(1) At low temperatures p-type (Hg,Cd)Te has by far the longest Auger lifetime.

(2) At higher temperatures p-type (Hg,Cd)Te and (Pb,Sn)Te have similar lifetimes for moderate carrier concentrations. In (Pb,Sn)Te the lifetime decreases as the carrier concentration increases, while it remains reasonably constant in (Hg,Cd)Te. The theory for (Pb,Sn)Te should be re-examined at these temperatures.

(3) At low temperatures in n-type material, (Pb,Sn)Te has an edge over (Hg,Cd)Te insofar as the Auger lifetime is concerned. At 200K they are within about a factor of three of each other. In the expressions for the lifetime for these two materials the overlap integrals have been approximated and in different ways so order of magnitude deviations are not significant.

(4) At moderate carrier concentrations, for the examples used in Figures 3.7 and 3.8, the Auger lifetime is limiting for three of the four situations. Only for p-type (Hg,Cd)Te at 77K does the radiative lifetime limit the recombination.

3.2.3 Conclusions

The best-developed and most versatile infrared quantum detector materials are the $Hg_{1-x}Cd_xTe$ and $Pb_{1-x}Sn_xTe$ alloys. Of these materials only p-type $Hg_{1-x}Cd_xTe$ offers weak Auger recombination. Other possible detector materials may also have weak Auger recombination, such as p-type InSb and p-type InAs, as well as semiconductors not yet developed as infrared quantum detector materials. But of the well-developed materials designable to various wavelengths, p-type $Hg_{1-x}Cd_xTe$ is the best choice with respect to Auger recombination.

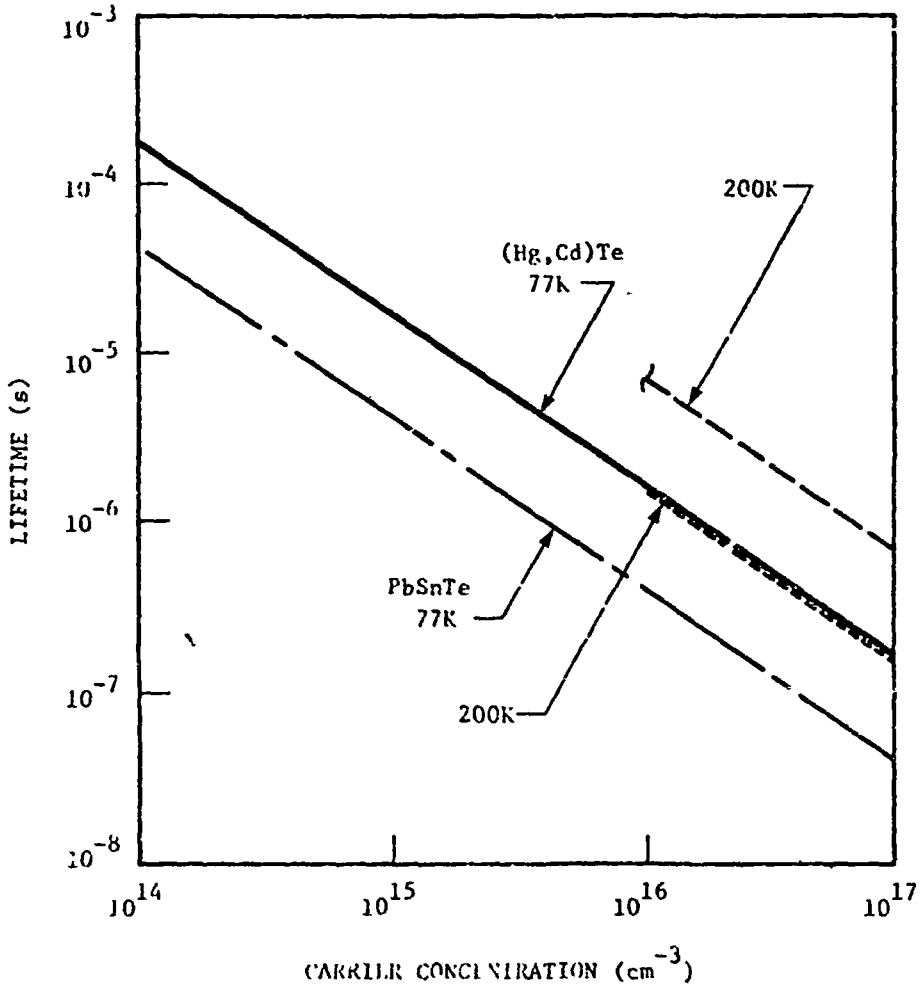

Figure 3.8 RADIATIVE LIFETIME FOR (Pb,Sn)Te AND (Hg,Cd)Te AS A FUNCTION OF CARRIER CONCENTRATION. THE ENERGY GAP IS CONSTANT (0.1 eV) FOR BOTH MATERIALS.

Even though, as indicated in 3.2.1, there is not yet a complete Auger recombination theory generalizable to all possibly useful semiconductor materials, we can still draw some general conclusions from the known results. Materials with "many-valley" band structures are probably undesirable because of the possibility of intervalley transitions like those which give strong Auger recombination in $Pb_{1-x}Sn_xTe$. On the other hand, materials with "direct" $k = 0$ energy gaps and greatly dissimilar valence and conduction band effective masses can have weak Auger recombination like that in p-type $Hg_{1-x}Cd_xTe$. These conclusions are probably much more widely applicable than one might at first think, because the possible different forms of band structure fall within only a few classes, as Herman emphasized many years ago.[3.15] Thus we do not have a choice from among a great many different band structures to achieve the minimum Auger recombination.

3.3 RADIATIVE RECOMBINATION

Radiative recombination involves the recombination of an electron-hole pair by emission of a photon with approximately the gap energy. If the transition is between band extrema located at the same point in k-space, then it is "direct" radiative recombination and involves only the photon emission. If the band extrema are at different k's, a phonon must also be involved to help conserve energy, and it is then "indirect" radiative recombination. The lowest possible thermal generation rate in an effectively perfect semiconductor crystal occurs when Auger recombination is negligible so that only radiative recombination remains. Thus to maximize the detector performance, one always wants to reach the "radiative recombination limit" of the detector material.

Van Roosbroeck and Shockley[3.16] showed originally that the radiative recombination rate is given in general by:

$$R_r = \frac{8\pi k_B^3 T^3}{h^3 c^2} \int_{U_g}^{\infty} \frac{n_1^2 \alpha U^2 dJ}{\exp U - 1}, \qquad U_g = \frac{E_g}{kT}. \tag{3.20}$$

If $R_A << R_r$, then the quantity we want to minimize is actually R_r/α; see equation 3.5. Let us assume for now that n_1^2 and α are both constant, since they both are in fact weak functions of U compared to expU; we will reconsider this assumption later. Also, for the cases of interest here $E_g >> k_B T$, so that we can assume expU >> 1 to a good approximation. The integral in equation 3.18 then becomes:

$$\int_{U_g}^{\infty} U^2 \exp(-U)\,dU = U_g^2 \exp(-U_g),$$

since $U_g >> 1$. Thus we have:

$$\frac{R_r}{\alpha} \simeq \frac{8\pi k_B^3 T^3}{h^3 c^2} U_g^2 \exp(-U_g)\, n_1^2 = 8\pi \frac{kT}{h^3 c^2} n_1^2 E_g^2 \exp(-E_g/kT) \quad (3.21)$$

For a given wavelength response, which fixes E_g and thereby U_g at a certain temperature T, the only material parameter on which R_r/α depends is the index of refraction n_1. Consequently, from equation 3.5 we have:

$$D^*_\lambda(\max) \propto n_1^{-1}. \quad (3.22)$$

That is, the maximum possible D^*_λ varies inversely as the index of refraction. To this approximation the index of refraction is the only parameter differentiating between different detector materials.

In fact, however, the U dependence of α should be considered, including the point that this U dependence differs for direct and indirect radiative transitions. Before doing that mathematically, let us consider it qualitatively and physically. To do so we can use Figure 3.9 as an example. It shows curves of optical absorption coefficient vs wavelength near the intrinsic absorption edge for two well-known and typical semiconductors:

- GaAs, which has a direct gap at k = 0;
- Si, which has an indirect gap.

We recall that photon wavelength is related to energy by $\lambda(\mu m) = 1.24/E(eV)$. To be useful as an intrinsic infrared detector material, the semiconductor must have a reasonably high absorption coefficient at the wavelength to be detected. This is for the reasons both of technological practicality (so that the detector need not be inconveniently thick to achieve high quantum efficiency) and for the absorption length (α^{-1}) to be shorter than the minority-carrier diffusion length, so that a "high-low" interface can be effective in enhancing pv detector performance. Referring to Figure 3.9, a relatively high absorption coefficient of $\sim 10^3$ cm^{-3} is achieved by both materials at the same wavelength, but the indirect gap semiconductor (Si) must have a longer cutoff wavelength (narrower energy gap) to do so because of its less steep absorption edge. At the shorter wavelengths both materials show about the same dependence of α on λ, but the values of α are higher in GaAs. Since the indirect-gap semiconductor requires a narrower energy gap to realize high absorption coefficients at the wavelengths to be detected than does the direct-gap semiconductor, a direct-gap semiconductor with its larger U_g will offer a lower value of R_r/α (see equation 3.19) and a correspondingly higher maximum possible D^*_λ. So a direct-gap semiconductor is qualitatively preferable.

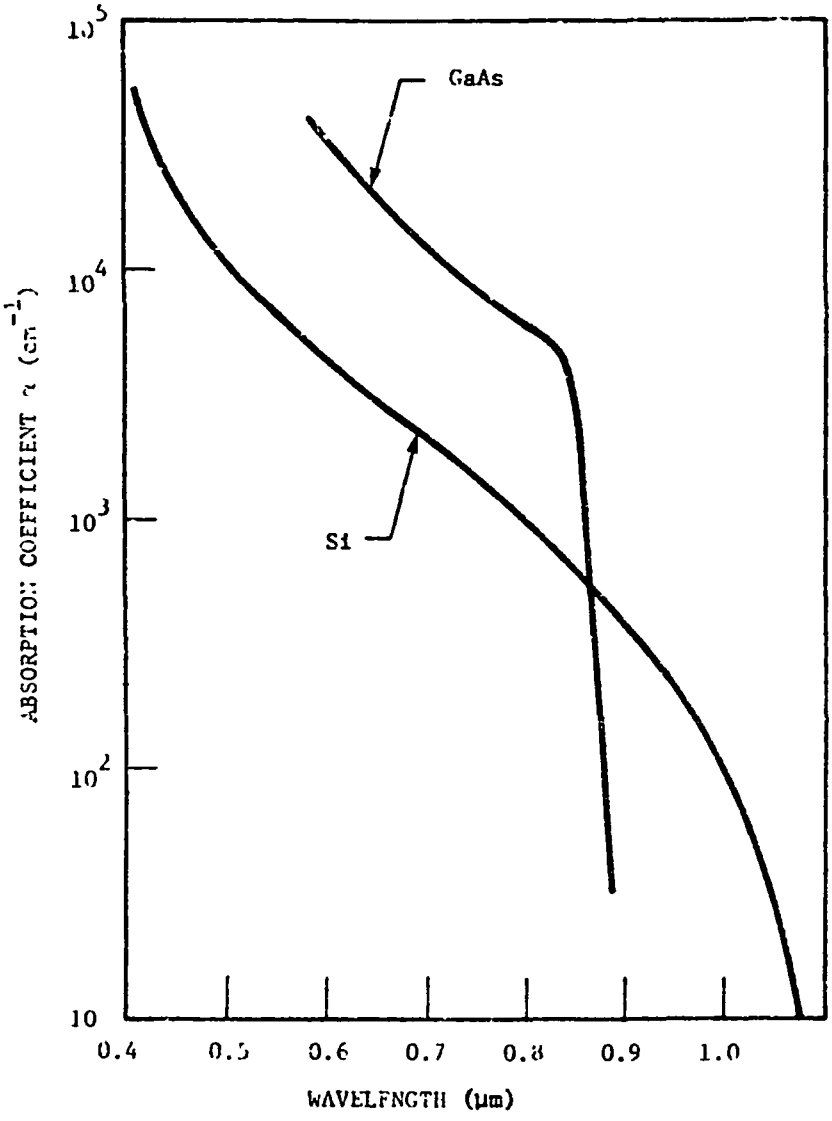

Figure 3.9 ABSORPTION COEFFICIENT VS WAVELENGTH FOR Si AND GaAs

Let us return now to consider the effect of the energy dependence of the absorption coefficient. For direct transitions we have in general:

$$\alpha \propto (U - U_g)^{1/2}.$$

Thus instead of the integral evaluated to obtain equation 3.21 above, we have in this more rigorous consideration the integral:

$$I = \int_{U_g}^{\infty} (U-U_g)^{1/2} U^2 \exp(-U) dU. \tag{3.23}$$

When $U_g >> 1$, the solution to this integral is:

$$I = \frac{\sqrt{\pi}}{2} U_g^2 \exp(-U_g), \tag{3.24}$$

which differs by only $\sqrt{\pi}/2 \approx 0.9$ from the result obtained above by assuming α = constant; the conclusions made above are thus good to within this relatively insignificant numerical discrepancy.

3.4 MATERIAL PARAMETERS

In this subsection we will review and summarize what is known about the parameters of semiconductor materials that are useful as infrared quantum detector materials. These parameters will be needed in the calculations in the following sections. The parameters required to determine D* can be divided into two categories: material parameters and device design parameters. The important material parameters include n_i, μ_e, μ_h, τ_e, τ_h, and ϵ_s. The device design parameters are N_A, N_D, and device geometry.

3.4.1 Mercury-Cadmium Telluride

Material parameters for $Hg_{0.8}Cd_{0.2}Te$ have been determined by the Honeywell Corporate Research Center in past work, and are published in the literature.[3.18] The intrinsic carrier concentration is given by:

$$n_i(cm^{-3}) = (8.445 - 2.2875x + 0.00342T) \times 10^{14} \tag{3.25}$$
$$E_g^{3/4} T^{3/2} \exp(-E_g/2kT),$$

where E_g is the energy gap in eV and T the temperature in degrees Kelvin. For a given x-value, the temperature dependence of the energy gap is given by:

$$E_g = -0.25 + 1.59x + 5.233 \times 10^{-4} (1-2.08x)T + 0.328x^3. \tag{3.26}$$

Electron and hole mobilities for $Hg_{1-x}Cd_xTe$ have been determined by Hall effect data. For $Hg_{0.8}Cd_{0.2}Te$, the temperature dependence of the mobilities can be fitted by the expressions:

$$\mu_e = 5.0 \times 10^9 T^{-2.3} \text{ cm}^2/\text{V-s} \quad (T > 30\text{K})$$
$$= 2.0 \times 10^5 \text{ cm}^2/\text{V-s} \quad (T < 30\text{K}); \quad \leftarrow T^{-?} \tag{3.27}$$

$$\mu_h = 7[illegible].0 \times T^{-0.4} \text{ cm}^2/\text{V-s}. \tag{3.28}$$

Mobility ratio data from photoconductive measurements indicate that μ_h is approximately the same in n-type as in p-type material.

The final material parameters are the electron and hole minority carrier lifetimes. There are three different processes which can contribute to recombination in (Hg,Cd)Te. These are Auger, radiative, and Shockley-Read. Expressions for Auger and radiative recombination have been determined; however, there is insufficient information about the nature and cross sections of Shockley-Read centers in (Hg,Cd)Te to make calculations.

For intrinsic material, the radiative recombination time is given by:[3.3]

$$\tau_{r,i} = n_i/2R_r, \tag{3.29}$$

where:

$$R_r^{-1} = \frac{5.8 \times 10^{-13} \varepsilon_\infty^{1/2}}{n_i^2} \left[\frac{m_o}{m_e^*} + \frac{m_o}{m_h^*}\right]\left[1 + \frac{m_o}{m_e^*} + \frac{m_o}{m_h^*}\right]\left[\frac{300}{T}\right]^{3/2} E_g^2. \tag{3.30}$$

For n-type material, the recombination time is $\tau = n_i^2/R_r N_D$. For both radiative and Auger processes, the minority and majority carrier recombination times are equal. For p-type material, $\tau = n_i^2/R_r N_A$.

Expressions for Auger recombination in n-type material have been determined. For intrinsic material:

$$\tau_{A,i} = \frac{7.6 \times 10^{-18} \varepsilon_\infty^2 (1+\mu)^{1/2}}{\frac{m_e^*}{m_o} |F_1 F_2|^2 \left(\frac{kT}{E_g}\right)^{3/2}} (1+2\mu) \exp\left\{\frac{1+2\mu}{1+\mu} \frac{E_g}{kT}\right\}, \tag{3.31}$$

where $\mu = m_e^*/m_h^*$, ε_∞ is the optical dielectric constant, and $|F_1F_2|$ is the band overlap integral. In n-type, $\tau = \tau_{A,i} (n_i/N_D)^2$. Theoretical values of $|F_1F_2|$ are accurate only to an order of magnitude. Experimental determinations of $\tau_{A,i}$ have been made by Kinch et al[3.3] for x = 0.2 material, and values of $|F_1F_2|$ appropriate to these measured recombination times are used.

In p-type $Hg_{1-x}Cd\ Te$, Auger recombination is much less probable than in comparably doped n-type due to the large hole mobility. For low and moderate carrier concentration p-type, electron-electron collisions are the dominant Auger process with $\tau = \tau_{A,i}$ ($N_A \lesssim 8.0 \times 10^{17} cm^{-3}$). For higher carrier concentration p-type, the full expressions in Section 3.2.2 must be used to include both hole-hole and electron-electron collisions.

The third recombination mechanism is Shockley-Read recombination. As analysis of data on current (Hg,Cd)Te photodiodes and direct measurements on p-type (Hg,Cd)Te will show, the latter mechanism is predominant both in present p-type (Hg,Cd)Te and in the depletion layer of present (Hg,Cd)Te photodiodes. Although a model for these Shockley-Read centers can be formulated, the model is not sufficiently developed to determine the recombination analytically. Therefore, the Shockley-Read combination time in p-type (Hg,Cd)Te will be used as a parameter in fitting measured diffusion current to the model, and the recombination time in the depletion layer as a parameter in fitting g-r current.

3.4.2 Lead-Tin Telluride Material Parameters

Material parameters for PbSnTe have been summarized by Melngailis and Harman.[3.6] The intrinsic carrier concentration is given by:

$$n_i(cm^{-3}) = 2.9 \times 10^{15} (TE_g)^{3/2} \exp(-E_g/2kT), \tag{3.32}$$

where E_g is in eV and T in degrees Kelvin. For a given x-value, the temperature dependence of the energy gap of $Pb_{1-x}Sn_xTe$ is given by:

$$E_g = 0.181 + 4.52 \times 10^{-4} T - 0.568 \times +5.8x^4. \tag{3.33}$$

One is often able to use the relationship between E_g and λ_{co}:

$$\lambda_{co} = 1.24/E_g(eV). \tag{3.34}$$

However, one must be very cautious in using this for two reasons. First, the optical absorption edge is gradual ($\sim 0.1\ \lambda_{co}$). Thus, the cutoff wavelength determined from the above may be longer than that measured in a device due to loss of photogenerated carriers deep in the junction. Second, at high doping levels n-type (Hg,Cd)Te and both n- and p-type PbSnTe exhibit the Burnstein shift. In the Burnstein effect "sharp" (low m^*) bands fill up rapidly at moderate dopant levels. Thus, material with a gap corresponding to 12 μm may not respond even at 10 μm. This problem is more severe in (Pb,Sn)Te than in p-type (Hg,Cd)Te due to low effective hole and electron masses in (Pb,Sn)Te.

Mobilities for $Pb_{0.8}Sn_{0.2}Te$ have been determined from Hall data. These data give majority carrier mobility. In using these values, one is assuming that the mobility can be extrapolated to minority-carrier transport. Mobility is strongly dependent on crystal growth techniques in (Pb,Sn)Te. The values for (Pb,Sn)Te films are used here[3.5]; values for bulk (Pb,Sn)Te are somewhat higher. The mobility in (Pb,Sn)Te is known to decrease at doping above 10^{16} cm^{-3}. The mobility also increases as the gap decreases due to the decreasing effective mass; we use $\mu \propto m^{*-1/2}$ to match experimental data. As $m^* \propto E_g$, $\mu \propto E_g^{-1/2}$:

$$\mu_e = 2.4 \times 10^9 T^{-5/2} (0.103/E_g)^{1/2} (1.0 \times 10^{16}/N_A)^{1/2} cm^2/V\text{-}s; \quad (3.35)$$

$$\mu_h = 2.4 \times 10^9 T^{-5/2} (0.103/E_g)^{1/2} (1.0 \times 10^{16}/N_D)^{1/2} cm^2/V\text{-}s. \quad (3.36)$$

There are three recombination mechanisms possible in semiconductors: Auger, radiative, and Shockley-Read. Expressions for Auger and radiative recombination have been determined; however, there is insufficient information about the nature of Shockley-Read centers in (Pb,Sn)Te to make calculations. The expression for radiative recombination was calculated by Melngailis and Harman:[3.6]

$$R_r^{-1} = \frac{2.5 \times 10^{14}}{n_i^2 n_1 E_g} N_V (kT)^{3/2} K_o^{1/2} (2+1/K_o)^{3/2} (m_e^*/m_o)^{5/2}, \quad (3.37)$$

where:

N_V = number of equivalent band extrema = 4

K_o = ratio of longitudinal to transverse effective mass ≈ 10

n_1 = index of refraction ≈ 6

m_e^*, m_h^* = electron, hole effective masses.

The minority carrier recombination times are given by:

$$\tau_e = n_i^2/N_A R_r, \quad \tau_p = n_i^2/N_D R_r. \quad (3.38)$$

The expression for Auger recombination has recently been determined by P.R. Emtage:[3.5]

$$\tau_{A,i} = \frac{\varepsilon_\infty^2 E_g^{7/2} m_\ell^{1/2} m_t^{3/2}}{3(2\pi)^{5/2} n_i^2 e^4 h^3 (kT)^{1/2}} \exp\left[\frac{m_t E_g}{m_\ell 2kT}\right], \quad (3.39)$$

where m_t and m_ℓ are the transverse and longitudinal effective masses and ϵ_∞ is the optical dielectric constant. The effective masses increase as the bandgap:

$$m_t \simeq 0.014\ m_o\ (E_g/0.10\ eV); \tag{3.40}$$

$$m_\ell \simeq 0.014\ m_o\ (E_g/0.10\ eV). \tag{3.41}$$

The ratio m_t/m_ℓ is 0:1 and accounts for the rapid Auger recombination in (Pb,Sn)Te. The Auger recombination time decreases as the square of the doping:

$$\tau_e = \tau_{A,i}(n_i/N_A)^2 \quad \tau_h = \tau_{A,i}(n_i/N_D)^2 \tag{3.42}$$

Since (Pb,Sn)Te devices are generally formed from heavily-doped material due to the difficulty of achieving low carrier concentration (Pb,Sn)Te, the Auger recombination can be significant.

3.5 FEASIBILITY OF NEW MATERIALS

Throughout Section 3 we have assumed the achievability of nearly perfect detector material, in which crystal defects do not limit device performance. Such a situation is achievable or within the realm of possibility for the presently well-developed materials, $Hg_{1-x}Cd_xTe$ and $Pb_{1-x}Sn_xTe$, at relatively high operating temperatures; see Sections 6 and 7. The incentive for finding and developing new materials can therefore only exist if either serious technological difficulties or fundamental limitations of the present materials exist. We will now conclude Section 3 by discussing the feasibility of new materials with respect to fundamental limitations.

We have shown in Section 3 that <u>fundamentally</u> for maximum D*, one needs a detector material satisfying three criteria:

a. Auger recombination should be weak or negligible compared to radiative recombination.

b. If (a) is satisfied then the material should have the lowest possible index of refraction.

c. And a material having a direct energy gap is preferred over an indirect-gap material, so that the detector material need not be so thick to achieve the optimum αt, that the advantageous use of a "high-low" or electrically-reflecting back contact in a photovoltaic detector is lost.

Auger recombination is strong in n-type $Hg_{1-x}Cd_xTe$ and apparently also in both types of $Pb_{1-x}Sn_xTe$, but it is relatively weak in p-type $Hg_{1-x}Cd_xTe$. It is unlikely that a new, different semiconductor could be found with Auger recombination significantly weaker than that in p-type $Hg_{1-x}Cd_xTe$.

The index of refraction of the $Hg_{0.8}Cd_{0.2}Te$ and $Pb_{0.8}Sn_{0.2}Te$ alloys used for 8 to 14-μm infrared detection and of a few other well-known semiconductors are listed below. These values illustrate the fact that the index of refraction varies little among different semiconductor materials. Therefore, only minor improvement in the maximum possible D* could be expected if another 8 to 14-μm material were found.

INDICES OF REFRACTION OF SEMICONDUCTORS

MATERIAL	INDEX OF REFRACTION
$Pb_{0.8}Sn_{0.2}Te$	6
$Hg_{0.8}Cd_{0.2}Te$	4.4
InSb	4
InAs	3.5
Ge	4
Si	3.4

We believe that the small improvement which could be expected at best does not warrant the extensive research which would be required to find such a material and develop its technology.

The presently well-developed materials, $Hg_{1-x}Cd_xTe$ and $Pb_{1-x}Sn_xTe$ both have direct energy gaps and therefore satisfy criterion(c).

Thus we conclude that p-type $Hg_{1-x}Cd_xTe$, employed in the photovoltaic detection mode, is nearly as good a material for maximum D* and high-temperature detector operation as one could ever hope to find. This is a fundamental conclusion derived from basic theory and assuming essentially perfect crystal material. It would therefore not be realistic to initiate a search for new materials.

3.6 REFERENCES

3.1 See for example Kruse, McGlauchlin, and McQuistan, "Elements of Infrared Technology," Wiley (1962).

3.2 P.E. Petersen, J. Appl. Phys. 41, 3465 (1970).

3.3 M.A. Kinch, M.J. Brau, and A. Simmons, J. Appl. Phys. 44, 1649 (1973).

3.4 P.E. Peterson,
To be published.

3.5 P.R. Emtage, J. Appl. Phys. 47, 2565 (1976).

3.6 I. Melngailis and T.C. Harman, Semiconductors and Semimetals 5, Ed. by R.K. Willardson and A.C. Beer (Academic Press, New York 1970) pp 111-174.

3.7 W. Shockley, Bell Sys. Tech. J. 28, 435 (1949).

3.8 S. Schulde, Honeywell Technical Memo, May 11, 1976.

3.9 J.S. Blakemore, Semiconductor Statistics, Pergamon Press, 1962.

3.10 A.R. Beattie and P.T. Landsberg, Proc. Roy. Soc. London A244, 16 (1959).

3.11 J.L. Schmit and E.L. Stelzer, J. Appl. Phys. 40, 4865 (1969).

3.12 E.O. Kane, J. Phys. Chem Solids 1, 249 (1957).

3.13 A.R. Beattie and P.T. Landsberg, Proc. Phys. Soc. 258, 486 (1960).

3.14 J. Baars and F. Sorgen, S. S. Comm. 10, 875 (1972).

3.15 F. Herman, Proc. IRE 43, 1703 (1955).

3.16 W. van Roosbroeck and W. Shockley, Phys. Rev. 94, 1558 (1954).

3.17 See, for example, F. Stern, Solid State Physics 15, 299 (1963), specifically Sections 35 and 36.

3.18 D. Long and J.L. Schmit, Semiconductors and Semimetals 5, Ed. by R.K. Willardson and A.C. Beer (Academic Press, New York 1970) pp 175-255

SECTION 4

PERFORMANCE LIMITATIONS OF 8-14μm PHOTODIODES AT ELEVATED TEMPERATURES

4.1 INTRODUCTION

In this section, the status of present 8-14μm photodiodes is assessed, the ultimate performance determined, and the factors limiting present devices isolated. This analysis consists of five parts:

- An analytical model of photodiode performance is developed which allows performance to be calculated giving material parameters and device design;
- The performance of present (Hg,Cd)Te and (Pb,Sn)Te photodiodes is modeled and key parameters limiting performance isolated;
- The ultimate performance of (Hg,Cd)Te and (Pb,Sn)Te photodiodes at elevated temperatures is determined.
- Improvements in both device design and in material parameters required to achieve ultimate performance are explored.
- Coupling conditions for interfacing diodes to amplifiers and to charge coupled devices are determined.

Semiconductors other than (Hg,Cd)Te and (Pb,Sn)Te are also assessed. However, these semiconductors are close relatives of either (Hg,Cd)Te or (Pb,Sn)Te. Thus, the performance of devices fabricated from these other materials is unlikely to be substantially better.

4.2 THEORETICAL MODEL OF PHOTODIODE PERFORMANCE

In this section, an analytical model of photodiode performance is developed. The model will have three purposes:

- To model performance of current devices
- To determine limitations of present devices with respect both to material parameters and device design.
- To determine optimum device design and ultimate performance.

To develop the model, the expression for signal and noise in photodiodes will be outlined.

The performance of a detector is usually characterized by its D*, or signal-to-noise ratio normalized for area and bandwidth:

$$D^* = R_i \sqrt{A\Delta f} \; / \; i_n \tag{4.1}$$

where:

R_i = current responsivity

A = area

Δf = bandwidth

i_n = noise current

For a photodiode, the responsivity is determined by the quantum efficiency η and the wavelength λ:

$$R_i = \eta q \lambda / hc \tag{4.2}$$

where h is Planck's constant and c is the speed of light.

The noise sources associated with a photodiode are Johnson noise due to the junction resistance R_o, background induced noise current, and 1/f noise i_f:

$$\frac{i_n^2}{\Delta f} = \frac{4kT}{R_o} + 2\eta q^2 \phi_B A + \frac{i_f^2}{\Delta f} \tag{4.3}$$

where ϕ_B is the background flux and k is Boltzmann's constant.

Because 1/f noise is process dependent and cannot be treated analytically, it will not be discussed in this section. For the best present 10-micrometer diodes the background flux is the limiting factor; for a 180-degree FOV the background-limited D^*_λ (11 μm, η=1) is 5.0×10^{10} cm $Hz^{1/2}/W$. However, to evaluate detectors the detector noise rather than the background noise is of interest. In addition, for direct coupling to a CCD, the critical parameter is R_oA. Thus background noise will not be considered in this section.

Substituting the expressions for R_i and i_n, the expression for D^* becomes:

$$D^*_\lambda = \frac{\lambda q \eta}{hc} \sqrt{\frac{R_o A}{4kT}} \tag{4.4}$$

There are three current mechanisms which contribute to R_oA. These are generation-recombination current, diffusion current and surface leakage current (shunt). If there are no contacts or surfaces within a diffusion length of the diode, the R_oA product due to diffusion current can be written as:

$$(R_oA)^{-1} = \left[\frac{n_i^2}{N_A}\sqrt{\frac{\mu_e}{\tau_e}} + \frac{n_i^2}{N_D}\sqrt{\frac{\mu_h}{\tau_h}}\right] q\sqrt{\frac{q}{kT}} \qquad (4.5)$$

where:

n_i = intrinsic carrier concentration

μ_e, μ_h = electron and hole (minority carrier) mobility

τ_e, τ_h = electron and hole (minority carrier) recombination time

N_A, N_D = dopant concentrations on p and n sides (acceptor and donor concentrations)

Diffusion current is due to the diffusion of thermally generated minority carriers from the n and p sides of the semiconductor to the depletion layer at the p-n interface. The volume of semiconductor which contributes to diffusion current is given by the diode area times the diffusion length for a minority carrier. The minority carrier diffusion length is given by:

$$L = \sqrt{\frac{kT}{q}\,\mu\,\tau} \qquad (4.6)$$

The volume of semiconductor required to generate the signal is the diode area times the optical absorption depth required to absorb 90% of the incoming radiation:

$$L_{opt} = 2.5/\alpha \qquad (4.7)$$

where α is the absorption coefficient, typically 5×10^3 cm^{-1}. Thus, $L_{opt}\approx5\mu m$. In most cases, the minority carrier diffusion lengths are considerably longer than 5μm; thus, a substantial volume of the semiconductor is contributing noise without contributing signal.

It is possible to shrink the effective semiconductor volume to the volume necessary for signal collection by use of "reflective" contacts.[4.1] The use of heavily doped p+ and n+ regions in back of the p and n regions creates a space-charge barrier to minority carrier diffusion and reduces minority carrier density in the heavily doped regions.

The R_oA for the case when reflective contacts are used is given by:

$$(R_oA)^{-1} = q\sqrt{\frac{q}{kT}}\left[\frac{n_i^2}{N_A}\sqrt{\frac{\mu_e}{\tau_e}}\tanh\left(\frac{b_p}{L_e}\right) + \frac{n_i^2}{N_D}\sqrt{\frac{\mu_h}{\tau_h}}\tanh\left(\frac{b_n}{L_p}\right)\right] \quad (4.8)$$

where b_p and b_n are the distances from the junction to the p and n side space-charge barriers.

Generation-recombination (g-r) current is due to thermal generation and recombination of carriers in the depletion layer. Generation and recombination can be due to three processes: radiative, Auger, and Shockley-Read.

The expression for R_oA for g-r current has been derived by Sah, Noyce and Shockley.[4.2] For bias voltages near V ~ 0:

$$(R_oA)^{-1} = \frac{qn_iW\,f(b)}{V_{bi}\sqrt{\tau_{no}\,\tau_{po}}} \quad (4.9)$$

where:

$$W = \text{depletion layer width} = \sqrt{\frac{2\varepsilon_s(V_{bi} + V)}{q\,N_B}} \quad (4.10)$$

$$V_{bi} = \text{built-in voltage} = \frac{kT}{q}\ln\frac{(N_A\,N_D)}{n_i^2} \quad (4.11)$$

τ_{no}, τ_{po} = minority carrier lifetimes on n and p sides of the junction

and f(b) is a function depending on the position of the Shockley-Read centers with respect to the conduction and valence bands. For centers in mid-gap, f(b) = 1.

The theoretical limit to g-r noise in defect-free material is the radiative recombination limit. D. Long[4.3] has shown that for radiative recombination

$$\sqrt{\tau_{no}\,\tau_{po}}\ /f(b) \qquad (4.12)$$

should be replaced by the radiative recombination time in intrinsic material, τ_{ri}.

Since diffusion-limited R_oA increases as n_i^{-2} as the temperature is lowered while generation-recombination noise increased as n_i^{-1}, there is a temperature at which the diode switches from diffusion to g-r limited behavior. This is shown in Figure 4.1. The increase in R_oA will not continue indefinitely as the temperature is decreased further; at some temperature the surface leakage resistance (shunt resistance) dominates the R_oA becomes independent of temperature.

4.3 PRESENT STATUS OF 11-μm (Pb,Sn)Te PHOTODIODES

4.3.1 p-n Junctions

In this section, the present status of (Pb,Sn)Te photodiodes is reviewed. Analysis of data on (Pb,Sn)Te devices will yield the following information:

- Temperature range over which diffusion current is dominant
- Temperature range over which generation-recombination current is dominant
- Depletion layer lifetime.
- Minority carrier lifetimes on n and p-side.

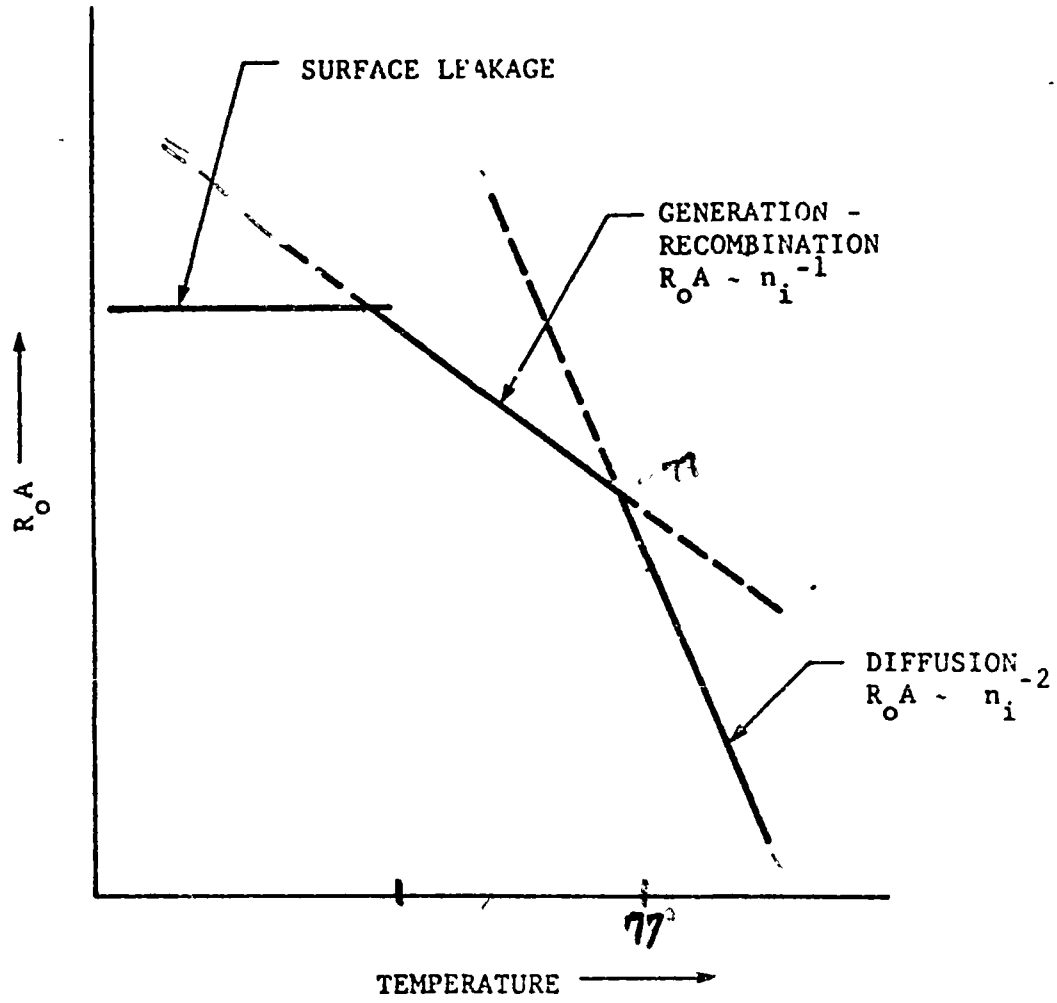

Figure 4.1 R_oA VS TEMPERATURE FOR A pn JUNCTION PHOTODIODE, SHOWING REGIONS OF TEMPERATURE OVER WHICH THE JUNCTION R_oA PRODUCT IS LIMITED BY VARIOUS MECHANISMS.

Three types of devices have been made in (Pb,Sn)Te: ordinary p-n diodes, heterojunctions and Schottky barrier diodes. Diodes in (Pb,Sn)Te are fabricated from either bulk material[4.4, 4.8, 4.9, 4.10] or from layers deposited by vapor[4.5, 4.6, 4.7] or liquid phase epitaxy. The as-grown material is generally high carrier concentration ($>10^{17}cm^{-3}$) and requires annealing to achieve low carrier concentration. A donor dopant is then diffused to create an n-layer. Because of the symmetry of the conduction and valence bands in (Pb,Sn)Te, the theoretical performance of n+ on p and p+ on n are equivalent.

Figure 4.2 shows R_oA as a function of temperature for a (Pb,Sn)Te diode fabricated by DeVaux, et al.[4.11] The devices were fabricated using indium diffusion to form an n-layer on a p-type (Pb,Sn)Te wafer. The donor and acceptor concentrations were $N_D \sim 1.0 \times 10^{17}$ cm^{-3} and $N_A \sim 2.0 \times 10^{16}$ cm^{-3}. For temperatures below 77K, the device was limited by generation-recombination current and displayed $R_oA = 2.0\ \Omega$-cm^2. The model of the previous sections with the depletion layer lifetime as the fitting parameter yields $\tau_o \sim 20$ ns for an abrupt junction. For T > 77K, the device is limited by diffusion current. DeVaux, et al, assumed a constant lifetime of 1.7×10^{-8} s to fit this data. However, calculations based on the theory of Auger recombination is (Pb,Sn)Te by Emtage[4.12], indicate that the recombination time was limited by Auger recombination. The Auger recombination lifetime for $N_A \cong 3 \times 10^{15}$ cm^{-3} is 3.5×10^{-8} s, and is relatively insensitive to temperature until the semiconductor becomes intrinsic ($n_i > N_A$). Thus, it is possible that the (Pb,Sn)Te diode of DeVaux, et al, was limited by diffusion current from both the n and p-sides, with an effective lifetime of ~30 ns limited by Auger recombination.

Figure 4.3 shows data from DeVaux et al,[4.11] for a (Pb,Sn)Te diode fabricated from a higher p-type carrier concentration wafer. Theoretically, R_oA should increase as N_A for a Shockley-Read limited lifetime, as $N_A^{1/2}$ for radiative and would be independent of N_A for Auger-limited. As can be seen from Figure 4.3, R_oA decreased with N_A, implying either Auger-limited behavior or a Shockley-Read limited in which stoichiometric-related defects play a role *

Figure 4.4 shows R_oA as a function of N_A for diodes fabricated by DeVaux. For a constant lifetime τ_o, R_oA should increase as N_A; for a radiative-limited lifetime, R_oA should increase as $N_A^{1/2}$, and for Auger-limited lifetime, R_oA is independent of N_A. As can be seen, the experimental data decreases slightly with N_A, indicating Auger-limited lifetime.

Wang et al[4.10] have fabricated p-n homojunctions using epitaxial (Pb,Sn)Te. The heavily doped side had a carrier concentration of 1.0×10^{17} cm^{-3} while the lightly doped side was 2.8×10^{16}cm^{-3}. Capacitance-voltage data indicated that the junction was graded with a grading constant $a = 2.0 \times 10^{21}$cm^{-4}. Wang et al reported temperature dependence of the R_oA product. At temperatures below 80 K the diodes were limited by generation-recombination current with an effective depletion-layer lifetime of 70 ns. At temperatures above 80K the diodes were limited by diffusion current. Modeling of the temperature dependence of the R_oA product

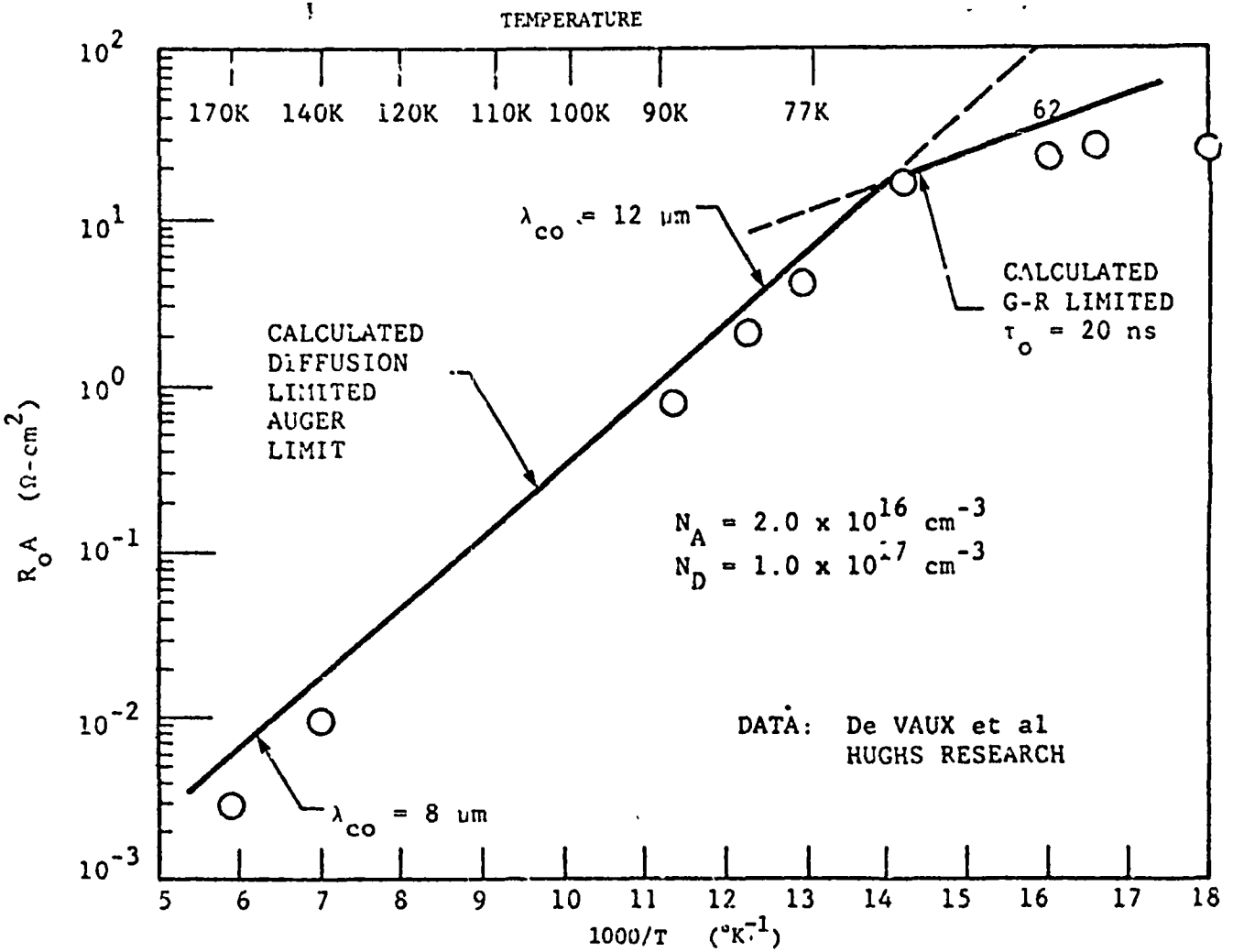

Figure 4.2 R_oA VS TEMPERATURE : (Pb,Sn)Te (From Reference 4.11)

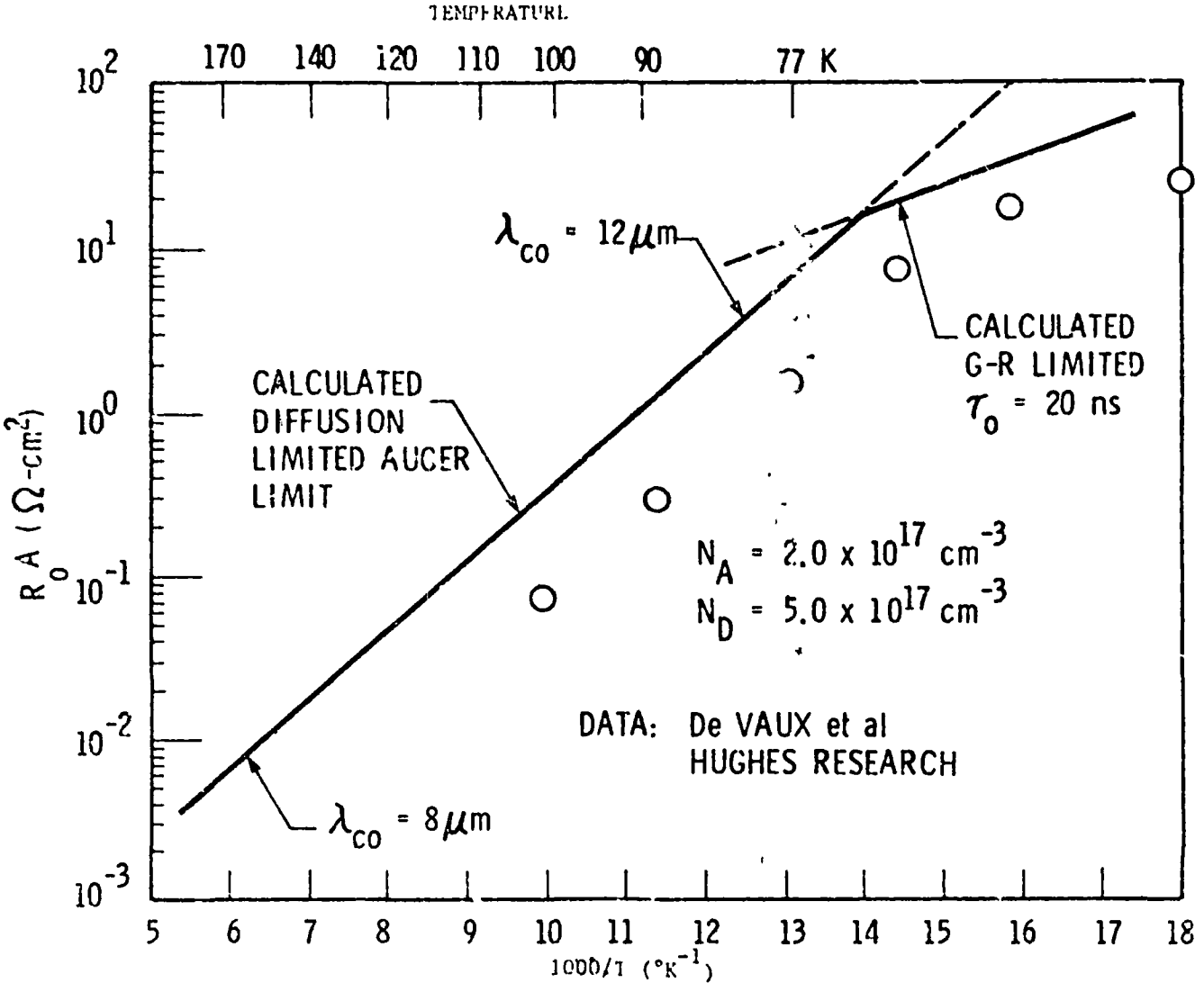

Figure 4.3 $R_o A$ VS TEMPERATURE: (Pb,Sn)Te (From Reference 4.11)

indicated a lifetime of approximately 40ns. The Auger-limited lifetime calculated using the theory of Emtage for a carrier concentration of 2.8×10^{16} cm^{-3} and a 0.11 eV bandgap is 82ns. Thus, it is possible that the devices were achieving lifetimes limited by Auger recombination.

4.3.2 (Pb,Sn)Te Schottky Barrier Diodes

A number of contractors have fabricated Schottky barrier diodes on (Pb,Sn)Te. The devices have shown performance equivalent to that obtained in p-n photodiodes and heterojunctions at 77K; however, no data at elevated temperature has been published.

For a true Schottky barrier, the maximum barrier height ϕ_B is the energy gap E_g. Using $\phi_B = E_g$ and the expression for R_oA for a Schottky barrier given in Section 4.3.5, the calculated R_oA is $0.2\Omega\text{-cm}^2$ at $\lambda_{co} = 12$ µm and $1.6\Omega\text{-cm}^2$ at $\lambda_{co} = 11$µm. The measured data is often well above $0.3\Omega\text{-cm}^2$. D. Bellavance and M. Johnson of Texas Inst.[4.13] report $R_oA \sim 1.0\Omega\text{-cm}^2$ at 77K for arrays using In or Pb electrodes on epitaxial (Pb,Sn)Te with $\lambda_p = 10.7$µm. However, Schottky barrier diodes fabricated on (Pb,Sn)Te are probably not true Schottky barriers due to the presence of an inversion layer under the electrode. For In electrodes, the large metal work function appears to result in strong band-banding. This gives rise to an inversion layer[4.14]. The result is a p-n junction with a barrier to current flow given by $E_F - \delta$. For a degenerate semiconductor, the Fermi level is in the band and $E_F - \delta \geq E_g$. The device formed in this manner would not perform as a true Schottky barrier, but rather similar to a p-n diode.

4.3.3 Heterojunctions

There has been extensive development of (Pb,Sn)Te heterojunctions for both thermal imaging and space-borne applications.[4.8,4.9,4.10] The heterojunction is formed by liquid-phase epitaxial (LPE) growth of (Pb,Sn)Te on PbTe substrate, or LPE growth of PbTe on a (Pb,Sn)Te substrate. Due to the 5 µm cutoff of PbTe, the junction can be back-side illuminated.

The lattice match between PbTe and $Pb_{0.8}Sn_{0.2}Te$ is sufficiently good that the density of interface states is quite small. The use of heterojunction instead of p-n homojunctions has a number of advantages. The epitaxial films have lower defect density and greater uniformity in composition than bulk (Pb,Sn)Te. Also, the carrier concentration in bulk (Pb,Sn)Te is generally limited by stoichiometry to values greater than $1.0 \times 10^{17} cm^{-3}$; at this high a carrier concentration both n and p-type are degenerate and exhibit a Burstein shift and a short minority carrier lifetime. The use of epitaxial growth makes possible low carrier concentrations ($< 5.0 \times 10^{15} cm^{-3}$). Finally, the thickness of the LPE layer can be adjusted to be equal to an optical absorption depth, effectively reducing the volume of semiconductor generating noise.

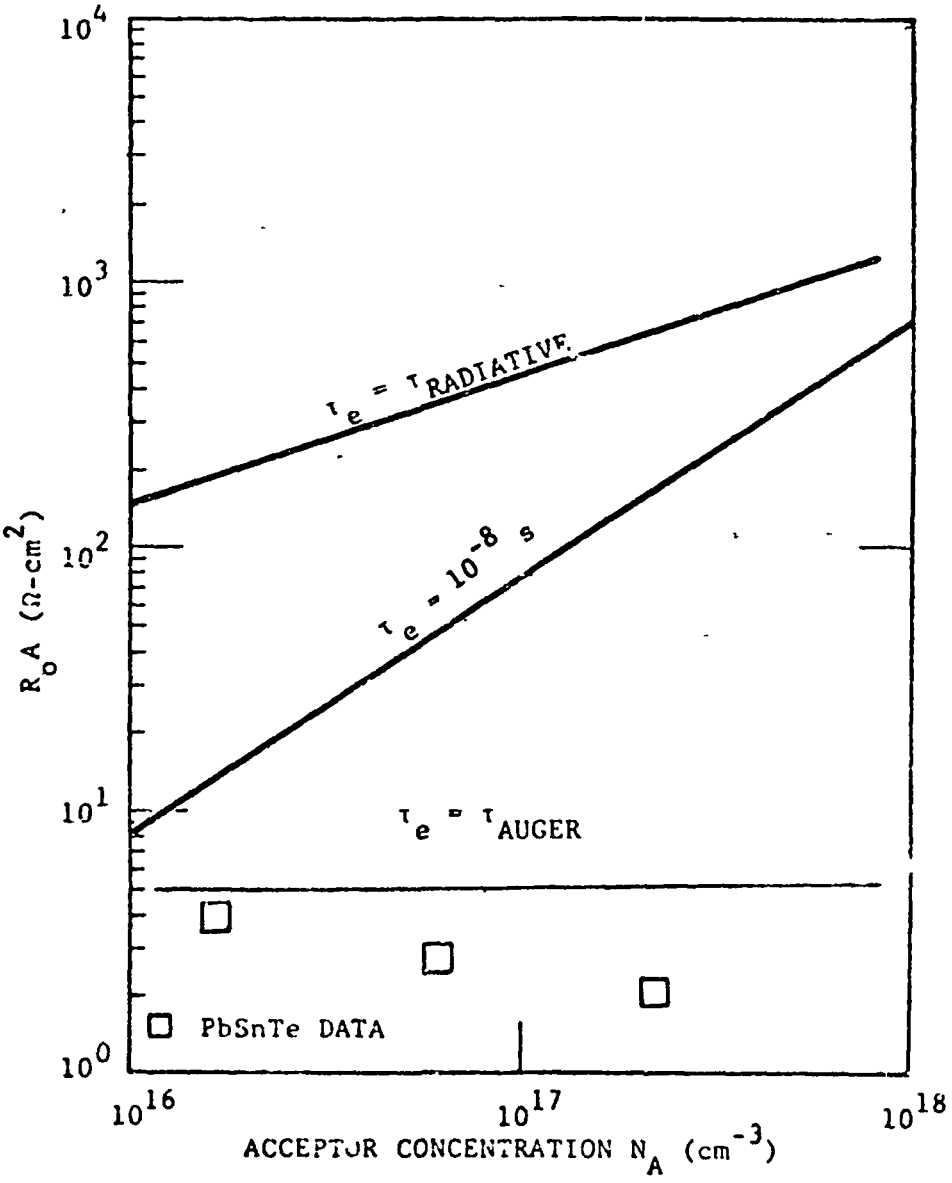

Figure 4.4 R_oA VS DOPANT CONCENTRATION FOR (Pb,Sn)Te p-n PHOTODIODES (Data from Reference 4.11)

Figure 4.5 shows R_oA as a function of temperature for a PbTe/ (Pb,Sn)Te heterojunction[4.15] at temperatures T < 50K. The device had a cutoff wavelength of 10.6μm at 77K and 14.5μm at 30K. The data was fitted using the model of the previous section. The device was limited by g-r current over the full temperature range; the depletion layer lifetime used to fit the data was 5ns. The theory is for an abrupt junction. In fact, the device was graded instead of abrupt and so had a correspondingly longer lifetime.

Lockwood et al[4.9] have reported a (Pb,Sn)Te based heterostructure with high R_oA product at 77K ($R_oA \cong 10.0\Omega\text{-cm}^2$). The device structure was not disclosed; as a result it was not possible to model the performance. The theoretical limit for a p-n (Pb,Sn)Te homojunction at 77K with a 0.10 eV bandgap is of order $6.0\Omega\text{-cm}^2$ (assuming the Auger-limited lifetimes as determined by Emtage). As the expressions for Auger lifetime are approximate, the data of Lockwood could be modeled by assuming diffusion current from the (Pb,Sn)Te side of the heterostructure. However, the minority carrier diffusion length calculated assuming Auger-limited lifetime in (Pb,Sn)Te doped at 1.0×10^{16} cm^{-3} is 52μm. As the depth required for signal collection is only ~8μm, a factor of 6-7 improvement in R_oA could be realized by limiting the thickness of the active (Pb,Sn)Te epitaxial layer to ~8μm and either passivating or accumulating the surface to reduce surface generation of carriers. Thus, the theoretical upper limit for a (Pb,Sn)Te hererojunction using a 8-μm thick active layer is $R_oA \sim 40.0\Omega\text{-cm}^2$. Thus, the data of Lockwood et al is well within the theoretical limits for a thin (Pb,Sn)Te film.

In summary, data on (Pb,Sn)Te p-n junctions has been modeled using the expressions developed in Section 4.1. The highest R_oA values reported can be fit assuming diffusion-current limited R_oA with the minority carrier lifetimes on the n and p sides limited by Auger recombination. This would suggest that the best (Pb,Sn)Te photodiodes currently achieve close to the theoritical limit R_oA at elevated temperatures. However, the calculation of Auger lifetime in (Pb,Sn)Te is probably not accurate to within a factor of 2-5, so the conclusion must remain tentative. A substantial amount of (Pb,Sn)Te data with lower R_oA products has been reported; these devices appear limited either by surface leakage or by a short minority-carrier lifetime probably associated with Shockley-Read centers.

4.4 PRESENT STATUS OF 11-μm (Hg,Cd)Te PHOTODIODES

In this section, data on 8-14μm (Hg,Cd)Te photodiodes are reviewed and compared to the model developed in the previous section. Data analysis will yield the following information:

- Recombination time in p-type (Hg,Cd)Te
- Depletion layer lifetime.
- Temperature range over which diffusion current is dominant
- Temperature range over which generation-recombination current is dominant
- Shunt-resistance limit of current devices

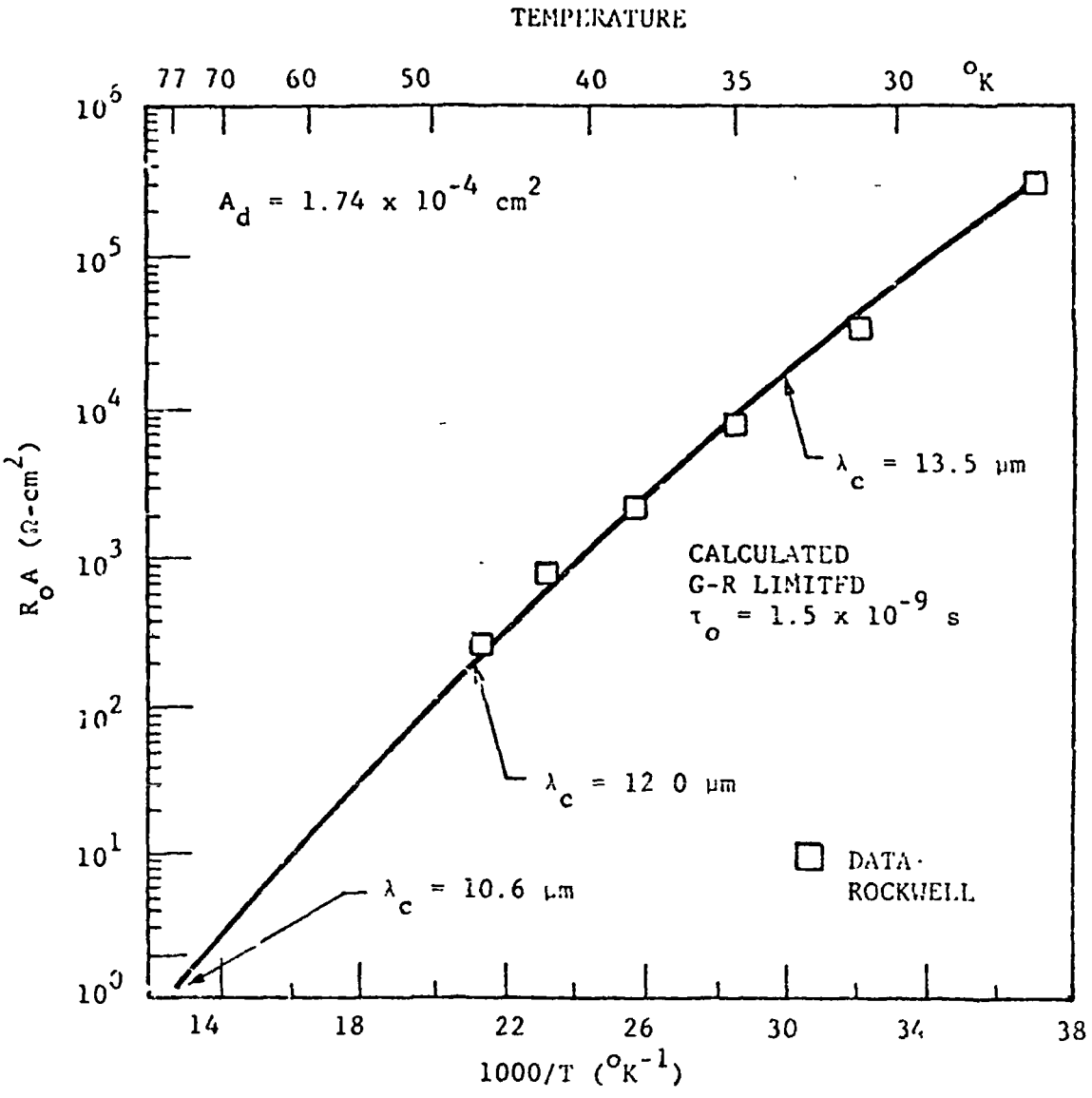

Figure 4.5 R_oA VS TEMPERATURE· (Pb,Sn)Te hFTERO.'UNCTION (Reference 4.15)

77-1-6

4.4.1 n- on p

Three types of devices have been fabricated in (Hg,Cd)Te: n- on p, n+ on p and p+ on n. The three device structures are shown in Figure 4.6 The n- on p diode is formed as follows. At the high temperatures at which (Hg,Cd)Te is grown, a substantial number of metal (Hg and Cd) vacancies are present in (Hg,Cd)Te; these vacancies act as acceptors. By introducing Hg or Cd into the lattice, in a low temperature anneal, these vacancies are filled, reducing the acceptor concentration to a low value ($\sim 10^{14}$ cm^{-3}). If donor impurities at the low 10^{14} cm^{-3} level are present in the lattice, the annealed region becomes n-type. Thus, an n-region is formed in a p-type (Hg,Cd)Te wafer. The junction depth, typically 4-μm, is controlled by the diffusion time and temperature. The n+ on p structure can be formed either by ion implant or diffusion of a donor into p-type (Hg,Cd)Te. Similarly, the p+ on n structure can be formed by ion implant or diffusion of an acceptor into n-type (Hg,Cd)Te.

Figure 4.7 shows R_oA as a function of temperature for a (Hg,Cd)Te n- on p photodiode.[4.16] The diode cutoff wavelength was 11μm at 77K and 9μm at 150K (the shift due to the change in energy gap in (Hg,Cd)Te with temperature). The dopant levels were $N_D = 2.0 \times 10^{14}$cm^{-3} and $N_A = 1.0 \times 10^{17}$cm^{-3}. At low temperatures (T < 105K), the R_oA product increases as n_i^{-1}, where n_i is the intrinsic carrier concentration. This indicates that the diode was dominated by g-r current. This has been confirmed both by the slope of the forward I-V characteristics ($I \propto e^{qV/2KT}$) and the reverse I-V characteristics ($I \propto V^{1/2}$). The model developed in Section 4.2 was used to fit the data using the depletion layer lifetime as the variable. The analysis indicated a lifetime $\tau_o = 30$ns. As 30ns is a factor of 100 shorter than τ_{R1} or τ_{A1}, the short lifetime is presumably due to Shockley-Read centers.

At elevated temperatures (T > 105K), the R_oA product varies as n_i^{-2}, indicating diffusion-limited current. This has been confirmed by forward I-V ($I \propto e^{qV/KT}$) characteristics.

To determine whether it is the n-side or the p-side which limits the diode, it is necessary to determine the minority carrier lifetimes on the two sides. On the n-side, the theoretical limiting lifetime mechanism is Auger recombination. Measured lifetimes in bulk n-type $Hg_{0.8}Cd_{0.2}Te$ have been measured by Kinch et al[4.17] and were Auger limited. Measurements of minority carrier lifetimes on the n and p sides of n- on p diode have been made using the rolloff frequencies of the i-f signal in laser heterodyne measurements.[4.16] These measurements confirm an Auger-limited lifetime on the n-side of the diode. The p-side lifetime determined from these measurements was $\sim 1.0 \times 10^{-8}$s, considerably shorter than the radiative recombination lifetime which is the theoretical upper limit in p-type (Hg,Cd)Te at 77K.

Using these lifetimes and the model of Section 4.2, it can be shown that the p-side limits the R_oA product of the n$^-$-on-p diode. The p-side lifetime determined from modeling the data shown in Figure 4.16 was 30ns. The radiative limit at 110K is 200ns. The Auger limit is considerably longer for both electron-electron and hole-hole processes. Thus, the 30ns lifetime is due to Shockley-Read recombination.

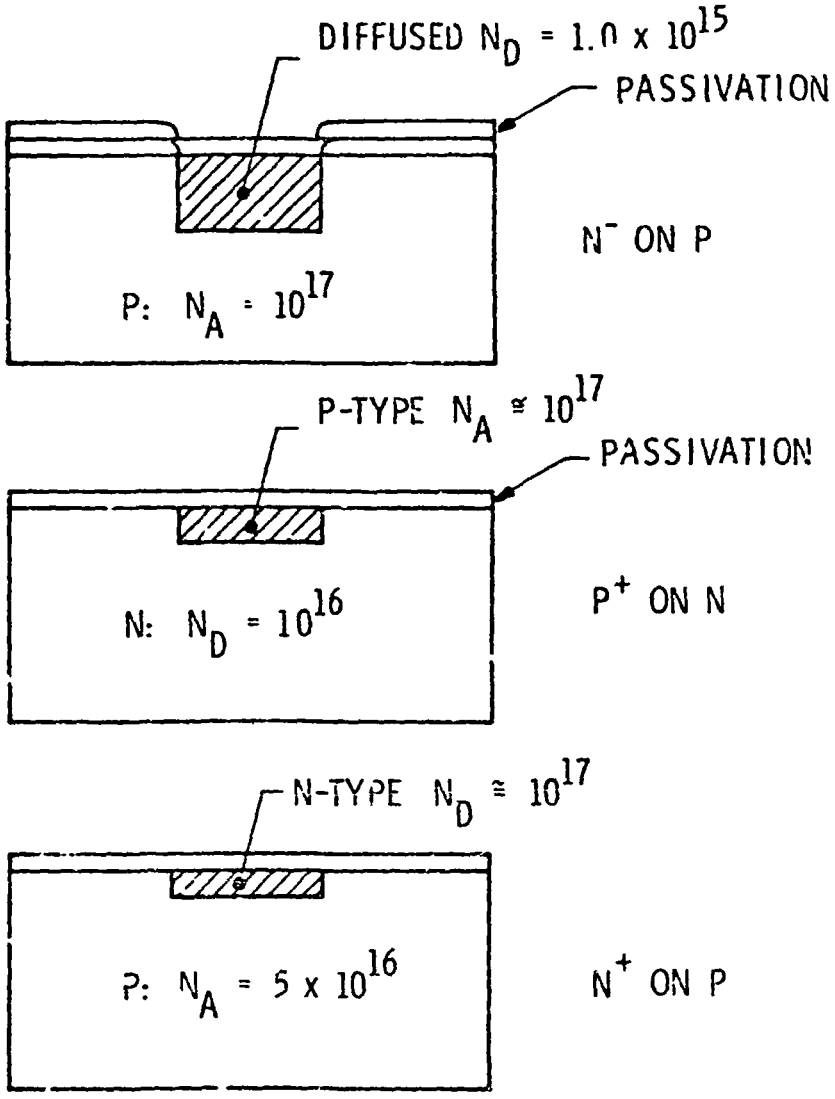

Figure 4.6 (Hg,Cd)Te PHOTODIODE STRUCTURE

ORIGINAL PAGE IS
OF POOR QUALITY

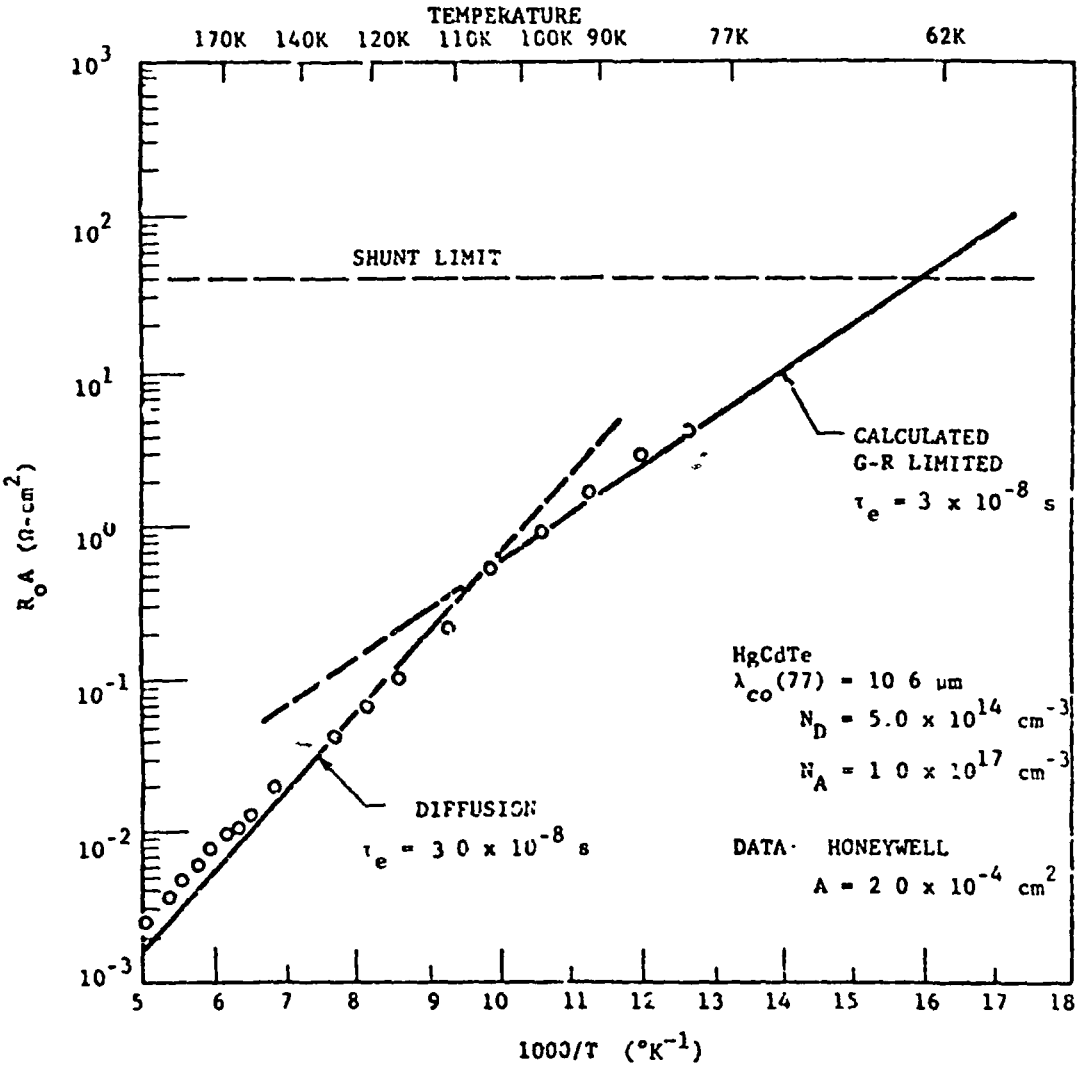

Figure 4.7 R_oA VS TEMPERATURE n⁻ ON p (Hg,Cd)Te PHOTODIODE

The data on present n- on p (Hg,Cd)Te photodiodes can be summarized as follows:

- At low (T < 110K) temperatures, the diodes are limited by generation-recombination current. At 77K, the best (Hg,Cd)Te devices display R_oA products of 1.0 to 4.0Ω-cm^2, corresponding to $D^*(\eta = 0.5) = 7\times10^{10} - 1.4\times10^{11}$ cm Hz$^{1/2}$/W. In practice, 1/f noise reduces measured D^*_λ below these values.

- The depletion-layer lifetimes determined using the model of the previous section and (Hg,Cd)Te diode data range from 1×10^{-9}s to 3×10^{-8}s. These lifetimes are much shorter than the intrinsic Auger and radiative lifetimes and are due to a Shockley-Read center.

- At elevated temperatures (T > 105K), (Hg,Cd)Te diodes are limited by diffusion current. At 120K, the R_oA of a device with λ_{co}(120K) = 9.2μm was 0.1 -cm^2, corresponding to $D^*_\lambda = 1.4\times10^{10}$cm Hz$^{1/2}$/W. At 200K, the device R_oA was 2.5×10^{-3}, corresponding to $D^*(\lambda_{co}=8.5\mu m) = 1.6\times10^{9}$cmHz$^{1/2}$/W. The diffusion current is from the p-side and can be modeled by a minority-carrier lifetime $\tau_e \sim 3\times10^{-6}$s.

- Independent measurements of the minority carrier lifetimes have been made using laser heterodyne mixing; these measurements confirm the Auger-limited lifetime on the n-side and the short, Shockley-Read limited lifetime on the p-side.

4.4.2 n+ on p (Hg,Cd)Te Photodiodes

The n+ on p diode structure is fabricated using either an implantation or diffusion of a donor into a p-type wafer. The p-type wafer may be moderately doped (1.0×10^{16}cm^{-3}) or heavily doped ($\sim2.0\times10^{18}$cm^{-3}). The n-side is typically doped $N_D = 1.0\times10^{17}$cm^{-3} to $N_D = 1.0\times10^{18}$cm^{-3}.

The use of the high dopant concentration on the n-side considerably changes the analysis of junction properties. Due to the low conduction-band effective mass in (Hg,Cd)Te, the n-type (Hg,Cd)Te becomes degenerate at relatively low ($\sim 2.0\times10^{15}$cm^{-3} @ 77K) carrier concentrations. In this case the Fermi level is well above the conduction band. Using the usual expressions for the electron carrier concentration.[4.18]

$$n_o = N_C F_{\frac{1}{2}}(\eta)$$

where:

N_C = conduction band density of states

$$= 4.8\times10^{15} \left(\frac{M_c^*}{M_o}\right)^{3/2} T^{3/2} = 1.2\times10^{15} \text{cm}^{-3}$$

$$\eta = (E - E_C)/kT$$

$$F_{\frac{1}{2}}(\eta) = 2\pi^{-\frac{1}{2}} \int_0^\infty \frac{\varepsilon^{\frac{1}{2}}\, d\varepsilon}{1 + \exp(\varepsilon-\eta)}$$

For $N_D = 1.0\times10^{16}$, $E_F - E_C = 10kT$. So for the n+ side of the n+ on p (Hg,Cd)Te diode the Fermi level is well into the conduction band.[4.19]

The degeneracy on the n-side strongly affects Auger lifetimes. This can be seen qualitatively as follows. Generation of carrier by Auger mechanism takes place by impact ionization, as shown in Figure 4.8. For Auger generation to occur, states 1 and 2 must be occupied while states 1' and 2' must be unoccupied. For low n-side doping levels ($N_D \lesssim 1\times10^{15}\text{cm}^{-3}$) the final states (1' and 2') are unoccupied near the conduction band edge. Hence, the energy change ΔE, in the transistion, is approximately a bandgap Eg. The Auger mechanism decreases in probability as $\exp(-\Delta E/KT)$. For heavy doping levels on the n-side, the n-side is degenerate and the Fermi level is well up into the conduction band. Therefore, the states 1' and 2' near the band edge are filled and the normal Auger process is shut off. The only possible process would require states 1' and 2' near the Fermi level. Thus, the energy change $\Delta E'$ involved in the transition in degenerate n-type (Hg,Cd)Te is much greater and the transition rate is drastically reduced. Calculations performed by Paul Peterson[4.20] have confirmed this reduction in Auger recombination in degenerate n-type (Hg,Cd)Te. If the Auger recombination rate calculated using degenerate statistics is in fact much lower than that calculated using nondegenerate statistics, then the diffusion current from the n-side will be reduced substantially.

Thus, the Auger lifetime calculated using non-degenerate statistics predicts a much shorter lifetime than what is estimated for degenerate statistics. Thus, the n-side can often be neglected in calculating diffusion current in a n+ on p diode provided the n-side Shockley-Read lifetime is not extremely short. It should be kept in mind that the use of doping levels well above those required for degeneracy shifts the absorption edge well away from the cutoff of intrinsic material (this is known as the Burstein shift). Thus, the n-side acts as a window and the radiation is absorbed on the p-side.

n^+ on p (Hg,Cd)Te photodiode have been fabricated by J. Marine and C. Motte of S.A.T.[4.21] for the 8 - 14 μm spectral region and by T. Tredwell of Honeywell in the 2 μm spectral region.[4.22] Figure 4.9 shows data of Marine and Motte. The curve is for a diode with λ_{co} = 13 μm at 77 K.

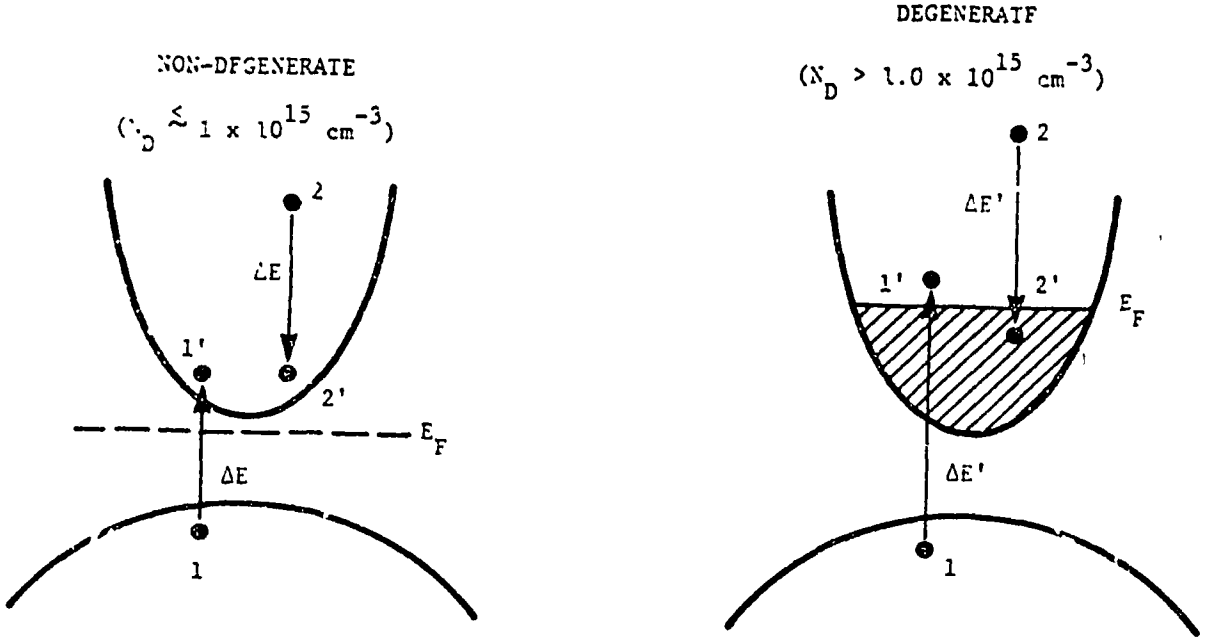

Figure 4.8 AUGER GENERATION (IMPACT IONIZATION)

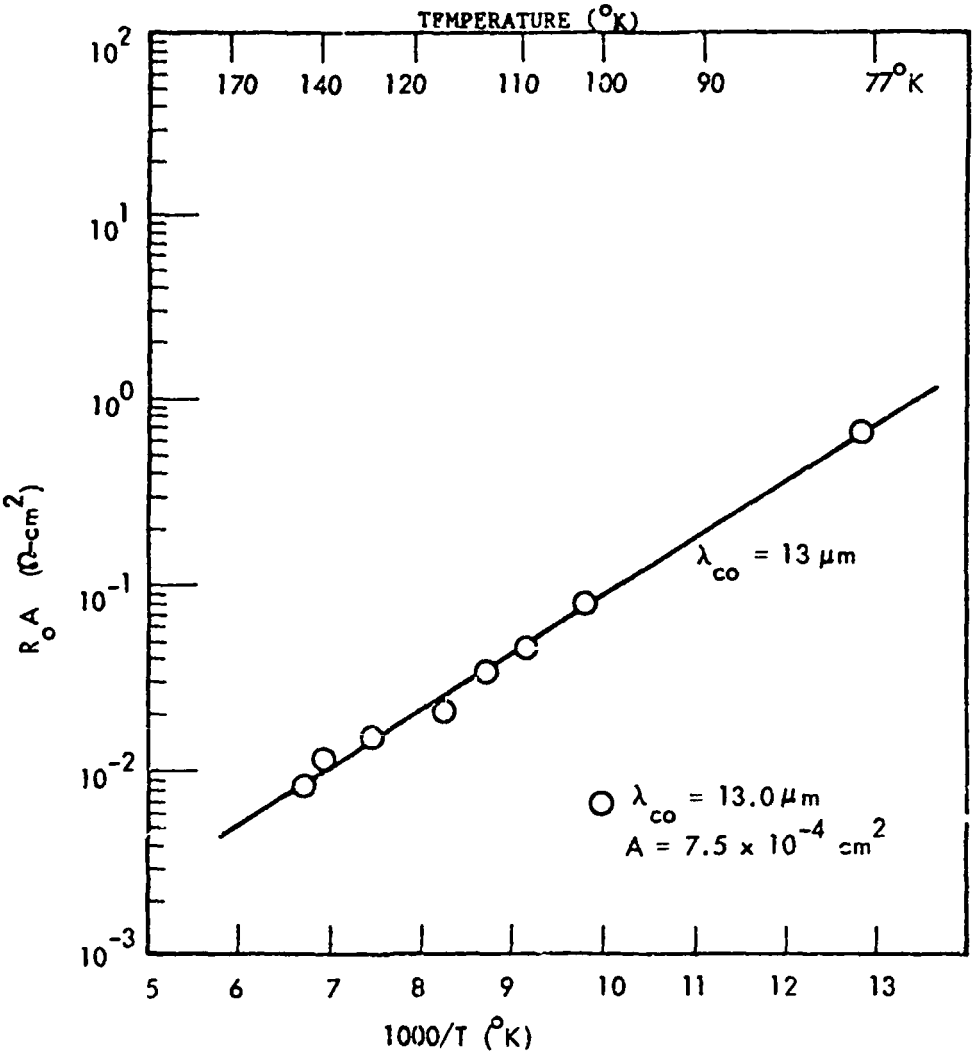

Figure 4.9 $R_o A$ VS TEMPERATURE n^+ on p (Hg,Cd)Te PHOTODIODES
(Data from Reference 4.21)

The data was modeled using the expressions given in Section 4.2. The Auger lifetime on the n-side was assumed to be sufficiently long that diffusion current from the n-side did not limit device performance. The 13-μm diode data followed the generation-recombination current expression over the full temperature range. As capacitance-voltage characteristics indicated an abrupt junction, it is possible to determine the depletion layer lifetime; the lifetime determined in this manner was 2ns. The fact that no diffusion current was seen, even at elevated temperatures, makes it possible to set a lower limit to the minority carrier lifetime on the p-side, τ_e. This lower limit is $\tau_e > 100$ns, very near the radiative recombination limit at this temperature.

The shorter wavelength device has been modeled in a similar manner. The diode also appears to be limited by generation-recombination current over the full temperature range, with an effective depletion layer lifetime of $\tau_o \sim 10$ns.

Results on n+ on p (Hg,Cd)Te photodiodes may be summarized as follows:

- The high n-side doping level makes the n-side degenerate. As a result Auger recombination is significantly reduced and so diffusion current from the n-side also reduced. Also, the n-side will be transparent to the radiation and so the optical absorption takes place on the p-side.
- Analysis of present 8-14μm n+ on p diode data indicated that the devices are limited by generation-recombination current over the full temperature range with an effective depletion-layer lifetime of ~5ns. The lifetime is probably due to Shockley-Read center. However, use of minimum doping levels above that used in the n- on p diode has reduced the g-r current.

4.5 THEORETICAL PERFORMANCE LIMITS OF 8-14μm (Pb,Sn)Te PHOTODIODES

In this section, the ultimate performance of (Pb,Sn)Te photodiodes is determined. Two types of devices are considered: p-n diodes and Schottky barriers. For each, the present limit to device performance is calculated using the lifetimes determined from measurements on (Pb,Sn)Te diodes. Two types of improvements are then assumed: improvements in material parameters (largely in minority carrier lifetime) and improvements in device design. The performance limits of devices with these improvements are then calculated.

4.5.1 (Pb,Sn)Te p-n Junctions

The analysis of the previous section has indicated that the best (Pb,Sn)Te photodiodes are limited by the short Auger lifetime in (Pb,Sn)Te. Calculations using the expression for Auger lifetime derived by Emtage fit the data of DeVaux, et al, to within a factor of two. The analysis indicated that (Pb,Sn)Te photodiodes will be limited by diffusion current for T > 77K.

Using the Auger-limited lifetime, the R_oA of (Pb,Sn)Te diodes at elevated temperatures is shown in Figure 4.10 for a constant λ_{co} = 12μm. Since the bandgap of (Pb,Sn)Te changes with temperature, no one single device would have λ_{co} = 12μm at all temperatures; for Figure 4.10 the $Pb_{1-x}Sn_xTe$ composition x is varied to achieve a 12μm cutoff at all temperatures.

$D^*\lambda$ is related to R_oA by

$$D^* = \frac{\lambda \eta}{h c} \sqrt{\frac{R_o A}{4kT}} = 1.08 \times 10^{11} \lambda_p \eta \sqrt{\frac{R_o A}{T}}$$

where background and amplifier limits have not been included. The calculations indicate that $D^*\lambda = 1.0 \times 10^{10}$ cmHz$^{\frac{1}{2}}$/W is possible at 120K.

Two types of improvements are possible: improvements in material parameters and improvements in device design. The only material parameters which can be changed are the minority carrier lifetimes on the n- and p-sides. However, in the best (Pb,Sn)Te photodiodes the minority carrier lifetimes appear to be limited by Auger recombination and so could not be improved.

Some improvements in device design are possible The equation for for R_oA is:

$$(R_oA)^{-1} = q\sqrt{\frac{q}{kT}} \left[\frac{n_i^2}{N_A}\sqrt{\frac{\mu_e}{\tau_e}} + \frac{n_i^2}{N_D}\sqrt{\frac{\mu_h}{\tau_h}} \right]$$

One way to increase R_oA might seem to be to use higher dopant levels, since $R_oA \propto N_A$. However, for Auger-limited lifetimes, the lifetime decreases as N_A^2, thus cancelling out the advantage gained by heavier doping unless the doping is such as to make the material degenerate. For a (Pb,Sn)Te diode:

$$(R_oA)^{-1} = \sqrt{\frac{\gamma}{kT}}\, q\, n_i^2 \left[\sqrt[4]{\mu_n^{\gamma}} + \sqrt{\mu_n^{-1}} \right]$$

where γ is the Auger recombination coefficient. Thus, no advantage is gained by heavier dopant concentrations.

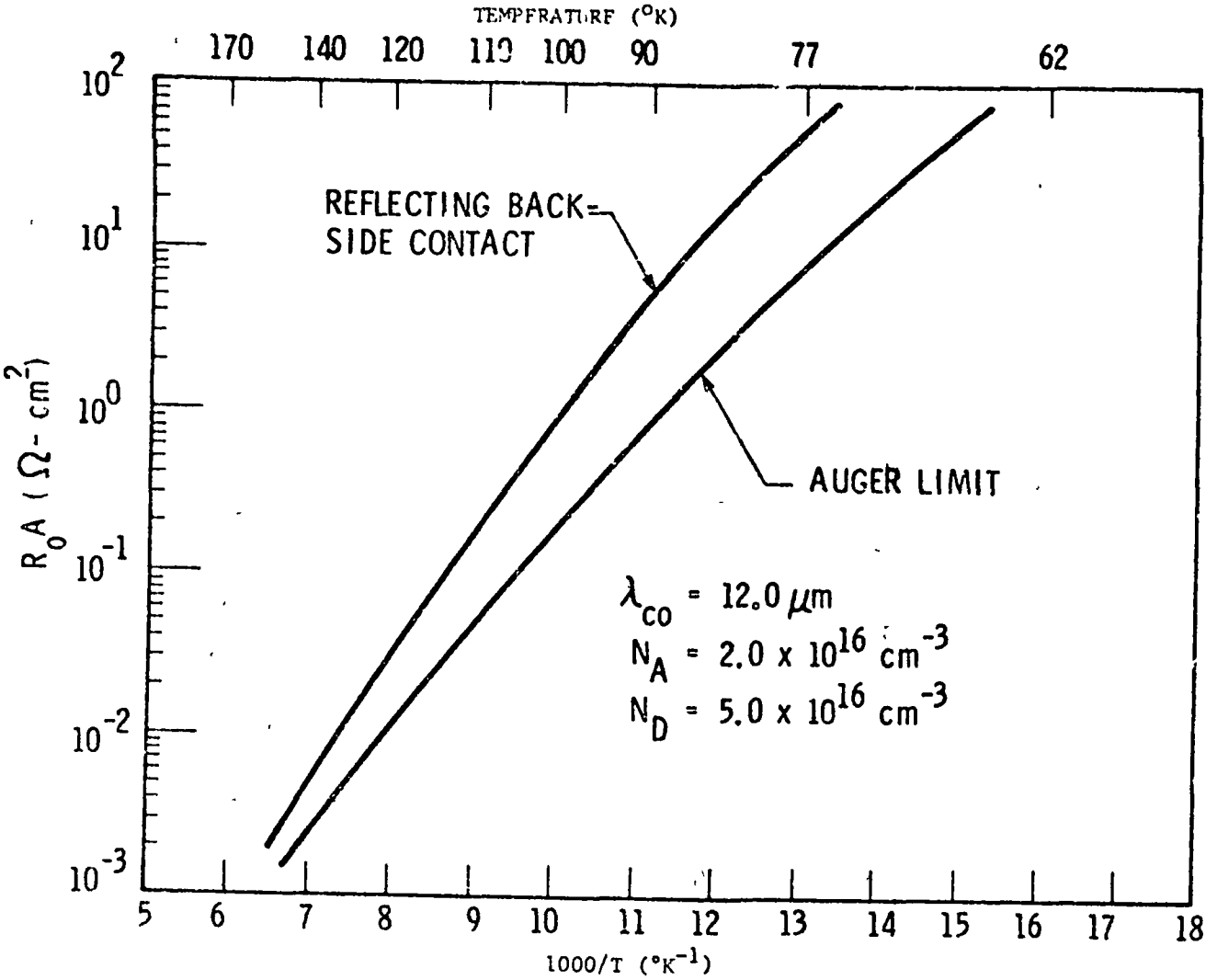

Figure 4.10 R_oA VS TEMPERATURE: (Pb,Sn)Te HETEROJUNCTION

The other way to increase R_oA is the use of reflective back-side contacts. Reflective back-side contacts could be realized in a number of ways. Examples include thin (Pb,Sn)Te films on a substrate such as BaF_4 or epitaxial (Pb,Sn)Te on PbTe. In order for the full potential of the reflective contact to be realized, the density of interface states or surface states must be sufficiently low that minority carrier generated from the interface or surface states are fewer than those which would be generated from within a diffusion length from the junction. Due to the relatively short Auger lifetime in n and in p-type (Pb,Sn)Te, the advantage to be gained from the reflective contact is small. The diffusion length for (Pb,Sn)Te doped at $1.0\times10^{16}cm^{-3}$ is 52μm at 80K and 20μm at 120K; at least 8μm are required for collection of signal. Therefore, the reflecting back-side contact results in less than a factor of 7 improvement in R_oA for (Pb,Sn)Te at 80K and a factor of 3 at 120K. The improvement is also shown in Figure 4.10.

4.5.2 (Pb,Sn)Te Heterojunctions

(Pb,Sn)Te heterojunctions are fabricated by growth of an epitaxial (Pb,Sn)Te layer on a PbTe substrate. The PbTe substrate is usually p-type with $N_A \sim 10^{17}cm^{-3}$; the epitaxial layer is doped or annealed to n-type $N_D \sim 3.0\times10^{16}cm^{-3}$. To calculate the heterojunction performance we assume that the electron affinities of PbTe and (Pb,Sn)Te are equal. As $\Delta E_c >> \Delta E_v$ for a p-type PbTe substrate and an n-type (Pb,Sn)Te film, it is assumed that the dominant source of current is hole diffusion current. For a heterojunction,

$$(R_oA)^{-1} = q\sqrt{\frac{q}{kT}}\,\frac{n_i^2}{N_D}\sqrt{\frac{\mu_h}{\tau}}\,\frac{N_{cp}}{N_{cn}}\,\tanh\frac{b}{L_h}$$

as $N_c \propto m^{*\,3/2} \propto E_g^{\,3/2}$, $N_{cp}/N_{CN} = 0.27$. For $N_D \sim 1\times10^{16}$, $L_h \cong 30\mu m$ at 120K. The distance b must be at least 8μm for signal collection; thus, the improvement from reflecting contacts is approximately a factor of 4.

4.5.3 (Pb,Sn)Te Schottky Barrier Diodes

The expression for R_oA for a Schottky barrier diode is given in Section 4.6.5. The best (Pb,Sn)Te devices exceeded the limit for true Schottky barriers. The metal work function was much greater than the band gap; thus, an inverted region below the metal caused the device to behave more like a conventional p-n diode than a Schottky barrier. The limiting performance for a (Pb,Sn)Te Schottky barrier is shown in Figure 4.11 for $\phi_B = E_g$, which is the maximum ϕ_B possible without inversion. The corresponding operating temperature for $R_oA = 0.01$ is 100K, well below the corresponding operating temperature for p-n diodes.

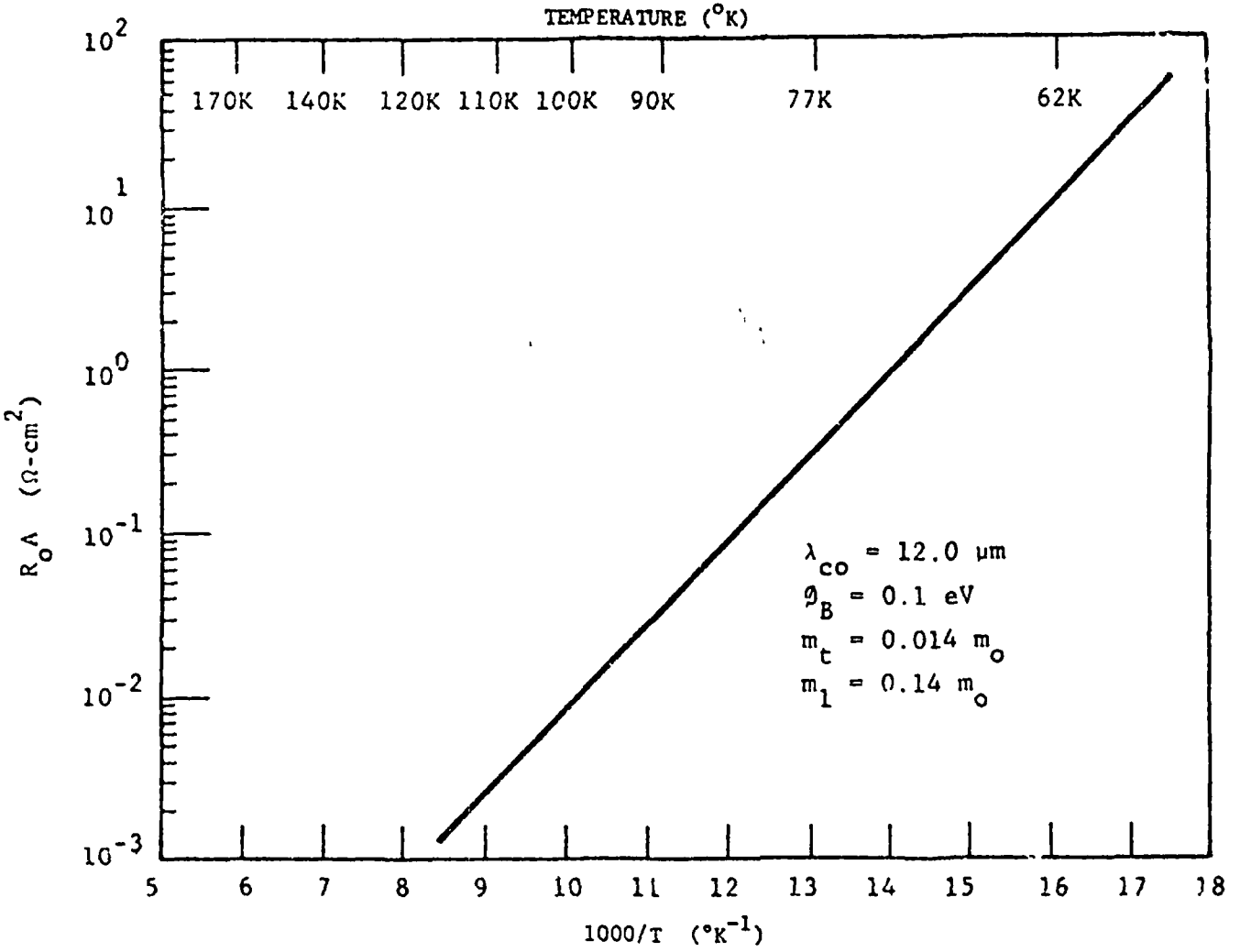

Figure 4.11 R_oA VS TEMPERATURE: (Pb,Sn)Te SCHOTTKY BARRIER

4.5.4 Summary: (Pb,Sn)Te

The optimum device design for elevated temperature operation for (Pb,Sn)Te is the p-n photodiode. Neither heterojunctions nor Schottky barrier diodes can achieve performance superior to p-n junctions at elevated temperatures, although heterojunctions can obtain equivalent performance. The maximum operating temperature for a (Pb,Sn)Te photodiode with reflecting back-side contacts is 135K for $D^* = 8.0 \times 10^9$ cm $Hz^{1/2}/W$ at $\lambda_{co} = 12\mu m$. The ultimate device performance is limited by high diffusion current due to a short Auger-limited lifetime; present devices approach this limiting performance. Thus, further improvement in (Pb,Sn)Te performance at elevated temperatures is unlikely.

4.6 PERFORMANCE LIMITS FOR (Hg,Cd)Te PHOTODIODES

In this section the limits for 12-μm (Hg,Cd)Te photodiodes at elevated temperatures are determined. Three types of devices are considered: p-n junctions, heterojunctions and Schottky-barrier diodes. The performance for 12-μm devices fabricated using presently available materials and device technology is calculated and the performance possible with improved materials and improved device design determined.

Due to the assymetry of the conduction and valence bands in (Hg,Cd)Te, three device designs with different performance characteristics are possible: n- on p, n+ on p and p+ on n. We consider each device type.

4.6.1 n- on p (Hg,Cd)Te Photodiode

We consider first the device design presently used for wide bandwidth applications, i.e., a lightly doped ($5 \times 10^{14} cm^{-3}$) n-layer on a heavily doped ($1 \times 10^{17} cm^{-3}$) p-type wafer. The depth of the junction below the surface is 2μm, limited by the diffusion time and temperature. As the surface is doped n+, the front contact is effectively a reflecting contact with b = 2μm.

Figure 4.12 shows R_oA as a function of temperature for both the n and p sides. Present devices are limited by the short recombination time in p-type (Hg,Cd)Te with $\tau_e \sim 3 \times 10^{-8}$s. If the p-side lifetime is increased to the radiative limit, a factor of five improvement in diffusion current is possible. If the lifetime is increased to the radiative limit, the diffusion length on the p-side is increased to 200μm for $N_A = 5 \times 10^{16} cm^{-3}$. However, only 10μm are required for signal collection. Thus, a factor of 20 increase in R_oA is possible with a reflecting back-side contact; this is also shown in Figure 4.11.

At elevated temperatures, however, the diffusion current from the n-side dominates. For a n-side doped $1.0 \times 10^{15} cm^{-3}$, the Auger-limited lifetime is 1.5μs at 77K and 37ns at 160K.* On the p-side, doped $N_A \sim 1.0 \times 10^{17} cm^{-3}$, the radiative-limited lifetime is not strongly temperature dependent.

* The n-side becomes intrinsic above 120K and at 160K $n_i = 7.5 \times 10^{15} cm^{-3}$

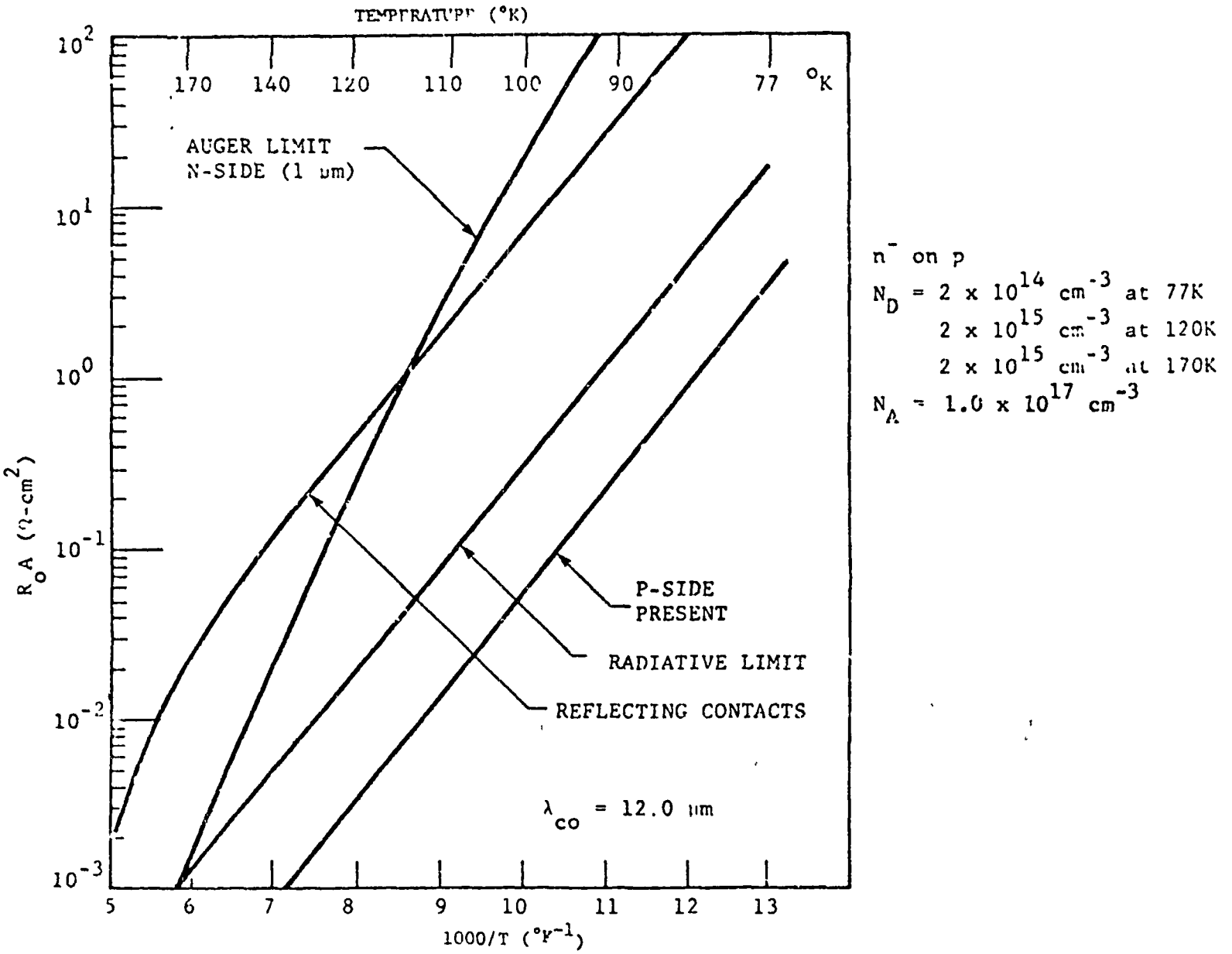

Figure 4.12 R_oA VS TEMPERATURE: n$^-$ ON p (Hg,Cd)Te PHOTODIODE

4.6.2 n+ on p (Hg,Cd)Te Photodiode

The n+ on p is formed by ion implant or diffusion of a n+ layer on a p-type wafer. As discussed in the previous section, the n+ doping concentration ($\sim 1.0 \times 10^{17} - 5.0 \times 10^{18} cm^{-3}$) renders the n-side degenerate. This results in an increased Auger lifetime and lower minority carrier density on the n-side, thus substantially improving the performance at elevated temperatures. The analysis of the previous section indicates that the device would be limited by diffusion from the p-side.

Figure 4.13 shows the calculated R_oA as a function of temperature for a diode with an acceptor concentration $N_A = 5.0 \times 10^{16} cm^{-3}$. The lowest curve is for a 30ns Shockley-Read limited lifetimes presently observed in p-type (Hg,Cd)Te. The electron diffusion length is ~34μm, so reflective back-side contacts would improve R_oA by a factor of 3. If the lifetime can be improved to the radiative limit, the operating temperature is increased. However, the diffusion length is increased to 176μm; use of a reflective contact can result in a factor of 18 improvement in R_oA. This is also shown in Figure 4.13.

At temperatures below 150K the p-side lifetime is ultimately limited by radiative recombination. However, above 150K electron-electron Auger recombination becomes dominant and limits device performance (in p-type (Hg,Cd)Te doped $N_A < 1.0 \times 10^{18} cm^{-3}$ electron-electron Auger processes dominate hole-hole processes; the Auger lifetime is given by the intrinsic Auger lifetime τ_{A1}). Thus, above 150K the R_oA of a n+ on p junction with reflecting contacts rolls off rapidly due to electron-electron Auger processes.

A device design using a more heavily doped p-side has somewhat better performance at elevated temperatures. For $N_A = 1.0 \times 10^{18} cm^{-3}$ the radiative lifetime is ~20ns, which is shorter than the Auger lifetime and shorter than Shockley-Read lifetimes observed on present p-type (Hg,Cd)Te. Thus, the p-side lifetime could be radiatively-limited over virtually the full temperature range up to 190K. As the results of sections 2 and 3 indicated, for a p-n junction with reflecting contact limited only by radiative recombination the R_oA is independant of doping level. Thus, a n+ on p+ device design offers the best performance at elevated temperatures. At temperatures below 150K the performance is equivalent to the n+ on p design. Figure 4.14 shows R_oA as a function of temperature for a n+ on p+ design.

4.6.3 p+ on n (Hg,Cd)Te Photodiode

The p+ on n design would be fabricated by ion implant of a thin (1000Å) p+ layer on an n-type wafer. The device is very attractive at low temperatures for the following reason. Low carrier concentration n-type (Hg,Cd)Te displays lifetimes close to the Auger limit while in p-type the lifetime is shorter than the radiative limit due to a Schockley-Read center.

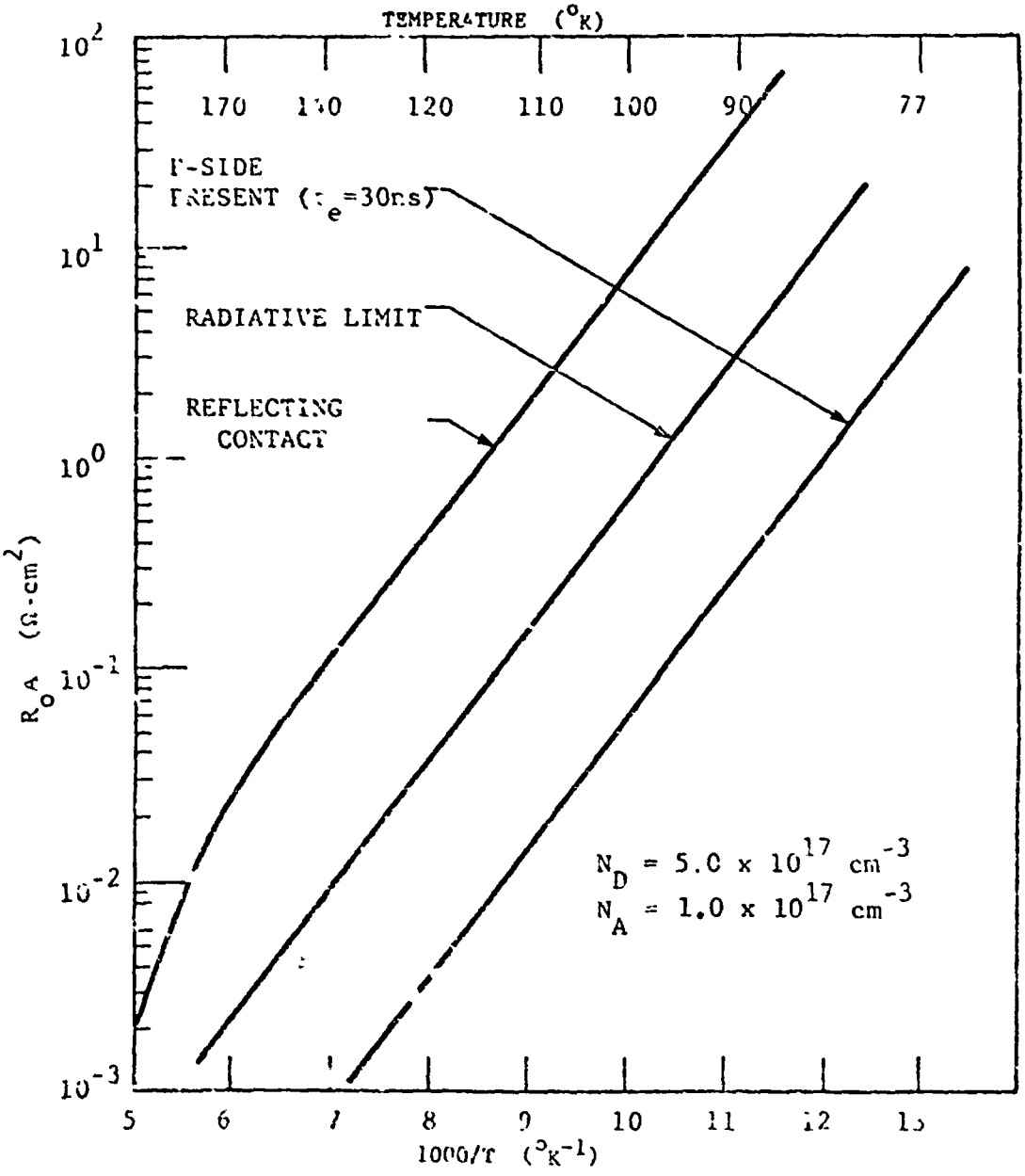

Figure 4.13 $R_o A$ VS TEMPERATURE: n+ on p (Hg,Cd)Te PHOTODIODE

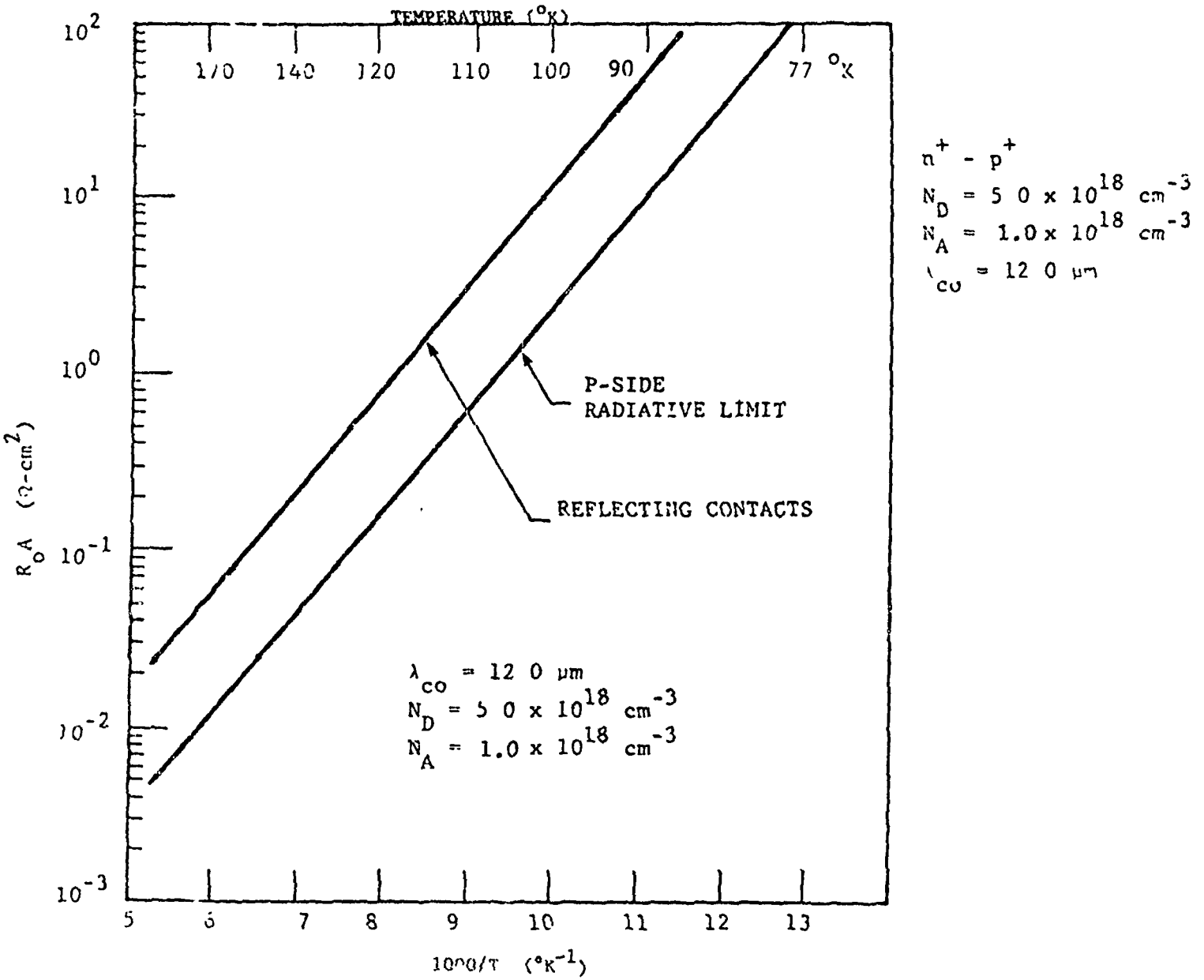

Figure 4.14 $R_o A$ VS TEMPERATURE: n+ on p+ (Hg,Cd)Te PHOTODIODE

If a thin p+ layer were implanted, the diffusion length in the p-type material would be restricted to the 1000Å implant depth and the p-side would contribute negligible diffusion current. Thus, no effort to improve the lifetime in p-type (Hg,Cd)Te would be required. At 77K, the diffusion-limited R_oA for this device would be 15.0Ω-cm^2. For $N_D = 2x10^{14}$, the Auger lifetime is 6μs and the diffusion length is 30μm. However, at elevated temperatures, higher dopant levels are required to maintain $N_D > n_i$. At 170K, for example, $n_i = 1.0x10^{16}$ cm^{-3} and the Auger-limited lifetime for $N_D = 2x10^{16}$ is 5ns. This results in a diffusion length of 800Å, much too short to collect the signal. Thus, the device is limited by the short hole diffusion length in n-type (Hg,Cd)Te at elevated temperatures. The maximum operating temperature determined by the necessity to have $L_h > 8\mu m$ is 120K. The D* obtained at 120K would be $3.0x10^{10}$ cm $Hz^{1/2}/W$. Figure 4.15 shows R_oA and diffusion length for a p+ on n structure.

4.6.4 Heterojunctions

The fundamental advantage gained in using a heterojunction for (Hg,Cd)Te instead of a homojunction is that one side can be made of a sufficiently wide bandgap that diffusion noise from that side is reduced to a small value. As the limiting factor in a p-n (Hg,Cd)Te homojunction could ultimately be diffusion current from the n-side, the use of a wide bandgap n-side would eliminate this limitation. The R_oA for the diffusion current in a heterojunction with the wide-bandgap side n-type is:

$$(R_oA)^{-1} = q\sqrt{\frac{q}{kT}}\ \frac{n_i^2}{N_A}\ \frac{N_{CN}}{N_{CP}}\ \sqrt{\frac{\mu_e}{\tau_e}}$$

and the generation-recombination limited R_oA is:

$$(R_oA)^{-1} = \frac{q\,W}{2\,V_D}\left(\frac{n_{i,p}}{2\,\tau_{op}} + \frac{n_{i,n}}{2\,\tau_{on}}\right)$$

where:

$$V_D = kT\ \ln\left(\frac{N_A\,N_D}{n_{i,p}^2}\ \frac{N_{CP}}{N_{CN}}\right)$$

As the conduction-band density of states N_C is proportional to $(M^*/M_o)^{3/2}$, the ratio of the densities of states is:

$$\frac{N_{CN}}{N_{CP}} = \left(\frac{M^*_{e,n}}{M^*_{e,p}}\right)^{3/2} = \left(\frac{E_{g,n}}{E_{g,p}}\right)^{3/2}$$

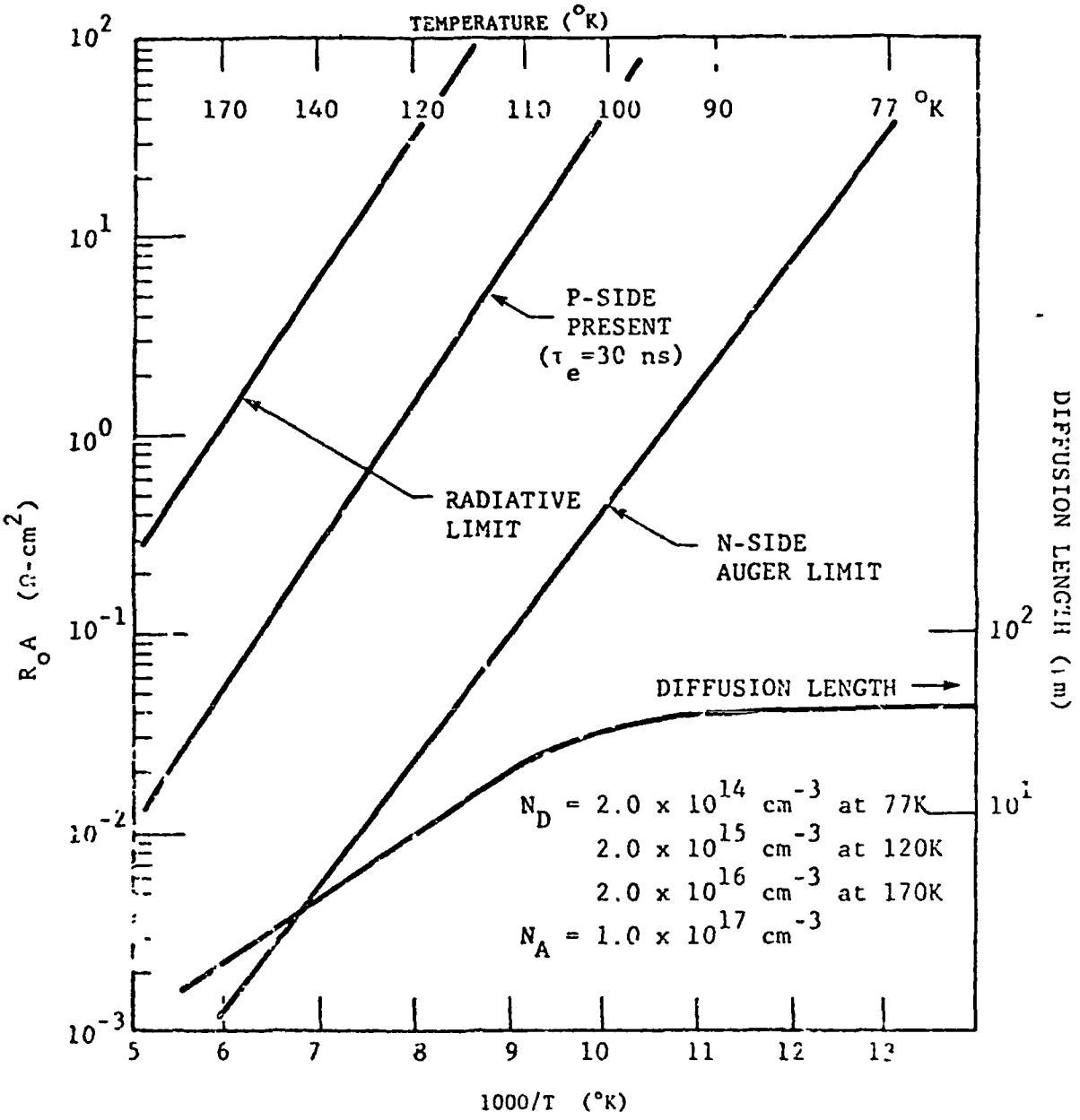

Figure 4.15 $R_o A$ VS TEMPERATURE p+ ON n (Hg,Cd)Te PHOTODIODE

77-1-6

which is a small factor as long as the gaps on the p and n side are not greatly different. Thus, the heterojunction theoretically offers R_oA values equivalent to a p-n junction. The heterojunction would reduce n-side diffusion current. n-side diffusion current is not thought to be a limiting factor in n+ on p diodes, but the uncertainty of Auger lifetime calculations in degererate n-type (Hg,Cd)Te makes the conclusion tentative. Should n-side diffusion current be a significant factor in improved n+ on p diodes, then a heterojunction would improve R_oA.

4.6.5 (Hg,Cd)Te Schottky Barrier Photodiodes

The R_oA for a Schottky Barrier photodiode is given by:

$$R_oA = \frac{K}{q\ A^*\ T} \exp\ (q\ \phi_B/KT)$$

For a true Schottky barrier, $\phi_B \leq Eg$. Figure 4.17 shows calculated R_oA versus temperature for a 12-μm (Hg,Cd)Te Schottky Barrier. The best performance is with n-type (Hg,Cd)Te due to the low effective mass. The limiting operation temperature for $D^* = 8.0 \times 10^9$ cm $Hz^{\frac{1}{2}}/W$ is 135K. This is lower than either the n+ on p homojunction or the heterojunction device design.

It is possible to achieve higher R_oA by using a metal with a work function such that $\phi_B >> Eg$. This results in an inversion layer under the metal and the resulting device is not a true Schottky barrier, but rather a p-n junction with the inverted surface strongly degenerate.

The performance would be similar to the n+ on p diode for a p-type wafer or p+ on n for a n-type wafer. The Schottky Barrier diode thus offers no advantages over ordinary p-n diodes.

4.6.6 Summary

The analysis of the previous section has indicated that device design has a substantial impact on elevated temperature performance. Six (Hg,Cd)Te device designs were considered: n- on p, p+ on n, n+ on p+, heterojunctions and Schottky Barrier photodiodes. The n- on p and p+ on n designs were found to have poor elevated temperature performance due to high n-side diffusion current resulting from the short, Auger-limited lifetime in n-type (Hg,Cd)Te. By doping the n-side into degeneracy, the Auger recombination mechanism is greatly reduced in strength and the n-side diffusion current reduced accordingly. Thus, device designs using a n+ doping offer improved performance at elevated temperatures.

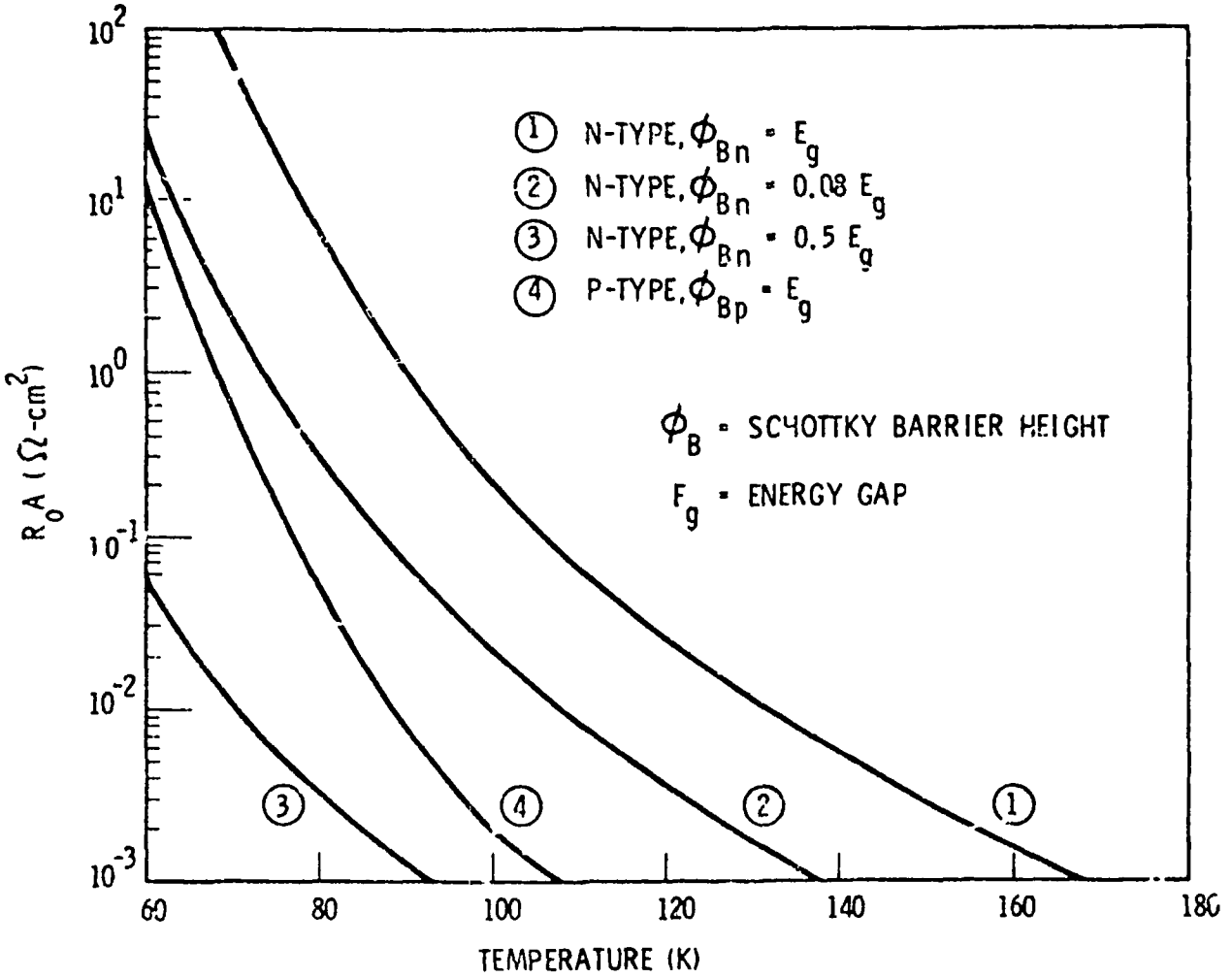

Figure 4.17 R_oA TEMPERATURE FOR SCHOTTKY PHOTODIODES $Hg_{1-x}Cd_xTe$, with λ_{co} = 12 μm

The n+ on p and the n+ on p+ design can achieve radiative-limited lifetimes and hence performance at the theoretical limit for quantum detectors at low and moderate temperatures. However, to achieve radiative-limited lifetimes above 150K the p-side must be doped at $N_A \cong 1.0 \times 10^{18} cm^{-3}$. Thus, only the n+ on p+ design is capable of performance at the theoretical limit for a quantum detector at high (150K-200K) temperatures. Heterojunctions offer performance nearly equivalent to p-n junctions. Only if the n-side diffusion current in n+ on p diodes is a limiting factor could heterojunctions offer improved performance. Schottky barrier photodiodes do not appear to offer good elevated temperature performance.

Present 12-μm (Hg,Cd)Te photodiodes achieve performance considerably below the theoretical limit due to a short, Schockley-Read limited lifetime in moderately p-type (Hg,Cd)Te. If the lifetime is improved, then use of reflective back-side contacts can result in a substantial improvement in R_oA. Finally, for elevated (150-200K) operation the p-side doping level must be increased to $N_A \sim 1.0 \times 10^{18} cm^{-3}$ to achieve radiatively-limited lifetimes.

4.7 REFERENCES

4.1 See Section 2.3 of this report.

4.2 Sah, R. Noyce and W. Shockley, Proc. IRE, September 1957.

4.3 D. Long, Topics in Applied Physics, R.J. Keyes, ed., Ch. 3 to be published.

4.4 H. Kimura, "Single Crystal Growth of (Pb,Sn)Te," J. Electronic Mtls. 1, 166 (1972)

4.5 R. Johnson and S. Parker, "(Pb,Sn)Te Single Crystals," Final Report, Texas Instruments, Contract DAAK02-72-C-0389, Jan. 1973.

4.6 H. Holloway, Lead Telluride Photodiodes for Operation at 170K, Final Report Contract DAAK02-73-C-0225.

4.7 R.E. Callender, R.E. Flannery and D.R. Kaplan, Proceedings of the IRIS Specialty Group on Infrared Detectors, Dec. 1976, Vol. 1, p. 261.

4.8 P.S. Chia, et al, National IRIS Meeting, Dayton, Ohio, May 1974.

4.9 A. Lockwood, J.R. Balon, P.S. Chia, R.M. Hoendervoogt and F.J. Renda, Proceedings of the IRIS Specialty Group on Infrared Detectors, Dec. 1976. Vol. 1, p. 275.

4.10 C.C. Wang, M.K. Kalisher, J.M. Traby, J.E. Clarke and J.T. Longo, Proceedings of the IRIS Specialty Group on Infrared Detectors, Dec. 1976. p 285

4.11 L.H. DeVaux, et al, "Thermal Limitations in (Pb,Sn)Te Detectors," IRIS Detector Specialty Meeting.

4.12 P.R. Emtage, J. Appl. Phys. 47, 2565 (1976).

4.13 D. Bellavance and M. Johnson, IRIS Specialty Group Meeting March, 1975. Proceedings, p.41.

4.14 Morris, Chapman and Guldi, 1974, IRIS Specialty Group Meeting Proceedings, p. 223.

4.15 Rockwell International Detector, tested by General Dynamics, "Characterization of (Pb,Sn)Te Detectors at Intermediate Temperatures and Backgrounds".

4.16 Data of T. Kochler, Honeywell Radiation Center.

4.17 M.A. Kinch, J.J. Brau and A. Simmons, J. Appl. Phys., 44, 1649 (1973).

4.18 See, for example, Blakemore, Semiconductor Statistics, Ch. 2.

4.19 For the p-side, the higher valance-band density of states requires much higher dopant levels to achieve degeneracy:

$$P_o = N_V F_{\frac{1}{2}}(\eta)$$

where:

N_V = valance band density of states

$= 1.5 \times 10^{18}$ cm^{-3} at 77K for $E_g = 0.1$ eV

4.20 P. Peterson, to be published.

4.21 J. Marine and C. Motte, Appl. Phys. Lett. 23, 450 (1973).

4.22 T.J. Tredwell, Optical Engineering 16, 237 (1977).

Section 5

PERFORMANCE LIMITATIONS OF 8 TO 14 MICROMETER PHOTOCONDUCTORS AT ELEVATED TEMPERATURES

5.1 INTRODUCTION

Photoconductors have been used for several earth-sensing satellite applications in the 8 to 12-micrometer spectral region. These devices were necessarily cooled by cryogens, to obtain high sensitivities. Cryogenic cooling, however, requires large commitments of space, power, and weight, all at a premium in spacecraft applications, and furthermore limits the useful lifetime of the detector. Operation of photoconductors at non-cryogenic temperatures, while maintaining high sensitivity, would vastly increase their desirability and potential applications; this has been a goal of infrared device research for years. In this section we explore the present and ultimate limitations of photoconductors in the 8 to 12-micrometer region, with an eye to future high sensitivity, high operating temperature, and multielement detector arrays.

Two variable-bandgap semiconductors, mercury-cadmium telluride (Hg,Cd)Te and lead-tin telluride (Pb,Sn)Te can be tailored to the 8 to 12-micrometer region, and so qualify as candidate materials. (Hg,Cd)Te has been used extensively as a photoconductor, while (Pb,Sn)Te has to date been used primarily as a photodiode material; both will be fully examined as to high-temperature photoconductive applicability. A model of photoconductors is developed in Section 5.2 and used both to predict theoretical limits, and to analyze present device performance. The materials are compared as to present and projected performance, and promising areas of research noted.

5.2 MODEL

A computer model was developed to predict the performance of photoconductive detectors. Detectivity and power dissipation, as a function of operating temperature, were the calculated quantities of most interest; resistance, lifetimes, carrier concentrations, and noise voltages were also program outputs. In formulating the model, the philosophy was to use the most general expressions available, to allow comparison on a common basis of various detector materials, carrier types, and doping levels. Wherever possible, quantities of interest were calculated from fundamental material parameters (Section 5.3), rather than assuming values, to preserve the generality of the model. Lifetimes are a good example of this. Differentiation between the various detectors come about through inputs to the program, which include mobilities, intrinsic carrier concentration, effective masses, cutoff wavelength, and doping level.

The model assumes non-degenerate statistics are valid, this is the case for the low doping levels commonly used in photoconductors. Trapping effects and Shockley-Read recombination, both of which depend heavily on the particular piece of material used, are not taken into account by the model. They are, however,

discussed in the text. With these qualifications, the model is as follows.

In order to be useful at any operating temperature, a device must have a high detectivity (D^*_λ). The defining equation for D^*_λ is:

$$D^*_\lambda = R_\lambda \sqrt{A\ \Delta f}/I_n \tag{5.1}$$

where these and all symbols used in this section are defined in Table 5.1. The noise current (I_n) may come from several sources. Johason or thermal noise due to the random thermal motion of charge carriers, is given by the familiar expression:

$$\bar{I}_J^{\,2} = 4\ KT\ \Delta f/R \tag{5.2}$$

Another mechanism, generation-recombination (g-r) noise, results from statistical variations in the rates of generation and recombination of charge carriers in the device. The carriers may be either thermally generated, or created by photons from the background. The expression for g-r noise is:

$$I_{gr}^{\,2} = 4q^2\ G^2\ g\ \Delta f \tag{5.3}$$

where g is the generation rate, given by:

$$g = \frac{n\ p}{\tau\ (n+p)}\ At \tag{5.4}$$

Here, n and p include both thermal equilibrium and background generaced carriers; the expression for g-r noise includes both mechanisms. Other noise mechanisms, such as 1/f noise, and amplifier noise are not included in the model, but are discussed later.

The responsivity (R_λ) is in general:

$$R = q\ \eta\ \lambda\ G/hc \tag{5.5}$$

where G is the photoconductive gain factor, given by:

TABLE 5.1

DEFINITIONS OF SYMBOLS

SYMBOL	UNITS	DEFINITION
A	cm^2	Area of device
b	----	mobility ratio, μ_e/μ_h
c	3×10^{10} cm/s	speed of light
D*	cm watt^{-1} Hz$^{\frac{1}{2}}$	detectivity at wavelength λ
E	volt/cm	electric field
E_g	eV	energy gap
Δf	Hz	bandwidth
F_1, F_2	----	overlap integrals of Bloch functions
G	s^{-1}	carrier generation rate
g	----	photoconductive gain
h	6.627×10^{-34} J s	Planck's constant
i_{gr}	A	g-r noise current
I_J	A	Johnson noise current
I_n	A	noise current
K	1.38×10^{-23} J K^{-1}	Boltzmann's constant
L	cm	length of device
m_e^*/m_o, m_h^*/m_o	----	electron, hole effective mass
n,p	cm^{-3}	electron, hole concentration
n_b	cm^{-3}	background generated carrier density
n_o, p_o	cm^{-3}	equilibrium electron, hole concentration
P	watts	Power dissipation for element
q	1.6×10^{19} coul	electron charge
R	ohms	device resistance
R_λ	A/watt	responsivity at wavelength λ
t	cm	thickness of device
T	K	temperature
t_d	s	diffusion time
V	volt	bias voltage
w	cm	width of device
ϵ_∞	----	high frequency dielectric constant
η	----	quantum efficiency
λ	μm	wavelength of radiation
μ	----	effective mass ratio, m_e^*/m_h^*
μ_a	cm^2 volt-s	ambipolar drift mobility
μ_e, μ_h	cm^2/volt-s	electron, hole mobility
τ	s	effective lifetime
τ_A	s	Auger lifetime
τ_{Ai}	s	intrinsic Auger lifetime, e-e process
$\tau_{Ai'}$	s	intrinsic Auger lifetime, h-h process
τ_r	s	radiative recombination lifetime
τ_{so}	s	sweepout lifetime

$$G = \tau / t_d = \tau \, (\mu_e + \mu_h) \, V/\ell^2 \tag{5.6}$$

The two expressions for D^*_λ, based on the two noise mechanisms, can be defined; the limiting D^*_λ being the smaller of the two. Equations 5.1, 5.2, 5.5 and 5.6 lead to the expression for Johnson-limited D^*_λ,

$$D^*_J = \frac{\eta \lambda \tau (b+1)}{2hct(n_o b + p_o + n_b(b+1))} \left(\frac{P}{\ell w KT}\right)^{1/2} \tag{5.7}$$

where the new symbols are power dissipation $P = V^2/R$, and the mobility ratio $b = \mu_e/\mu_h$. Equations 5.1, 5.3, 5.4, 5.5 and 5.6 give the g-r limited D^*_λ:

$$D^*_{gr} = \frac{\eta \lambda}{2hc} \left(\frac{\tau(n_o + p_o + 2n_b)}{\tau(n_o + n_b)(p_o + n_b)} \right)^{1/2} \tag{5.8}$$

The carrier lifetime τ appears in both D^*_λ expressions, and is an extremely important material parameter. It may be limited by any of several mechanisms: (1) Radiative recombination, (2) Sweep-out, (3) Auger recombination and (4) Shockley-Read recombination.

(1) Radiative Recombination

A general treatment of radiative recombination, found in Kinch,[5.1] defines the radiative lifetime as:

$$\tau_r = \left[B \, (n_o + p_o + n_b) \right]^{-1} \tag{5.9}$$

where B is the capture probability. Assuming parabolic bands at k = 0, non-degeneracy, and a theoretical expression for the absorption coefficient, B is given by:

$$B = 5.8 \times 10^{-13} \, \varepsilon_\infty^{1/2} \left(\frac{m_e^*}{m_o} + \frac{m_h^*}{m_o} \right)^{-3/2} \left(1 + \frac{m_o}{m_e^*} + \frac{m_o}{m_h^*} \right) \left(\frac{300}{T} \right)^{3/2} E_g^{\,2} \tag{5.10}$$

(2) Sweep-out

With large enough bias on a device, the minority carriers may be swept out to the contacts and recombine, which limits carrier lifetimes. (Majority carriers are also swept out to the contacts, but charge neutrality prevents them from recombining faster than the minority carriers.) This sweepout is dependent on the ambipolar drift mobility,[5.2,5.3]

$$\mu_a = \frac{n_o - p_o}{\frac{n_o}{\mu_h} + \frac{p_o}{\mu_e}} \tag{5.11}$$

which indicates no sweep-out will occur in intrinsic material. The time for a carrier to be swept out by the electric field E is then:

$$\tau_{so} = \frac{\ell}{\mu_a E} \tag{5.12}$$

(3) Auger Recombination (Band-to-Band)

Due to the different band structures of (Hg,Cd)Te and (Pb,Sn)Te, each has a different expression for Auger lifetime.

(Hg,Cd)Te:

Depending on the type and doping of the material, either electron-electron or hole-hole collisions may dominate the Auger recombination process. Taking into account both these phenomena, Blakemore [5.4] gives:

$$\tau_A = \frac{n_i^2}{(n_o + p_o + n_b)\left(\frac{n_o + n_b}{\tau_{Ai}} + \frac{p_o + n_b}{\tau_{Ai}}\right)} \tag{5.13}$$

where τ_{Ai} is the Auger lifetime in intrinsic material for electron-electron processes,

$$\tau_{Ai} = \frac{7.58\times10^{-18}\ \epsilon_\infty^{\,2}(1+\mu)^{\frac{1}{2}}(1+2\mu)\ \exp\left[\frac{1+2\mu}{1+\mu}\ \frac{E_g}{KT}\right]}{\left(\frac{KT}{E_g}\right)^{3/2}\ \left|F_1F_2\right|^2\ \left(\frac{m_e^*}{m_o}\right)} \tag{5.14}$$

and τ_{A_i} is the intrinsic lifetime for hole-hole collisions, arrived at by interchanging m_e^*/m_o and m_h^*/m_o in the expression for τ_{Ai}. Here $\mu = m_e^*/m_h^*$ is the effective mass ratio, and F_1 and F_2 are overlap integrals of the periodic part of Bloch functions for the conduction and valence bands. These overlap integrals can only be approximated theoretically, and as Kinch [5.1] points out, limit the calculation to order-of-magnitude accuracy. Experimental lifetime data has been obtained by Kinch et al and is used to determine $|F_1F_2|$

(Pb,Sn)Te

A calculation of the Auger lifetime in (Pb,Sn)Te has recently been done by Emtage.[5.5] He derives the following expression for n-type material:

$$\tau_A^{-1} = (2\pi)^{5/2} \frac{N'}{N^2} n^2 \frac{q^4}{\epsilon_\infty^2} (KT)^{\frac{1}{2}} E_g^{-7/2} \frac{n^3}{m_\ell^{\frac{1}{2}} m_t^{3/2}} \exp\left[\frac{-r E_g}{2 KT}\right] \qquad (5.15)$$

where: N = number of conduction band valleys

N' = number of valence bands that each conduction band can scatter into

m_ℓ = longitudinal effective mass

m_t = transverse effective mass

$r = m_t/m_\ell \approx 0.1$

Using values of $T = 77^o$ and $E_g = 0.1$, he obtains $\tau_A^{-1} = 5\times10^{-26}\, n^2$. Incorporating the dependence $m^* \propto E_g$, the following expression for any temperature and bandgap is found:

$$\tau_A = 2\times10^{25} \left(\frac{77}{T}\right)^{\frac{1}{2}} \left(\frac{E_g}{0.1}\right)^{\frac{1}{2}} \exp\left[\frac{r}{2K}\left(\frac{0.1}{77} - \frac{E_g}{T}\right)\right] n^{-2} \qquad (5.16)$$

The conditions on the validity of the calculation are $r \ll 1$ and $KT/2rE_g \ll 1$. For (Pb,Sn)Te, $r \approx 0.1$, so the first condition is probably true. However, for 12μm material at 180K, $KT/2rE_g = 0.78$. This leads one to expect only order-of-magnitude accuracy for the calculation, making Auger lifetime a critical point in the model for both (Pb,Sn)Te and (Hg,Cd)Te.

The effective lifetime (τ) of the carriers is limited by the shortest of the three mechanisms:

$$\frac{1}{\tau} = \frac{1}{\tau_r} + \frac{1}{\tau_{so}} + \frac{1}{\tau_A} \qquad (5.17)$$

Other effects, such as Shockley-Read recombination, are not specifically included in the model, but are considered in evaluating its results.

One noteworthy aspect of the model is the use of an energy gap value which remains constant with temperature, whereas an actual device has a temperature-dependent bandgap. The reason is straightforward: this study deals with the performance of devices with a particular cutoff wavelength (11.5μm was chosen),

operating at various temperatures. Therefore, it must be kept in mind that the predicted curves of D^*_λ versus temperature represent the locus of detectors operating with a specified cutoff (hence, energy gap), rather than any particular device, which would have a different cutoff for each temperature.

An alternate version of the program was also prepared, which accepts the x-value in $Hg_{1-x}Cd_xTe$ or $Pb_{1-x}Sn_xTe$, rather than the cutoff wavelength, as an input. Expressions for the energy gap as a function of x and temperature are then used to calculate the cutoff wavelength as it changes with temperature. This version, which models the behavior of particular devices, is used in evaluating measured data from present-day detectors.

5.3 MATERIAL PARAMETERS

Values of the material parameters used in the model are presented in Table 5.2, with references. The table is self-explanatory, with the exception of the expressions for mobility. Mobility values used in the model are fits to experimental data, rather than purely theoretical calculations. In this it is believed that device performance will be more accurately predicted. Theoretical expressions for mobility do not fit the data over a substantial range of temperatures (see Scott's analysis[5.6] of electron mobility in (Hg,Cd)Te, while experimental mobility data are generally available. The origins of the expressions for mobility in Table 5.2 are discussed below.

(Hg,Cd)Te Mobility:

The electron mobility in (Hg,Cd)Te as a function of temperature and composition has been measured by Scott.[5.6] A good empirical fit to his data, for x = 0.20, is given by:

$$\mu_e = 7.73\times10\ T^{-1.94} \quad , \quad 55 < T < 300$$
$$\mu_e = 3.3\times10^5 \quad , \quad T < 55 \qquad (5.18)$$

with T given in K.

Direct measurements of the hole mobility versus temperature in x = 0.20 (Hg,Cd)Te are not available; consequently, the hole mobility is arrived at from the electron mobility and the mobility ratio $b = \mu_e/\mu_h$. The best measurement of b available comes from the data of Emmons and Ashley[5.7] on 77° minority carrier sweepout in $Hg_{0.8}Cd_{0.2}Te$. They find $\mu_h \approx 700$ cm^2/volt-s, but do not measure μ_e. From Scott's data on material like that used by Emmons and Ashley, $\mu_e = 1.7\times10^5$ at 77°, yielding b = 240. This value compares favorably with the value $b \approx 200$ found by Reynolds[5.8] at 77°, and $b \approx 100$-200 in the 77°-100°K range found by Tasch, et al,[5.9] both for x = 0.20 material.

TABLE 5.2

MATERIAL PARAMETERS

Parameter	(Hg,Cd)Te Value	Ref	(Pb,Sn)Te Value	Ref
ϵ_∞	13	1	36	7
$\lvert F_1 F_2 \rvert$	0.5	2	--	
m_e^*/m_o	0.075	3	0.7 Eg	8
m_h^*/m_o	0.55	4	0.7 Eg	8
μ_e	$7.73\times10^8\ T^{-1.94}$; 3.3×10^5 for $T<55^\circ K$	5	$1.449\times10^{20} T^{-5/2} (n_o+n_b)^{-2/3} \exp(-6.93Eg)$	5
μ_h	$\mu_e/240$	5	$1.449\times10^{20} T^{-5/2} (p_o+n_b)^{-2/3} \exp(-6.93Eg)$	5
n_i	$(8.455-2.2875x+0.00342T)\ 10^{14} Eg^{3/4} T^{3/2} \exp(-Eg/2KT)$	6	$2.9\times10^{15} \left(\frac{T}{E_\delta}\right)^{3/2} \exp(-Eg/2kT)$	9
E_g	$1.59x-0.25+5.233\times10^{-4}(1-2.08x)T+0.327x^3$	2	$0.181+4.52\times10^{-4}T-0.568x+5.8x^4$	9

1. J. Baars & F. Sorgen, S.S. Comm. 10, 875 (1972)
2. M.A. Kinch, et.al., J. Appl. Phys 44, 1649 (1973)
3. Kinch & Buss, Proc. Conf. on Phys of Semimetals & Narrow-Gap Semiconductors, (Pergamon 1970) p. 461.
4. R.R. Galazka & T. Zakrzewski, Phys. Stat. Sol. 23, K39 (1967).
5. See Section 5.3
6. From J. Schmit, J. Appl. Phys. 41, 2876 (1970), multiplied by 1.5 to fit experimental data
7. Estimated from refractive index = 6, in Ref. 9
8. From Ref. 9, p. 159, m^* proportional to Eg, and $m^* = 0.07m$ from Eg = 0.1
9. Semiconductors & Semimetals, 5, Ed. R.K. Willardson & A.C. Beer (Academic Press, 1970) Ch. 4

(Pb,Sn)Te Mobility:

Because of the band structure symmetry in (Pb,Sn)Te, hole and electron mobilities will be equivalent, for the same temperature and carrier concentration. An expression for the mobility as a function of temperature, carrier concentration, and energy gap has been derived as follows: The temperature dependence has been experimentally found[5.10] to closely follow the relationship predicted by phonon scattering; namely, $\mu \propto T^{-5/2}$, for temperatures of interest. The dependence of the mobility on carrier concentration has been found by Zoutendyk[5.11] to be $\mu_e, \mu_h \propto n^{-2/3}, p^{-2/3}$, for T = 77° and x = 0.20. The dependence of the mobility on the bandgap is not available for (Pb,Sn)Te; this functional relationship, which should be similar to that for (Hg,Cd)Te, was consequently derived from Scott's[5.6] (Hg,Cd)Te data. From this source one obtains μ versus x, which can be directly transformed to μ versus E_g. Collecting these functional dependences, and fitting Zoutendyk's curve for x = 0.2, T = 77K, we obtain:

$$\mu_{e,h} = 1.16 \times 10^4 \left(\frac{T}{77}\right)^{-5/2} \left(\frac{n,p}{10^{18}}\right)^{-2/3} \exp\left[-6.93\ (E_g - 0.1)\right]$$

$$= 1.207 \times 10^{21}\ T^{-5/2}\ (n,\ p)^{-2/3}\ \exp\left[-6.93\ E_g\right] \qquad (5.19)$$

Measured data at low carrier concentrations and temperatures reveal the limits of this expression. No mobilities above 3×10^4 are reported, and Melngailis and Harman see nearly constant mobilities at this level, for low carrier concentrations. A saturation at $\mu_{e,h} = 3 \times 10^4$ is, therefore, incorporated in the model.

5.4 PERFORMANCE OF PRESENT 8-14μm PHOTOCONDUCTORS

5.4.1 N-Type (Hg,Cd)Te

Currently available n-type (Hg,Cd)Te photoconductors operate near the theoretical limits for detectivity; a representative case is presented in Figure 5.1.[5.12] Measured D* values for a 12-element linear array at 105K are shown, along with the theoretical D* curve calculated using the material parameters of the devices (x = 0.20, $N_D - N_A = 2.7 \times 10^{14}$, Area = 5x5 mils). Note the uniformity achieved over 12 elements. The quantum efficiencies of the devices were not measured, so curves are included for both the ideal case, and a more realistic η = 0.7. Measured values are within a factor of two of the calculated limits, indicating lifetimes close to the theoretical expressions. Assuming these devices follow the calculated temperature dependence, the best of them should reach the 8×10^9 D* level at 126K.

Higher temperature data is also available, this time for a single element detector. Operating under a reduced field of view (110°), the device obtained $D^*_\lambda = 2.6 \times 10^{10}$ at 120K. This corresponds to a D^*_λ under full field of view of 1.7×10^{10}, very near the calculated limit for 120K operation. In addition to near-theoretical D*, the device had the small area (4x4 mils) required for large array applications. Apparently very little development is necessary to approach the ultimate performance limits for n-type (Hg,Cd)Te in this elevated-temperature application.

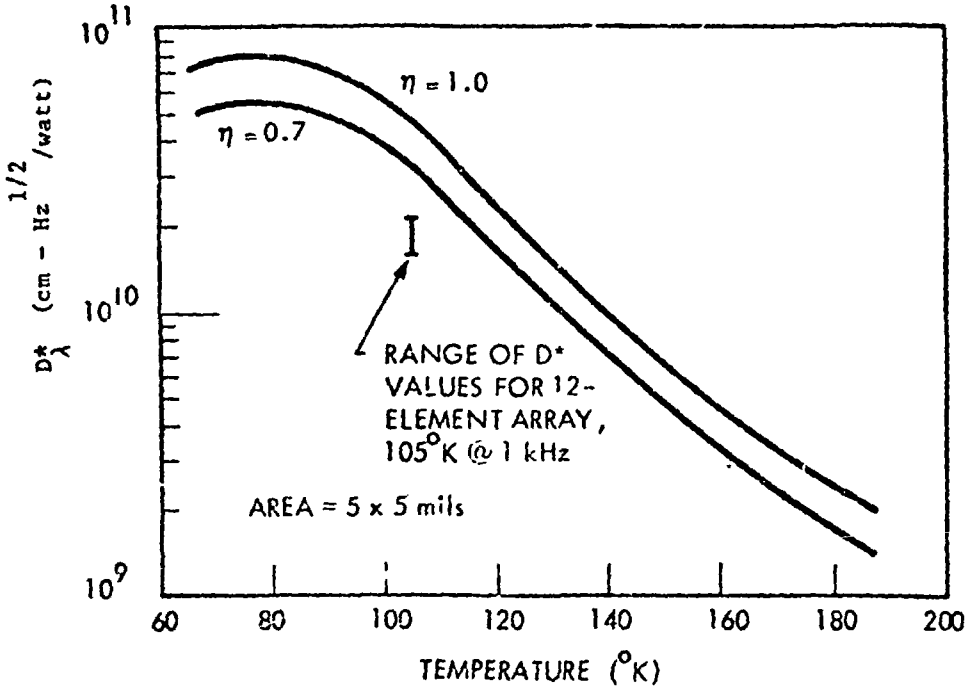

Figure 5.1 COMPARISION OF CALCULATED AND MEASURED D^*_λ , FOR n-TYPE (Hg,Cd)Te PHOTOCONDUCTOR

5.4.2 P-Type (Hg,Cd)Te

Very little data exists on p-type (Hg,Cd)Te photoconductors. Historically, low carrier concentrations were obtained only in n-type; hence, development efforts concentrated on it. However, recent research by Stelzer and Schmit[5.13] has produced rather low carrier concentrations in p-type material ($p_o \sim 10^{15}cm^{-3}$), and exploratory development of photoconductors is just getting underway.

To date, only devices with x = 0.365 (λ_{co} = 3.4μm at 200K) have been fabricated.[5.14] However, an understanding of the processes limiting performance in 3-micrometer material is useful in predicting 12-micrometer device performance. The fabricated devices, with $p_o = 3x10^{16}cm^{-3}$, were simulated on a computer, using the model of Section 5.2 and physical parameters reported for the devices. The results of the calculations are presented in Figure 5.2, with the data points. At 77°, the measured D* is near the predicted g-r limited value, indicating a nearly theoretical lifetime (the model indicated radiative recombination is the dominant process over the illustrated temperature range). At 300 K, Johnson noise limits the D* for the bias used; the measured value is again close to the calculated value. This agreement with theoretical D* values is rather remarkable, considering the first-shot nature of the work, and demonstrates the high quality of the available p-type material. Further development will be expected to raise the performance even closer to the ideal limit.

In this preliminary study, noise in the detector was found to be constant for bias currents less than 0.5 mA; above this value, a super-linear increase in noise with increasing bias was observed. Attributed to electrical contact problems by the authors, the problem will require further work. 1/f noise below 1 kHz is another non-ideal characteristic of the devices, but this little-understood source of noise is one common to photoconductors.

The work to data on x = 0.365 (λ_{co} = 3.3μm) material looks encouraging for the development of x = 0.2 (12μm) devices. Good material with x = 0.2 has been grown, although lifetimes have generally been short, 20 ns for the best Further development work is called for, especially on the source of the short lifetimes.

5.4.3 (Pb,Sn)Te

Although principally used as a photodiode material, (Pb,Sn)Te has been fabricated into photoconductive detectors by several researchers.[5.15-5.17] However, it has not been specifically employed for elevated temperature operation; detectivity data is available only for 77K and lower. In general, these devices have been of substantially lower performance than either (Pb,Sn)Te photodiodes or (Hg,Cd)Te detectors of either mode. Understanding the performance limiting mechanisms is a prerequisite to fabricating (Pb,Sn)Te devices for high temperature operation.

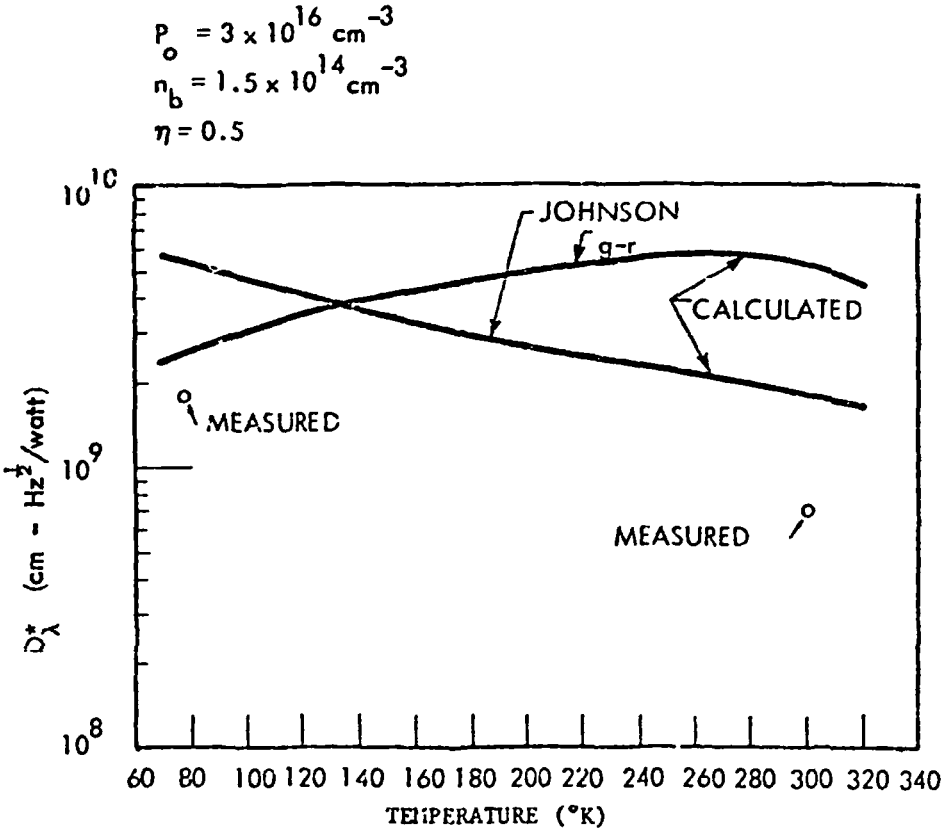

Figure 5.2 3-μm p-TYPE (Hg,Cd)Te DETECTOR. DATA ARE FROM REFERENCE 5.14.

One of the most serious problems with the material has been the difficulty of obtaining low carrier concentrations. (A low carrier concentration is necessary to produce high resistance, and hence, low thermal noise current. This constraint is much less severe for photodiode applications, where the junction resistance dominates.) As-grown material is typically in the $10^{19}cm^{-3}$ range; various annealing procedures are used to reduce this value. Lowering the concentration below $10^{17}cm^{-3}$ is extremely difficult by simple annealing, however; the reason is apparent in Figure 5.3, reproduced from reference 5.17. The range of isothermal annealing temperatures for low mobility is so minute as to be nearly unattainable.

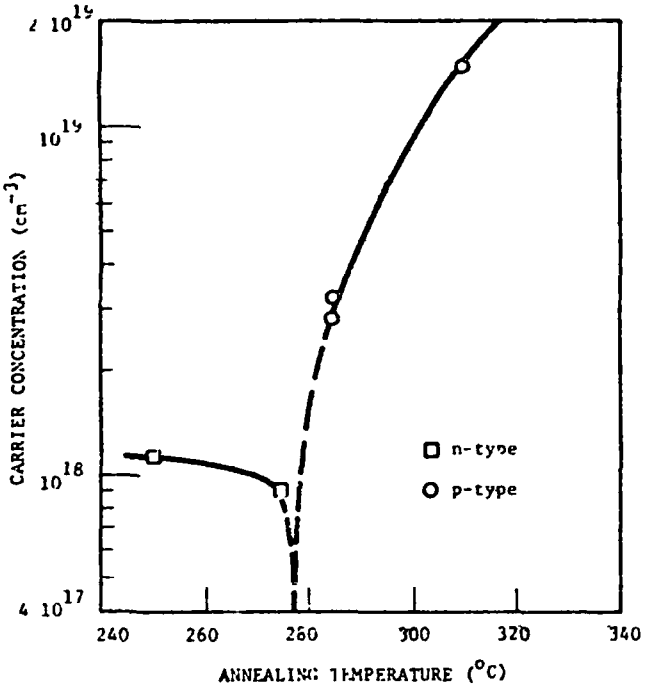

Figure 5.3 CARRIER CONCENTRATION VS ANNEALING TEMPERATURE FOR ISOTHERMAL Te-RICH ANNEALING OF $Pb_{0.80}Sn_{0.20}$FILMS. FROM REFERENCE 5.17

Different annealing procedures have been used to get around this: Melngailis[5.15] achieved 2 to $8x10^{15}$ concentrations in bulk crystals, using a very long (60 days) two-temperature annealing process; Logothetis[5.16] reports concentrations of $3.9x10^{16}$ in epitaxial (Pb,Sn)Te, after annealing in the presence of metal-rich bulk material; sputtered films of high quality have recently been reported[5.17] with $10^{16}cm^{-3}$ effective carriers, when deposited in the presence of gaseous additives. Thus, it is presently possible to get fairly low carrier concentrations, with substantial effort, although not as low as that achieved in (Hg,Cd)Te ($\sim 10^{14}$). As the elevated temperature performance is critically dependent on carrier concentration, this is one of the major factors currently limiting device performance.

Another serious problem has been short effective carrier lifetimes, which lower D* well below the theoretical limits (Johnson noise limited D* is proportional to the lifetime τ, while the g-r limited D* is proportional to $\tau^{\frac{1}{2}}$). Lifetime data was obtained by Melngailis[5.15] for Bridgman-grown and annealed single crystals; this data is compared to theoretical calculations of the lifetime (using the model of Section 5.2 and Melngailis' device parameters) in Table 5.3

TABLE 5.3

COMPARISON OF MEASURED AND CALCULATED
LIFETIMES IN (Pb,Sn)Te PHOTOCONDUCTOR

Temp. (K)	Measured τ_{eff}	Radiative Lifetime	Auger Lifetime[5.18]	Sweepout Lifetime
77	1.5×10^{-8}	1.3×10^{-6}	1.0×10^{-6}	1.3×10^{-5}
198	3×10^{-8}	1.2×10^{-6}	1.6×10^{-7}	5.3×10^{-5}
300	4×10^{-8}	4.2×10^{-7}	7.4×10^{-9}	3.6×10^{-3}

It is seen from Table 5.3 that none of the calculated mechanisms account for the observed lifetimes, at least below 300K. Melngailis attributes the short lifetime to dislocations and other crystal imperfections (providing Shockley-Read recombination centers) and it appears that the problem with imperfect material is widespread. Logothetis estimates lifetimes in the range 10^{-8} to 10^{-7}s at 77K from responsivity values; the General Dynamics group found $\tau \leq 7\times10^{-6}$ at 77K, although this is an upper limit imposed by the measurement equipment. Thus, Shockley-Read processes are apparently dominant at elevated temperatures in the material currently produced. The exact mechanism is not well understood by any means, and the road to a solution is not clear.

Poorly understood noise processes are also a problem in (Pb,Sn)Te. Both Melngailis[5.15] and Logothetis[5.16] report a noise component which increases with bias, and decreases with frequency. Logothetis interprets this as a contact noise and has determined the frequency dependence as $(\text{frequency})^{-\frac{1}{2}}$. The General Dynamics group[5.17] also reports an excess noise, neither Johnson nor g-r in origin; it follows a 1/f dependence up to a breakpoint in the 1-10 kHz region, after which the noise spectrum is flat. Although contact problems are suspected, the exact source of these noises are uncertain. They do provide limitations to device performance at low frequencies, and at moderate to high biases.

The best reported performances for (Pb,Sn)Te photoconductors in the long wavelength region are summarized in Table 5.4. It must be noted that the D* values are for 77K; at elevated temperatures the detectivity would be significantly lower. The problems which limit good performance-high carrier concentration, short lifetimes and poorly understood noise processes, are ones which would require a substantial effort to solve if a solution is possible. Thus, (Pb,Sn)Te is clearly unsuitable for photoconductive operation at elevated temperatures in its present state of development.

TABLE 5.4

PRESENT-DAY PERFORMANCE OF (Pb,Sn)Te PHOTOCONDUCTORS

Ref.	Material	Cutoff Wavelength (K)	Temperature (K)	D^*_λ (cm watt^{-1}/Hz$^{\frac{1}{2}}$)
5.15	Bulk single crystal	11	77	3×10^8
5.16	Epitaxial	10.8	77	6.6×10^8
5.17	Sputtered [5.19]	11	77	5.4×10^8

5.5 LIMITATIONS AND ULTIMATE PERFORMANCE

To evaluate the ultimate performance limits expected for photoconductors, and to discuss the sources of problems in present-day devices, the model of Section 5.2 was employed. The (Hg,Cd)Te and (Pb,Sn)Te of both n and p-types were examined, varying parameters such as carrier concentration and bias to obtain the optimum performance at high temperatures for each material.

Several parameters of the model were given standard values through all the computer runs, either to fit the desired application of the devices, or to provide a uniform basis for comparison between the different materials. A simple device structure was assumed; (shown in Figure 5.4) the cutoff wavelength was 11.5μm; individual elements were 4x4 mil^2 for array applications; the material thickness, which should be minimized for good D* while still large enough for good quantum efficiency, was 5μm; quantum efficiency was 1, as best possible case. A D^*_λ of 8×10^9cm Hz$^{\frac{1}{2}}$/W, was adopted as the minimum detectivity of interest. The density of background generated carriers (n_b) was computed from the expression $n_b = \tau\eta\, Q_B/t$, where Q_B is the photon flux from a 300° background, and τ is the lifetime necessary to produce a D* of 8×10^9. All other parameters are as described in Section 5.2 or input as variable parameters.

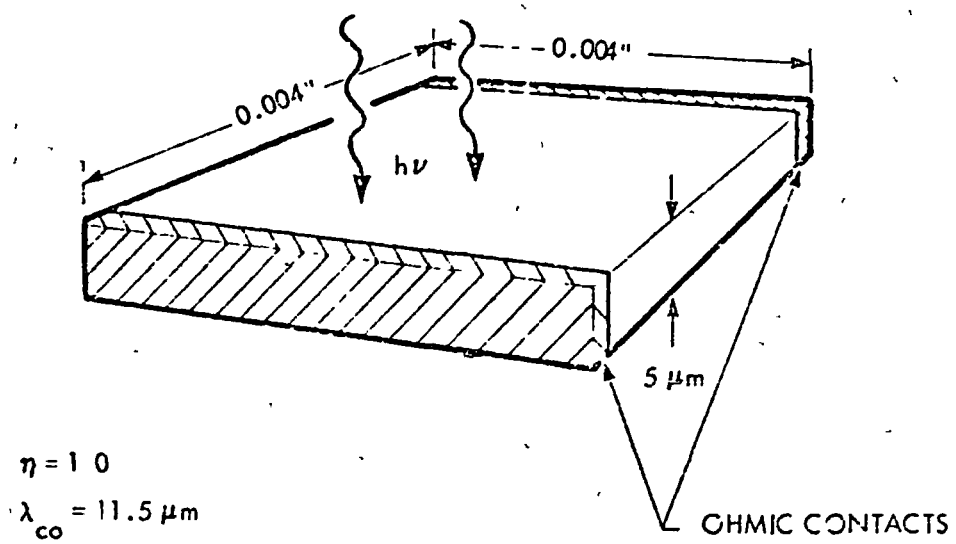

Figure 5.4 SINGLE DETECTOR ASSUMED PARAMETERS

5.5.1 N-Type (Hg,Cd)Te

The determination of optimum device performance is complicated by the dependence on bias and doping. These dependencies are displayed in Figures 5.5 and 5.6. It is readily seen that doping levels should be minimized for highest D*, but the dependence on bias is not so straightforward. For maximum detectivity, the Johnson-limited D* should be boosted above the g-r limited D* by increasing the bias. However, excessive bias results in sweepout of minority carriers, which causes a decrease in D*. In addition, power dissipation is proportional to the square of bias. As these detectors are to be used in large arrays, power dissipation must be kept to a minimum. The optimum performance at elevated temperatures, in terms of high operating temperature, high D*, and low power dissipation, is obtained as follows: the bias is adjusted to have the Johnson D* above the g-r D* up to the point at which D* = 8×10^9, and no further. In Figure 5.5 for example, the optimum bias would be approximately 30 mV, giving the highest operating temperature with minimum power dissipation.

In Figure 5.7 are shown the optimum elevated-temperature performance curves for several material dopings. The critical dependence on carrier concentration is evident. From these curves, several conclusions can be drawn:

1. The maximum operating temperature for a D* of 8×10^9 is 139K. This is limited by the intrinsic carrier concentration of the material.
2. The material is intrinsic above 140K for dopings of 3×10^{15} or less; hence, very low carrier concentrations are not necessary for highest temperature performance.
3. At dopings much above 5×10^{15}, it is impossible to achieve D* = 8×10^9, no matter what the temperature.

The upper limit of 139 K on operating temperature would seem to be a rather firm one. The limiting value here is the g-r D*, which is given by:

$$D^*_{g\text{-}r} = \frac{\eta \lambda}{2 hc} \sqrt{\frac{\tau}{t} \frac{(n_o + p_o + 2n_b)}{(n_o + n_b)(p_o + n_b)}}$$

Examination of the equation reveals that all parameters are either fixed or cannot be improved upon, save possibly the lifetime. The calculated lifetimes are shown in Figure 5.8 for the best-case detector; Auger lifetime is seen to be the sole important one at elevated temperatures. As noted in

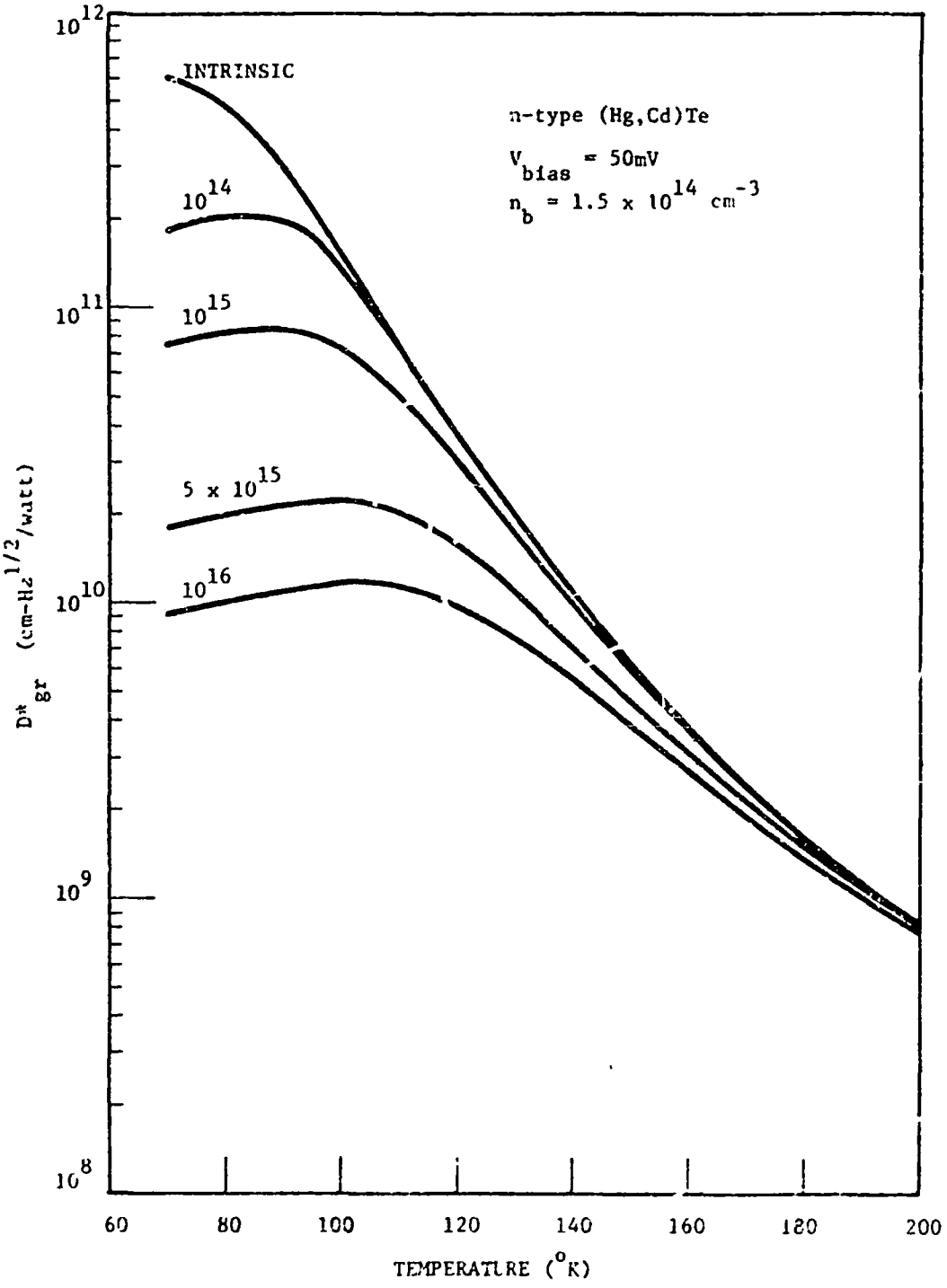

Figure 5.5 g-r D* VS TEMPERATURE FOR SEVERAL DOPING LEVELS

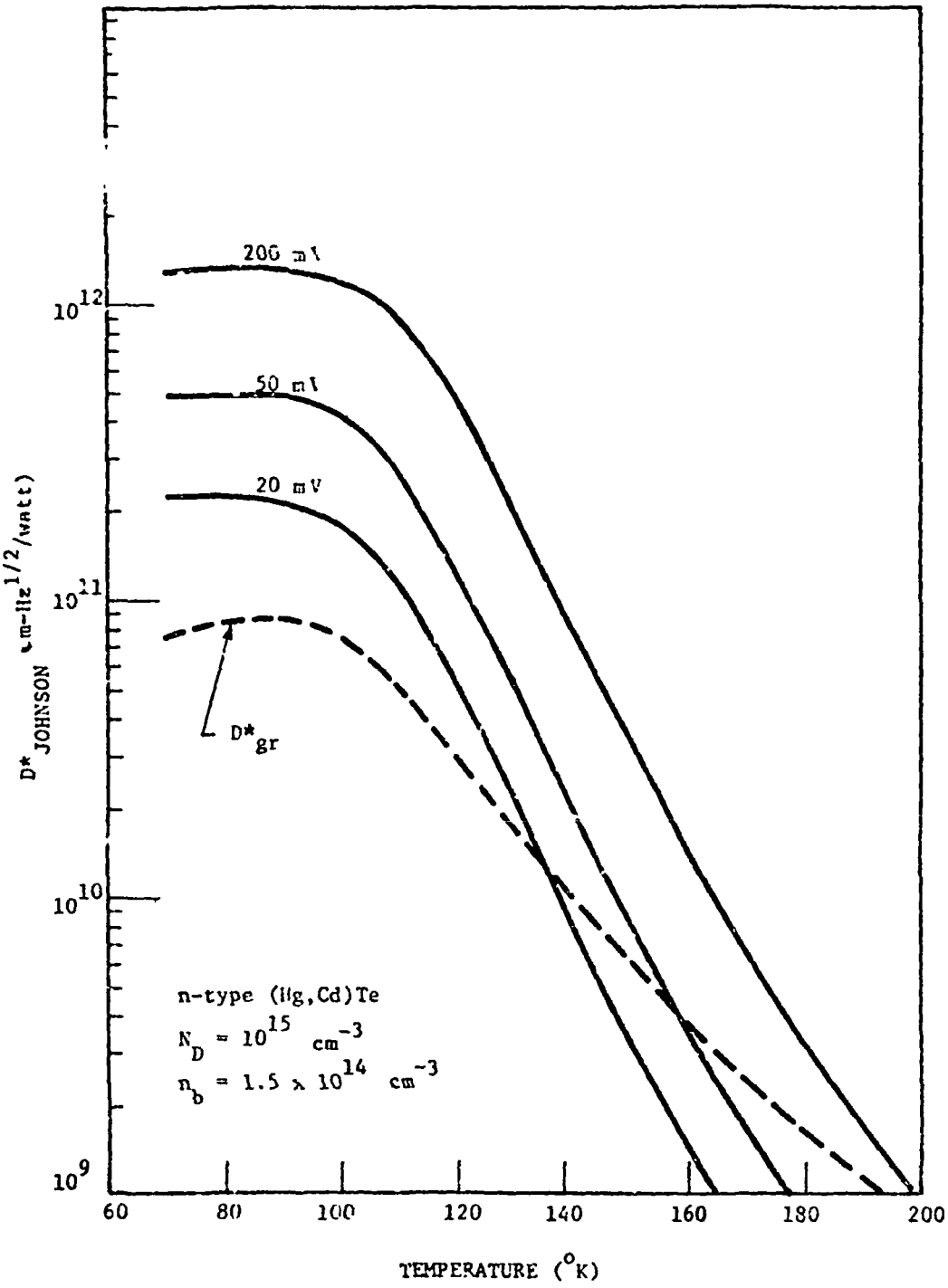

Figure 5.6 JOHNSON D* VS TEMPERATURE FOR VARIOUS BIASES

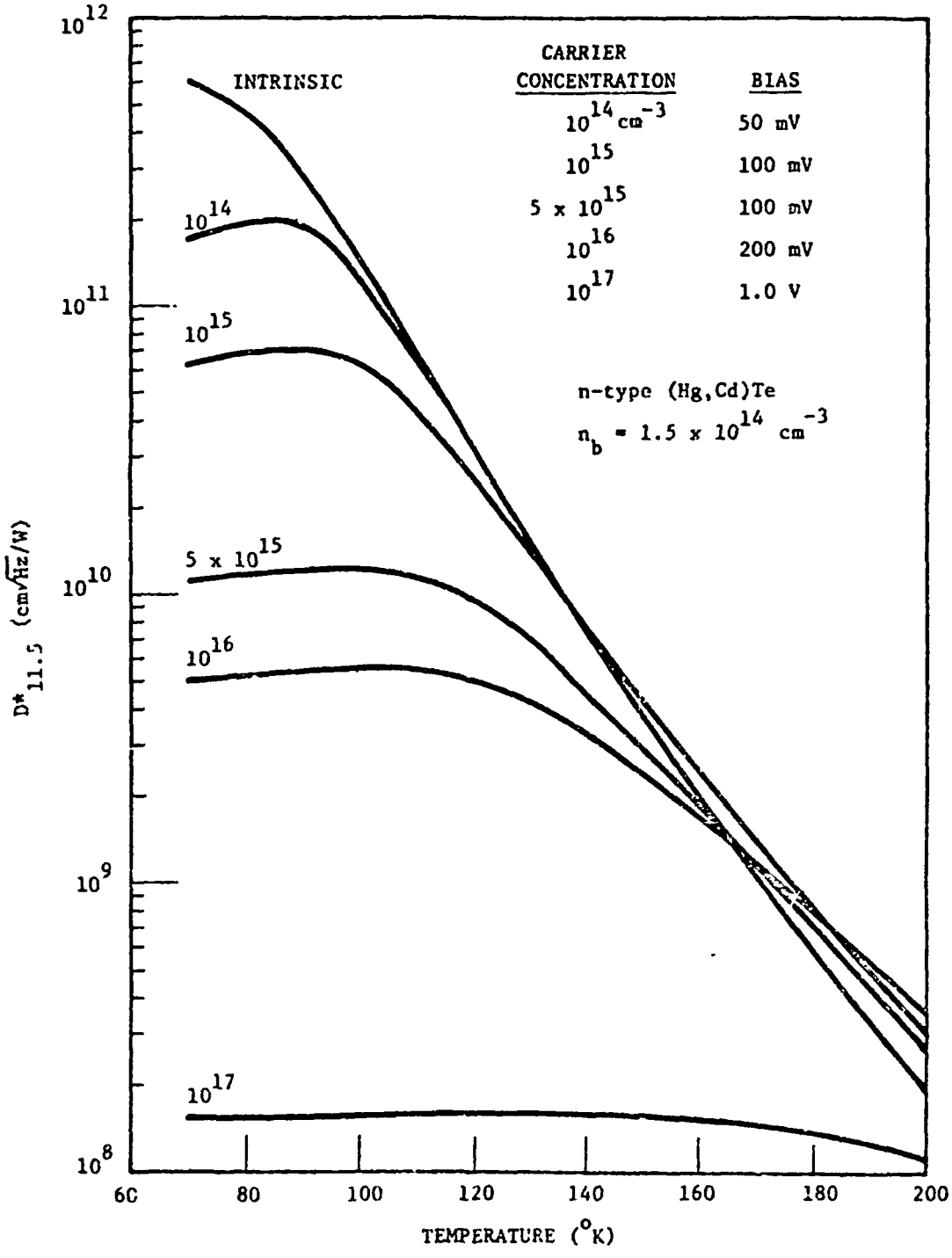

Figure 5.7 BEST D* VS TEMP PERFORMANCE FOR n-TYPE (Hg,Cd)Te PHOTOCONDUCTORS

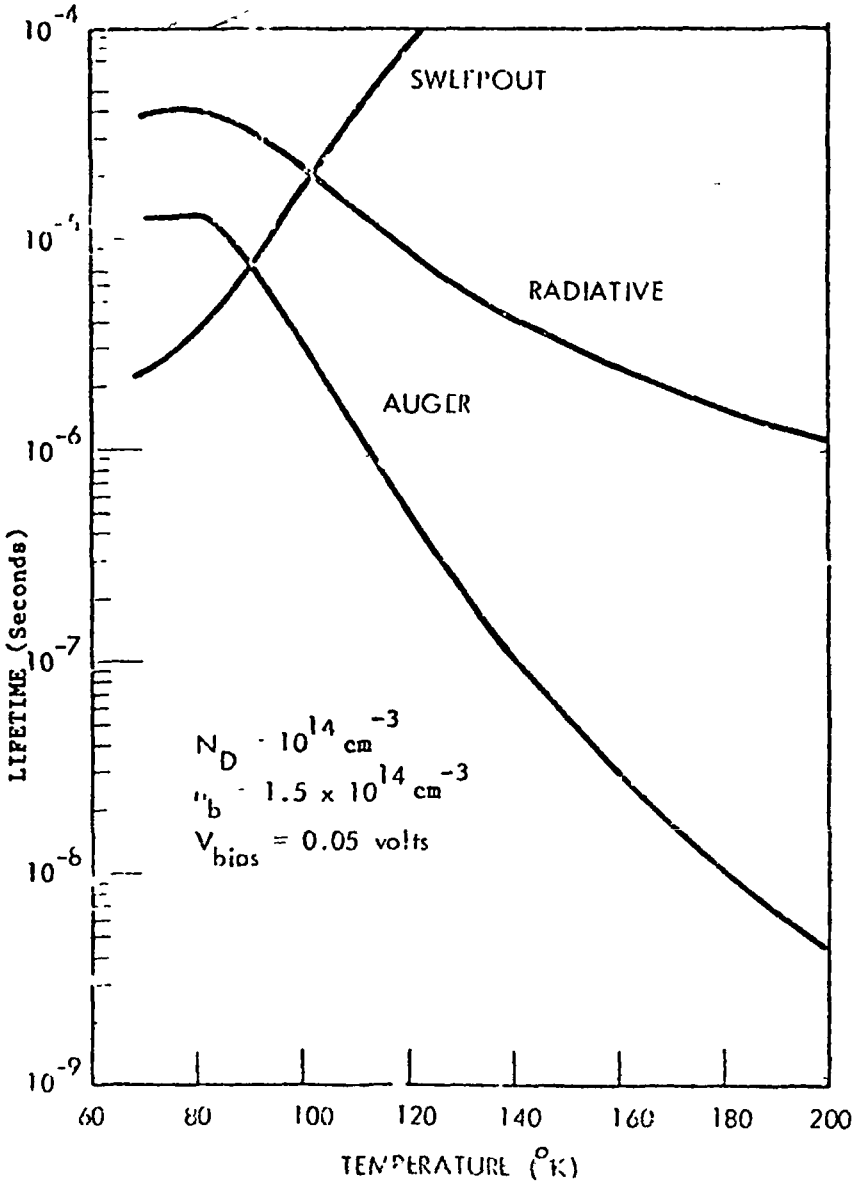

Figure 5.8 CALCULATED LIFETIMES FOR n-TYPE (Hg,Cd)Te PHOTOCONDUCTORS

Section 5.2, calculations of Auger lifetime are somewhat uncertain due to approximated overlap integrals. A factor of 4 uncertainty in the value of τ_A produces a factor of 2 variation in D^*_{gr}; this results in a possible spread of 129-149° in the maximum operating temperature. Because the amount of uncertainty in τ_A is unknown, the calculated values will be referred to from now on with no error bar analysis attached; however, this possible factor should be kept in mind.

An improvement in lifetime could come from trapping, which has been observed in n-type (Hg,Cd)Te. However, it has always been at temperatures of 80 K and lower, and there is no evidence to suggest a trapping mechanism operating as high as 140 K. This operating temperature is then the most reliable maximum available, based on theory for 8×10^9 D* performance in n-type (Hg,Cd)Te.

5.5.2 P-Type (Hg,Cd)Te

The situation in p-type (Hg,Cd)Te is not analogous to that in n-type due to asymmetry in the energy bands. Because of this asymmetry, the Auger lifetime in p-type can be much longer than in n-type at low temperatures. In Figure 5.9 calculated Auger lifetimes for 10^{17} cm^{-3} doped material of both types are shown, illustrating the advantage in p-type. Since the Auger lifetime is dominant at elevated temperatures (see Figure 5.10 for a representative case), higher D* values can theoretically be achieved in p-type, and hence, higher operating temperatures.

In Figure 5.11 are displayed D^*_{gr} versus T curves for different p-type dopings. Consider the behavior of the curves as the doping is increased. As expected, the maximum D* for each curve decreases with increased doping. However, another effect is observed; the point at which the exponential decrease in D* begins is shifted to higher temperatures. The result is a D* advantage for higher dopings, at elevated temperatures. Contrast this with the behavior of n-type material (Figure 5.5) in which the higher doped material never exceeds the performance of the lower. Therefore, increasing the doping results in progressively higher operating temperatures, until the lowering of peak D* with temperature becomes dominant, dropping the curve below the minimum acceptable D* level. This behavior defines a maximum operating temperature. The optimum doping for high temperature operation in (Hg,Cd)Te is $N_A = 10^{16}$; this doping allows an operating temperature of 149K for a D*) for 8×10^9.

The noticeable dissimilarities in the D* behavior of n and p-type material are due to the Auger lifetime. A plot of the τ_A versus temperature curves for various doping in p-type (Figure 5.12) reveals the same advantage of higher doping levels at elevated temperatures seen in the D* curves. Similarly, for the case of n-type, the D* curves reflect the advantage of low doping levels, at all temperatures, found in the curves of Auger lifetime (Figure 5.13). These lifetimes are quantitatively and qualitatively different because hole-hole interactions are the dominant process in p-type material, while electron-electron processes determine

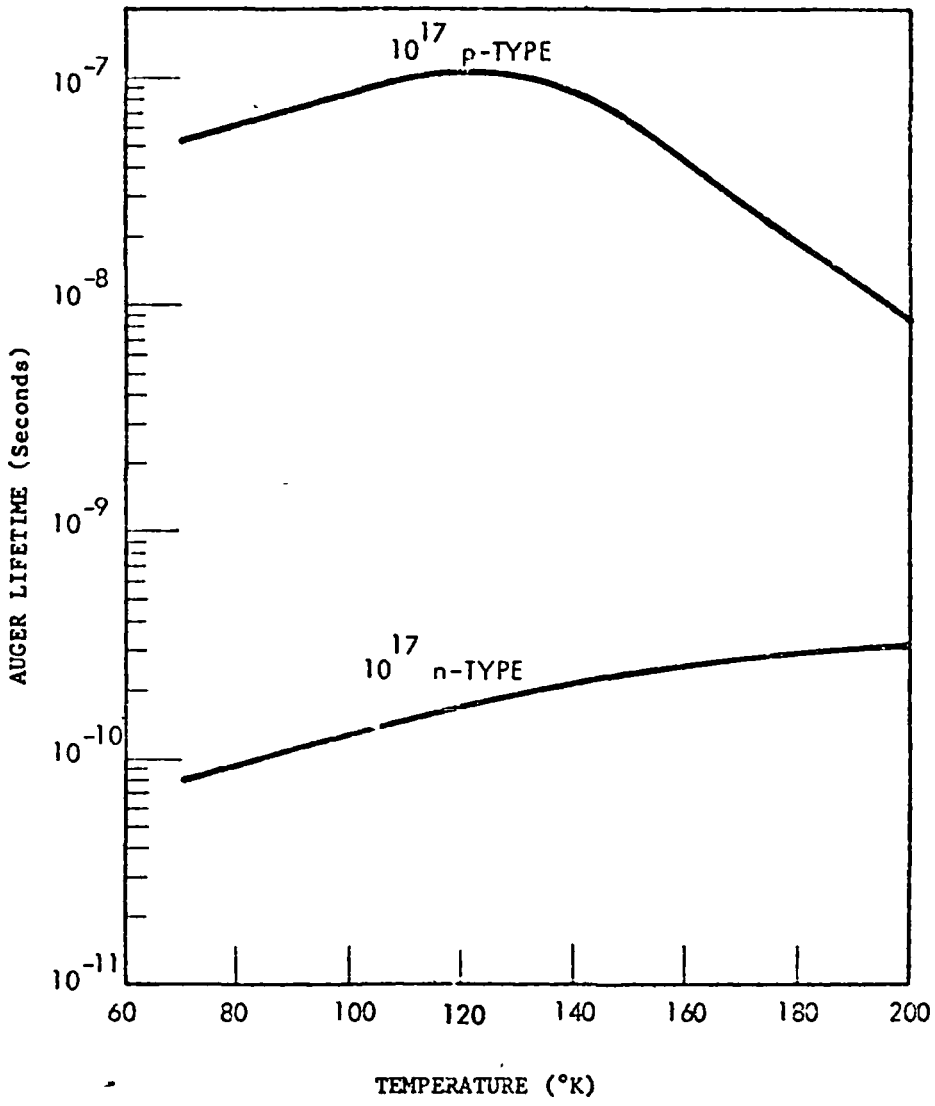

Figure 5.9 AUGER LIFETIME IN 12-μm (Hg,Cd)Te

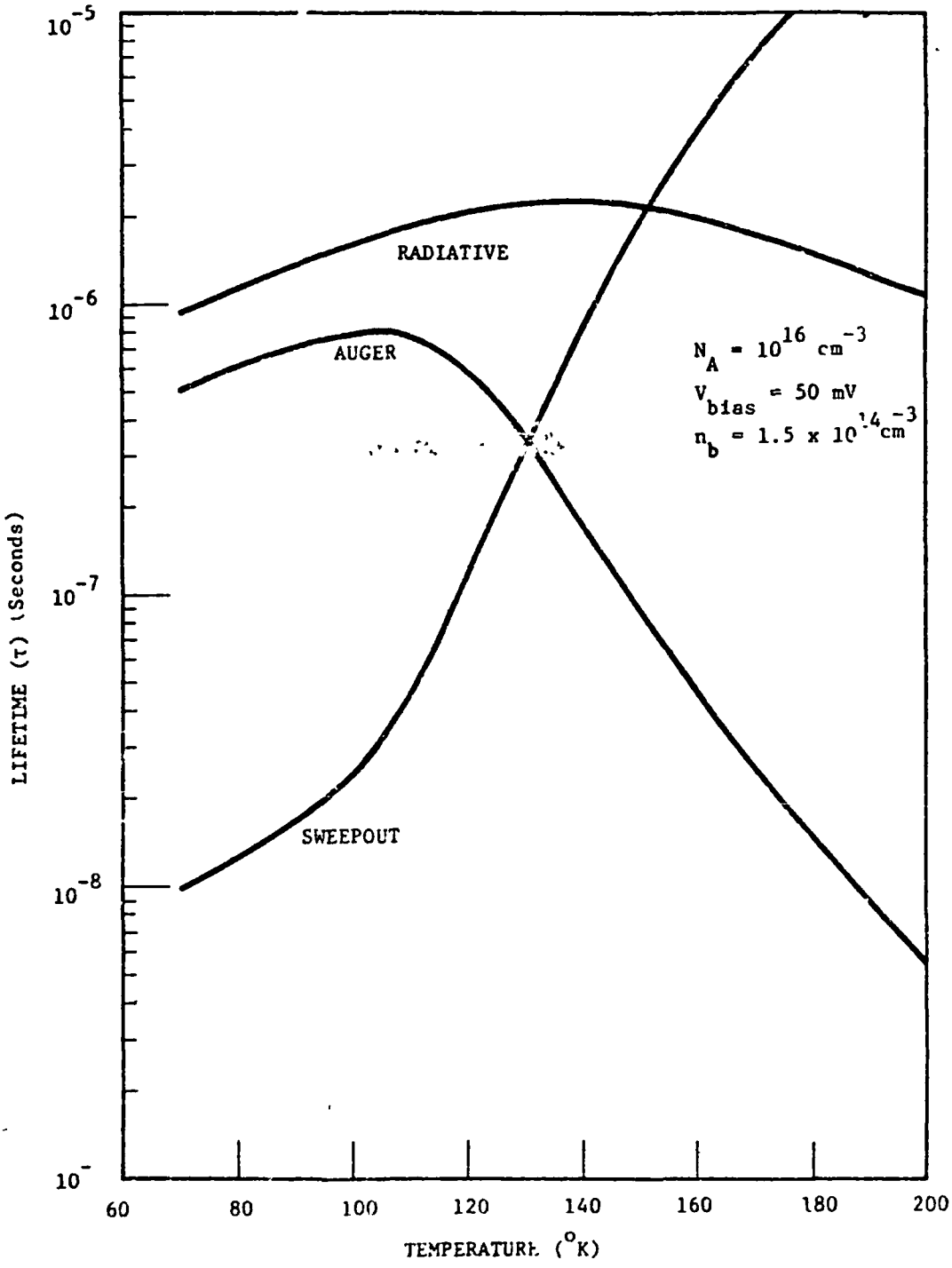

Figure 5.10 COMPARISON OF LIFETIMES IN p-TYPE (Hg,Cd)Te

77-1-6

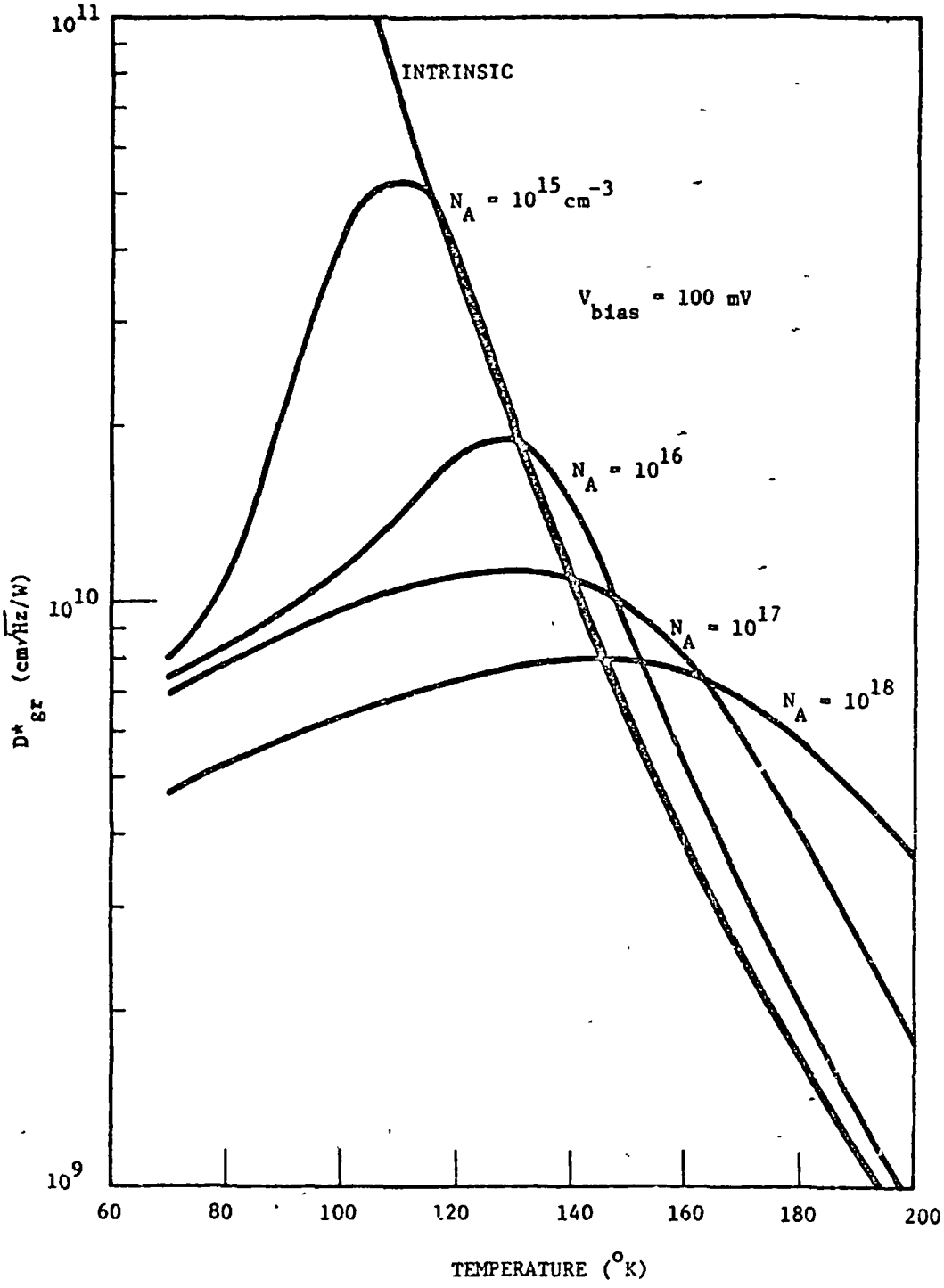

Figure 5.11 D^*_{gr} VS T FOR VARIOUS DOPINGS IN p-TYPE (Hg,Cd)Te

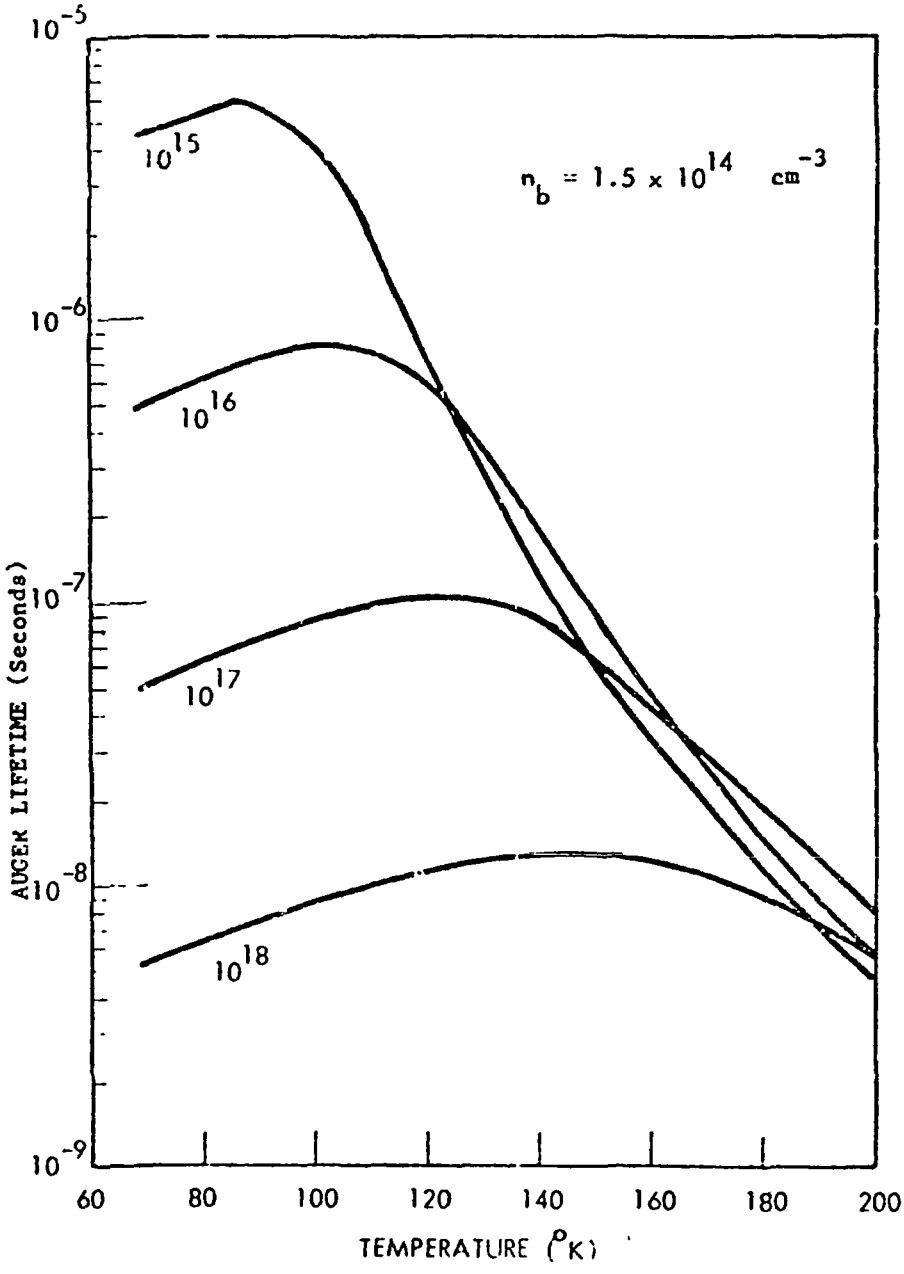

Figure 5.12 AUGER LIFETIME IN p-TYPE (Hg,Cd)Te, AS A FUNCTION OF DOPING

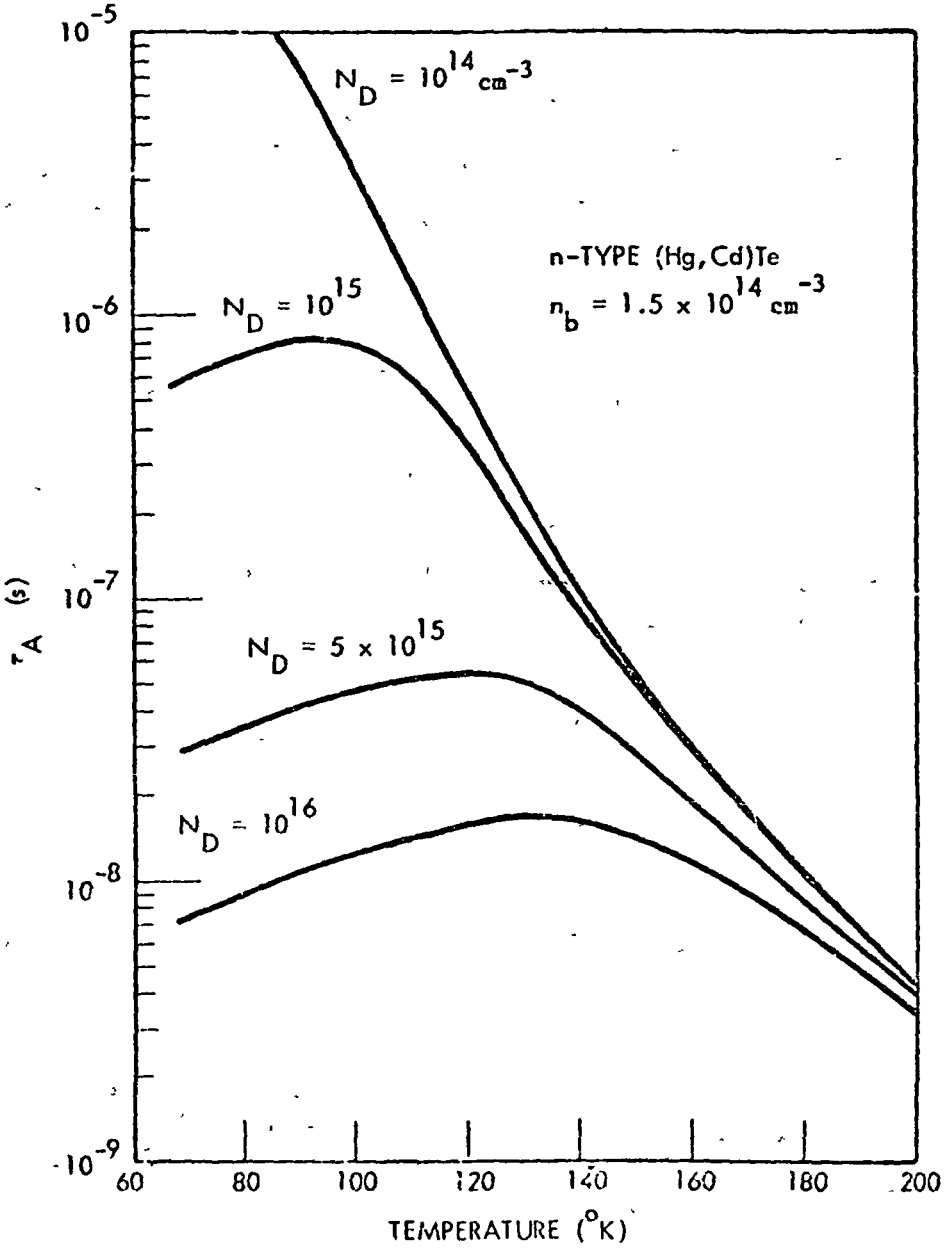

Figure 5.13 AUGER LIFETIME IN n-TYPE (Hg,Cd)Te, AS A FUNCTION OF DOPING

77-1-6

the lifetime in n-type; the great difference in effective masses makes the processes involving holes much less frequent. This is an inherent feature of (Hg,Cd)Te, and one that makes p-type material attractive for elevated temperature applications.

Another asymmetry of (Hg,Cd)Te, the large electron-to-hole mobility ratio, makes minority carrier sweepout a more prominent process in p-type material, as seen in Figure 5.10. The bias can then be critical; too much will make the device sweepout rather than Auger lifetime limited, while too little results in Johnson rather than g-r noise limitation. Either case may give a significant decrease in operating temperature. This is illustrated in Figure 5.14, where changing the optimum bias of 100 mV by a factor of two in either direction results in a decrease of peak D*. This dependence is only crucial for dopings of 10^{17} and higher, however, where the lifetime can be dominated by sweepout at elevated temperatures. For lower dopings, sweepout is restricted to low temperatures, and is not a factor over relatively wide ranges of bias.

The main obstacle to theoretical performance in x = 0.2 (Hg,Cd)Te is the carrier lifetime at the present time. Lifetimes better than 40 ns have not been measured in the material; this lifetime is independent of the temperature. Such behavior points to Shockley-Read recombination, due to crystal imperfections or other recombination centers in the lattice. At present the problem is poorly understood, and basic research needs to be done here to discover the exact cause of the short lifetimes. Until this problem is solved, the high operating temperatures predicted by theory cannot be achieved. Figure 5 15 shows a theoretical curve of D* versus T for a device with a constant 20 ns lifetime, and doping of 10^{15}; this is the performance to be expected from current material.

5.5.3 (Pb,Sn)Te

Effective masses and carrier mobilities for holes and electrons are the same in (Pb,Sn)Te, due to the symmetry of the electronic energy bands. This implies that neither n nor p-type has an inherent advantage as a photoconductor; the behavior should depend only on doping. The results of the model then apply equally well to n or p-type material.

The best calculated high temperature performances for a range of dopings are shown in Figure 5.16. These are the curves for devices operated at a sufficient bias to make gr noise greater than Johnson noise. Several points are worth noting for the graph.

1. The maximum operating temperature for (Pb,Sn)Te photoconductors is 180K; this limit is imposed by the intrinsic carrier concentration. Material doped $2x10^{14}$ or less is intrinsic at this temperature.

2. For a doping of $1.0x10^{15}cm^{-3}$, $D^* = 8x10^9$ is achieved at 176K.

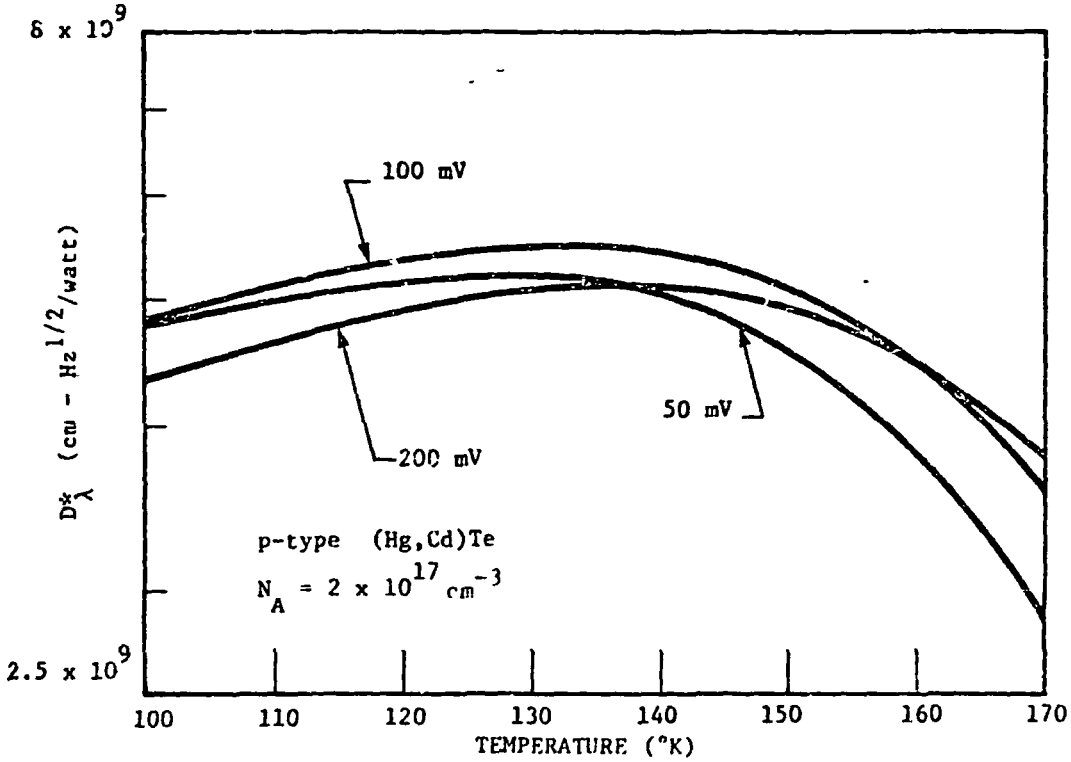

Figure 5.14 PEAKING OF D^*_λ WITH BIAS

77-1-6

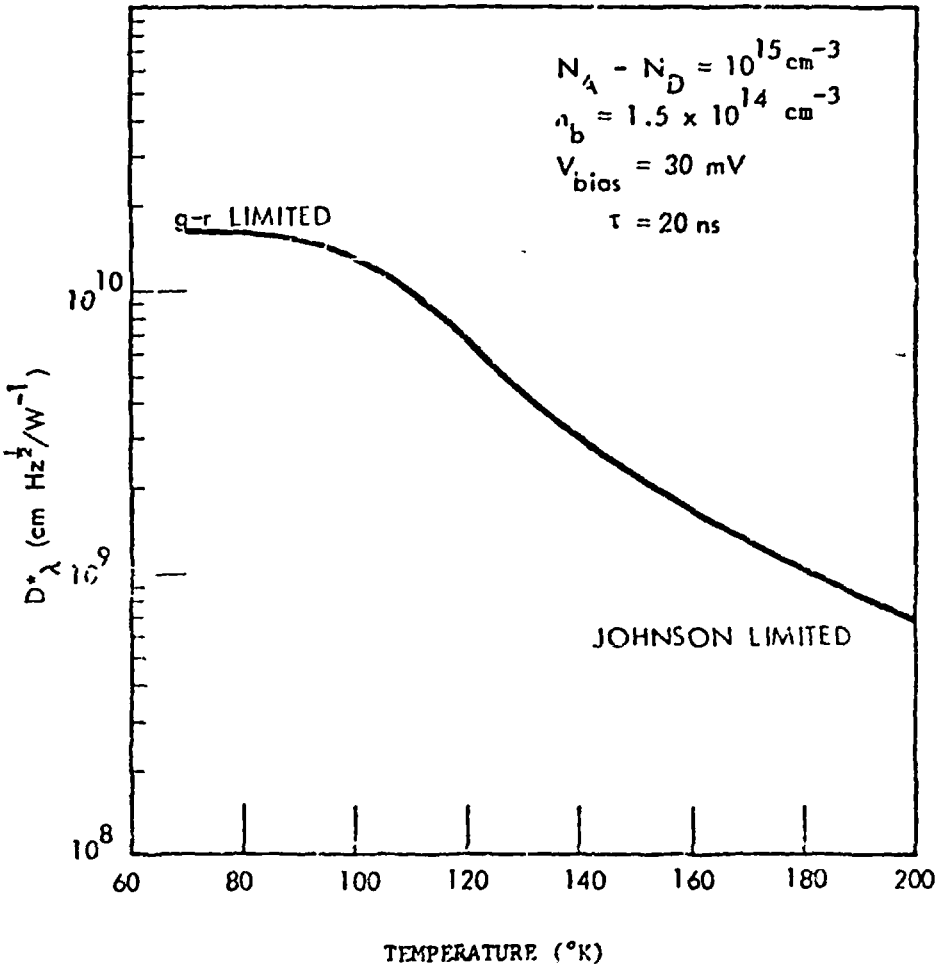

Figure 5.15 CALCULATED PERFORMANCE OF p-TYPE (Hg,Cd)Te PHOTOCONDUCTORS CALCULATED FROM τ = 20 ns

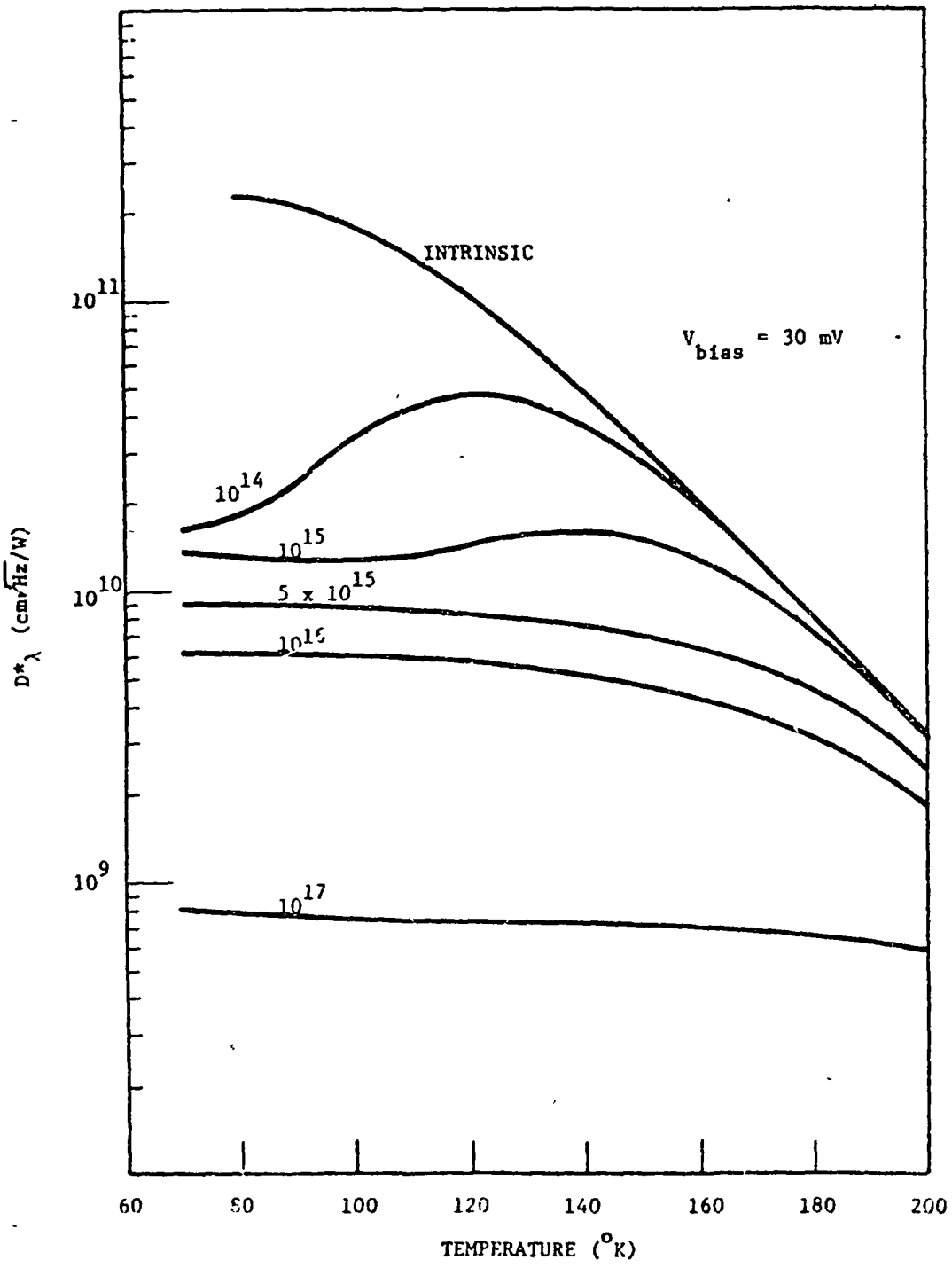

Figure 5.16 BEST HIGH TEMPERATURE PERFORMANCE OF (Pb,Sn)Te DEVICES, FOR VARIOUS DOPINGS.

3. The desired D* cannot be obtained at any temperature for dopings much greater than 5×10^{15}.

An ability to achieve high operating temperatures in (Pb,Sn)Te therefore hinges on obtaining low carrier concentrations.

Analysis of the calculated lifetimes reveals all three lifetime processes are important in these devices. Figure 5.17 presents the lifetimes for a device doped $10^{15} cm^{-3}$, which seems to be the lower limit of current technology, operated at an optimum bias. Sweepout is important here, as in p-type (Hg,Cd)Te, due to the high minority carrier mobility; again the bias is critical in avoiding either sweepout or Johnson limited operation.

Auger recombination is the dominant process at temperatures above 160K. Since the assumption $KT/2rE_g << 1$ used in deriving at τ_A becomes questionable in this temperature region ($KT/2rE_g = 0.63$ at 160K), some degree of uncertainty in the calculated value τ_A is present. It is expected that this variation would not be large; since D^*_{gr} is proportional to $\tau^{\frac{1}{2}}$, and the D* versus T curve is steep in this temperature region, the effect on operating temperature should be minimal. Examination of the model reveals all other parameters are firm, so 176K should be a reliable theoretical limit on operating temperature for this material.

How close to the calculated limits can one hope to come in practice? As noted earlier, carrier concentrations near $10^{15} cm^{-3}$ are necessary for the best performance; with a large amount of work, this should eventually be obtainable. Low carrier concentration must be coupled with excellent crystallinity, to obtain near-theoretical lifetimes. To date, this combination has not been achieved, lifetimes in lightly doped material are an order of magnitude or more shorter than calculated values. Quantum efficiency is another important consideration. The ideal quantum efficiency of 1.0 used in the model will not be achieved in practice, although antireflection coatings give some improvement; since D* is directly proportional to η, this factor could be significant. The steep slope of the D* versus T curve, for intrinsic material, indicates that any factor affecting D* will have a large effect on the maximum operating temperature. A 50% decrease in D* below the ideal limit, which could come from quantum efficiency, for example, would prevent 10^{15} material from reaching the desired D* at all. A factor of 3 reduction in D*, which could easily come from non-theoretical lifetimes, would lower the operating temperature of 10^{14} material from 180 to 153K. The conclusion is this: high temperature operation of (Pb,Sn)Te photoconductors is highly unlikely with present state-of-the-art technology.

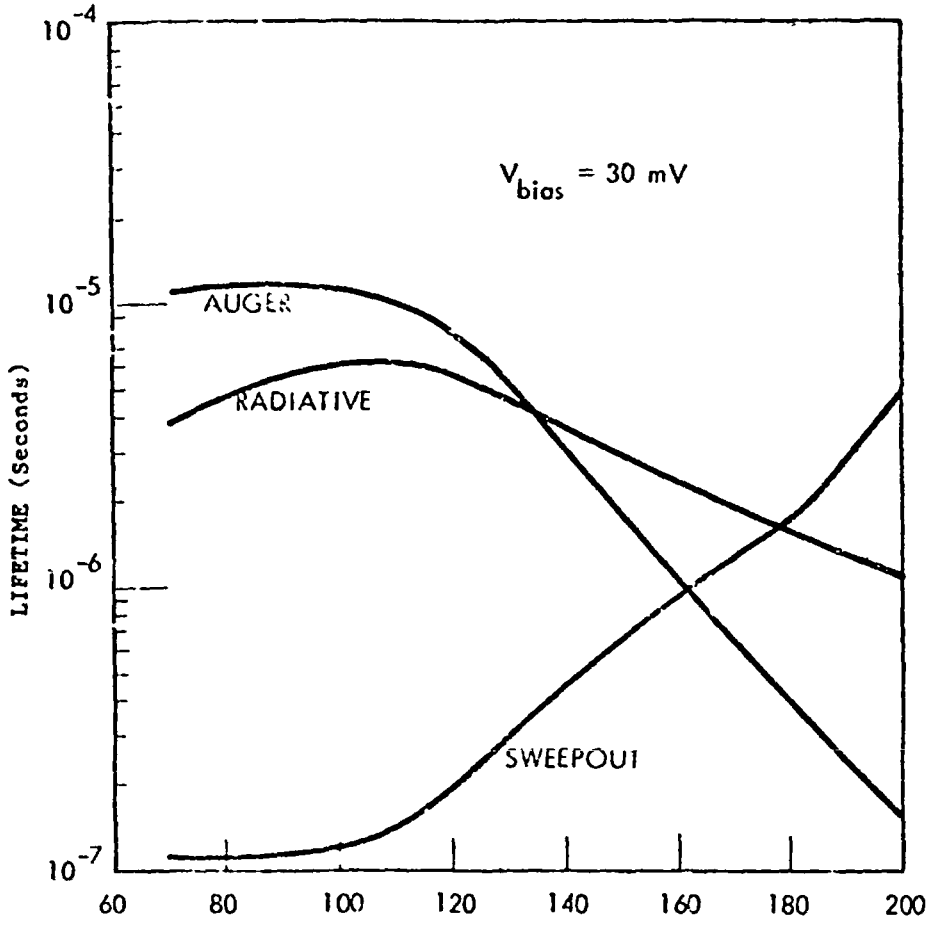

Figure 5.17 CALCULATED LIFETIMES FOR 10^{15} cm^{-3} DOPED (Pb,Sn)Te

5.6 OTHER LIMITATIONS

Several other considerations, not specifically included in the photoconductor model, may provide constraints on the selection of a detector. These include 1/f detector noise, amplifier noise, power dissipation, and constraints imposed by incorporation with a CCD for signal processing.

5.6.1 1/f Noise

This problem has been mentioned in the preceding discussions of (Hg,Cd)Te and (Pb,Sn)Te present-day devices. As noted, it is a poorly-understood noise problem present in all photoconductors. Phenomenologically, it is a bias-dependent detector noise which depends on frequency as $f^{-\frac{1}{2}}$. As the frequency increases, 1/f noise is eventually lost under the g-r noise; which is constant with frequency. The frequency at which 1/f and g-r noises is equal is called the 1/f corner frequency (f_o). Then 1/f noise can be modeled as $(f_o/f)^{\frac{1}{2}} V_{g-r}$.

For the present-day (Pb,Sn)Te and p-type (Hg,Cd)Te devices discussed earlier, f_o is usually in the 1-10 kHz neighborhood. Because this phenomenon is common to detectors made from both materials, it constitutes no real criterion for discrimination between them. It must be kept in mind, however, that D* will be degraded for low frequency measurements.

5.6.2 Amplifier Noise

In the preceding analysis, the effect of noise in the amplifier associated with each detector has been ignored. In a real system this must be taken into account, because the signal-to-noise ratio may be limited by amplifier noise rather than the device itself. Impedance matching between the amplifier and device must also be considered, because device impedance becomes quite small at elevated temperatures.

State of the art low-noise amplifiers operate at about 0.5 $nV/\sqrt{Hz}$, and are built to match impedances from 50 ohms to several thousand. Amplifiers can be built to match impedances of less than 50 ohms, but these are not in common usage. Currently produced photoconductors, operated at cryogenic temperatures, have higher impedances, so there has been no real need for low-impedance amplifiers. There is no fundamental principle prohibiting them, however, they would require high power dissipation. For the devices in this study with the best theoretical performances, the impedance can generally be matched with present-day amplifiers Curves of impedance vs temperature are plotted in Figure 5.18, for selected devices. The (Hg,Cd)Te devices of both n and p types fall into the desired impedance range, for all temperatures up to and including their maximum operating temperatures (139K for n-type, 149K for p-type). The (Pb,Sn)Te devices would require the development of new amplifiers for operation above 155K, but the impedance drops only to 25 ohms, which should offer no serious problems in amplifier design. Impedance matching is, therefore, not a critical area in developing elevated-temperature devices.

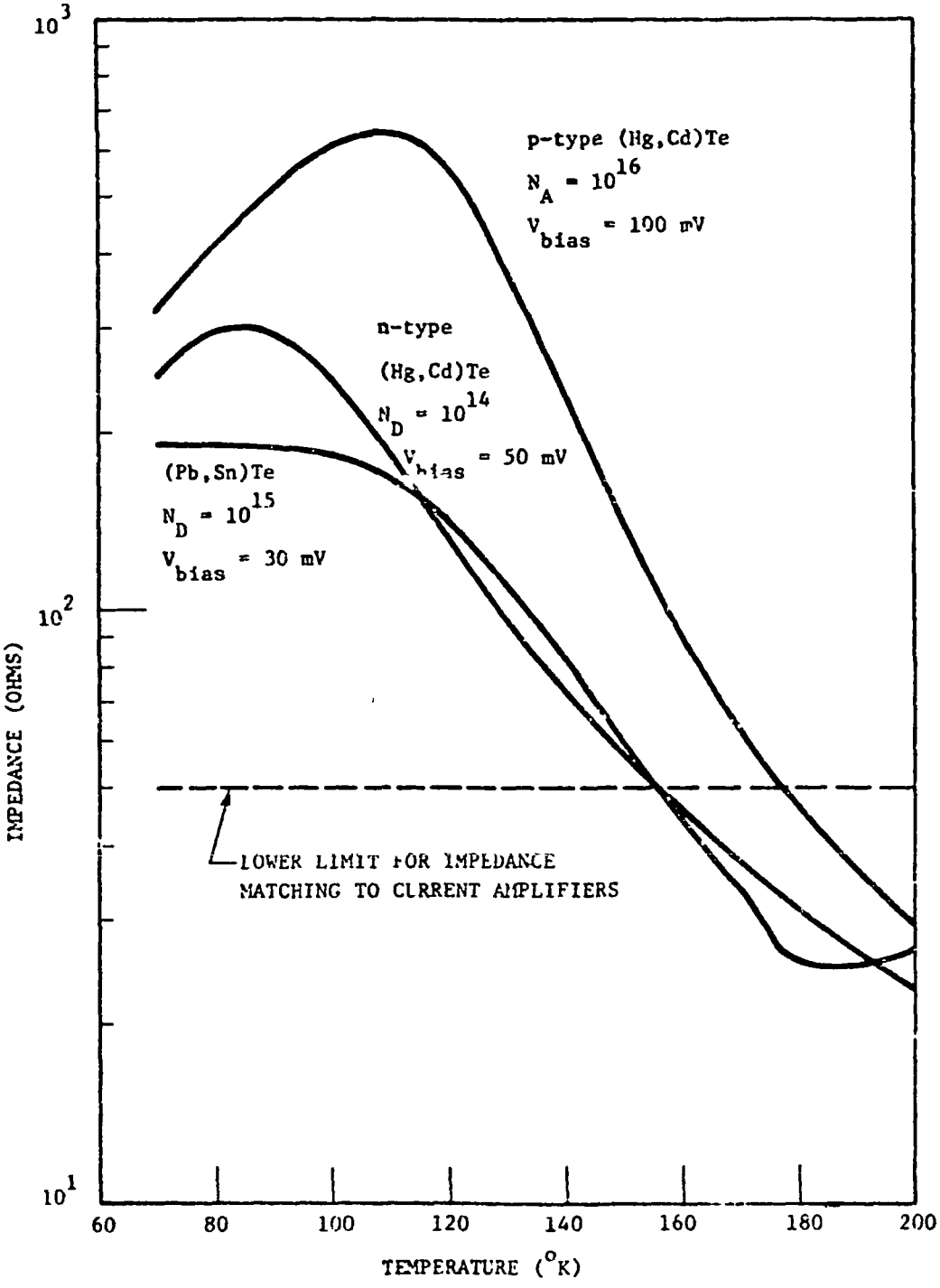

Figure 5.18 IMPEDANCE CURVES CALCULATED FOR SEVERAL DEVICES

The other area of concern is absolute noise levels in the system. To realize maximum performance, the noise voltage of the device (g-r plus Johnson noise) must exceed the noise voltage of the amplifier. In Figures 5.19-5.21 are plotted the noise voltages vs temperature, from which it is seen that in all cases the device noise exceeds amplifier noise. This holds true for all those devices studied in which the desired D^*_λ of 8×10^9 is achieved. For higher carrier concentrations (approximately 10^{16} in (Pb,Sn)Te and n-(Hg,Cd)Te, and 10^{18} in p-(Hg,Cd)Te, amplifier noise does dominate device noise, but at these concentrations the detectivity is very low. Devices of interest are not limited by amplifier noise.

Amplifier noise, however, must be added in with other noise mechanisms to determine the effective D^*_λ of the device. The results of this added noise are seen in Figure 5.22, and tabulated below.

Material	Carrier Concentration	Maximum Operating Temp. Without Amp.	With Amp.
n-(Hg,Cd)Te	10^{14} cm^{-3}	139 K	136 K
p-(Hg,Cd)Te	10^{16}	149	147
(Pb,Sn)Te	10^{15}	176	169

The effect of D^*_λ is not major; operating temperature is merely lowered a few degrees. Amplifiers do not, therefore, present a problem in developing elevated temperature photoconductors.

5.6.3 Power Dissipation

Power dissipation becomes an important criterion for large arrays of detectors, insofar as resistive heating places extra demands on the array cooling system, and available power may be at premium in non-laboratory settings. The expression for power dissipation per element is as follows:

$$P = V^2 \frac{q\, w\, t}{\ell} (\mu_e n + \mu_h p)$$

In the calculated model, physical dimensions ℓ and w are assumed equal; t is the minimum value necessary for good quantum efficiency, and q is the electron charge. Power dissipation is then a function of the bias V, mobilities μ_e and μ_h, and carrier concentrations n and p. In general, carrier concentration is constant at low temperatures, as the material doping dominates the intrinsic carriers, then rises exponentially with temperature (for majority carriers) as the material goes intrinsic. The mobility generally decreases exponentially with temperature, from a roughly constant level at low temperatures. The temperature dependence of power dissipation is, therefore, not a simple function. Representative calculated curves for the best device of each material type are found in Figure 5.23.

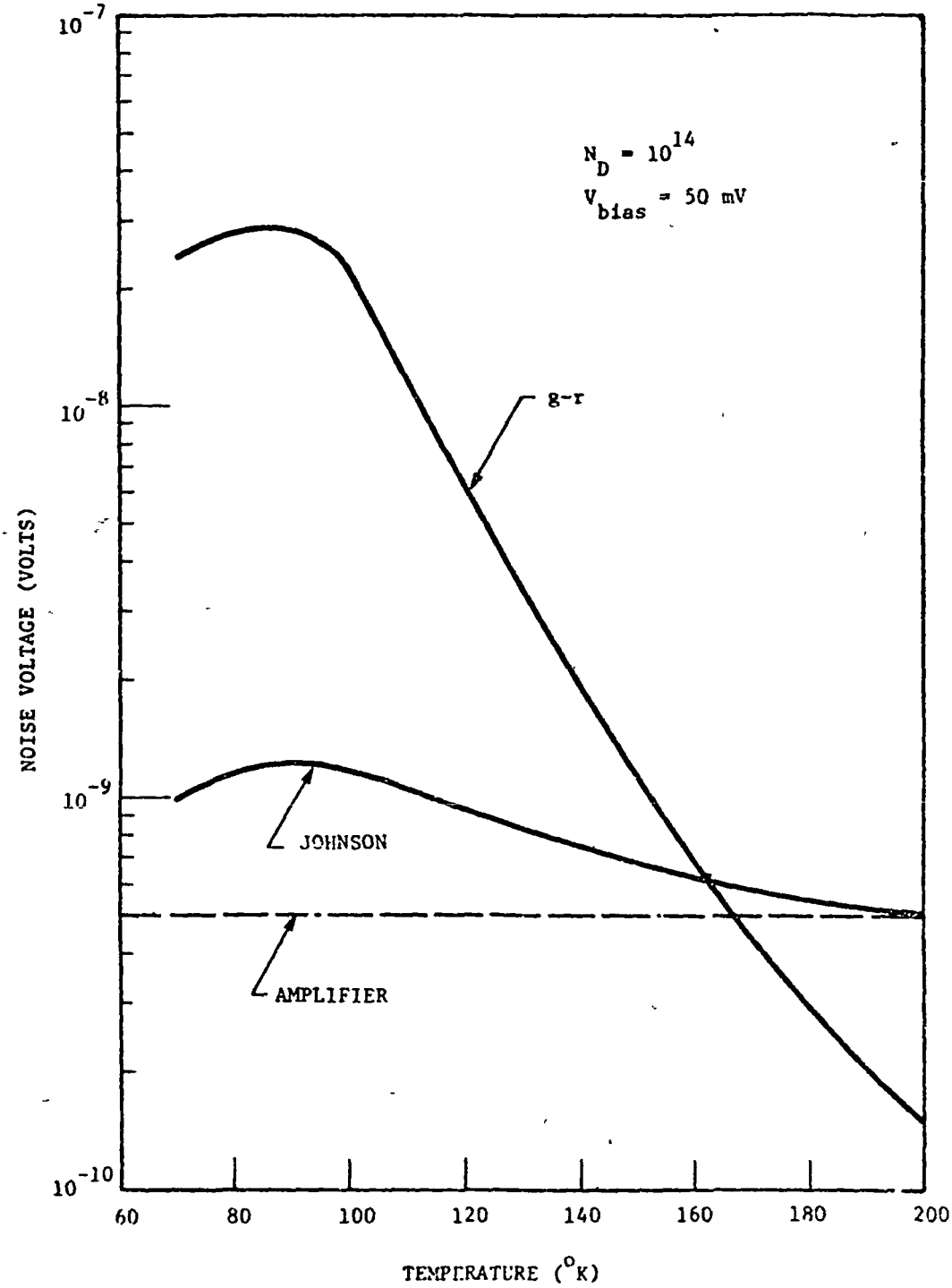

Figure 5.19 NOISE VOLTAGES FOR n-TYPE (Hg,Cd)Te PHOTOCONDUCTOR

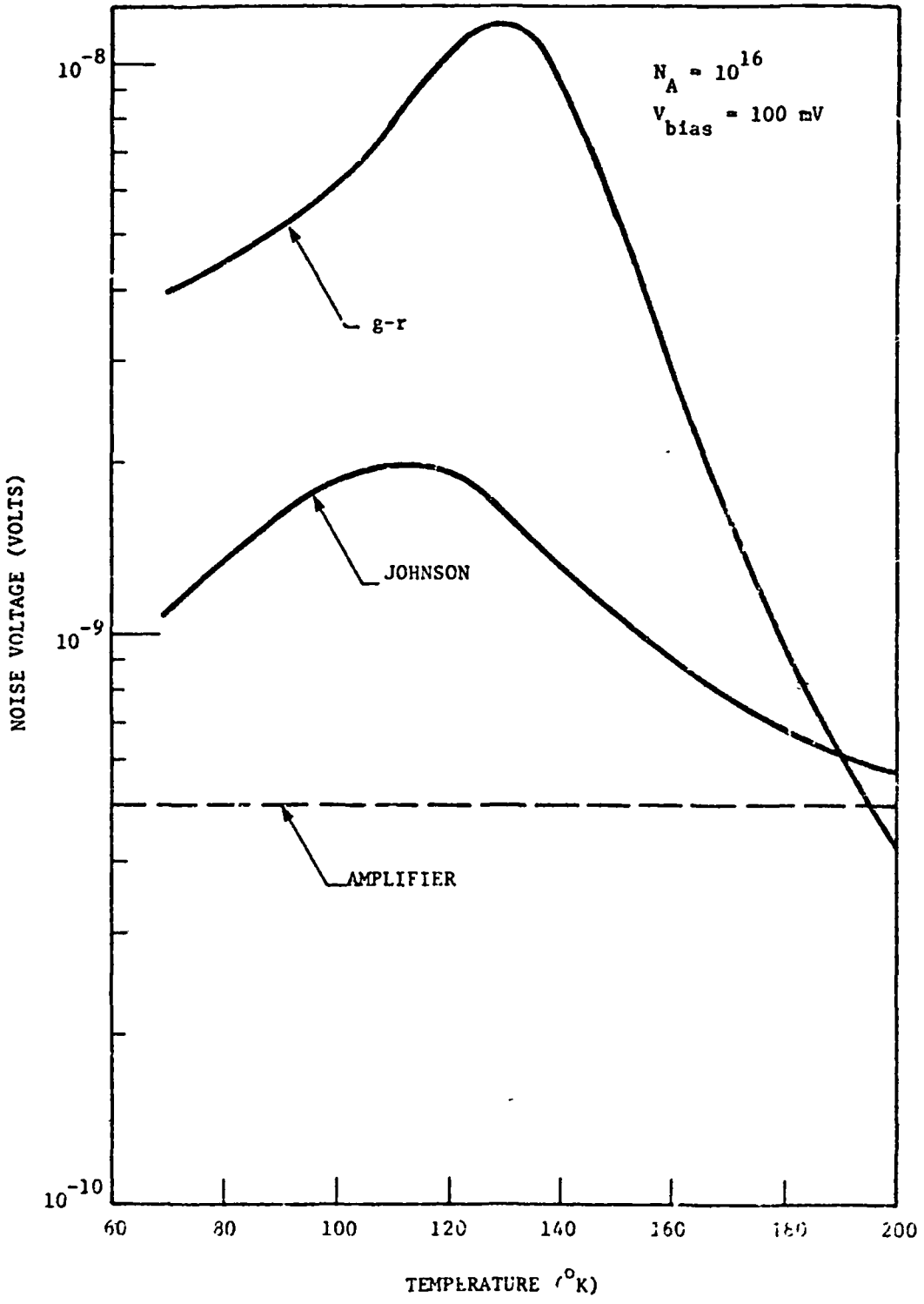

Figure 5.20 NOISE VOLTAGES FOR p-TYPE (Hg,Cd)Te PHOTOCONDUCTOR

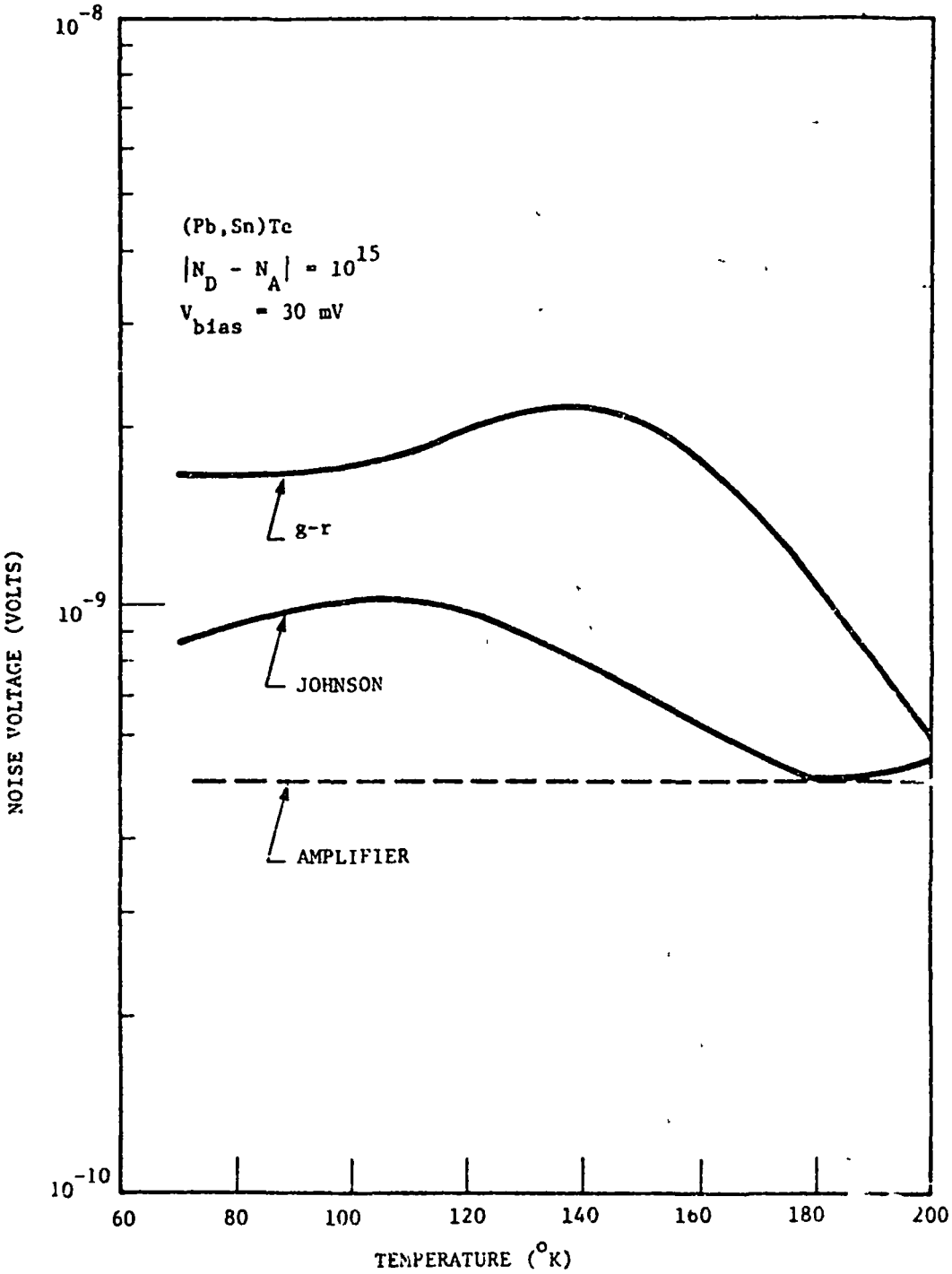

Figure 5.21 NOISE VOLTAGES FOR (Pb,Sn)Te PHOTOCONDUCTOR

77-1-6

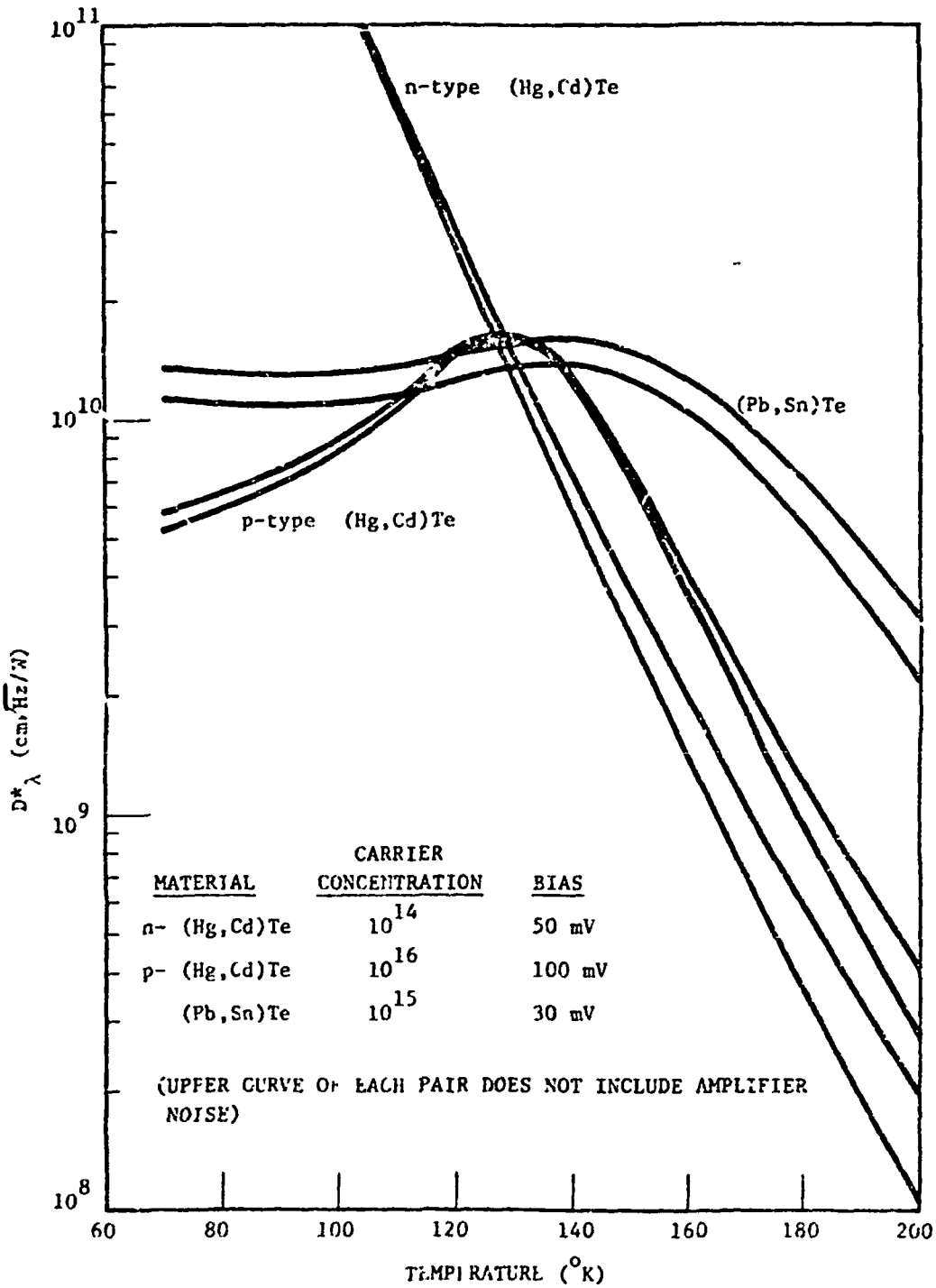

Figure 5.22 EFFECT OF AMPLIFIER NOISE ON CALCULATED D* CURVES

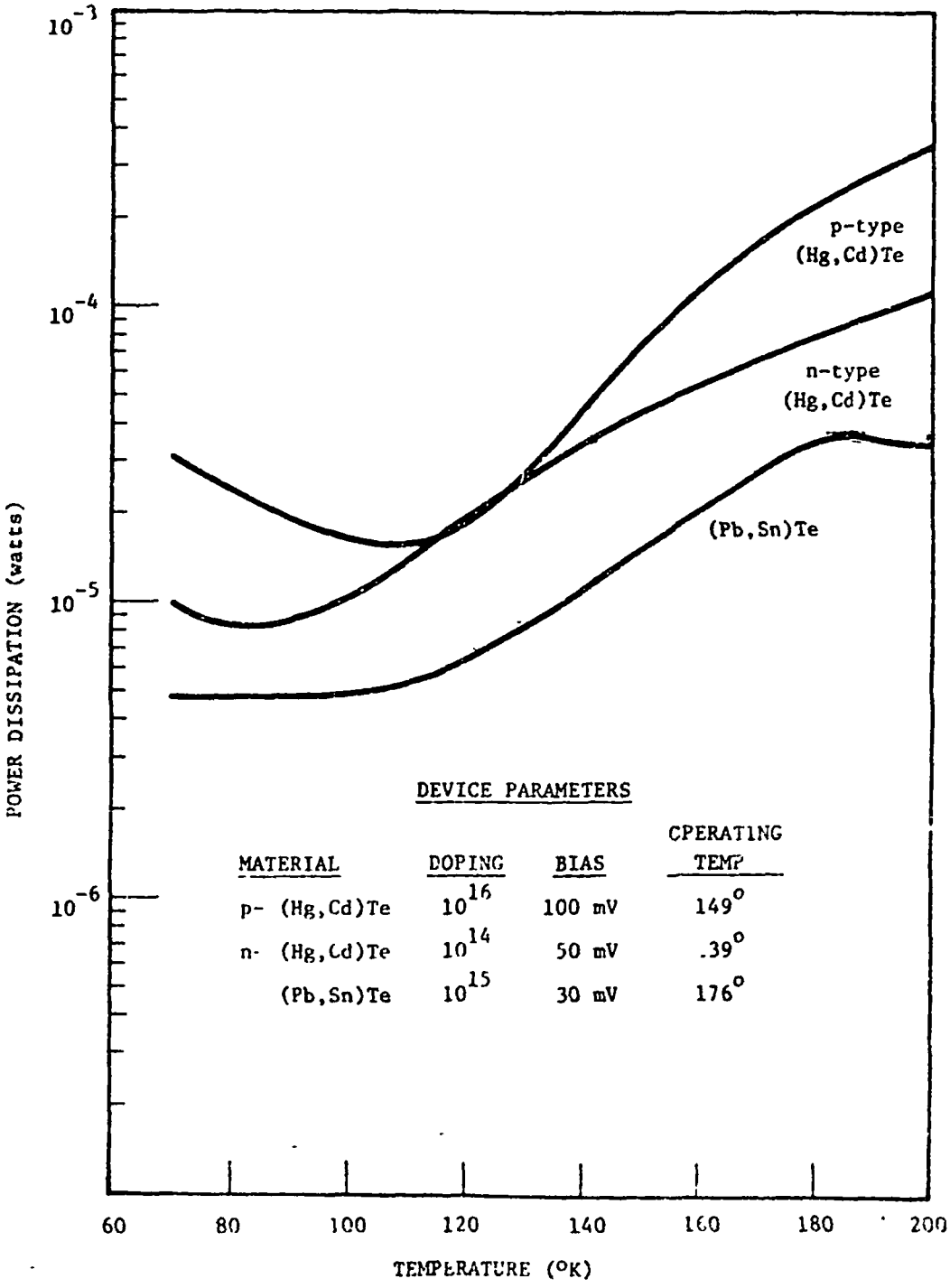

Figure 5.23 CALCULATED POWER DISSIPATION PER ELEMENT VS TEMPERATURE FOR SELECTED DEVICES

Calculated power dissipations for selected devices are presented in Table 5.5. The devices in the table are generally those which give the highest operating temperatures for the materials under study. The power dissipation listed is at the maximum operating temperature.

TABLE 5.5

CALCULATED POWER DISSIPATION FOR SELECTED DEVICES

Material	Doping (cm^{-3})	Bias (mV)	Max Operating Temperature	Power dissipation/ Element (μW)
(Pb,Sn)Te	10^{15}	30	176	32
(Pb,Sn)Te	10^{15}	10	167	2.8
p-(Hg,Cd)Te	10^{16}	100	149	56
p-(Hg,Cd)Te	10^{16}	30	145	6.2
n-(Hg,Cd)Te	10^{14}	50	139	34
n-(Hg,Cd)Te	10^{14}	20	134	4.7

The table shows power dissipations for the best devices of each material type (in terms of operating temperature) are all in the range 30-60 μW/element. However, a roughly one order of magnitude decrease in power dissipation is possible without substantial loss of operating temperature, if the bias is divided by 3. This loss in operating temperature may be quite acceptable, depending on the particular application of the device. For a 1000-element array, the difference between 4 and 40 mW of power is considerable in terms of the system design.

5.6.4 Interface With CCD

The future of infrared detection seems to be in large arrays of detectors, utilizing charge coupled devices for signal processing. The limitations imposed by interfacing with CCD's are then a major consideration in choosing a detector for future applications.

The direct coupling of photoconductive detectors with CCD's is made difficult by the large inherent impedance mismatch between these devices. The very high input impedance of the CCD causes its input noise to dominate the noise of the relatively low impedance (tens or hundreds of ohms) detectors, resulting in a loss of effective D*. Transfer of signal power is also less efficient because of the impedance mismatch.

As a consequence of these obstacles, indirect coupling through a buffer amplifier is usually employed. Bipolar transistors exist with sufficiently high

β's at detector operating temperatures (140-200K) for use in the common-base (CB) amplifier configuration. CB amplifiers provide an effective impedance transformation between the photoconductive detector and the CCD input. These amplifiers can be made with low enough noise and high enough gain to cause the detector noise to exceed the CCD input noise, thereby achieving detector-limited system performance. This capability has been demonstrated by Honeywell with (Hg,Cd)Te photoconductors operating at 77°; virtually no degradation in D* was observed from the detector itself to the CCD input.

Interfacing with a CCD through indirect coupling, therefore, imposes no new limitations on the operation of photoconductors. Also, as the impedance of any of the devices considered for elevated temperature operation may be matched using this method, CCD interfacing provides no basis for selection of one material over another.

5.7 CONCLUSIONS

Of the photoconductors covered in this study, p-type (Hg,Cd)Te seems to hold the most promise for elevated temperature development, although none are available over a short-term time scale. It is theoretically limited to 149K for operation with $D^* \geq 8 \times 10^9$ cm $Hz^{\frac{1}{2}}$/watt, at a power dissipation of 56 μW per element. This power dissipation can be decreased by a factor of 10, with a loss in operating temperature of 4°.

N-type (Hg,Cd)Te is by far the most developed photoconductive material of those studied, with near-theoretical performance in present-day devices. However, it is limited in theory to operation below 139K, if a D* of 8×10^9 is desired. This makes it unsuitable for operation in the specified 150-250K temperature region, unless a lower detectivity value is acceptable.

The other two material types have theoretically better performance, but suffer from a lack of development. The (Pb,Sn)Te has a maximum operating temperature of 176K, making it theoretically the best of the photoconductive materials studied. However, previous attempts to fabricate devices from this material have met with several problems: preparing crystals of low carrier concentration and very good crystallinity is extremely difficult, and lifetimes have been consistently shorter than those calculated from theory. Since the higher theoretical D* of (Pb,Sn)Te at elevated temperatures is due to longer calculated lifetimes, its advantage over (Hg,Cd)Te cannot be realized without an improvement in lifetime. Until more basic research is done on these problems, the near-theoretical D* necessary for this high operating temperature cannot be achieved.

P-type (Hg,Cd)Te has seen extremely little development as a photoconductor, although it has been used for photodiodes, and relatively good material is available. The first use of p-type (Hg,Cd)Te for photoconductors had very encouraging results, and it is believed that much of the knowledge accumulated about

n-type photoconductors will be applicable to p-type also. An added asset of p-type material is the slight theoretical advantage of moderately doped ($5x10^{16}$) material over intrinsic, making the growth of very low carrier concentration, very good crystallinity material unnecessary. The results of work in this area are quite uncertain, however, simply because 12-micrometer p-type photoconductors have never been attempted before.

The problem with Shockley-Read lifetime must be solved before theoretical detectivities can be approached. Development of a near-theoretical elevated temperature photoconductor would then seem to be a long-term rather than short-term possibility, depending first on some basic research.

5.8 REFERENCES

5.1 M.A. Kinch, M.J. Brau, and A. Simmons, J. Appl. Phys. 44, 1649 (1973).

5.2 R.S. Rittner, Photoconductivity Conference , ed. Breckenridge (John Wiley & Sons, 1956)

5.3 R.L. Williams, Infrared Phys. 8, 337 (1968).

5.4 J.S. Blakemore, Semiconductor Statistics (Pergamon, 1962) Chapter 6.

5.5 P.R. Emtage, J. Appl. Phys. 47, 2565 (1976).

5.6 W. Scott, J. Appl. Phys. 43, 1055 (1972).

5.7 Emmons and Ashley, Appl. Phys. Lett. 20, 162 (1972).

5.8 Reynolds, et al, Proc. Conf. on Semi-metals and Narrow-Gap Semiconductors, Pergamon (1970) p. 511.

5.9 Tasch, Chapman, Breazeale, J. Appl. Phys. 41, 4202 (1970).

5.10 "Lead-Tin Telluride Sputtered Thin Films for Infrared Sensors," General Dynamics Pomona Division (June 1975), p. 3-107 AFML-TR-75-63.

5.11 P.J.A. Zoutendyk, Proc. Semi-metals and Narrow-Gap Semiconductors Conf. (Pergamon, 1971), p. 421.

5.12 Honeywell unpublished data.

5.13 Interim Technical Report on "Exploratory Development of $Hg_{1-x}Cd_xTe$ Improvement," Phase II, E.L. Stelzer and J.L. Schmit, Jan 1975. Air Force Materials Laboratory Contract F33615-74-C-5041.

5.14 Interim Technical Report on "Exploratory Development of $Hg_{1-x}Cd_xTe$ Improvement, "Phase II, J.L. Schmit and E.S. Johnson, July 1976. Air Force Materials Laboratory Contract F33615-74-C-5041.

5.15 I. Melngailis and T.C. Harman, Appl. Phys Lett. 13, 180 (1968)

5.16 E.M. Logothetis and H. Holloway, J. Appl. Phys. 43, 256 (1972).

5.17 "Lead-Tin Telluride Sputtered Thin Films for Infrared Sensor, "General Dynamics Pomona Division, (June 1975), AFML-TR-75-63

5.18 The approximations used in deriving the Auger expression are invalid at 300^{o}, and marginal at 198^{o} (see Section 5.1); this explains the measured value of τ_{eff} larger than τ_A at 300^{o}.

5.19 Abnormally high D* values (up to 10^{10} in an isolated case) were reported, for short-wavelength detectors only. The response in these devices, with $\lambda_p \leq 6\mu m$, was apparently due to some form of carrier compensation, and was not reproducible. The uncertain nature of this process, and the fact that it was confined to short wavelength materials, makes it an interesting area for study, but of questionable promise for 12μm detection.

SECTION 6

PYROELECTRIC DETECTORS

6.0 INTRODUCTION

The two main classes of infrared detectors are thermal detectors and photon detectors. In a photon detector, an incoming quantum of radiation causes an observable electrical effect in the detector. A thermal detector senses infrared radiation by first absorbing the radiation and converting it to heat. The resulting change in temperature is then measured.

From the signal generation point of view, photon detectors are simpler than thermal detectors, since the detection process in photon detectors is essentially a one-step process rather than a two-step process in thermal detectors. In recent years, very sensitive photon detectors have been developed and are becoming common. However, all photon detectors sensitive to wavelengths longer than 2 micrometers must be cooled below room temperature for best sensitivity. This fact, together with the need for infrared imaging system, has led to renewed interest in thermal detectors.

All thermal detectors have in common the conversion of incoming radiation to heat. Different thermal detectors use different methods for converting heat into an observable outpu which is usually, but not always, electrical. In principle, any material property which is temperature dependent may be utilized to make a thermal detector. The most popular thermal detectors include the thermocouple (using the thermoelectric effect), the Golay cell (using thermal expansion of a gas), and the pyroelectric detector which uses the temperature dependence of the spontaneous polarization of a ferroelectric material.

6.1 SIGNAL AND NOISE IN PYROELECTRICS

6.1.1 Signal in Pyroelectrics

The pyroelectric effect is exhibited by temperature sensitive pyroelectric crystals, among which are certain ferroelectric crystals TGS (tryglycine sulfate), SBN ($Sr_{1-x}Ba_xNb_2O_6$), PLZT (lanthanum doped lead zirconate titanate) and $LiTaO_3$. Recently, a number of polymers have been shown to exhibit this pyroelectric effect. Such crystals exhibit spontaneous electric polarization which can be measured as a voltage by electrodes attached to the sample. At constant temperature, however, the internal charge distribution will be neutralized by free electrons and surface charges, so no voltage is detectable. If the temperature is rapidly changed, the internal dipole moment will change, producing a transient voltage. This pyroelectric effect can be exploited as a sensitive detector of modulated radiation, operating at ambient temp rature. 6.1

The first step in the detection process is the conversion of incident radiation to heat. For a pyroelectric detector, the signal is a change in the

spontaneous polarization which is sensed as a voltage change by a preamplifier. This is shown schematically in Figure 6.1

One can define a temperature responsivity, R_T, for a pyroelectric detector which is the change in the detector bulk temperature per watt of incident radiation. For sinusoidally modulated radiation of the form

$$P_1(t) = \tfrac{1}{2}P_o\ (1 + \sin \omega t) \qquad (6.1)$$

heating a pyroelectric detector which is thin enough so that the change in temperature ΔT is uniform throughout the detector, the time-dependent temperature change $\Delta T(t)$ is given by [6.1]

$$\eta P_1(t) = c\rho Ad \frac{d}{dt} \Delta T + gA\Delta T \qquad (6.2)$$

where:

η = the emissivity of the detector surface. For a blackened surface $\eta = 1$.

$c\rho$ = the volume specific heat of the detector material (in Joules-cm^{-3}-$^oK^{-1}$)

g = the thermal conductance per unit area, which controls the heat loss to the environment by radiation, and the substrate by conduction.

A = detector area

d = detector thickness

The magnitude of the temperature change ΔT in a pyroelectric detector is hence

$$\Delta T = \frac{\eta P_o}{qA} \left(\frac{1}{1 + \omega^2 \tau_T^2} \right)^{\frac{1}{2}} \qquad (6.3)$$

where

$$\tau_T = c\rho d/g \qquad (6.4)$$

is the thermal time constant.

Equations 6.3 and 6.4 assume that the thermal conductance is independent of frequency. In fact, thermal conductance is frequency dependent, with the specific mounting support techniques used determining both the magnitude and frequency dependence of g. In the limit of

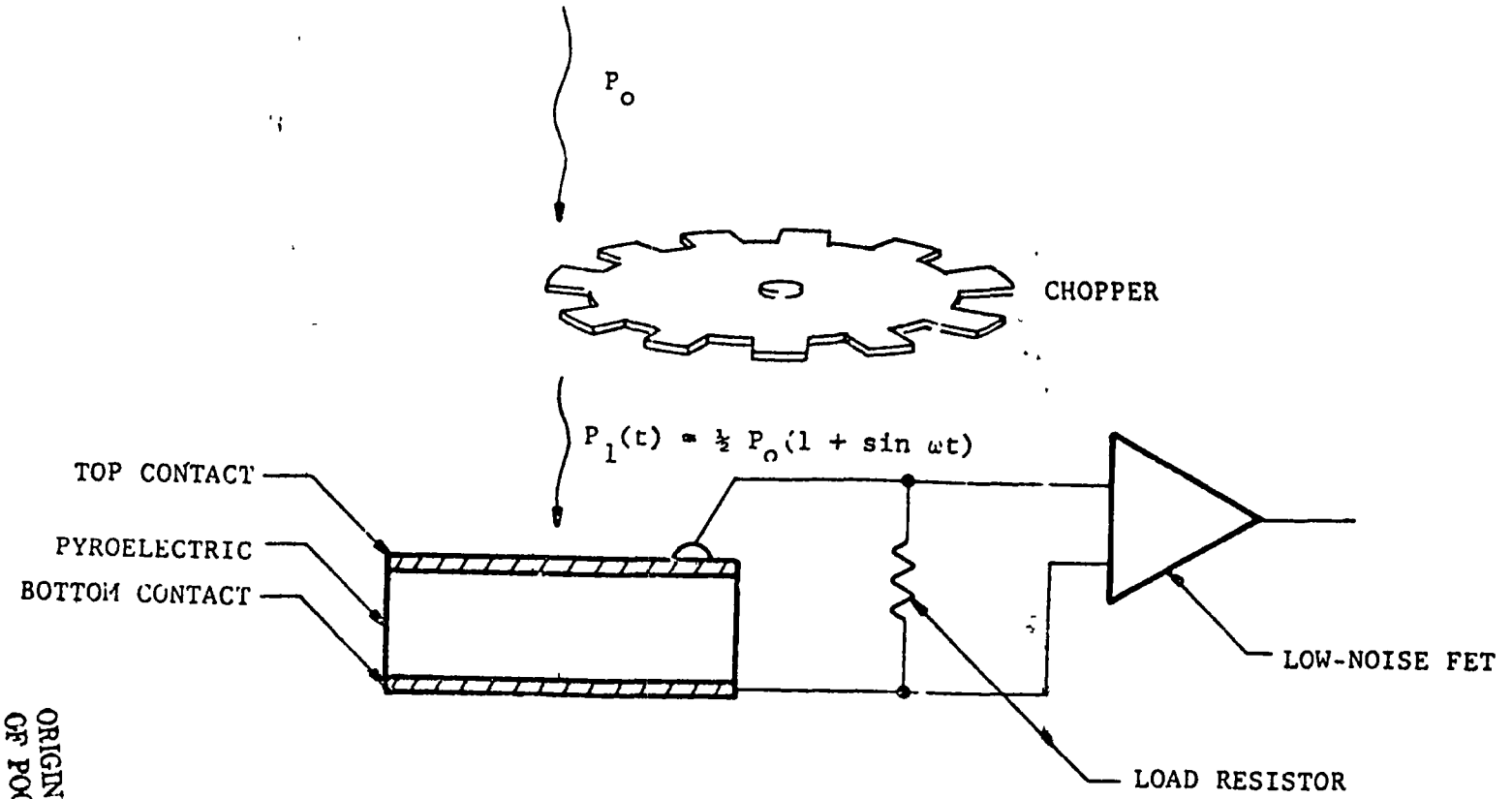

Figure 6.1 PYROELECTRICS SIGNAL MECHANISMS

radiative heat transfer between pyroelectric and environment, g is independent of frequency. For the sake of simplicity, we consider only the case where g is independent of frequency.

The temperature responsivity, defined by $R_T = \Delta T/P_o$ is hence

$$R_T = \frac{\eta}{gA}\left(\frac{1}{1+\omega^2\tau_T^2}\right)^{\frac{1}{2}} \tag{6.5}$$

at low modulation frequencies,

$$R_T \simeq \frac{\eta}{gA} \qquad \omega\tau_T << 1 \tag{6.6}$$

and at high frequencies,

$$R_T \simeq \frac{\eta}{c\rho dA\omega} \qquad \omega\tau_T >> 1 \tag{6.7}$$

The rolloff frequency is given by

$$\omega_o = 2\pi f_o = \frac{1}{\tau_T} = \frac{g}{c\rho d} \tag{6.8}$$

Figure 6.2 is a schematic representation of R_T versus modulation frequency for three thermal conductance values. It is evident that the rolloff frequency, f_o, can be pushed to higher frequencies by increasing g by increasing thermal contact between the detector and the surroundings. But this degrades the temperature responsivity due to a large heat loss to the substrate and the surroundings.

The thickness of the detector, d, plays a very significant role in the performance of a pyroelectric detector. It determines the thermal mass of the detector, and hence, also the thermal time constant (Eq. 6.4). Reducing the thickness will not affect the low-frequency thermal responsivity, but will directly increase the high-frequency thermal responsivity (Eq. 6.7).

The next step in the detection process is the conversion of the temperature change in the detector into an electrical signal. In a pyroelectric, a change in the temperature of the material produces a change in polarization and hence, in surface charge. The material is characterized by a pyroelectric coefficient p which is the change in surface charge per unit area due to a temperature change. The change in surface charge Δq on the detector is given by

$$\Delta q = p\ \Delta T \tag{6.9}$$

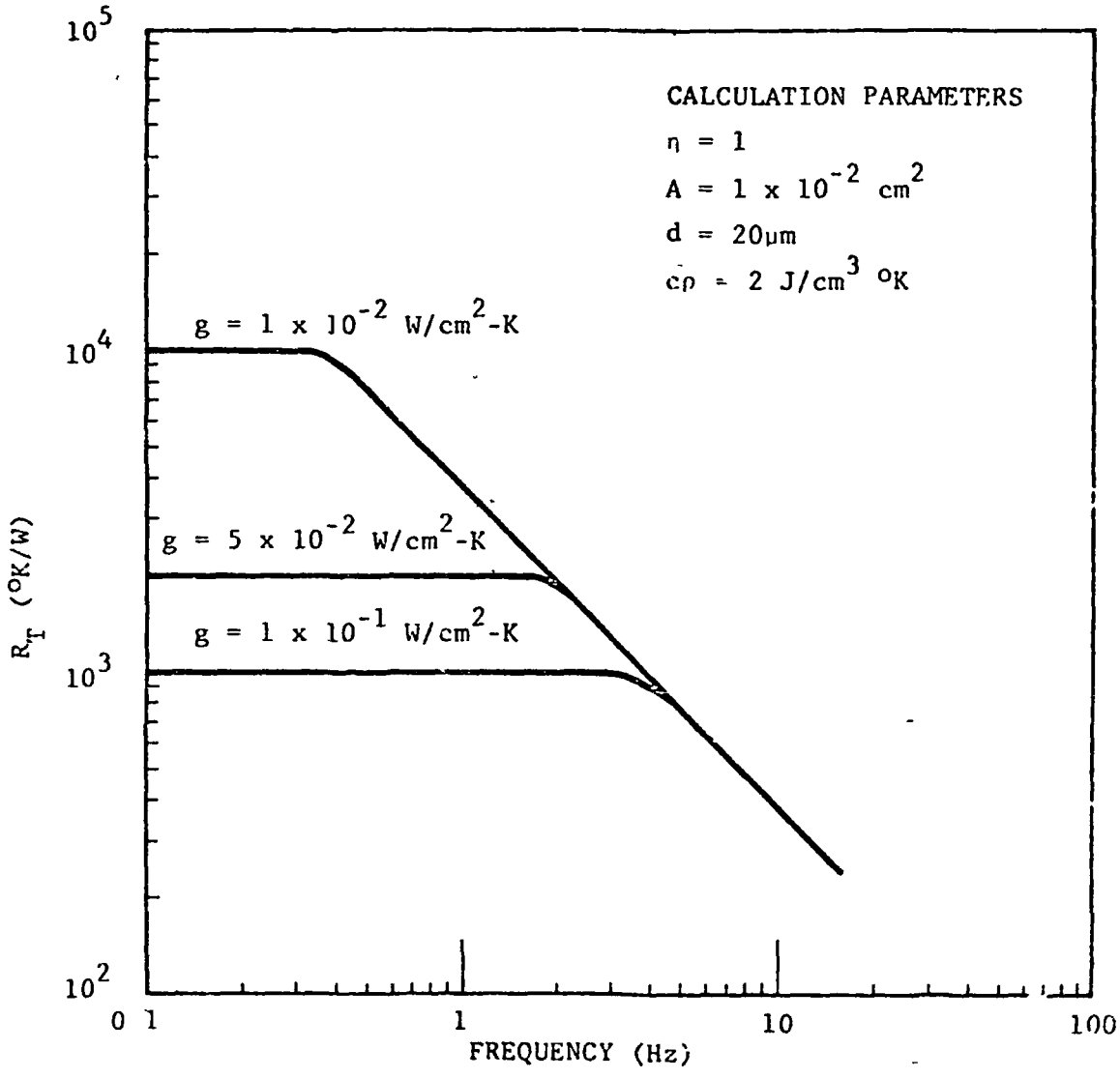

Figure 6.2 CALCULATED THERMAL RESPONSIVITY VS FREQUENCY FOR A PYROELECTRIC DETECTOR (Eq. 6.5)

The signal current I_s is hence

$$I_s = \frac{\Delta q}{\Delta t} = pA \frac{\Delta T}{\Delta t} = pAR_T \omega P_o \tag{6.10}$$

The current responsivity, defined by I_s/P_o, is hence

$$R_i = pAR_T\omega \tag{6.11}$$

Figure 6.3 is a plot of R_i as a function of frequency.

The voltage responsivity is the current responsivity divided by the admittance of the circuit seen by the detector

$$R_V = R_i/|Y| \tag{6.12}$$

For just the detector alone,

$$|Y_d| = R_d^{-1} (1 + \omega^2 C_d^2 R_d^2)^{\frac{1}{2}} \tag{6.13}$$

where R_d is the resistance of the pyroelectric (usually $\sim 10^{12}$ Ω, due to surface leakage), C_d is the capacitance. The voltage responsivity at very low frequencies is directly proportional to the current responsivity. However, above a frequency corresponding to the electrical time constant of the pyroelectric:

$$\tau_E = R_d C_d \tag{6.14}$$

the voltage responsivity rolls off, due to the pyroelectric capacitance.

The voltage responsivity over the full frequency range is

$$R_V = \frac{\eta p}{c\rho d} \frac{\omega\tau_T}{(1 + \omega^2\tau_T^2)^{\frac{1}{2}}} \frac{R_d}{(1 + \omega^2\tau_E^2)^{\frac{1}{2}}} \tag{6.15}$$

For frequencies beyond both the thermal and electrical time constants:

$$R_V = \frac{\eta p}{(2\pi f)c\rho d C_d} \tag{6.16}$$

Figure 6.4 illustrates the frequency dependence of the voltage responsivity.

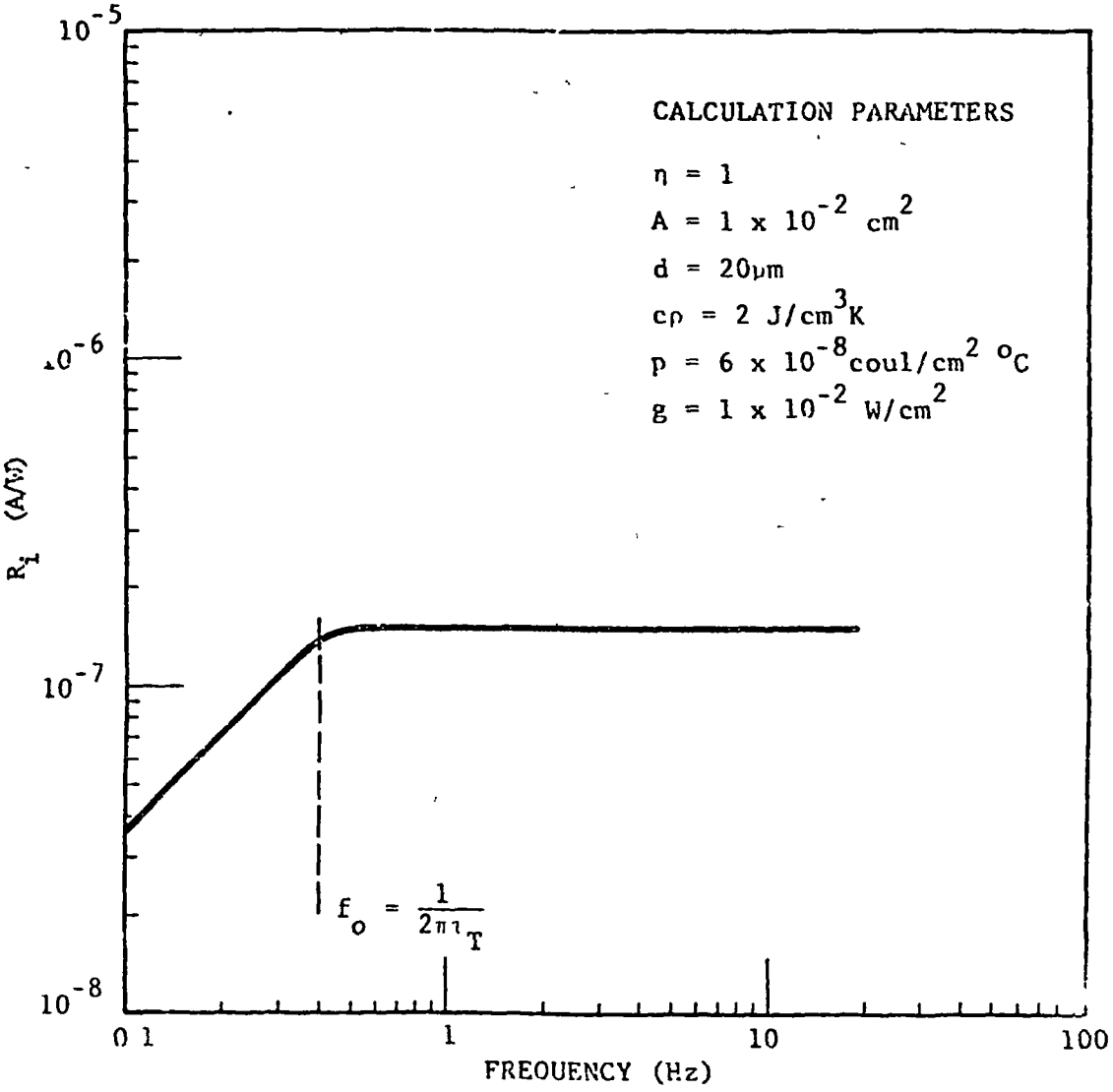

Figure 6.3 CALCULATED CURRENT RESPONSIVITY VS FREQUENCY (Eq. 6.11)

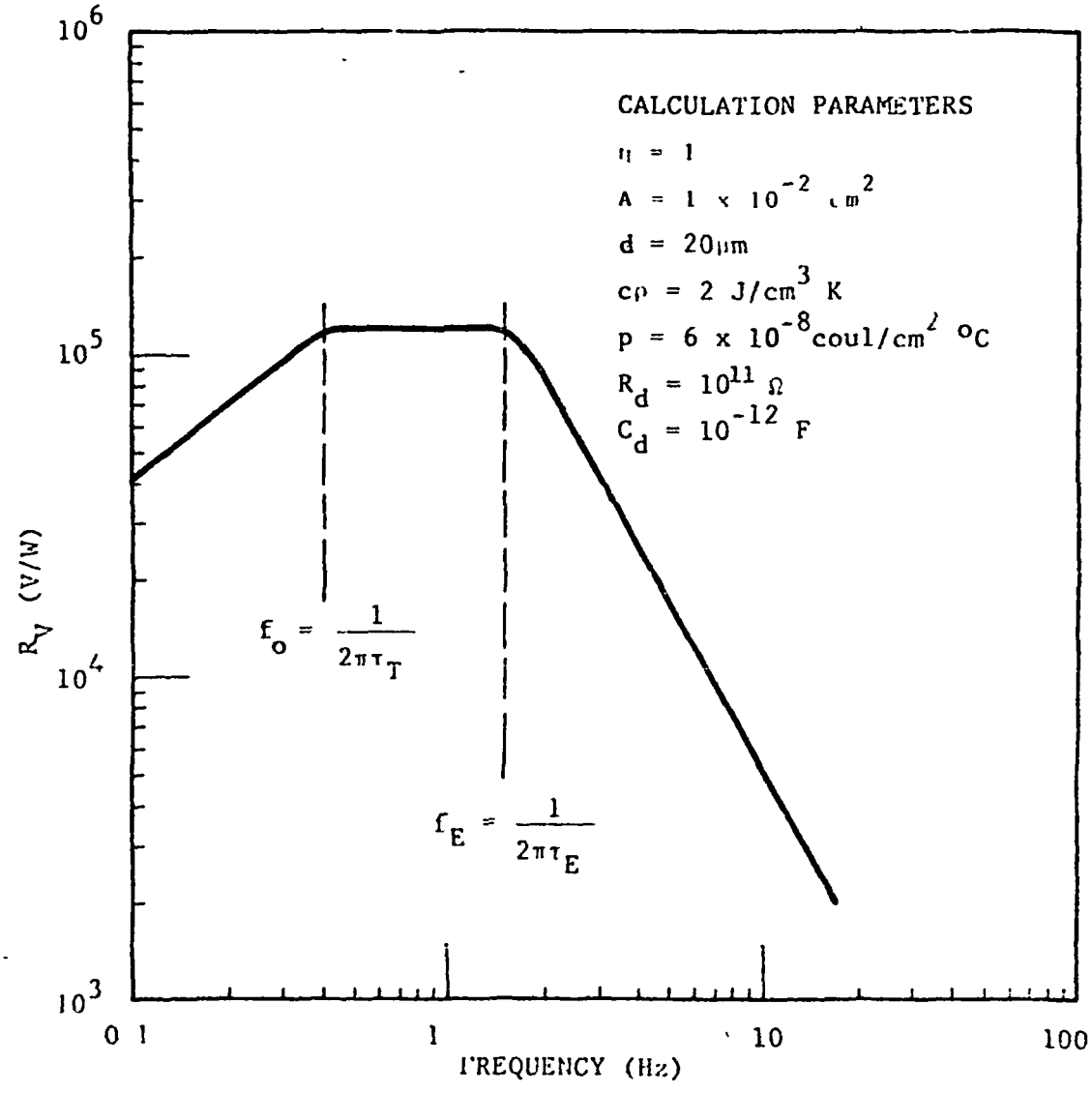

Figure 6.4 CALCULATED VOLTAGE RESPONSIVITY VS FREQUENCY (Eq. 6.15)

6.1.2 Noise Sources in Pyroelectric Detectors

Noises of a pyroelectric detector/preamplifier assembly arise from a number of sources. These sources can be represented by the equivalent circuit shown in Figure 6.5. The total noise, i_N, is given by[6.1, 6.2]

$$i_N^2 = i_T^2 + i_d^2 + i_c^2 + i_a^2 + i_{R_n}^2 \tag{6.17}$$

where

i_T = temperature fluctuation noise

i_d = detector thermal noise

i_c = amplifier load resistance noise

i_a = amplifier current noise

i_{R_n} = amplifier voltage noise

Temperature Fluctuation Noise

The temperature fluctuation noise represents the ultimate limit to performance of a pyroelectric detector. When a small body is in thermal equilibrium of its surroundings at a temperature T, via a thermal conductance g, the net power flow between the body and its surroundings is zero. However, it will have a fluctuation spectrum with a rms value.[6.3]

$$\Delta W_T = (4KT^2 g\ A)^{\frac{1}{2}} \tag{6.18}$$

$$i_T^2 = R_i^2\ 4KT^2 g\ A \tag{6.19}$$

where R_i is the current responsivity of the detector. The minimum temperature fluctuation noise occurs when g is dominated by radiative exchange alone; heat transfer by conduction to the detector mount or through any gas used for backfill would increase the temperature fluctuation noise by increasing g.

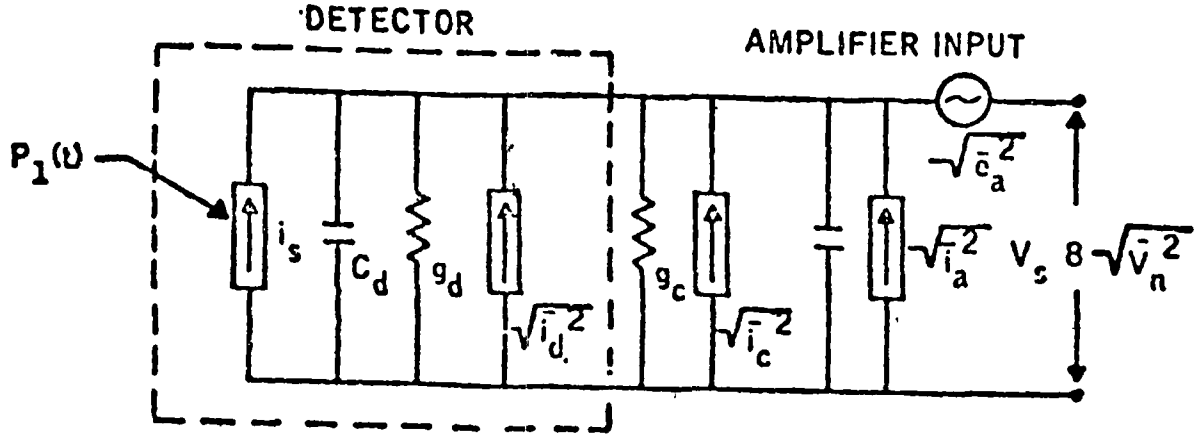

Figure 6.5 PYROELECTRIC DETECTOR/AMPLIFIER EQUIVALENT CIRCUIT

Detector Thermal Noise

There will be Johnson noise associated with any element with resistance, given by:

$$i_d^2 = \frac{4KT}{R} = 4KT\, g_d \qquad (6.20)$$

There are two sources of conductance in a pyroelectric: (a) the dielectric loss with conductance $g_d = \omega C_d \tan\delta$, and (b) leakage conductance is normally negligible in comparison with the dielectric loss. Dielectric loss is due to a number of factors, some associated with material defects and some with device fabrication.

Input Circuit Thermal Noise

The input circuit utilizes a load resistor R_L in order to operate the JFET amplifier in a stable configuration. The load resistor is normally chosen to be sufficiently high (10^{12} Ω) that is does not contribute excess noise. The noise is given by the Johnson noise of the load resistor R_L.

$$i_c^2 = 4KT/R_L \qquad (6.21)$$

Amplifier Current Noise

Any circuit can be represented by a combination of a voltage generator in series with the input and a current generator in parallel of the input. Either of these noise sources may dominate the total noise depending on the impedance of the detector and amplifier.

The preamplifier usually consists of a low-noise JFET and associated biasing circuitry. All FETs have gate leakage current I_g associated with them; this leakage current is a source of shot noise i_a where:

$$i_a^2 = 2\, q\, I_g \qquad (6.22)$$

where q is the electronic charge.

Different types of JFETs show wide variations in I_g; the present state-of-the-art is about 0.2 pA.

Amplifier Voltage Noise

The amplifier voltage noise is specified either in terms of e_n or an equivalent noise resistance R_n. The noise is given by:

$$i_{R_n}^2 = 4KT\, R_n \left[(g_c + g_d)^2 + \omega^2 (C_d + C_a)^2\right] = e_n^2 |Y|^2 \qquad (6.23)$$

where e_n is the amplifier noise voltage and $g_c + g_d$ and $C_d + C_a$ are the total conductance and capacitance of the input circuit, respectively. Typical JFETs have $e_n \sim 10$ nV/$\sqrt{\text{Hz}}$. Figure 6.6 illustrates the frequency dependence of the noise sources. The relative magnitudes of the various noise sources will, of course, depend on variables such as detector material, detector area, amplifier characteristics etc.

6.1.3 Detectivity of a Pyroelectric Detector

The detectivity, D*, is defined by

$$D^* = \frac{i_s}{i_N} \frac{\sqrt{A}}{P_o} \qquad (6.24)$$

By combining the signal current I_s from equation 6.10 and the noise current i_N from equation 6.17, the detectivity of a pyroelectric detector/amplifier assembly can be determined. However, it is instructive to estimate a thermodynamic-limited detectivity D^*_T for a pyroelectric detector. The ultimate limit occurs when the only noise contributing to i_N is the temperature fluctuation noise due to the fluctuations in the thermal equilibrium between the detector and its surroundings. In this limit,

$$i_N \rightarrow i_T = R_i \sqrt{4KT^2 gA} \qquad (6.25)$$

Also

$$i_s = R_i P_o \qquad (6.26)$$

Hence

$$D^*_T = (4KT^2 g)^{-\frac{1}{2}} = (16\, K\sigma T^5)^{-\frac{1}{2}} \qquad (6.27)$$

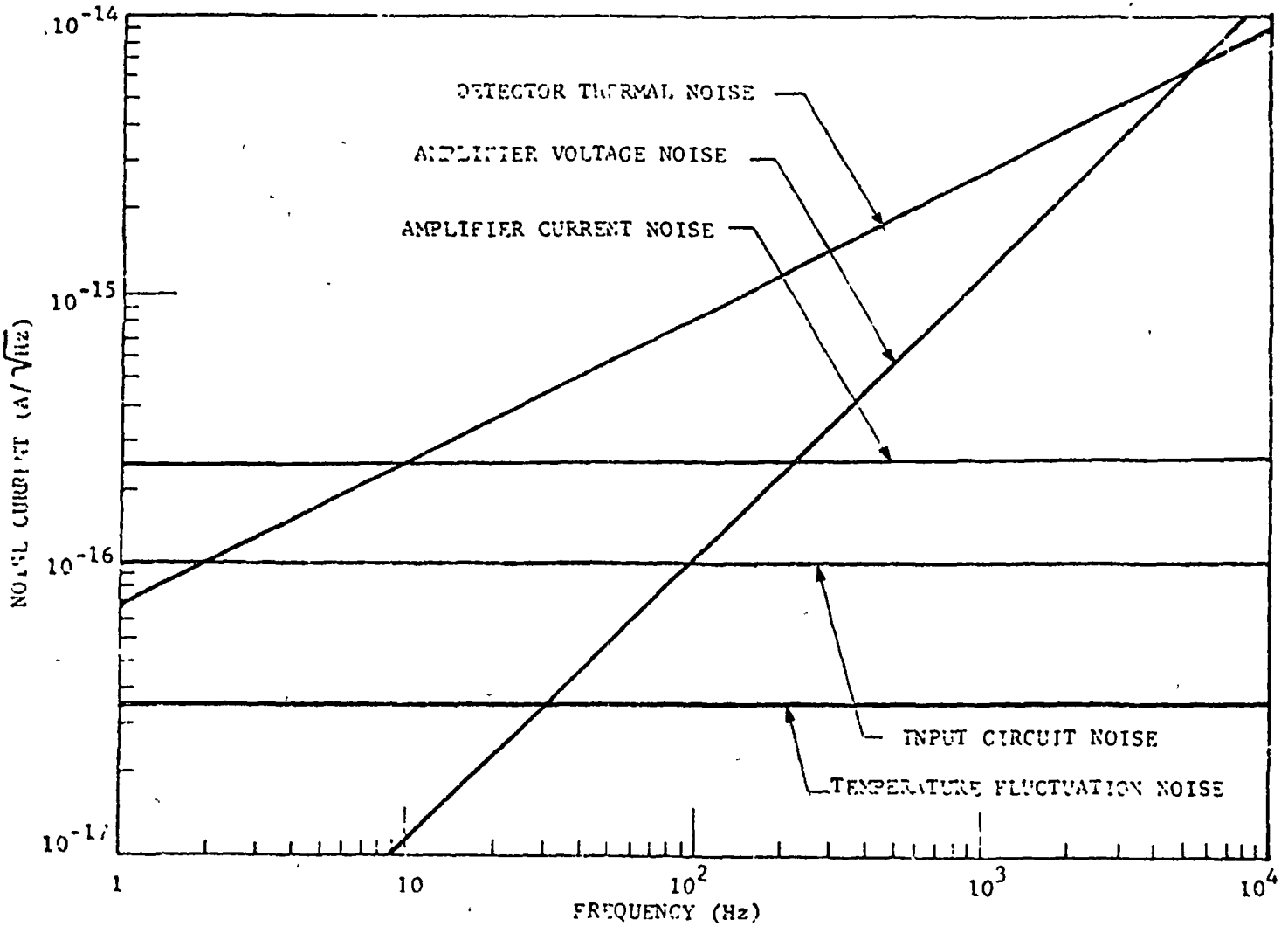

Figure 6.6 NOISE IN PYROELECTRICS i_n VS FREQUENCY

where $g = 4\sigma T^3$, $\sigma = 5.67 \times 10^{-12}$ w/cm^2-K^4 is the Stefan-Boltzmann constant. For T = 300K, $D^*_T = 1.8 \times 10^{10}$ cm Hz$^{\frac{1}{2}}$/W, which is the theoretical limit for all pyroelectric detectors at room temperature.

In a similar manner the detector-limited detectivity D^*_d can be defined as

$$D^*_d = \frac{i_s}{i_d} \frac{\sqrt{A}}{P_o}$$

$$= \frac{p}{c\rho\sqrt{\epsilon}} \left(\frac{1}{\tan\delta}\right)^{\frac{1}{2}} \left(\frac{1}{4KT\epsilon_o d}\right)^{\frac{1}{2}} \left(\frac{1}{\omega}\right)^{\frac{1}{2}} \frac{\omega\tau_T}{(1 + \omega^2\tau_T^2)^{\frac{1}{2}}} \qquad (6.28)$$

where the only noise assumed is that due to the detector dielectric loss (given by Eq. 6.20).

It is convenient to lump the last factor into a single thermal degradation term, T_r. Hence

$$D^*_d = \frac{p}{c\rho\sqrt{\epsilon}} \left(\frac{1}{\tan\delta}\right)^{\frac{1}{2}} \left(\frac{1}{8\pi KT\epsilon_o d}\right)^{\frac{1}{2}} \left(\frac{1}{f}\right)^{\frac{1}{2}} T_r \qquad (6.29)$$

The thermal degradation T_r is due to thermal loss of the detector to the black front coating and the supporting structures and substrate.

The detector-limited detectivity displays all the characteristics necessary to optimize the performance of the detector. Firstly, the detectivity improves as the thickness of the detector is reduced. The present state-of-the-art pyroelectric detector thickness is 10 micrometers. Thinner detectors are possible with improvement in fabrication techniques. Secondly, the detectivity increases with reductions in the dielectric loss tanδ. Currently, tanδ is on the order of 10^{-3} for good pyroelectric material. Finally, D^*_d is proportional to the material constant $p/c\rho\sqrt{\epsilon}$, which can be viewed as a figure-of-merit in choosing a detector material.

Figure 6.7 illustrates the frequency response for a pyroelectric detector. The magnitude of the D^*_λ will, of course, depend on the pyroelectric material parameters and amplifier; for Figure 6.7 the calculated detectivity was for a Strontium Barium Niobate (SBN) detector 10μm thick with tanδ = 0.002 and operated at room temperature. The thermal fluctuation limit ($D^*_\lambda = 2.0 \times 10^{10}$ cm Hz$^{\frac{1}{2}}$/W) is also shown, this limit assumes a 300°K background.

One of the major factors in the pyroelectric detector design is the minimization of the preamplifier noise. The detector/amplifier detectivity can be written as

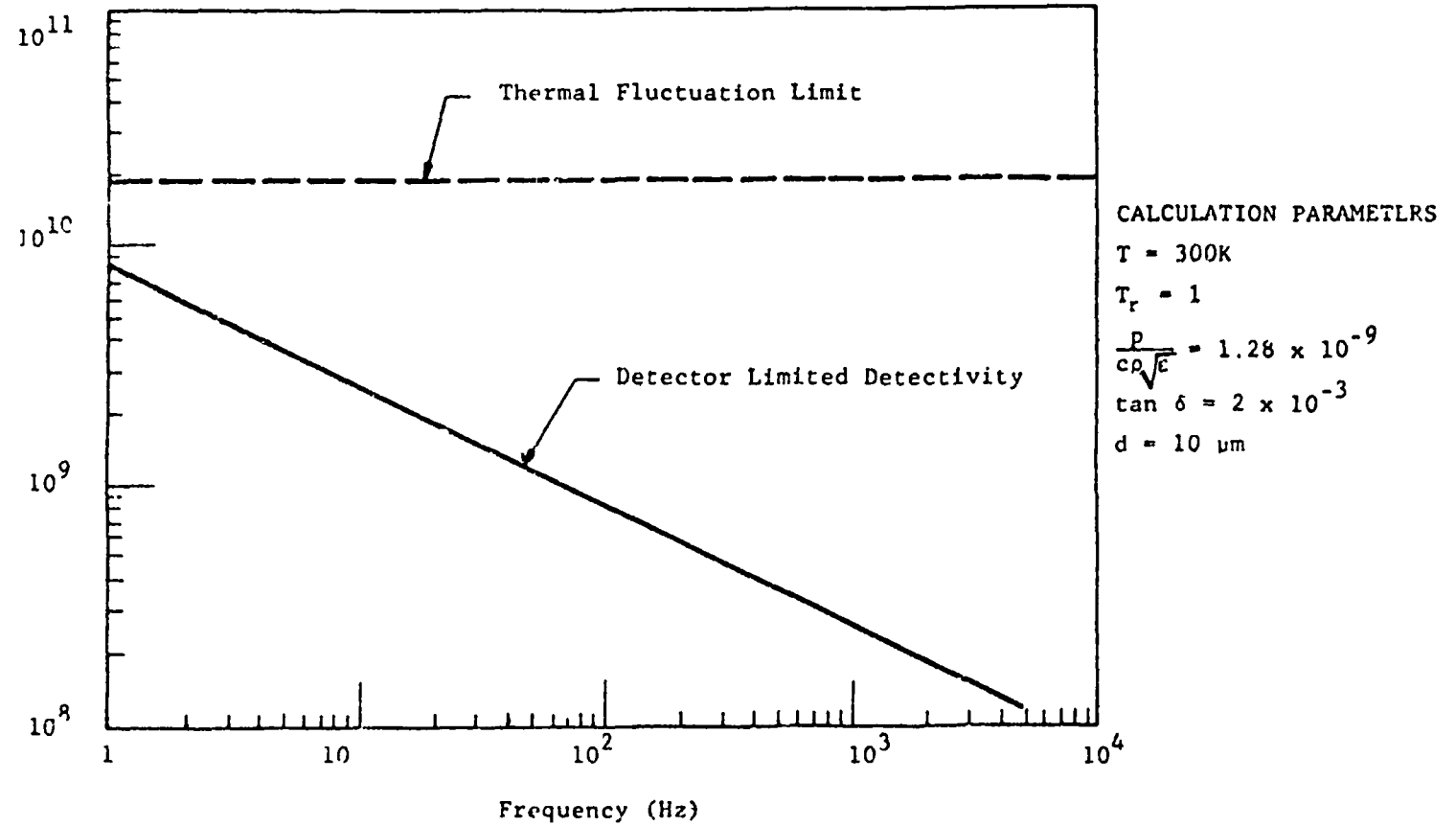

Figure 6.7 CALCULATED DETECTIVITY OF A SBN PYROELECTRIC DETECTOR (Eq. 6.29)

$$D^* = D^*_d / F^{\frac{1}{2}}$$

$$= \frac{p}{c\rho\sqrt{\epsilon}} \left(\frac{1}{\tan\delta}\right)^{\frac{1}{2}} \left(\frac{1}{8\pi KT\epsilon_o d}\right)^{\frac{1}{2}} \left(\frac{1}{f}\right)^{\frac{1}{2}} (T_r) \left(\frac{1}{F}\right)^{\frac{1}{2}} \qquad (6.30)$$

where

$$F = \frac{i_d^2 + i_c^2 + i_a^2 + i_{R_n}^2 + i_T^2}{i_d^2} \qquad (6.31)$$

The term $(1/F)^{\frac{1}{2}}$ represents the noise degradation and can be calculated from the amplifier characteristics to optimize D* with respect to parameters such as detector capacitance, etc.

Section 6.1.4 includes a brief discussion of the thermal degradation factor T_r and the noise degradation $(1/F)^{\frac{1}{2}}$. The material figure-of-merit and the dielectric loss are discussed in Section 6.3.

6.1.4 Thermal and Electrical Degradation

Two additional sources of noise not included in the detector-limited D*d were the thermal degradation factor, T_R, and the amplifier-related degradation F. In principle both could be reduced to negligible levels, but in practice they often limit pyroelectric performance.

Thermal Loss

The thermal loss factor arises as follows: if a pyroelectric detector were completely freehanging, the thermal conductance to the substrate would be determined only by heat loss to the environment by radiation. In fact, a pyroelectric must be supported and the support structure will also result in heat loss due to its thermal conductance g. As Figure 6.2 shows, the higher the thermal conductance between the pyroelectric and its surroundings, the lower the responsivity at low frequencies and hence the lower the detectivity.

In addition to affecting detectivity by decreasing responsivity at low frequencies (Eq. 6.6), thermal loss also appears to affect detectivity by affecting the dielectric loss factor tanδ (Eq. 6.28). S. Stokowski and N. Byer[6.4, 6.5] and, independently, A. Chiang and N. Butler[6.6] have shown that the measured dielectric loss factor tanδ is due not only to the pyroelectric material loss tangent, $\tan\delta_o$, but also to thermal interchange with the environment. This may be seen below.

It is well-known that when a pyroelectric detector is in thermal equilibrium with its environment at a temperature T via a thermal conductance G, there will be no heat flux between the detector and its surroundings. However, a thermal fluctuation exists which gives rise to a current fluctuation noise in the pyroelectric.

$$i_T = (4KT^2G)^{\frac{1}{2}} R_i (\Delta f)^{\frac{1}{2}} \tag{6.32}$$

where Δf is the bandwidth and the current responsivity R_i is given by:

$$R_i = \frac{pA\omega}{G(1+\omega^2\tau_T^2)^{\frac{1}{2}}} \tag{6.33}$$

p, A, and τ_T are the detector pyroelectric coefficient, area and thermal time constant, respectively. Since a pyroelectric detector is basically a capacitor, this noise term must appear as a noise due to an effective electrical conductance g_{eff}, that is

$$i_{n_{eff}} = (4KT\, g_{eff} A \Delta f)^{\frac{1}{2}} \tag{6.34}$$

The effective conductance g_{eff} can be calculated by equating equations 6.32 and 6.34. The result is

$$g_{eff} A = TG R_i^2 \tag{6.35}$$

Based on equation 6.35 the effective dielectric loss tangent, $\tan\delta_{eff}$ can be expressed in terms of the thermal conductance G (= gA):

$$\tan\delta_{eff} = \frac{TG R_i^2}{A\omega C_d} = \frac{p^2 T}{\epsilon \epsilon_0} \frac{g\omega d}{g^2 + (\omega cpd)^2} \tag{6.36}$$

Thus, a thermal conductance between pyroelectric and substrate gives rise to an electrical loss, and hence to Johnson noise. The electrical conductance due to $\tan\delta_{eff}$ is given by

$$g_{eff} = \omega C_d \tan\delta_{eff} \tag{6.37}$$

where C_d is the capacitance of the detector.

Stokowski and Byer[6.4,6.5] give a similar expression for the total loss tangent:

$$\tan\delta = \frac{p^2 T}{\epsilon \epsilon_0 C^E} \frac{(\omega\tau)}{\omega^2 + (\omega\tau)^2} + \tan\delta_0 \qquad (6.38)$$

where p is the pyroelectric coefficient, T the temperature, ϵ the dielectric constant, C^E the volume heat capacity and C the total heat capacity. The thermal conductance is taken to be independent of frequency. Measurements of tanδ by Stokowski and Byer[6.4,6.5] and by Chiang and Butler[6.6] under various conditions of thermal coupling between detector and environment have verified the effect. A direct comparison between measured tanδ and tanδ calculated using thermal conductivity measured independently has not been reported.

Electrical Noise Degradation

The noise degradation factor is given by

$$F = \frac{i_d^2 + i_c^2 + i_a^2 + i_{R_n}^2 + i_T^2}{i_d^2} \qquad (6.39)$$

The preamplifier-related degradation can be calculated from the amplifier characteristics and can be minimized with respect to the detector capacitance and operation frequency, etc. To find the minimum F, let us consider only the JFET-related noise terms, and assume that the load resistance R_L is sufficiently large ($10^{13}\Omega$) such that its noise can be neglected. F can be written as

$$F \simeq 1 + \frac{i_a^2 + e_n^2 \left[(g_c + g_d)^2 + \omega^2 (C_d + C_a)^2\right]}{8\pi KT\, f\, C_d \tan\delta} \qquad (6.40)$$

In Figure 6.8 F is plotted as a function of detector capacitance for two state-of-the-art JFETs. One can see that for a given JFET, there exists a detector capacitance such that the noise degradation due to the preamplifier is a minimum. For example, for the siliconix JFET U423, the optimum detector capacitance is 80 pF, whereas for the siliconix JFFT 2N4867A, the optimum detector capacitance is 400 pF. Therefore, the matching of the detector capacitance to a particular JFET is an important design feature of a pyroelectric detector.

Microphonics

A pyroelectric detector uses the pyroelectric effect of the material, $\partial P/\partial T|_{\epsilon,s}$, that is, a change in detector polarization, P, due to a change in detector temperature under zero electric field and zero stress. Actually, there are two contributions to the pyroelectric effect, namely,

- The primary effect, $\partial P/\partial T|_{\epsilon,s}$, is the change of polarization as a function of temperature under zero field and stress.

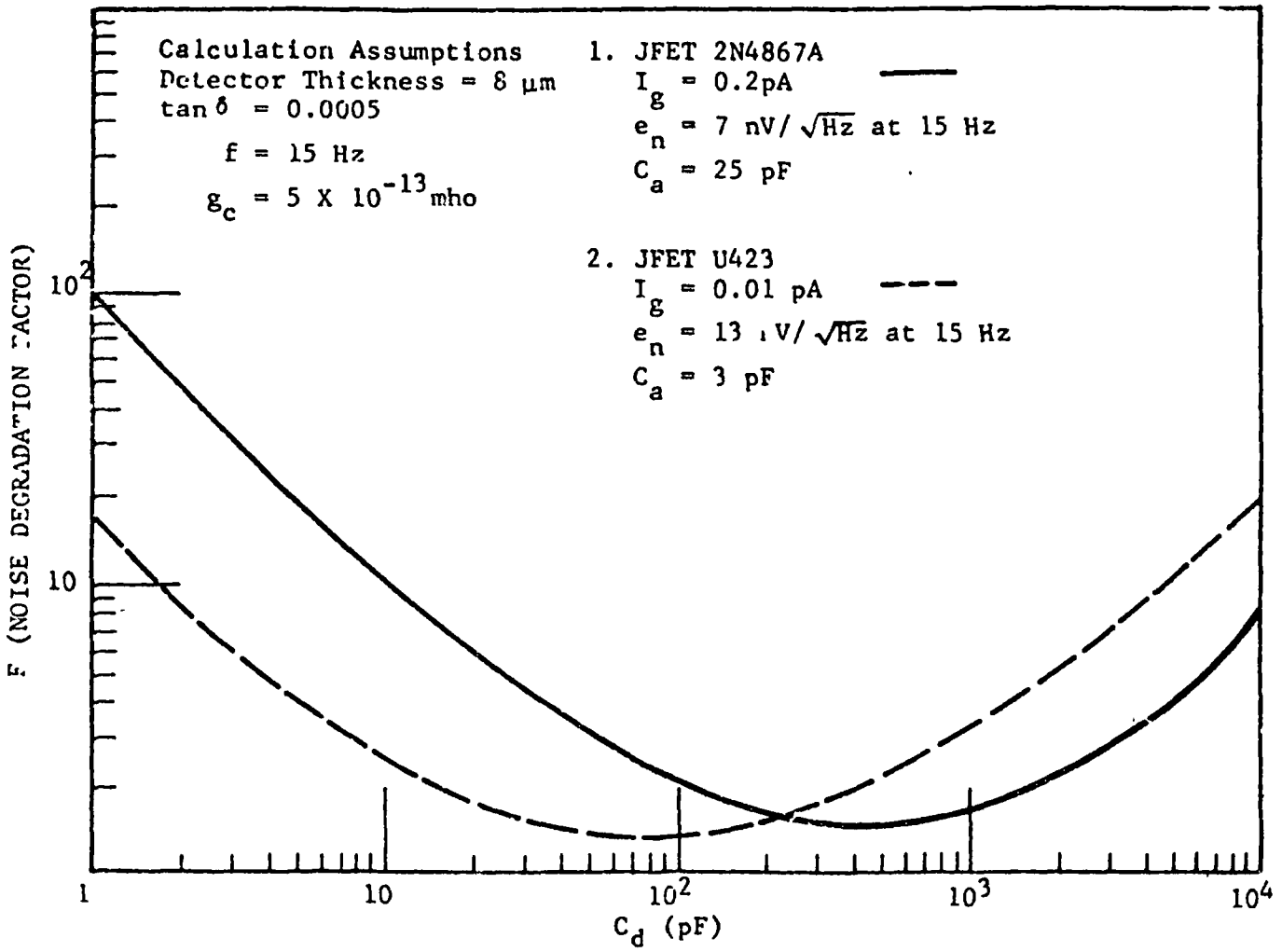

Figure 6.8 NOISE DEGRADATION FACTOR F VS DETECTOR CAPACITANCE FOR DIFFERENT JFETS

- The secondary effect is due to the piezoelectric effect, which is the stress induced polarization effect.

Piezoelectric effects and electromecnanical response are important in terms of microphonics. For high detectivity pyroelectric detector applications, it is important to choose a low piezoelectric coefficient material to minimize the secondary unwanted polarization and electromechanical effects. The design of a rigid supporting structure with minimal thermal contact is particularly important for very thin detectors.

6.2 PYROELECTRIC MATERIALS

6.2.1 Crystalline Pyroelectrics

Any crystal structure can be classified into 32 crystal classes based on the symmetries of its crystal structure. Of these 32 classes, eleven have inversion symmetry. The remaining do not have an inversion symmetry. All but one of the latter classes are piezoele tric, i.e., they exhibit an electric polarization under an applied stress. Of these, ten possess a polar axis and are spontaneously polarized along the polar axis. These classes can exhibit pyroelectricity.

In a pyroelectric material, a temperature change alters the lattice spacing of a nonsymmetrically located ion and alters the spontaneous polarization of the lattice. This change in polarization produces a surface charge. The change in surface charge is generally neutralized by stray charge in a short period of time (~minutes) in order to measure the surface charge produced by a temperature change. The incident radiation must be rapidly varying to avoid the charge neutralization.

A pyroelectric respons to changes in temperature rather than absolute temperature. The change in surface change $\Delta\sigma$ is given by

$$\Delta\sigma = \frac{\partial \vec{P}}{\partial T} \cdot \vec{n}\Big|_{\varepsilon,s} \Delta T = p\Delta T \qquad (6.41)$$

where

$\Delta\sigma$ = pyroelectric surface charge density (coul/cm^2)

$\vec{P}$ = spontaneous polarization

$\vec{n}$ = unit normal to crystal surface

p = pyroelectric coefficient (coul/cm^2 ^oC)

ΔT = temperature change

$\frac{\partial \vec{P}}{\partial T} \cdot \vec{n}\Big|_{\varepsilon,s}$ = change in polarization under zero field ε and stress s

Pyroelectricity occurs over a range of temperature up to a critical temperature, called the Curie temperature. At this temperature, a phase transition occurs. The dipoles become randomly oriented and the spontaneous polarization is lost. Upon cooling, this random orientation is sometimes "frozen in". In order to align the dipoles, the pyroelectric must be poled. Poling involves the application of a large electric field (> 20 Kv/cm) to the pyroelectric. The high field aligns the dipoles.

Curie temperatures of common crystalline pyroelectrics range from 49°C to 700°C. A material with low Curie temperature (< 100°C) poses difficulties in fabrication steps such as eletrode evaporation. Thus a pyroelectric with a high Curie temperature has a significant advantage in stability.

The important parameters for pyroelectrics are the pyroelectric coefficient p, the heat capacity, c, the density ρ, and the dielectric constant As indicated by equation 6.29, the figure-of-merit for the detectivity of a pyroelectric detector is given by

$$M = \frac{p}{c\rho\sqrt{\varepsilon}} \qquad \text{(coul-cm/Joule)} \qquad (6.42)$$

These parameters are characteristic of the pyroelectric material and are temperature dependent.

The pyroelectric coefficient, p, and the dielectric constant are strongly temperature dependent near the Curie temperature. Figure 6.9 illustrates the temperature dependence of these parameters in Strontium Barium Niobate (SBN).[6.7] Both parameters grow rapidly near the Curie temperature. For a high figure-of-merit, a SBN detector should be operated well below the Curie temperature due to the rapid decrease of ε at lower temperatures. c and ρ, on the other hand, are not very temperature dependent.

In addition to the figure-of-merit, the performance of a pyroelectric detector is influenced by the dielectric loss, which is represented by tanδ. Tanδ was believed to be functions of intrinsic material properties alone. However, very recently, it has been shown that the measured tanδ is actually composed of two contributions. The thermal contribution due to the thermal conductance and the intrinsic contribution due to material properties. Section 6.3 includes a discussion of the thermal contribution to the dielectric loss in a SBN pyroelectric detector. At present, values of the intrinsic tanδ are functions of material growth and fabrication rather than material limits. The factors causing loss are dislocations, crystallinity, surface damage, interface states, and a number of other parameters. The state-of-the-art material tanδ is on the order of 10^{-3} to 10^{-4}.* Further reduction in dielectric loss can be achieved

* The discovery of the effect of thermal conductance on measurements of tanδ may mean that the material tanδ is much better than the measurements to date have indicated.

by improvements in material development and fabrication techniques. The temperature dependence of the material tanδ for SBN is included in Figure 6.9.

In search of suitable or better materials,[6.8] a good many pyroelectric materials have been studied. Table 6.1 lists the room-temperature pyroelectric properties of some of the most well investigated crystalline materials.

6.2.2 Pyroelectric Polymers

Pyroelectricity in polymers is not well understood, since polymeric structures do not ordinarily exhibit spontaneous polarization. However, it is suspected that pyroelectricity can be imposed on polymers because of their high susceptibility to ordering by concomitant enhancement of crystallinity by orientation.

The most commonly used polymer, Polyvinylidene Fluoride (PVF_2) is a predominantly linear high polymer. The high value of n is 5000 to 10000.

It has been reported that the PVF_2 molecule (similar to many polymer molecules) has the form of a helix with a zigzag disposition, which results in a twist of 360°C about the molecule axis every arbitrary number of monomer units. The lack of ordering in the PVF_2 molecule leads to very weak pyroelectric response. However, at elevated temperatures, the carbon bonds become flexible and the molecule becomes ordered by "untwisting" along the molecule axis. Such properties are characteristic of most polymers. The most common method of preparing ordered polymer films is by drawing while still in semi-molten state. Alternatively, the polymer films can be poled. During poling, the high electric field aligns the molecule while the film cools slowly to room temperature. The resulting pyroelectric response depends on the degree of ordering imposed on the material.

Presently, the commonly used pyroelectric polymer materials are prepared by the extrusion and then stretching technique. Garn and Sharp[6.9] have made an extensive review recently of the pyroelectric properties of several polymers. Table 6.2, taken from their Table III, summarizes the room-temperature pyroelectric properties of several polymers. At present, the polymers are hampered by a weak pyroelectric coefficient, which is an order or more smaller in magnitude when compared with the better pyroelectric crystals. However, this may be largely overcome by proper poling procedures.

In terms of ease of detector fabrication, polymers enjoy an advantage over crystalline pyroelectrics such as SBN, $LiTaO_3$ and TGS. A polymer thickness of 5 micrometers is commercially available whereas a 5-micrometer thick single crystal pyroelectric detector requires considerable fabrication skill. Furthermore, polymer materials can be manufactured with a very high degree of bulk uniformity and hence, do not suffer from as many defects as crystalline pyroelectrics. This uniformity in bulk is preferred in large element thermal imaging applications.

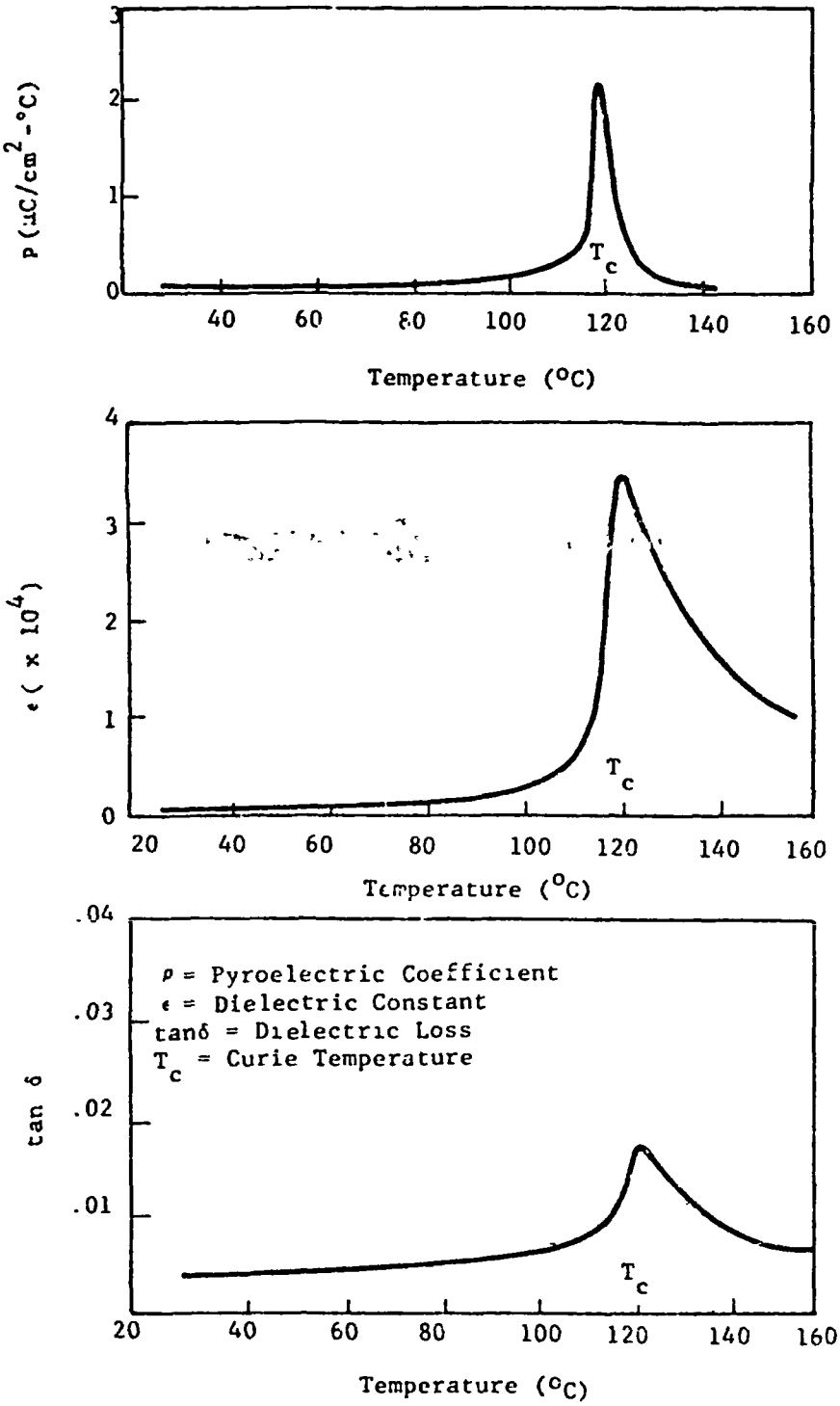

Figure 6.9 THE TEMPERATURE DEPENDENCE OF p, ε AND tanδ IN SBN (From Reference 6.7)

77-1-6

Table 6.1

ROOM TEMPERATURE PYROELECTRIC PROPERTIES OF

SEVERAL PYROELECTRIC DETECTOR MATERIALS

MATERIAL	CURIE TEMPERATURE ^{o}C	DIELECTRIC CONSTANT ϵ	PYROELECTRIC COEFFICIENT p $\frac{10^{-8}\ coul}{cm^2\ ^{o}K}$	DENSITY ρ $\frac{g}{cm^3}$	VOLUME SPECIFIC HEAT ρc $\frac{Joule}{cm^3\ ^{o}K}$	FIGURE OF MERIT $M=\frac{p}{\rho c\sqrt{\epsilon}}$ $\frac{10^{-9}\ coul\text{-}cm}{Joule}$	REFERENCE
TGS	49	35	4.0	1.66	2.5	2.7	6.8a
DTGS	61	18	2.7	1.7	2.5	2.5	6.8a
PLZT (6/80/20)	80	1010	7.6	7.8	2.6	0.9	6.8c
$Sr_{0.5}Ba_{0.5}Nb_2O_3$	121	400	6.0	5.2	2.3	1.3	6.8b
$Pb_5Ge_3O_{11}$	177	50	0.95	7.33			6.8d,e
$LiTaO_3$	618	43	1.76	7.45	3.2	0.83	6.8f,g

77-1-6

Table 6.2

ROOM TEMPERATURE PYROELECTRIC PROPERTIES OF SEVERAL POLYMERS

(Data are taken from Table III of Reference 6.9)

POLYMER	SPECIFIC HEAT CAPACITY c $\frac{\text{Joule}}{\text{g } ^{o}\text{K}}$	DENSITY ρ $\frac{\text{g}}{\text{cm}^3}$	DIELECTRIC CONSTANT ε	PYROELECTRIC COEFFICIENT p $\frac{10^{-8} \text{ coul}}{\text{cm}^2 \text{ } ^{o}\text{K}}$	FIGURE OF MERIT $M = \frac{p}{c\rho\sqrt{\varepsilon}}$ $\frac{10^{-9} \text{ coul-cm}}{\text{Joule}}$
Poly (vinyl chloride) PVC			5.33	0.01	
Poly (vinyl fluoride) PVF	1.67	1.38	5.0	0.1	0.21
Poly (vinylidene fluoride) PVF_2	1.3	1.76	11	0.3	0.40
Poly (acrylometride) PAN			7.7	0.01	

6-25

6.3 PERFORMANCE OF PRESENT PYROELECTRIC DETECTORS

In this section data on present pyroelectric detectors is presented, the data compared with theory, and the parameters limiting performance are determined. The pyroelectric detector materials commonly used for high detectivity applications are lithium tantalate ($LiTaO_3$), strontium barium niobate (SBN) and triglycine sulfate (TGS). Of these materials, we consider SBN and $LiTaO_3$, on which recent data have become available.

6.3.1 Strontium Barium Niobate Pyroelectric Detector Performance

Data on a 16-element SBN pyroelectric detector array have been reported recently [6.10]. The element size was 0.01" x 0.01" ($6.25 \times 10^{-4} cm^2$) and the average detectivity at 300°K, over the frequency range from 2 to 50 Hz, was $2 \times 10^8 cm\text{-}Hz^{\frac{1}{2}}/W$. Interelement crosstalk was less than 0.1%. Data for a single element SBN detector were also reported[6.10]; for an element size of $2.3 \times 10^{-3} cm^{-3}$, a detectivity of $9 \times 10^8 cm\text{-}Hz^{\frac{1}{2}}/W$ was achieved at 300°K at a 10 Hz modulation frequency. At 1 Hz, the detectivity was about $4 \times 10^8 cm\text{-}Hz^{\frac{1}{2}}/W$.

Efforts to improve the detectivity of SBN pyroelectric detectors are presently underway[6.6]. Figure 6.10 is a plot of detectivity, voltage responsivity and noise voltage (per root Hertz) for a SBN pyroelectric detector[6.11]. A detectivity in excess of $1 \times 10^9 cm\text{-}Hz^{\frac{1}{2}}/W$ is at a modulation frequency of 1 Hz. At 10 Hz, the detectivity is $1 \times 10^9 cm\text{-}Hz^{\frac{1}{2}}/W$. These data were taken with the detector/JFET at a temperature of 298°K.

Figure 6.11 shows data[6.11] for the same SBN detector/JFET combination at a lower temperature (273°K). A significant increase in detectivity was observed due to a decrease in noise voltage. A value for detectivity of $3.3 \times 10^9 cm\text{-}Hz^{\frac{1}{2}}/W$ at 10 Hz was achieved under these conditions.

Although the exact mechanism for the factor-of-three reduction in noise voltage is still under investigation[6.6], it is clear that the effect may have important consequences for those applications for which some minimal cooling of the detector/preamplifier package, e.g., via a one-stage thermoelectric cooler, can be used.

6.3.2 Lithium Tantalate Pyroelectric Detector Performance

Data on single-element pyroelectric detectors fabricated from lithium tantalate ($LiTaO_3$) have recently been reported by Stokowski, Byer et al.[6.4,6.5,6.12,6.13]. Detectivities (at 300°K) of $1.8 \times 10^9 cm\text{-}Hz^{\frac{1}{2}}/W$ at 10 Hz and $7.5 \times 10^8 cm\text{-}Hz^{\frac{1}{2}}/W$ at 100 Hz have been achieved in very thin (2.9 micrometers) $LiTaO_3$ detectors which are 0.97 mm in diameter.

A complementary domain structure[6.12] has recently been used in $LiTaO_3$ pyroelectric detectors to reduce the effects of microphonics; detectivities at 300°K of $1.9 \times 10^9 cm\text{-}Hz^{\frac{1}{2}}/W$ at 10 Hz were achieved in devices with active area of about 1 mm^2.

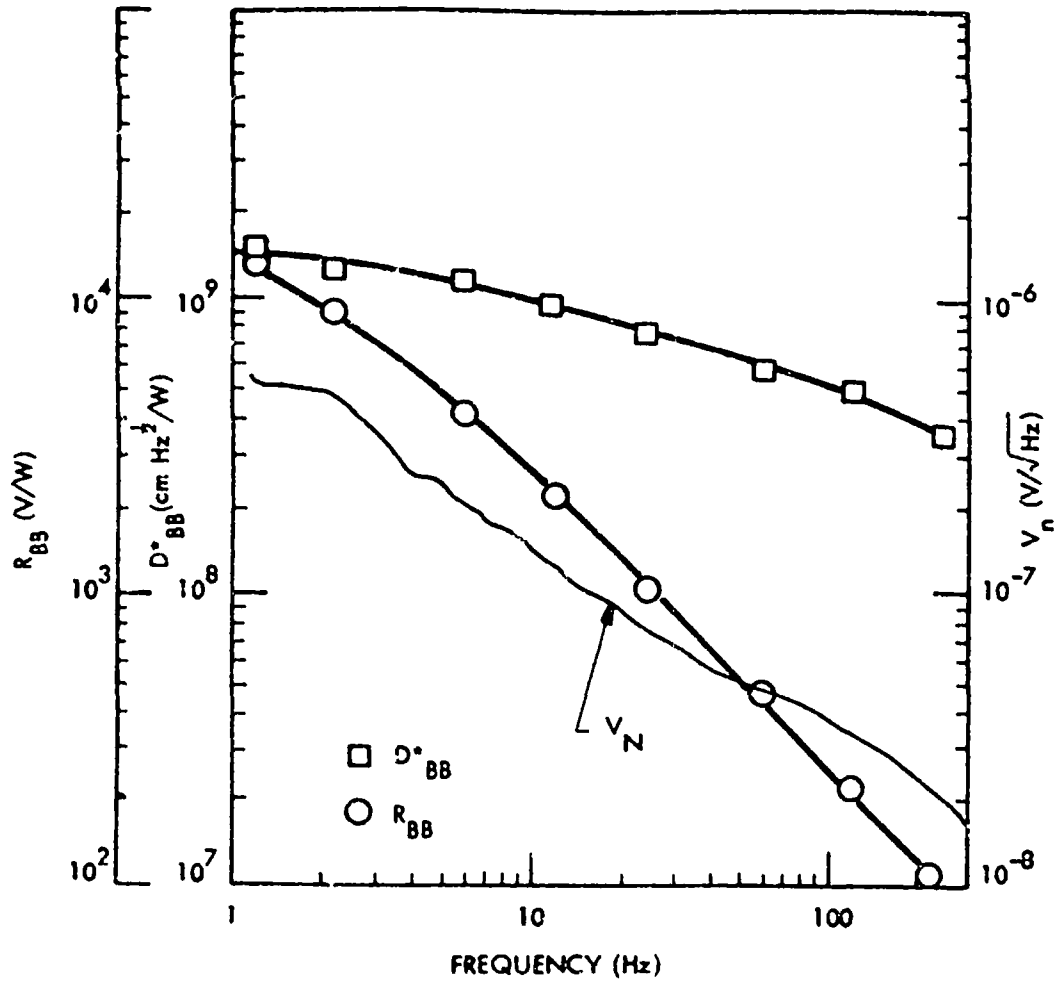

DETECTOR MATERIAL = SBN
DETECTOR ID = 061176 -3C
DETECTOR AREA = 3.7×10^{-3} cm^2
DETECTOR THICKNESS = 25 μm
DETECTOR tan δ = 0.002 at 100 Hz
TEST CONDITIONS:
DETECTOR IN VACUUM
DETECTOR TEMP = 25°C
BLACKBODY TEMP = 500°K
$H_{BB} = 9.16 \times 10^{-6}$ W/cm^2
JFET = U423
I_g < 0.1 pA
e_n = 13 nV/$\sqrt{Hz}$ at 15 Hz
C_a = 3 pF
$R_L = 5 \times 10^{11}$ ohm
D^*_{BB} = BLACKBODY DETECTIVITY
R_{BB} = BLACKBODY RESPONSIVITY
V_N = NOISE VOLTAGE

Figure 6.10 SBN PYROELECTRIC DETECTOR PERFORMANCE (From Reference 6.11)

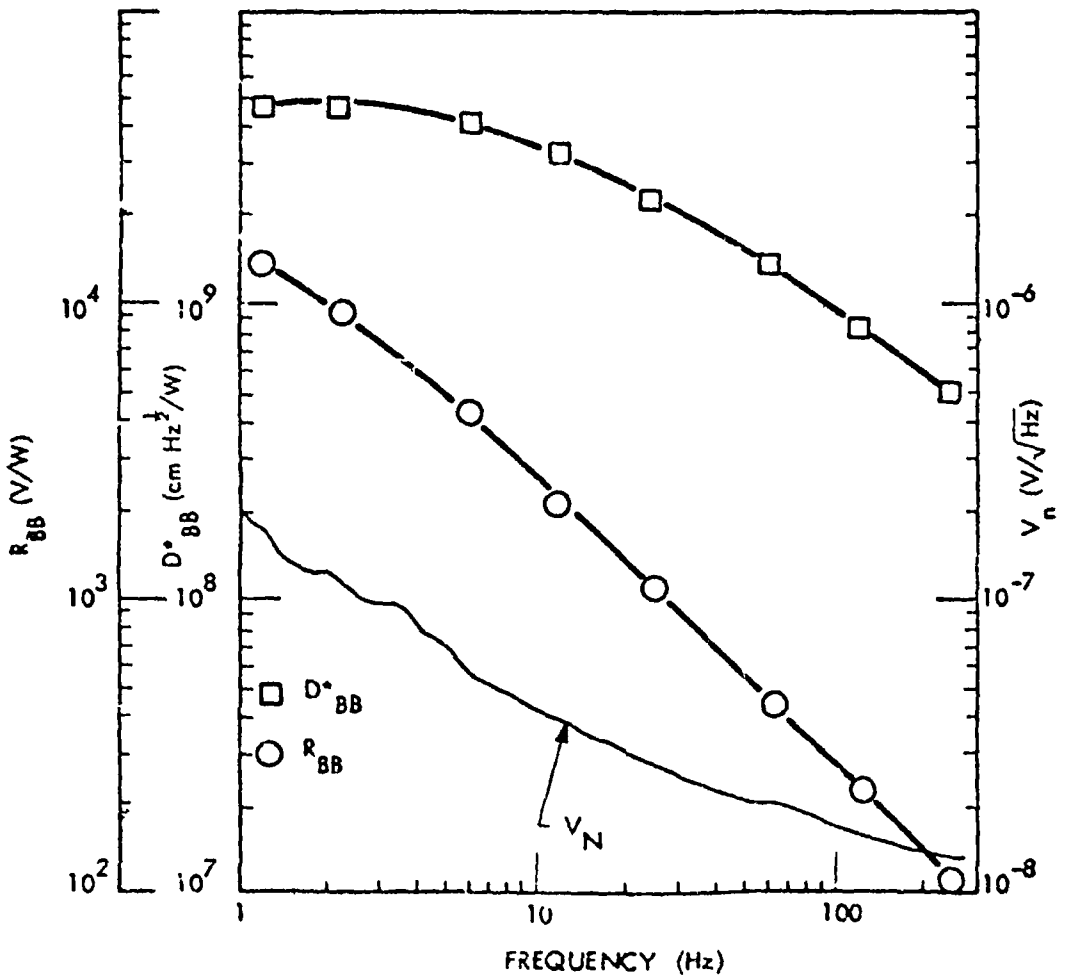

DETECTOR MATERIAL = SBN

DETECTOR ID = 061176 -3C

DETECTOR AREA = 3.7×10^{-3} cm^2

DETECTOR THICKNESS = 25 μm

DETECTOR tan δ = 0.002 at 100 Hz

TEST CONDITIONS:

- DETECTOR IN VACUUM
- DETECTOR TEMPERATURE 0°C
- BLACKBODY TEMP = 500°K
- $H_{BB} = 9.16 \times 10^{-6}$ W/cm^2
- JFET = U423
- $I_g < 0.1$ pA
- $e_n = 13$ nV/$\sqrt{Hz}$ at 15 Hz
- $C_a = 3$ pF

D^*_{BB} = BLACKBODY DETECTIVITY

R_{BB} = BLACKBODY RESPONSIVITY

V_N = NOISE VOLTAGE

Figure 6.11 SBN PYROELECTRIC DETECTOR PERFORMANCE (From Reference 6.11)

Data on arrays of $LiTaO_3$ pyroelectric detectors has recently been reported[6.14]. Detectivities of 4.7×10^8 cm-Hz$^{\frac{1}{2}}$/W at 50 Hz in elements with active area of 0.01" x 0.01" (6.25×10^{-4} cm^2) were achieved in 9-element staggered-linear arrays, interelement crosstalk was about 2% at 50 Hz. At 10 Hz, detectivities of about 1.1×10^9 cm-Hz$^{\frac{1}{2}}$/W were reported, with an increased interelement crosstalk at 10 Hz of about 12%.

6.4 IMPROVED PERFORMANCE OF PYROELECTRIC DETECTORS

In this section we discuss the ultimate feasibility of pyroelectric detectors approaching the thermal fluctuation sensitivity limit ($D^* = 1.8 \times 10^{10}$ cm Hz$^{\frac{1}{2}}$/W) at frequencies in the range from 1-10 Hz. We will show that such detectors must necessarily be very thin (on the order of 1 micrometer), and must be essentially self-supporting. Associated problems in the area of matched low noise amplifiers, low-loss black coatings, mechanical strength and stability, microphonics, and electrical contacts will be discussed.

Figure 6.12 shows calculated detectivities for pyroelectric detectors using the theory of the previous sections, and material properties of SBN (strontium barium niobate). The curves in Figure 6.12 are plots of Equation 6.8 for the following SBN material parameters:

$$c\rho = 2.3 \text{ joule cm}^{-3}\ ^{o}K^{-1}$$

$$p = 6 \times 10^{-8} \text{ coul cm}^{-2}\ ^{o}K^{-1}$$

$$\varepsilon = 3.5 \times 10^{-11} \text{ Farad cm}^{-1}$$

The dissipation factor $\tan\delta$ for SBN ranges form 1×10^{-4} in bulk samples to 3×10^{-3} in state-of-the-art detectors. The ordinate in Figure 6.12 is $d\omega/2\pi$, since in the theory d and ω always appear only in the product $d\omega$. This shows that the basic way to obtain response to higher frequencies for a given material is to fabricate thinner detectors. The present state-of-the-art data at 300°K for single element SBN detectors, taken from Figure 6.10, is also shown in Figure 6.12. This point corresponds to a measured D^* of 9×10^8 cm Hz$^{\frac{1}{2}}$/W at 10 Hz for a detector with d = 20 μm, and an estimated g for 3×10^{-2} W cm^{-2} °K.

Consideration of equation 6.28 shows that the requirements for high D^* are a material with high value of $p/c\rho\varepsilon^{\frac{1}{2}}$, material and processing which give a low value of $\tan\delta$, and a low value of g. Since $\omega_o = g/c\rho d$, high frequency operation requires a material with small value of $c\rho$, and a detector with a small value of d. Note that increasing g, although it increases ω_o, does not increase D^* at any frequency; therefore, g must remain as small as practical. Each of these conditions will now be considered.

Table 6.1 lists values of $p/c\rho\varepsilon^{\frac{1}{2}}$ for some typical pyroelectric materials. TGS, the material with the highest reported value for this figure-of-merit, has the undesirable properties of a relatively low Curie temperature and of being hygroscopic, so other materials are often used. In addition, there are some theoretical considerations[6.8] which suggest that $p/\varepsilon^{\frac{1}{2}}$ is constant so a considerably improved material is not anticipated. Therefore, the prospects of improving D^* by finding a better material do not look good.

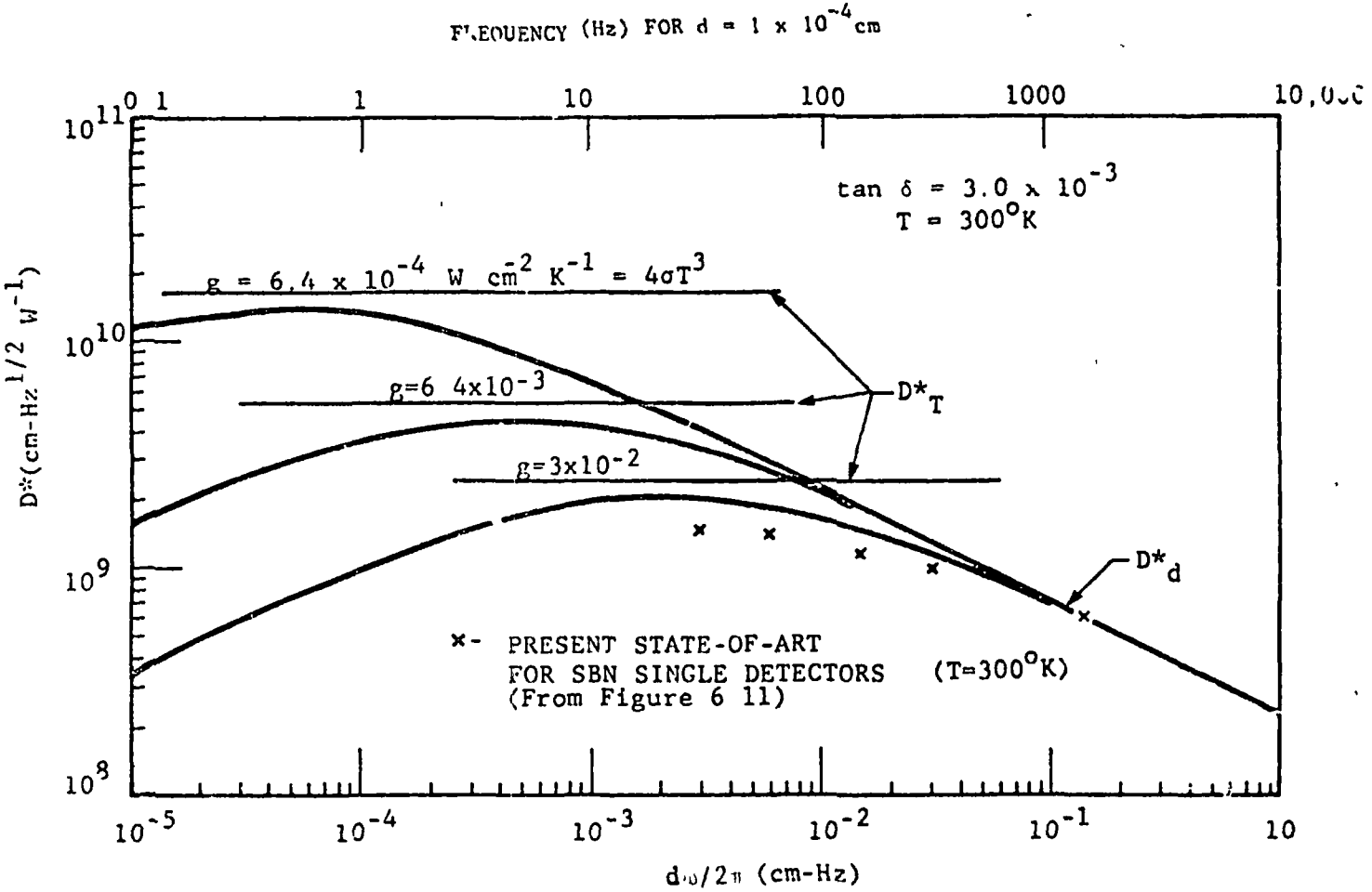

Figure 6.12 CALCULATED DETECTOR-LIMITED DETECTIVITY D^*_d FROM EQ. 6.28 (CURVES) AND CALCULATED THERMAL FLUCTUATION LIMITED DETECTIVITY D^*_T FROM EQ. 6 27 (HORIZONTAL LINES) FOR SBN PYROELECTRIC DETECTORS PLOTTED FOR VARIOUS VALUES OF THERMAL CONDUCTANCE g VERSUS THE PRODUCT OF DETECTOR THICKNESS d AND MODULATION FREQUENCY $\omega/2\pi$. DATA FOR SBN AT 300°K IS TAKEN FROM FIGURE 6.11 (REFERENCE 6.10).

There is no known lower limit to the value of tanδ for materials, so this might appear to be a promising way to improve D*. Notice, however, that the noise power from the detector is given by 4 KT tanδ. The best available preamplifiers produce a noise equivalent to about (KT)/2500. It can be shown that this noise is equivalent to a detector tanδ of 2×10^{-4}; thus the amplifier noise, rather than the detector noise, will dominate if the detector tanδ is less than 2×10^{-4}. In addition, the amplifier and detector must be carefully matched in order to obtain noise this small. Thus, increasing D* by reducing tanδ requires a very good amplifier. Therefore, increasing D* by reducing tanδ is not practical.

Reducing the thermal conductivity g results in increasing D* by increasing the thermal responsivity and also by reducing the statistical temperature fluctuations of the detector, as can be seen from Figure 6.12. A g value of less than about 5×10^{-3} W cm^{-2} K^{-1} is very difficult to obtain in practice, however. This topic will be discussed in more detail later.

The state-of-the-art pyroelectric detectors show a D* in the range of $0.5 - 2 \times 10^{9}$ cm Hz$^{1/2}$/W [illegible] with maximum response near 1 Hz. The only way to obtain a higher D* is to reduce g and reduce the detector thickness d. For example, if $g = 6.4 \times 10^{-3}$ W cm^{-2} K^{-1} and $d = 1 \times 10^{-4}$ cm, the detectivity is close to 4×10^{9} cm Hz$^{1/2}$/W from 1 Hz to 10 Hz. Thus, with the available materials, high D* in the 1 Hz to 10 Hz range requires detector thickness of the order of 1×10^{-4} cm with g values of 6×10^{-3} and less and a dielectric loss of 3×10^{-3}.

The ideal thermal detector, which was assumed for the theoretical portion, absorbs all incident electromagnetic radiation. Actual detectors, of course, will not absorb all the radiation. In particular, the intrinsic absorption of most pyroelectric materials is confined to a few bands in the infrared particularly for very thin samples. Therefore, a practical detector must have a "black" coating which actually absorbs the incident radiation and then transfers the heat to the detector itself. The thermal capacity of the black coating degrades the detector performance, so it must be kept small compared to the thermal capacity of the detector itself. For a thin detector then, a very thin black coating is required. Historically, a great deal of effort has been expended in developing a good, low thermal capacity black coating. There are several commonly used types: the blacks formed from a metal which is evaporated or electroplated at a rate too high to form a continuous film, pigment type blacks formed of, for example, a combination of graphite and silicates, and the blacks which absorb radiation by virtue of their surface resistivity. For a pyroelectric detector, if the black is conductive, it can also serve as the detector electrode, thus simplifying the fabrication. Also, the surface resistivity type of black is potentially the thinnest, with reported thicknesses of 250 Å and less. Therefore, it would appear that this type of black is the most promising for very thin pyroelectric detectors.

Perhaps the most difficult problem to solve is the thermal losses to the supporting structure. The theory allows for this in terms of a value for p, but this is only an approximation. More exact calculations[5,6] have been done for realistic structures; the results show that thinner structures have little, if any, advantage over thicker ones due to the thermal effect of the substrate. There does not appear to exist any material which is suitable as a substrate for high performance, thin detectors. The only solution appears

to be to support the detector by its edges. Since the detector must necessarily be very thin, the heat loss through the edges will be smaller than for a thicker detector. If the detector active area is defined by a combination black and electrode, the surrounding uncoated (but thin) detector material should serve as a reasonably good support with thermal isolation. The exact theory predicts that the degree of isolation will be a function of frequency, with the isolation being better at high frequencies. The exact characteristics will depend, of course, on the specific pyroelectric material selected.

While it is relatively simple to prepare thin films on a substrate, self-supporting thin films are much more difficult to fabricate. This is anticipated to be the most critical area in the fabrication of extended performance pyroelectric detectors. It is not known whether the various candidate materials have the required strength to form self-supporting structures of the required thickness. Also, all pyroelectric materials are also piezoelectric, which means that mechanical vibration will be transformed into an electrical signal. Clearly, the very thin self-supporting structures will be more susceptible to vibration than thicker structures; much more work, both theoretical and experimental, is needed to determine if this effect will be significant.

Heat conduction through the electrical leads may be a significant effect; pyroelectric detectors have an inherent advantage in this area, since they can tolerate a higher lead resistance than other types of thermal detectors. Electrical and thermal resistances tend to be proportional for conductors, so that a high thermal resistance in the leads implies a high electrical resistance as well. Heat conduction through the leads needs to be considered in actual device design, but it is expected that this effect can be minimized by careful design.

6.5 REFERENCES

6.1 E. H. Putley, Semiconductors and Semimetals, Vol. 5, Academic Press (1975); see also the review paper by S. T. Liu and D. Long, "Pyroelectric Detectors and Materials," Proc. IEEE, Jan. 1978 (to be published).

6.2 A. van der Ziel and S. T. Liu, Physica 61, 589 (1972).

6.3 R. C. Jones, Advanced Electronics 5, 1-96 (1953).

6.4 S. E. Stokowski, "Temperature Noise and Dielectric Loss in Pyroelectric Detectors." App. Phys. Letters 29, 393 (1976).

6.5 S. E. Stokowski and N. E. Byer, "Temperature Noise-Limited Pyroelectric Detectors," Technical Digest of the IEDM, Washington, D.C., 1976, p. 555.

6.6 Work being performed at the Honeywell Electro-Optics Center under NASA Langley Research Center Contract NAS1-14372.

6.7 S. T. Liu, "Critical Assessment of Pyroelectric Detectors," Ferroelectrics 10, 83 (1976)

6.8 S. T Liu, J. J. Zook and D. Long, "Relationships Between Pyroelectric and Ferroelectric Parameters," Ferroelectrics 9, 39 (1975)

6.8a H. P. Beerman, "Investigation of Pyroelectric Material Characteristics for Improved Infrared Detector Performance," Infrared Physics 15, 225 (1975).

6.8b R. B. Maciolek and S. T. Liu, "Preparations and Properties of Low Loss $Sr_{1-x}Ba_xNb_2O_6$ Ferroelectric Single Crystals," Jour. Electronic Materials 2, 191 (1973).

6.8c S. T. Liu and I. Kyonka, "Further Study of the Pyroelectric Properties of Lanthanum - Modified PZT Ferroelectric Ceramics," Ferroelectrics 7, 167 (1974).

6.8d T. Yamada et al, J. App. Phys. 43, 771 (1972); also J. App. Phys. 43, 4907 (1972).

6.8e G. R. Jones, N. Shaw and A. W. Vere, "Pyroelectric Device Using Lead Germanate," U.S. Patent 3,831,029, Aug. 20, 1974.

6.8f A. M. Glass, "Dielectric, Thermal and Pyroelectric Properties of Ferroelectric $LiTaO_3$," Phys. Rev. 172, 564 (1968).

6.8g C. B. Roundy and R. L. Byer, "Sensitive $LiTaO_3$ Pyroelectric Detectors," J. App. Phys. 44, 929 (1973).

6.9 L. L. Garn and E. J. Sharp, "Pyroelectric Vidicon Target Materials," IEEE Transactions on Parts, Hybrids and Packaging, Vol. PHP-10, 208 (1974).

6.10 A. M. Chiang, "High Performance SBN Pyroelectric Detector Arrays," Proc. IRIS Detector Specialty Group Meeting, March, 1976, Vol. 1, p. 399.

6.11 "Improved Detectivity of Pyroelectric Detectors," Quarterly Technical Progress Report for the period of July 11, 1976 - October 10, 1976, NASA Langley Research Center Contract NASI-14372.

6.12 N. E. Byer and S. F. Stokowski, "High Performance Pyroelectric Detectors," Proc. 1976 IRIS Detector Specialty Group Meeting, pp 121-133 (U); see also N. E. Byer, S. E. Stokowski and J. D. Venables, Appl. Phys. Letters 27, 639 (1975).

6.13 S. E. Stokowski, J. D. Venables, N. E. Byer and T. C. Ensign, "Ion-Beam Milled, High Detectivity Pyroelectric Detectors," Infrared Physics 16, 331 (1976).

6.14 S. E. Stokowski, "Performance Characteristics of Monolithic Pyroelectric Arrays," Proc. 1976 IRIS Detector Specialty Group Meeting, pp. 135-144 (U).

SECTION 7

CONCLUSIONS AND RECOMMENDATIONS

The objective of this study was to define the most promising technical approach for the advance of development of 8-12 micrometer detector operating at elevated temperatures. In achieving this objective three tasks were undertaken:

1. Determine the theoretical limits to performance of both thermal and quantum detectors for 8-12 micrometer infrared detection.
2. Identify candidate detector materials and determine material parameters
3. Determine the present status of both quantum and thermal detectors, isolate the parameters limiting performance, and assess the feasibility of achieving performance at the theoretical limit.

In this section the conclusion reached in these three tasks will be summarized and recommendations made for further development.

7.1 THEORETICAL LIMITS: QUANTUM DETECTORS

The limits to detectivity for both photovoltaic and photoconductive detectors were examined in Section 2.

7.1.1 Photovoltaic Detectors

The detector - limited D* for a photodiode at zero bias was found to reduce to

$$D^*_\lambda = \frac{\eta\lambda}{2hc}\sqrt{\frac{A}{g_{th}}} \qquad (7.1)$$

where g_{th} is the thermal generation rate of minority carriers in the volume of semiconductor defined by the device area and the depth below the junction from which minority carriers are collected.

The analysis does not consider other noise mechanisms which are not fundamental limitations. These include depletion layer generation-recombination noise, surface generation-recombination noise, and 1/f noise. In addition, tunneling current was not included as tunneling is unlikely to limit device performance at elevated temperatures.

In traditional p-n junctions, minority carriers are collected from a diffusion length ($L_e = \sqrt{k\,T_\mu\,\tau_e}$) below the junction. The diffusion length may be as long as 100 μm. However, 25% of the signal is collected from a depth below the semiconductor surface given by 2.0/α where α is the absorption coefficient.

For a direct-gap semiconductor, the signal is absorbed within about 10 μm of the semiconductor surface. Thus, the conventional p-n junction design can collect noise from a much larger volume of semiconductor (given by AL_c) than is needed to collect noise. An improved design developed on this program was the electrically reflecting backside contact. In this design the active volume of semiconductor is only as thick as needed to collect signal. The active area is defined by a more heavily doped contact which acts as an electrically reflecting barrier to minority carriers.

The critical factor in determining the limit to detectivity is to determine the theoretical limit for the thermal generation rate g_{th}. There are two fundamental processes which are responsible for thermal generation and recombination of carriers. One is radiative recombination, in which an electron and a hole recombine with emission of a photon. This is the inverse of the process responsible for generation of signal, in which an incoming photon is absorbed and an electron-hole pair created. Thus, choosing a semiconductor with a low radiative recombination rate does not improve detectivity, since both the signal and noise are generated by the same process. Radiative recombination thus defines the fundamental limit to detectivity in quantum detectors.

The second fundamental process responsible for thermal generation and recombination of carriers is Auger recombination.* In Auger recombination two electrons collide, one is excited higher into the conduction band, the other recombines by falling into the valence band. As the Auger process contributes only to thermal generation of noise and does not enter the signal generation process, one would want to choose the semiconductor which has the lowest Auger generation - recombination rate. The Auger recombination rate is quite sensitive to the exact shape of the semiconductor band structure and will be an important parameter in choosing the optimum band structure. The thermal generation rate is given by

$$g_{th} = A\,t(R_r + R_A) \tag{7.2}$$

where R_r is the radiative recombination rate and R_A is the Auger recombination rate. If a semiconductor is chosen which has low Auger recombination, then the limit to detectivity becomes (Equation 3.5).

$$D^*_\lambda = \frac{0.32\,\lambda}{hc}\sqrt{\frac{\alpha}{k_r}} \tag{7.3}$$

The radiative recombination rate R_r may be expressed in terms of the optical absorption coefficient α independent of band structure. If this expression for R_r is used in the expression for detectivity, the theoretical limit to detectivity for a p-n photodiode (with electrically reflecting backside contact)

* Schockley-Read recombination is often observed in real semiconductors; in this process recombination proceeds via a flaw or impurity state. However, this is not a fundamental limit.

becomes* (from Equation 3.21):

$$D^*_\lambda = \frac{0.32\,\lambda}{E_g\, n_1}\sqrt{\frac{h}{8\pi\, kT}}\ \exp\,(E_g/2kT) \qquad (7.4)$$

where

E_g = energy gap
n_1 = semiconductor index of refraction
λ = wavelength
k = Boltzmann's constant
h = Planck's constant
T = temperature

Thus, the theoretical limit to detectivity for quantum detectors has been reduced to an expression which depends only on the cutoff wavelength desired, the temperature and the index of refraction of the semiconductor. It is independent of band structure and so is independent of all the normal material and device design parameters such as intrinsic carrier concentration, mobility, dopant levels, etc. Semiconductor band structure and related material parameters enter only in factors which reduce D* below its theoretical limit, such as Auger recombiration, Figure 7.1 shows the limit to detectivity as a function of temperature for p-n photodiodes. An index of refraction of 4 was assumed.

7.1.2 Photoconductive Detectors

The expressions for signal and noise on photoconductive detectors were developed in Section 2.4. The detectivity of a photoconductor in general is given by

$$D^*_\lambda = \frac{\eta\lambda}{2hc\sqrt{g_{th/A} + kT/q^2G^2RA}} \qquad (7.5)$$

where g_{th} is the thermal generation rate, R is the resistance of the photoconductor and G is the photoconductive gain. If sufficiently high gain can be obtained, either by high bias fields or high mobility ratio, then the limiting detectivity for a photoconductor reduces to the same as for a photodiode:

$$D^*_\lambda = \frac{\eta\lambda}{2hc}\sqrt{A/g_{th}} \qquad (7.6)$$

---

* If the values of the fundamental constants are used and if λ_c is the cutoff wavelength eqn 7.3 becomes

$$D^*_\lambda = \frac{2.2 \times 10^8\ \lambda_c^{\,2}}{n_i\sqrt{T}}\ \exp\,(7.21 \times 10^3/\lambda_c\, T) \qquad (7.7)$$

where λ_c is in micrometers and T in degrees Kelvin.

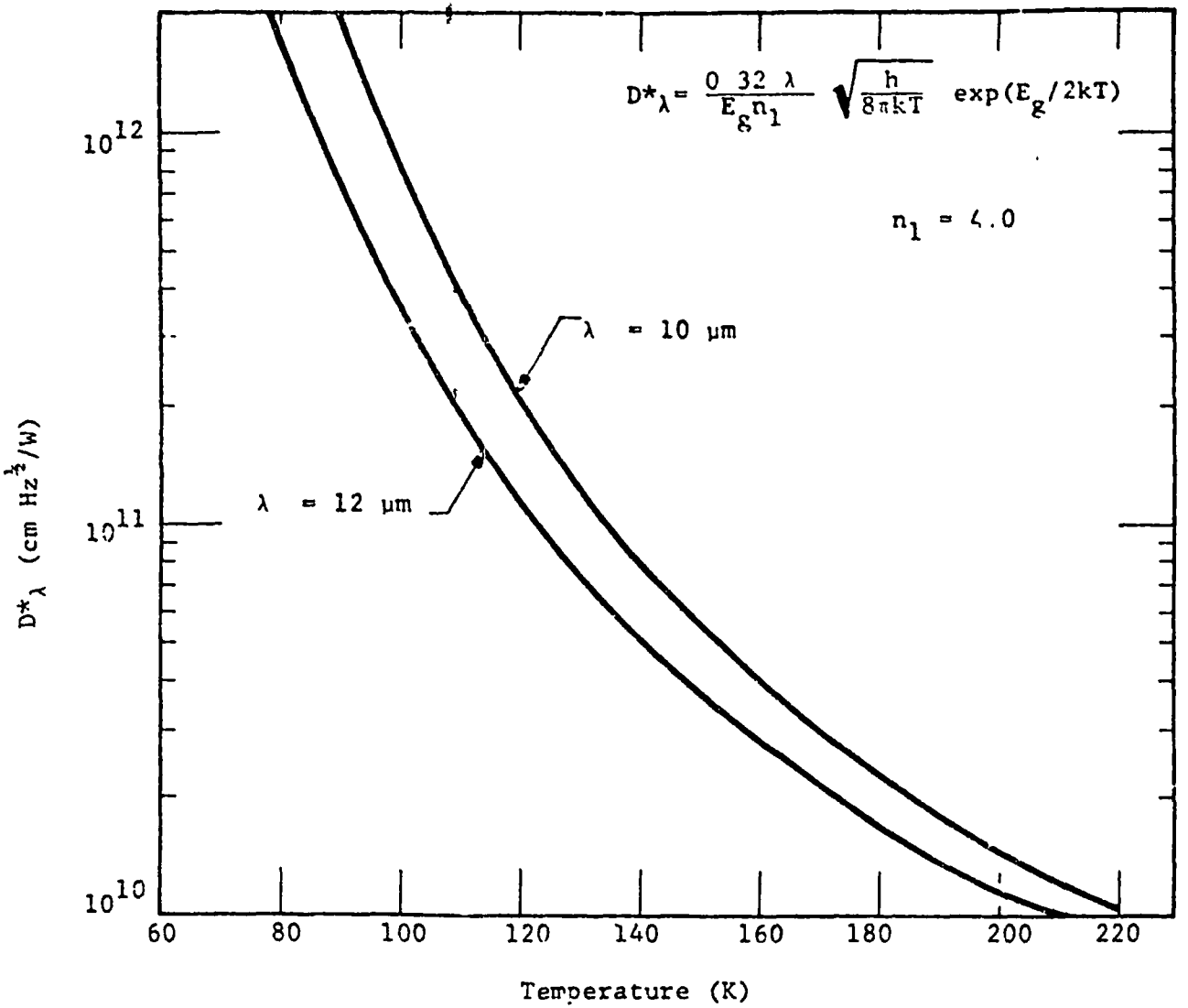

Figure 7.1 THEORETICAL LIMIT TO DETECTIVITY VS TEMPERATURE FOR AN IDEAL QUANTUM DETECTOR WITH AN INDEX OF REFRACTION OF 4.

As for a photodiode, the ultimate limit to the thermal generation rate g_{th} is radiative recombination. To achieve this limit one must choose the semiconductor material and the device design such that (a) radiative recombination dominates Auger recombination and (b) the gain and device resistance are sufficiently high that Johnson noise is lower than generation-recombination noise.

In summary both photodiodes and photoconductors have the same ultimate theoretical limit to detectivity, given by eqn 7.3. For photodiodes to reach this limit, an electrically reflecting back-side contact must be used and the choice of semiconductor material and device design must be such that radiative recombination rather than Auger recombination dominates. For photoconductors to reach this limit the semiconductor material and device design must be such that Johnson noise does not limit device performance and that radiative rather than Auger recombination dominates. In addition, the photoconductor thickness must be reduced to the thickness needed to collect signal.

7 2 MATERIALS FOR QUANTUM DETECTORS

The fundamental conclusion reached in the analysis of signal and noise in quantum detectors was that the ultimate limit to detectivity in a quantum detector (eqn 7.4) depended only on the wavelength, temperature and material index of refraction n. This ultimate limit could be met only if radiative, rather than Auger, recombination was the dominant recombination process. Thus, in evaluating semiconductor material classes for fundamental potential to achieve the theoretical limit to D*, the following criteria should be used

(a) Auger recombination should be weak or negligible relative to radiative recombination
(b) If (a) is satisfied then the material should have the lowest possible index of refraction

The two types of semiconductor materials discovered to date with bandgaps suitable for 8-14 μm detectors are those with a direct bandgap at the zone center and those with a direct gap near the zone edge. (Hg,Cd)Te and related compounds fall into the first class. They are characterized by a conduction band with a low density of states and a valence band with a high density of states. (Pb,Sn)Te and related compounds fall into the second class. They are characterized by ellipsoidal conduction and valence bands which are mirror images of each other.

The two classes have been investigated with regard to the Auger recombination rate. The shortest Auger lifetimes occur in n-type (Hg,Cd)Te or related compounds. This is due to the very low electron effective mass. However, it was discovered in the course of the program that if n-type (Hg,Cd)Te is made degenerate by doping at high levels the Auger recombination mechanism is considerably reduced in strength. While degenerate n-type (Hg,Cd)Te is unsuitable in itself for an active infrared detector due to the Burstein shift, the n-side of a p-n junction can be made degenerate to reduce the n-side diffusion current.

The Auger lifetime in p-type (Hg,Cd)Te was analyzed in detail for the first time on this program. Due to the assymetry of the valence bands in (Hg,Cd)Te the Auger lifetimes are considerably different in n-type and in p-type (Hg,Cd)Te. In lightly doped p-type electron-electron collisions were found to dominate while in very heavily doped p-type hole-hole collisions dominate. In both cases the Auger lifetime is considerably longer than in comparably doped n-type. Auger recombination is weaker than radiative recombination in moderately doped p-type (Hg,Cd)Te at temperatures below 150K; thus, it is possible to achieve detectivities at the theoretical limit for quantum detectors. To achieve radiatively limited lifetimes above 150K it is necessary to use higher dopant concentrations ($N_A = 1.0 \times 10^{18}$ cm^{-3}).

Auger recombination in (Pb,Sn)Te has been investigated by Emtage. Emtage found that the Auger mechanism on (Pb,Sn)Te was strong due to a high longitudinal-to-transverse effective mass ratio (m_l/m_t) in both the conduction and valence bands. As the (Pb,Sn)Te conduction and valence bands are equivalent, n- and p-type (Pb,Sn)Te have the same recombination times of equivalent dopings and temperatures. Calculations based on Emtage's expressions have indicated that moderately doped ($N_A > 1.0 \times 10^{16}$ cm^{-3}) (Pb,Sn)Te is limited by Auger recombination at temperatures above 80K, and thus could not achieve the theoretical limit for quantum detectors at elevated temperatures. Semiconducting compounds related to (Pb,Sn)Te but with a lower effective mass ratio (m_l/m_t) may be more promising for elevated temperature operation.

The third type of band structure common among semiconductors is an indirect gap. Examples of this type of band structure are silicon and germanium; no narrow band-gap (0.1 eV) examples of this band structure are known. However, it is possible to conclude that this type of band structure is unlikely to achieve the theoretical limit to detectivity. Due to the indirect gap, the radiative transition is weak. Thus optical absorption coefficients would be low and radiative lifetimes would be long. The chance of this type of semiconductor achieving

radiative-limited lifetimes would be poor since very long Shockley-Read lifetimes would be necessary for the radiative lifetime to be shorter than the Shockley-Read lifetime. Thus, even if a narrow band gap semiconductor existed with an indirect gap, it would be difficult to achieve performance at the theoretical limit.

In summary, the most important criteria for evaluating the potential of various semiconductors for achieving detectivity at the theoretical limit for a quantum detector is that Auger recombination be weaker than radiative recombination. Three basic types of band structure have been evaluated, with examples of two of the three evaluated in detail. For (Pb,Sn)Te and related semiconductors Auger recombination is dominant above 80K. If a semiconductor were found with band structure similar to (Pb,Sn)Te but less ellipsoidal conduction and valence bands, then Auger recombination would be weakened. For (Hg,Cd)Te and related semiconductors Auger recombination is dominant in non-degenerate n-type and lightly doped p-type (Hg,Cd)Te. In heavily doped p-type ($N_A \sim 1.0 \times 10^{18}$ cm^{-3}) radiative recombination is dominant up to 190K. Thus, p-type (Hg,Cd)Te or related appears to be the best candidate on a theoretical basis for achieving the theoretical limit to D* for elevated temperature operation.

7.3 PRESENT STATUS AND ULTIMATE LIMITS: PHOTOVOLTAIC DETECTORS

The status of present 8-14μm photovoltaic detectors was analyzed in an effort to determine the factors limiting performance. Two materials have dominated the field: (Hg,Cd)Te and (Pb,Sn)Te. As the analysis of Section 3 indicated, these materials are representatives of two different types of band structures; new materials with fundamentally different band structures are unlikely.

Of the two materials (Pb,Sn)Te has seen the most development for photodiodes. Data on present (Pb,Sn)Te photodiodes was analyzed to determine the limiting parameters. It was found that the best (Pb,Sn)Te photodiodes are limited by diffusion current for temperatures above 80K. The data was fit by using the Auger-limited lifetime for (Pb,Sn)Te. Thus, present (Pb,Sn)Te p-n junctions appear to achieve Auger-limited performance. Further improvements could come only from development of the electrically reflecting backside contact. Present (Pb,Sn)Te diodes prepared by liquid phase epitaxy on PbTe substrates effectively incorporate this structure as the (Pb,Sn)Te layers are approximately 10μm thick. No elevated temperature data on these devices has been published. The advantage gained from the reflecting contact is a factor of 2 in detectivity at elevated temperatures Figure 7.2 shows the R_oA calculated as a function of temperature for a constant 12μm cutoff assuming an Auger-limited lifetime. Figure 7.2 also shows the R_oA obtainable with an electrically reflecting backside contact.

To summarize, the present performance of (Pb,Sn)Te photodiodes at elevated temperatures is limited below the theoretical maximum for a quantum detector by a short Auger lifetime The short Auger lifetime is a consequence of the band structure of the material. Data on the best (Pb,Sn)Te photodiodes has been modeled.

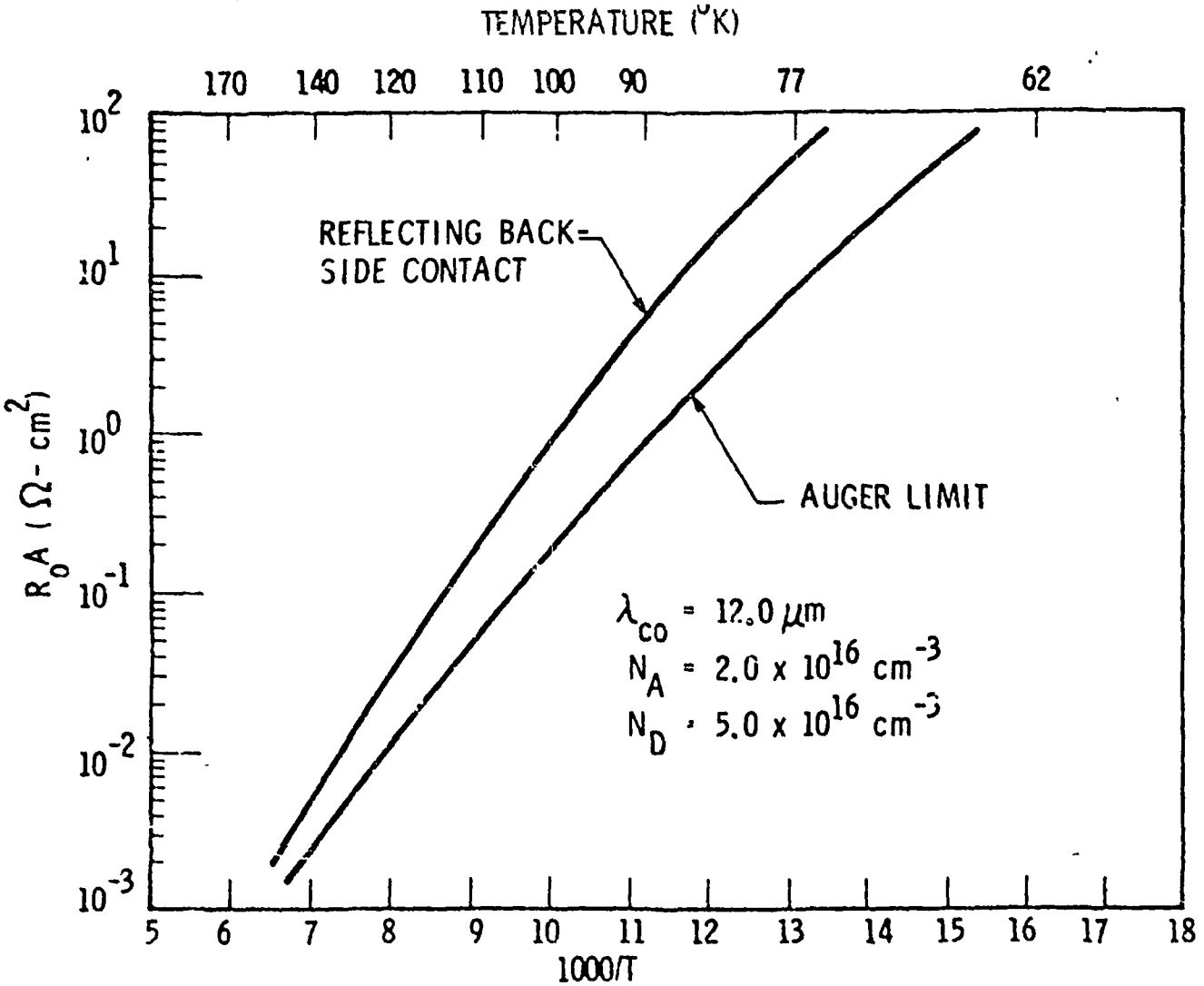

Figure 7.2 R_oA VS TEMPERATURE: (Pb,Sn)Te

Data on ordinary p-n junctions can be fit using lifetimes near the Auger limit; similarly, data on homojunctions formed on thin (Pb,Sn)Te epitaxial layers (on PbTe) can be fit assuming Auger-limited lifetimes and diffusion lengths limited by the thickness of the epitaxial layer. Thus, substantial improvement in the performance of (Pb,Sn)Te photodiodes at moderate and elevated temperatures appear unlikely.

8-14 μm (Hg,Cd)Te photodiodes have been developed primarily for wide bandwidth applications where low capacitance is required. The device structure developed for this application is a lightly doped n-layer on a moderately doped p-type wafer (n- on p). Data from n- on p (Hg,Cd)Te photodiodes has been analyzed. At low (T<110K) temperatures n- on p (Hg,Cd)Te photodiodes are limited by generation-recombination current, with an effective depletion-layer lifetime of 30 ns. At elevated temperatures, the diodes were limited by diffusion current with p-side lifetimes of 30 ns.

For (Hg,Cd)Te a n+ on p device design is superior to the n- on p for high detectivity applications for two reasons. First, the use of high n-side carrier concentrations reduces the width of the depletion layer and hence reduces depletion layer g-r current. Secondly, use of high n-side carrier concentrations makes the n-side degenerate, which was found to greatly reduce thermal generation by Auger processes. This, in turn, limits diffusion current from the n-side

The best device design for (Hg,Cd)Te for elevated temperature operation is n+ on p. Figure 7.3 shows R_oA as a function of temperature calculated for a constant 12-μm cutoff wavelength. The lowest curve corresponds to lifetimes currently measured in p-type (Hg,Cd)Te. The factor limiting R_oA is the p-side lifetime τ_c. The p-side lifetimes presently observed are considerably shorter than the radiative limit and is apparently due to a Shockley-Read center. If the lifetime can be improved to the radiative limit, then considerably improved R_oA can be achieved. This is also shown in Figure 7.3. Finally, if lifetimes near the radiative limit can be obtained, then the electron diffusion length on the p-side is quite long and use of the reflecting back-side contact can considerably improve R_oA. This is also shown in Figure 7.3.

At temperatures above 170K, electron-electron Auger recombination becomes significant in p-type (Hg,Cd)Te. Use of more heavily doped p-type wafers ($N_A \sim 1.0 \times 10^{18}$ cm^{-3}) would make radiative recombination dominant to ~190K. Thus, the optimum device design for (Hg,Cd)Te photodiodes for operation above 170K is a n+ -p+ design. If radiatively-limited lifetimes can be obtained in p-type (Hg,Cd)Te, then (Hg,Cd)Te photodiodes could achieve the theoretical limit to detectivity for quantum detectors (Figure 7.1).

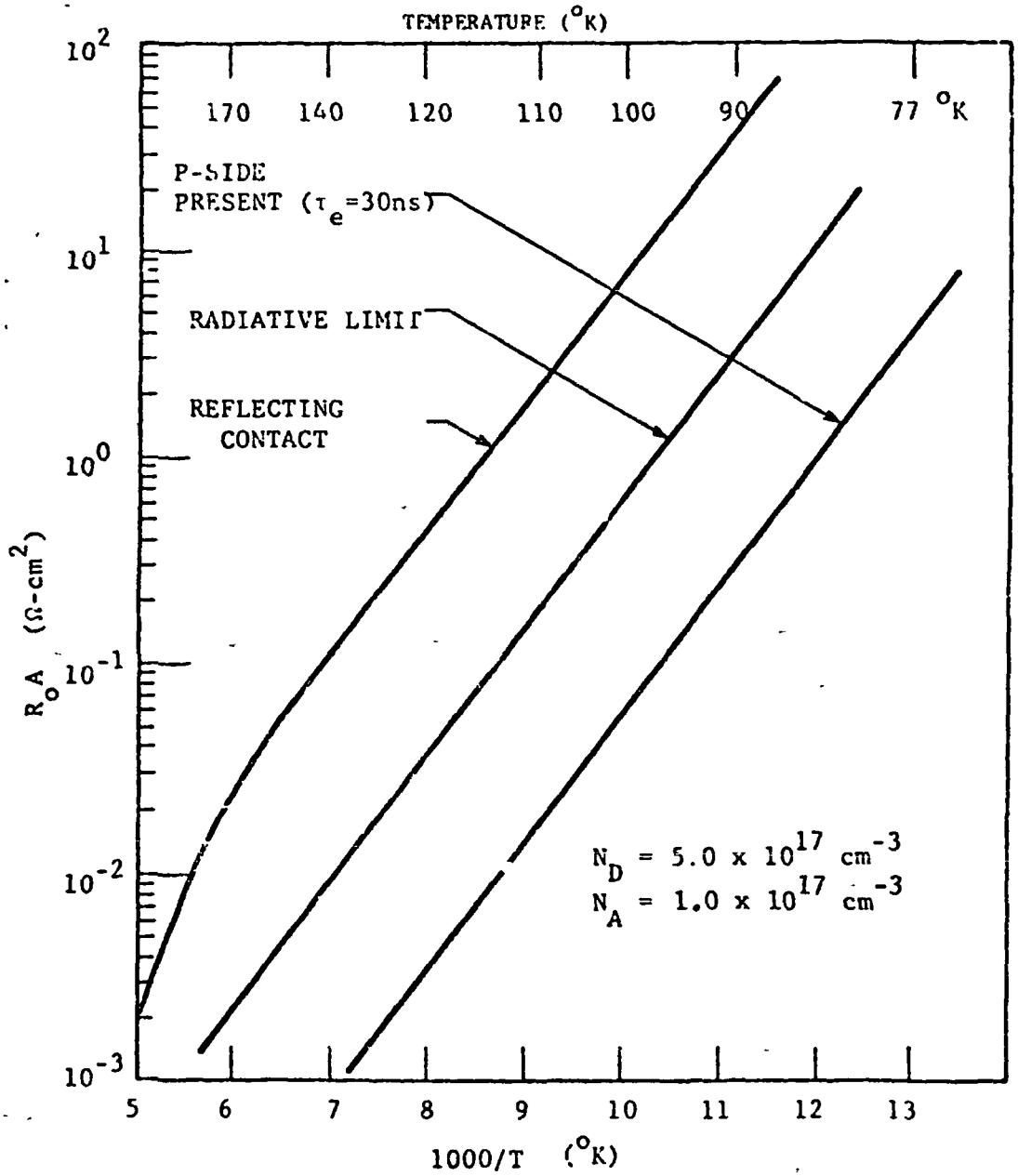

Figure 7.3 R_oA VS TEMPERATURE: n+ on p (Hg,Cd)Te PHOTODIODE

In summary, the ultimate performance of (Hg,Cd)Te photodiodes at moderate and elevated temperatures appears to be limited only by radiative recombination, thus they could achieve the ultimate limit for quantum detectors. The conclusions rest on two developments made during the program: (1) that doping n-type (Hg,Cd)Te to degeneracy significantly reduces Auger recombination, and (2) that Auger recombination is moderately doped ($4x10^{17} < N_A < 1.0x10^{18}$ cm^{-3}) is limited by electron-electron collisions with resulting Auger lifetimes substantially longer than n-type (Hg,Cd)Te and longer than the radiative lifetime. The device structure which can achieve the ultimate performance is a n+ on p design.

Performance of present (Hg,Cd)Te photodiodes have been analyzed. The devices are limited by a short, Shockley-Read limited lifetime on the p-side. This lifetime is approximately 30 ns. Improvements in this lifetime are crucial to achieving the theoretical limit to performance.

7.4 PRESENT PERFORMANCE AND ULTIMATE LIMITS: PHOTOCONDUCTIVE DETECTORS

The ultimate theoretical limit for a photoconductor is the same as that for a photodiode; Figure 7.1 shows the limit to detectivity which could be achieved. The ability of a photoconductor to achieve this detectivity depends on the following conditions:

1) Lifetime should be limited by radiative rather than Auger or Shockley-Read combination.

2) Generation-recombination noise should dominate Johnson noise

3) The thickness of the photoconductor must be approximately an optical absorption depth

in addition, 1/f noise should be negligible.

(Hg,Cd)Te has been the only material developed for 8-14 μm photoconductors. Present (Hg,Cd)Te photoconductors use n-type dopings as low as possible to achieve maximum detectivity; at moderate and elevated temperature th (Hg,Cd)Te would be intrinsic. The detectivity of the present best (Hg,Cd)Te photoconductors is limited by generation noise which is determined by Auger recombination. Thus, further significant improvement in (Hg,Cd)Te photoconductors at elevated temperatures is unlikely.

The ultimate limit to detectivity for n-type (Hg,Cd)Te photoconductors calculated for a constant 12-μm cutoff is shown in Figure 7.4. The detectivity falls well below the ultimate limit for quantum detectors at elevated temperatures due to the Auger lifetime. For moderate temperature (77-120K) operation however, (Hg,Cd)Te photoconductors could achieve detectivity within a factor of 3 of the theoretical limit for quantum detectors.

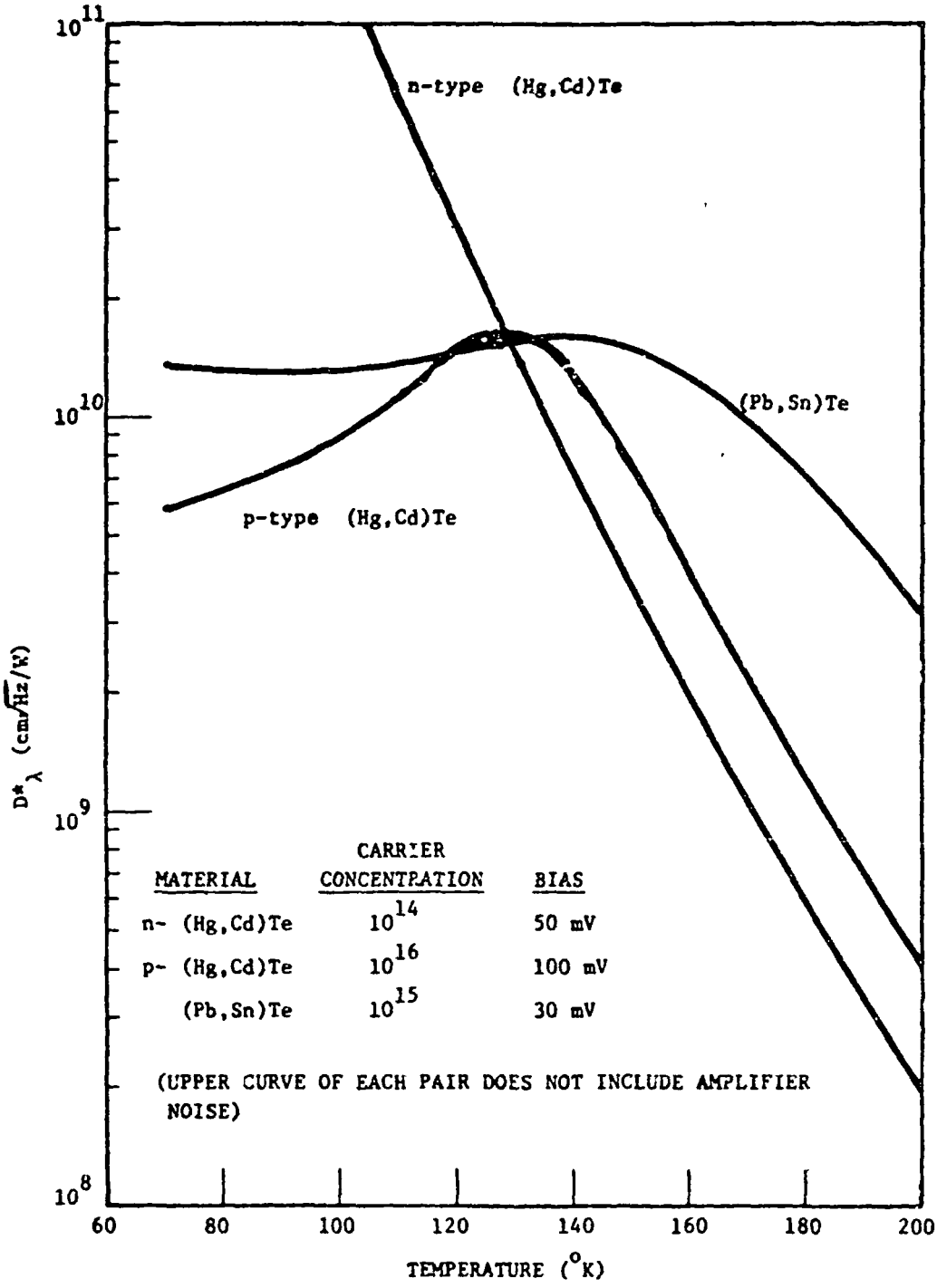

Figure 7.4 D^*_λ VS TEMPERATURE: LIMIT FOR (Hg,Cd)Te & (Pb,Sn)Te PHOTOCONDUCTORS

77-1-6

The p-type (Hg,Cd)Te photoconductors have not been developed, largely because the performance at moderate (less than 150K) temperature is considerably lower than n-type (Hg,Cd)Te. At elevated temperatures p-type (Hg,Cd)Te could offer performance superior to n-type due to the much longer Auger lifetime in p-type (Hg,Cd)Te. However, for temperatures above 150K detectivities above 8.0×10^9 cm $Hz^{\frac{1}{2}}/W$ cannot be attained, making p-type (Hg,Cd)Te photoconductors unattractive.

(Pb,Sn)Te has also been examined as a photoconductive material. The barrier to (Pb,Sn)Te as a photoconductor has historically been the high carrier concentration in both bulk and epitaxial (Pb,Sn)Te. For carrier concentrations above 1.0×10^{15} cm^{-3} detectivities above 1.0×10^{10} cm $Hz^{\frac{1}{2}}/W$ are not possible; carrier concentrations lower than 1.0×10^{16} cm^{-3} were not regularly obtained in (Pb,Sn)Te until recently.

If low carrier concentration (Pb,Sn)Te can be obtained ($N < 5 \times 10^{14}$ cm^{-3}) then (Pb,Sn)Te photoconductors are more attractive on a theoretical basis than n or p-type (Hg,Cd)Te for operating temperatures above 160K. However, due to the rapid Auger recombination in (Pb,Sn)Te, the theoretical limit for quantum detectors cannot be attained.

In summary, neither (Hg,Cd)Te nor (Pb,Sn)Te photoconductors appear capable of achieving the ultimate limit to detectivity for quantum detectors. At elevated temperatures, (Pb,Sn)Te theoretically appears to offer the best performance, but requires carrier concentrations below 1.0×10^{15} cm^{-3}. Carrier concentrations at this level have not been achieved. At low and moderate temperatures ($T < 140K$), n-type (Hg,Cd)Te theoretically offers the best performance and presently achieves performance near this level.

Both amplifier coupling and power dissipation have been examined. While it appears possible to design amplifiers for the very low resistance values typical of photoconductors at elevated temperatures, the amplifiers would have very high power dissipation and would be suitable only for off-focal-plane use. Power dissipation of the photoconductor alone is of order 10-60 μW per element and would not be a driving factor except in large focal planes.

7.5 THERMAL DETECTORS

Thermal detectors are a fundamentally different class of detectors than quantum detectors with different limitations. The type of thermal detector judged most likely to be useful in future NASA applications is the pyroelectric detector; thus, only pyroelectrics were examined in detail.

The ultimate limit to detectivity in pyroelectrics is temperature fluctuation noise between detector and environment. If g is the thermal conductivity between detector and its surroundings,

$$D^*_\lambda = (4kT^2g)^{-\frac{1}{2}} \qquad (7.8)$$

If the detector can be sufficiently well insulated thermally from its environment, then g is limited only by radiative heat flow given by $g=4\sigma T^3$ where σ is the Stefan-Boltzmann constant. The limit to D* for a pyroelectric is thus

$$D^*_\lambda = (16\, k\, \sigma\, T^5)^{-\frac{1}{2}} \qquad (7.9)$$

which for T=300K is 1.8×10^{10} cm $Hz^{\frac{1}{2}}/W$.

Performance of present pyroelectrics is limited by two factors: dielectric loss in the detector and high thermal conductance between detector and its surroundings. The detector limited D* is given by

$$D^*_d = \frac{p}{C\sqrt{\epsilon}}\left(\frac{1}{\tan\delta}\right)^{\frac{1}{2}}\left(\frac{1}{8\pi kT\epsilon_o d}\right)^{\frac{1}{2}}\left(\frac{1}{f}\right)^{\frac{1}{2}} T_r \qquad (7.10)$$

where

p = pyroelectric coefficient

C = volume specific heat of detector material = ρc

ϵ = dielectric constant

$\tan\delta$ = dielectric loss coefficient

d = detector thickness

f = frequency

T_r = thermal loss factor

Improvements in pyroelectrics will require (1) improvement in material parameters, (2) reduction of dielectric loss (3) decreased thickness d or (4) improved thermal isolation. Each of these was examined; the following conclusions were obtained:

(1) Material parameters. The figure of merit for a pyroelectric detector is $p/C\sqrt{\epsilon}$. Liu, Kook and Lone[6,8] have found that even though any one of the parameters may vary significantly among pyroelectric materials, the figure of merit was found to be constant to within approximately a factor of 2. It was concluded that it was unlikely new pyroelectric materials with significantly improved figures-of-merit would be found.

(2) Reduced dielectric loss. The origin of the dielectric loss ($\tan\delta$) is not well understood. Analysis of data on the best present pyroelectric detectors suggest that, at least at low frequencies, the measured loss is really

due to thermal exchange with the environment rather than a material or a processing phenomena. Further experimental investigation into the origin of dielectric loss in pyroelectric detectors is warranted. A practical limit to decreased loss is amplifier noise; as tanδ is reduced the pyroelectric noise can decrease below the noise of available amplifiers. This limit, of course, depends on parameters such as detector area and capacitance.

(3) Reduced thickness. Reducing pyroelectric thickness improves D* as $d^{-\frac{1}{2}}$. Over the past few years there has been substantial effort to improve D* by reducing the thickness in crystalline pyroelectrics. Present limits to thickness are 2 μm, achieved by ion beam milling. Further reductions in thickness of crystalline pyroelectrics will be limited by the necessity of having the detector self-supporting for thermal isolation. Thicknesses ~1 μm appear to be a reasonable limit.
Thinner detectors can be obtained using organic films. Films less than 1-μm thick appear practical. At present the films are limited by a low pyroelectric coefficient and high dielectric loss. However, substantial room for improvement remains and pyroelectric polymers may become important in the future

(4) Improved thermal isolation. Improving thermal isolation is the most important factor in improved detectivity. The present best pyroelectric detectors fabricated both from SBN and $LiTaO_3$ appear to have detectivity limited by thermal conductance between detector and surroundings. Further improvements, however, appear quite difficult. The best present pyroelectric detectors are usually in contact with the substrate only on supports well isolated thermally from the electrically active region and are operated in vacuum.

Figure 7.5 shows the detectivity for an SBN pyroelectric at 300°K as a function of the product of frequency times thickness. Curves are for a dielectric loss factor of 0.003 for various thermal conductances. Data on the best present SBN pyroelectrics are shown also. As Figure 7.5 indicates, high detectivity can be obtained only at relatively low frequencies even with very thin detectors. A detectivity of 5.0×10^9 cm $Hz^{\frac{1}{2}}/W$ could be achieved only out to 20 Hz for a detector 5-μm thick, or 50 Hz for a 2-μm thickness. High detectivity will be obtained only at relatively low frequencies. Achieving high detectivity will also require good thermal isolation; this will be difficult for small pyroelectric elements in array configurations. Higher frequency response can be obtained if the dielectric loss is improved. A 2-μm thick pyroelectric with $\tan\delta = 1.0\times10^{-4}$ could achieve $D^* = 5.0\times10^9$ cm $Hz^{\frac{1}{2}}/W$ at 500 Hz.

In summary, pyroelectrics offer room temperature operation with detectivity as high as 5.0×10^9 cm $Hz^{\frac{1}{2}}/W$. However, pyroelectrics for high detectivity applications will probably remain low frequency devices (~10-100 Hz) and appear difficult to realize in small device areas (< 10^{-3} cm^2). Difficulties such as thermal isolation of the detector will become increasingly a problem for higher detectivity and smaller element size.

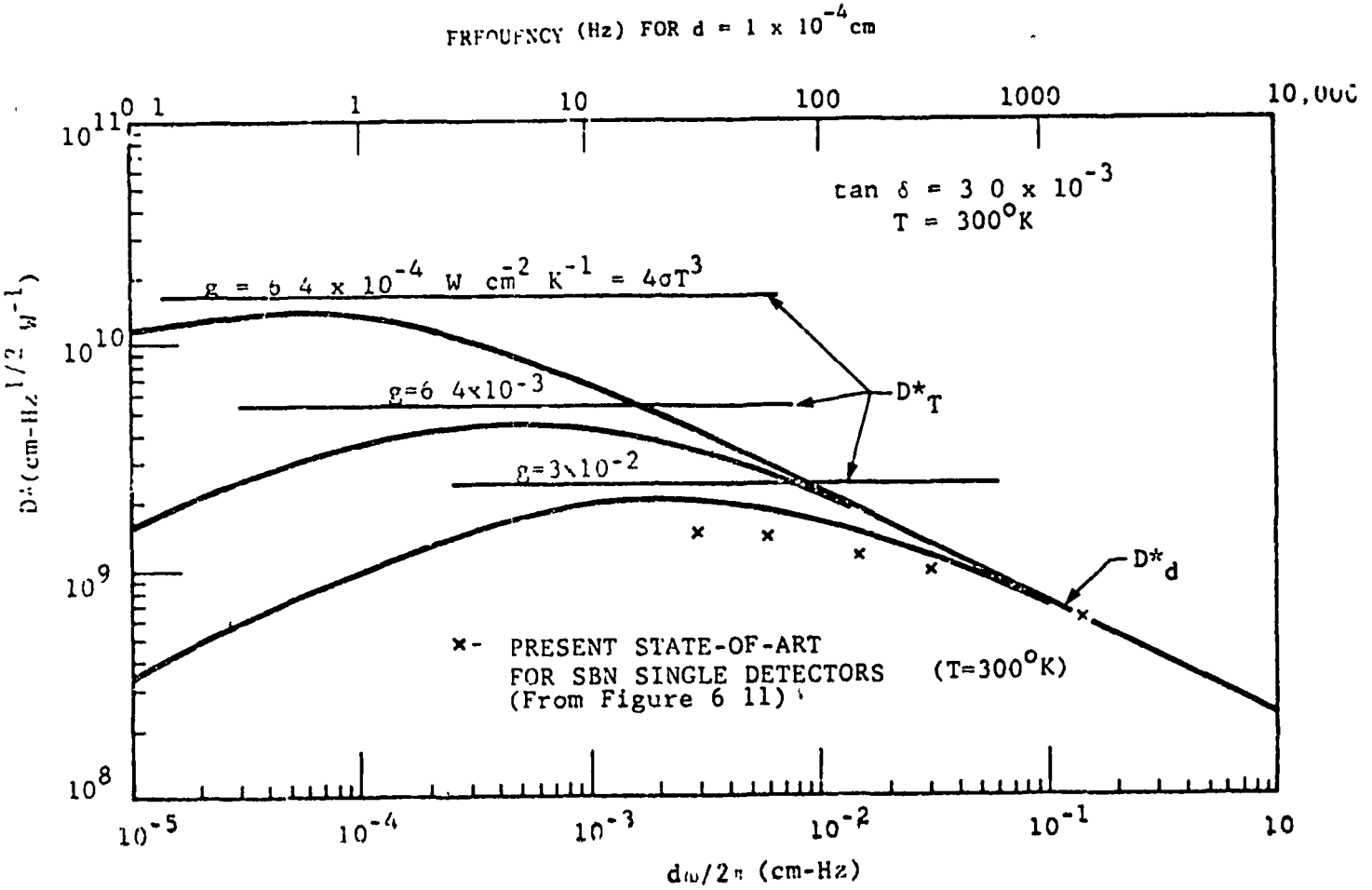

Figure 7.5 CALCULATED DETECTOR-LIMITED DETECTIVITY D^*_d FROM EQ. 6.28 (CURVES) AND CALCULATED THERMAL FLUCTUATION LIMITED DETECTIVITY D^*_T FROM EQ. 6.27 (HORIZONTAL LINES) FOR SBN PYROELECTRIC DETECTORS PLOTTED FOR VARIOUS VALUES OF THERMAL CONDUCTANCE g VERSUS THE PRODUCT OF DETECTOR THICKNESS d AND MODULATION FREQUENCY $\omega/2\pi$. DATA FOR SBN AT 300 K IS TAKEN FROM FIGURE 6.11 (REFERENCE 6.10).

APPENDIX A

STEADY STATE CALCULATIONS AND SWEEPOUT CORRECTION

The signal and noise mechanisms in photoconductors (Subsection 2.4) were found to depend upon the steady state electron and hole population densities and the effective incremental lifetime. The situation is complicated by ambipolar carrier drift in the applied field, which has the effect of reducing both the population densities and the lifetime. The procedure followed here is to calculate the populations and lifetime ignoring sweepout and then give an approximate correction method for sweepout.

In the ideal photoconductor considered here, the thermal generation-recombination mechanisms are the radiative and Auger. The rate equations are obtained from mass action principles as follows:

$$g_R = Bn_i^2 \quad \text{(radiative generation rate)} \tag{A.1}$$

$$r_R = Bnp \quad \text{(radiative recombination rate)} \tag{A.2}$$

$$g_A = G_{ee}\left(\frac{n}{n_o}\right) + G_{hh}\left(\frac{p}{p_o}\right) \quad \text{(Auger generation rate)} \tag{A.3}$$

$$r_A = G_{ee}\frac{n^2 p}{n_o^2 p_o} + G_{hh}\frac{p^2 n}{p_o^2 n_o} \quad \text{(Auger recombination rate).} \tag{A.4}$$

Here n_o and p_o are the electron and hole densities at thermal equilibrium, $n = n_o + \Delta n$, $p = p_o + \Delta n$, and $n_i^2 = n_o p_o$; B is the radiative capture probability (A.1) and G_{ee}^o and G_{hh} are equilibrium Auger generation rates. (A.2)

The net thermal recombination rate (which can be expressed as a function of n only since $p = n - [n_o - p_o]$) is:

$$R(n) = (r_R - g_R) + (r_A - g_A). \tag{A.5}$$

The steady state parameters for optical bias ϕ_B (zero electrical bias) are obtained by equating R to the externally stimulated generation rate:

$$R(n_B) = R(n_o + \Delta n_B) = \eta\phi_B/t. \tag{A.6}$$

The incremental lifetime is:

$$\hat{\tau}(n_B) = \left[\frac{d}{dn} R(n)\right]^{-1}_{n=n_B}. \tag{A.7}$$

When a bias voltage is applied to the detector, a nonuniform concentration profile is established between the electrodes due to ambipolar drift in the electric field.[A.3] If diffusion is neglected, the steady state relation describing this profile is:

$$R(n) = \mu_a(n)\, E \frac{dn}{dx} = \eta\phi/t, \tag{A.8}$$

with the ambipolar mobility μ_a given by:

$$\mu_a = \mu_e(n-p)/(bn+p). \tag{A.9}$$

If the coordirate direction is chosen so that x = 0 locates the electrode toward which the minority carriers drift, the appropriate boundary condition for ohmic contacts is $\Delta n = 0$ ($n=n_o$ and $p=p_o$) at $x = 0$. The average n_B corresponding to ϕ_B requires integrating (A.8), using $n(0) = n_o$, to obtain n(x) and then averaging:

$$n_B = \frac{1}{\ell}\int_o^{\ell} n(x)dx. \tag{A.10}$$

For low optical bias, μ_a is constant and $R = (n-n_o)/\tau_o$ where τ_o is constant. Then equations A.8 and A.10 yield:

$$n_B - n_o = \frac{\eta\phi_B\tau_o}{t}\left\{1 - \frac{\mu_a E\tau_o}{\ell}\left[1 - \exp\left(-\ell/\mu_a E\tau_o\right)\right]\right\} \tag{A.11}$$

For large optical bias μ_a and R may both vary appreciably with x so the exact determination of n_B requires numerical integration. However, this may be avoided by introducing into equation A.5 an empirical sweepout recombination term r_s:[A.4]

$$r_s(n) = \left(\frac{2V\mu_e}{\ell^2}\right)\frac{n_o-p_o}{bn_o+p_o}\left(\frac{bn_o+p_o}{bn+p}\right)^{0.75}\cdot(n-n_o) \tag{A.12}$$

$$R_{eff} = (r_R - g_p) + (r_A - g_A) + r_s \tag{A.13}$$

The approximate n_B is determined as the solution of:

$$R_{eff}(n_B) = \eta\phi_B/t, \tag{A.14}$$

and the effective ordinary and incremental lifetimes are analogous to the corresponding lifetimes defined in Subsection 2.3:

$$\tau_{eff} = (n_B - n_o)/R_{eff}(n_B) \tag{A.15}$$

$$\hat{\tau}_{eff} = \left[\frac{d}{dn} R_{eff}(n_B)\right]^{-1}. \tag{A.16}$$

The approximations A.12 through A.14 have been found to have a wide range of application in both n- and p-type calculations. Errors in n_B are negligible when r_s is very small or very large. Worst case errors, when $r_s \sim R$, are not more than 12% at low to moderate ϕ_B such that $n_B \sim 5(n_o+p_o)$.

REFERENCES

A.1 W. van Roosbroeck and W. Shockley, Phys. Rev. 94, 1556 (1954).

A.2 J.S. Blakemore, "Semiconductor Statistics," Pergamon, 1962.

A.3 See for example J.E. Hill and K.M. van Vliet, Physics 24, 709 (1958).

A.4 S.B. Schuldt, "Approximate Determination of Minority Carrier Sweepout in a Photoconductor at High Illumination Levels," Honeywell Corporate Research Center Memo, 1975.